Myosin structural dynamics: mechanistic insights and therapeutic technology developments

A THESIS SUBMITTED TO THE FACULTY OF THE
UNIVERSITY OF MINNESOTA
BY:

John A. Rohde

IN PARTIAL FULFILLMENT OF THE REQUIERMENTS FOR THE DEGREE OF
DOCTOR OF PHILOSOPHY

Advisor:

Dr. David D. Thomas

Department of Biochemistry, Molecular Biology, and Biophysics

March 2019

ACKNOWLEDGEMENTS

This work would not be possible without the insightful guidance and tireless support of my thesis advisor Dr. David D. Thomas – the William F. Dietrich Professor of Biochemistry, Molecular Biology and Biophysics. Thank you Dave for giving me confidence and always making my success your top priority. My progress and publications are also thanks to the support and mentorship of Dr. Joseph M. Muretta. Thank you Joe for your generosity and patience, for giving me a head start in graduate school with your dedicated training and attention, and for sharing your excitement and curiosity for science and the undiscovered. The DDT lab has been incredible: answering a million questions, providing training, tricks-of-the-trade, and all manner of assistance. All of the work with my name on it has been a team effort with contributions from dozens of my lab mates—thank you all. Special thanks to co-authors Sinzi Cornea, Dan Johnsrud, Osha Roopnarine, Piyali Guhathakurta, and Ewa Prochniewicz. The John Lipscomb lab and especially Dr. Melanie Rogers have been exceptionally generous with resources and time, and provided invaluable training that improved my research. Thank you also to my collaborators and co-authors in the Christopher Yengo lab at Penn State's Hershey Medical School, I have been lucky to work with such talented and hard-working individuals.

Thank you Dr. Staci Solin for inspiring me with your passion for discovery, tireless pursuit of knowledge, and commitment to excellence. I will always respect and be inspired by your spark and competitiveness.

Finally, thank you to the University of Minnesota, the College of Biological Science, the BMBB department, and the National Institutes of Health (NIH) for financial support over the past five years.

This dissertation contains material derived from my published articles, as defined at the start of each chapter or subsection. Some of this material is in the Introduction and Future Directions chapters.

DEDICATION

This work is dedicated to my parents, Chris and Mary Rohde. Thank you for always encouraging and believing in me, for sharing your perceptive worldview, your selflessness, your clever humor, and your focus on what is best in life. You have taught me so much, given me an excitement for learning and science, and always challenged me to dig deeper and go further. Thank you.

ABSTRACT

A major focus in molecular biophysics is to understand how protein structural isomerizations correspond to cellular and organismal physiology. The heart generates force to perfuse the body with oxygenated blood through contractile units in myocytes called sarcomeres. The primary force-generating protein in this contractile apparatus is myosin. Our lab has developed a strategic tool called transient time-resolved FRET, $(TR)^2$FRET, to measure directly, with sub-nanometer and sub-millisecond resolution, the structural and biochemical kinetics of muscle myosin. This tool allows us to directly determine how myosin's power stroke is coupled to the thermodynamic drive for force generation—the entropically-favored dissociation of inorganic phosphate.

My research revealed that actin initiates the force-generating power stroke before phosphate dissociation, revealing how power output and efficiency are regulated by the distribution of myosin's structural states. $(TR)^2$FRET is also a powerful tool to examine small-molecule perturbations of structural transitions within myosin's kinetic cycle. Omecamtiv mecarbil (OM), a putative heart failure therapeutic, increases cardiac contractility. My results demonstrate that OM stabilizes myosin's pre-powerstroke structural state and significantly slows the actin-induced powerstroke. I also used transient biochemical and structural kinetics to elucidate the molecular mechanism of mavacamten, an allosteric cardiac myosin inhibitor and prospective therapeutic for hypertrophic cardiomyopathy. I found that mavacamten stabilizes an auto-inhibited state of two-headed cardiac myosin that is not present in the single-headed myosin motor fragment. From these results, we predicted that cardiac myosin is regulated by an

interaction between its two heads and the thick filament, and proposed that mavacamten stabilizes this state.

In expressed myosin V, I investigated two mutations in the converter domain, and one mutation in the phosphate release tunnel, to examine how point mutations alter specific structural transitions in the ATPase cycle of the motor protein myosin. Transient kinetics and FRET-based experiments demonstrate that one mutation slowed the recovery-stroke rate constants, while a second mutation enhanced these steps. These mutations correspond to human mutations that give rise to dilated or hypertrophic cardiomyopathies, respectively.

Together these experiments reveal new and important mechanistic insights into myosin's structural dynamics and provide proof-of-concept results for developing therapeutic technology.

TABLE OF CONTENTS

LIST OF FIGURES

LIST OF TABLES

LIST OF ABBREVIATIONS

A	Actin
AF488	An AlexaFluor® dye with peak excitation at 488 nm
ADP	Adenosine diphosphate
ATP	Adenosine triphosphate
CaM	Calmodulin
cHMM	Cardiac heavy meromyosin
Cy3	An Invitrogen® dye with peak excitation at 532 nm
D	ADP
DCM	Dilated cardiomyopathy
DWR	Direct waveform recording
DTT	Diothiolthreitol
EDTA	Ethylenediaminetetraacetic acid
ELC	Essential light chain
EM	Electron microscopy
FlAsH	Fluorescin arsenical hairpin dye
FRET	Förster Resonance Energy Transfer
FWHM	Full width at half maximum
HCM	Hypertrophic cardiomyopathy
HMM	Heavy meromyosin
IHM	Interacting heads motif
IRF	Instrument response function
M	Myosin, or myosin's lever arm in a rigor-like orientation
M*	Lever arm in a "up" conformation (PDB: 1DFL)
M**	Lever arm in a "down" conformation (PDB: 1B7T)
M2β	β-cardiac myosin II
Mant	N' - Methylanthraniloyl
Mant-ADP	2'-(or-3')-O-(N-Methylanthraniloyl) ADP

Mant-ATP	2'-(or-3')-O-(N-Methylanthraniloyl) ATP
Mava	Mavacamten
MDCC	7-Diethylamino-3-((((2-Maleimidyl)ethyl)amino) carbonyl)coumarin
MV	Myosin V (five)
MYH7	β-cardiac myosin gene in humans
Myk-461	Mavacamten
OM	Omecamtiv Mecarbil
PBP	Phosphate binding protein
P_i	Inorganic phosphate ion
PIA	Pyrene iodoacetamide
QSY	QSY® dye, specifically QSY-9
R	Dye-dye distance
R_0	Förster distance
RLC	Regulatory light chain
S1	Single-headed myosin fragment post-digestion
SD	Standard deviation
SEM	Standard error of the mean
skHMM	Skeletal heavy meromyosin
SRX	Super-relaxed state
ss-FRET	Steady-state FRET
TCSPC	Time-correlated single photon counting
TR-FRET	Time-resolved FRET
$(TR)^2$FRET	Transient time-resolved FRET
T	ATP
V_i	Vanadate ion
WT	Wild type

CHAPTER 1: INTRODUCTION

This chapter contains material derived from my published papers[1-4], including reproduced and adapted figure subpanels and reproduced and paraphrased sections.

1.1 MUSCLE MYOSIN, PROTEIN DYNAMICS, AND STRUCTURAL KINETICS

Myosin-family proteins use the free energy of ATP hydrolysis to generate force and drive movements required for normal cellular physiology. These motor proteins drive muscle contraction, help control cell division and cellular motility, move organelles through the cytoplasm, and are crucial proteins in the cellular mechanical-sensing machinery [5, 6]. One method to understand how myosin and related enzymes function in cells, and how to modulate their activity to treat disease, is to determine how the structural dynamics and biochemical kinetics of this protein are coupled to one another. Even though high-resolution crystal structures provide single frozen protein structures in one or more biochemical states, the job of determining the physiological relevance of these still images remains a challenge generally in structural biophysics and in the myosin field.

Both skeletal and cardiac muscle is striated (Fig. 1A). The majority of the protein content in multi-nucleated myocytes of muscle tissue is made up of a contractile assembly called the sarcomere (Fig. 1B). There are three primary filaments inter-digitated within the sarcomeres: titin, actin, and myosin. Myosin is the force-generating, ATP-hydrolyzing mechanochemical enzyme within this assembly (Fig. 1C). Muscle myosin is a heterohexamer. This protein complex contains dimerized myosin heavy chains, via a coiled-coil domain, with each heavy chain bound by two light chains. Located nearest to myosin's ATP-binding and actin-binding catalytic domain (head) is the essential light

chain (ELC), followed by the regulatory light chain (RLC) (Fig. 1D). The primary function of muscle is to exert force, achieved through the structural isomerization of the motor protein myosin (Fig. 1E). Advancements in technology and newly developed, clinically-relevant small-molecule heart failure drugs make myosin's structural transitions an important and exciting area of study. Despite decades of research, myosin's structural transitions under load had never been directly detected in high resolution. The goal of my graduate research has been to (1) determine the structural dynamics of cardiac, skeletal, and non-muscle myosin's lever arm[1-4], (2) characterize the structural kinetics of the dimeric heads *in vitro*[3], (3) study changes to these structural transitions in the presence of small-molecule effectors[2, 3]; and (4) to perturb these structural transitions when the myosin complex is expressed with disease-causing, allosterically-disrupting mutations[4, 7]. The importance of understanding the force-generating structural dynamics of myosin and the interactions between actin, myosin, and other sarcomeric proteins is evident from the wide range of disease conditions that result from mutations to the thick and thin filament proteins[8] and the promising prospect of small-molecule effectors that bind myosin for treating these disease states[9].

Our lab has combined sub-nanosecond time-resolved FRET measurements with millisecond-resolved transient biochemical kinetics in order to measure sub-nanometer structural transitions in myosin during the actin-activated myosin power stroke and recovery stroke[10]. This intermolecular FRET measurement is accomplished in multiple ways with site-directed fluorescent labeling of myosin's regulatory light chain (RLC) and bound nucleotide (Fig. 1F-G; Chapters 2-4) [1]. An alternative site-directed labeling scheme on myosin's N-terminal domain and calmodulin (CaM) (Chapter 5) has also been

developed[4]. The former labeling scheme permits the measurement of transient time-resolved FRET, or $(TR)^2$FRET, without mutating the myosin heavy chain and permits the use of tissue-extracted myocardium. The later labeling scheme has been applied to both expressed non-muscle myosin V and human β-cardiac myosin.

The power stroke and recovery stroke are the two main structural isomerizations associated with force generation in the mechanochemical kinetic cycle of the motor protein myosin. Myosins use the chemical energy of ATP hydrolysis to generate movement in cells. But, how exactly this occurs remains debated [5, 6, 11] because, though high-resolution protein structures reveal discrete structural states of myosin, they do not show how these states exchange during multi-step enzyme cycling. This is a general problem requiring experimental approaches with both high structural and kinetic resolution.

One popular model [6, 12] for myosin's mechanochemical kinetic cycle proposes that after ATP hydrolysis, myosin interacts weakly with actin, and this interaction initiates an ordered series of structural and biochemical transitions. These transitions culminate in first, (1) the dissociation of the hydrolyzed γ-phosphate, followed by (2) an isomerization in the actin-binding interface of myosin to a state that binds actin with nanomolar (nM) affinity, and finally a rotation of the myosin light-chain domain (LCD, or lever arm) toward the plus end of the actin filament. This rotation couples the thermodynamic free energy of phosphate release and actin binding into mechanical work. A number of results question this model, however, including spectroscopic data showing that first, (1) a structural transition in the myosin relay helix, hypothesized to be coupled to lever arm rotation, precedes (2) P_i release [10] and separately, that force development precedes P_i release in muscle fibers [13].

Determining how these events take place in solution and in cells is an important question for the following reasons: (1) differences in the mechanics of different myosin isoforms likely reflect differences in how the biochemical and structural transitions, described above, are coordinated [12], (2) disease-causing mutations in the myosin heavy chain or its bound light chains should alter this coordination [14, 15], (3) studies demonstrate that perturbing mechanochemical coupling in myosin is a viable therapeutic approach to treat myosin-associated diseases [16, 17], and (4) myosin has been a model system for mechanochemical coupling in general. Thus, what we learn about the myosin power stroke will likely inform work on related enzymes [11]. In my graduate work I designed experiments to better understand the coordination of actin binding, phosphate release, and lever arm rotation to address each of these goals.

In non-muscle myosin V the Thomas Lab and the Yengo Lab at Penn State investigated two mutations in the converter domain (R712G and F750L) to elucidate how point mutations specifically alter structural transitions in the myosin ATP-hydrolyzing cycle; and how they affect myosin mechanochemistry [4]. The corresponding mutations in human β-cardiac myosin are associated with hypertrophic and dilated cardiomyopathy, respectively (HCM, DCM) [4]. Even though the mutants had similar steady-state actin-activated ATPase and unloaded *in vitro* motility sliding velocities compared to WT, both were less able to overcome frictional loads, as measured in the loaded motility assay. Transient kinetic analysis and stopped-flow FRET experiments showed that the R712G

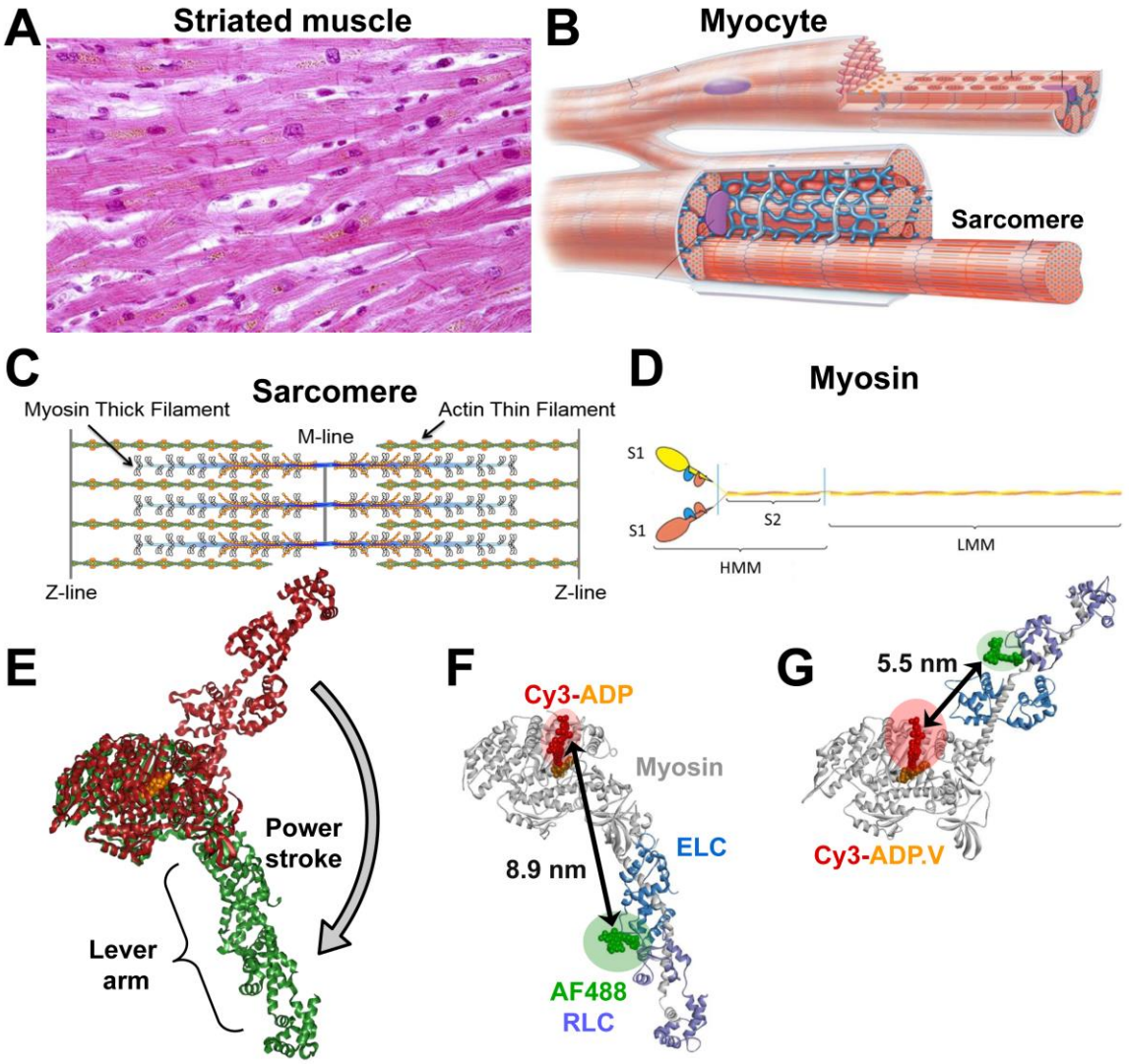

Fig. 1. Site-directed probes to detect the structural state of muscle myosin.
(A) Cardiac muscle is striated, image from ref. [18]. (B) Cartoon of a cardiac myocyte, with the cut-away emphasizing the contractile apparatus, the sarcomere, image from ref. [19]. (C) Two-dimensional depiction of the sarcomere, emphasizing the interdigitated thick and thin filaments. Two-headed myosin extends from the thick filament and generates force as it cyclically binds actin and ATP, and undergoes structural isomerizations; image from ref. [20]. (D) Cartoon depiction of the heterohexamer of myosin. The ATP-binding and actin-binding catalytic domaina or “heads” are shown on the left. The two light chains, the ELC and RLC, are depicted as crescents, and the long coiled-coil domain (LMM) are labeled; image from ref. [21]. (E) The single-headed myosin fragment (S1) is shown in two structural states: the lever-up, pre-powerstroke state (red, PDB: 1DFL) and the lever-down, post-powerstoke state (green, PDB: 1B7T). (F and G) One fluorescent labeling scheme showing the predicted change in inter-probe distance that accompanies the structural isomerization of the lever arm’s orientation (PDB: 1B7T and 1DFL respectively; dyes modeled). The colored circles emphasize the presence of a low-FRET state (F) or a high-FRET state (G). Adapted from [2].

mutation slowed the maximum ATP hydrolysis and recovery stroke rate constants, while the F750L mutation enhanced these steps [4]. In both mutants, the fast and slow power stroke as well as actin-activated phosphate release rate constants were not significantly different from WT [4]. Overall, this study demonstrates that myosin mutations in key allosteric pathways can shift the equilibrium and/or alter the activation energy associated with important structural transitions without altering the overall conformation of the pre- and post-power stroke states. Thus, therapies designed to alter the transition between structural states may be able to rescue the impaired motor function induced by disease mutations. Recently, the converter domain has been highlighted as hot spot for point mutations in cardiac myosin associated with inherited cardiomyopathies, indicating the importance of this region in mediating mechano-chemical coupling in all myosin motors [22].

Hypertrophic cardiomyopathy (HCM) is an extremely prevalent inherited heart disease, affecting approximately 1 in 200 individuals [23]. HCM is also the most common cause of sudden cardiac death in young people [24]. Clinically, HCM is characterized by left ventricular hypertrophy, myocyte disarray, fibrosis, and diastolic dysfunction [25-27]. Furthermore, the characteristic left ventricular hypertrophy is associated with increased contractility. Dilated cardiomyopathy (DCM) affects approximately 1 in 2500 individuals, and is the most common cause of heart failure in young adults [28]. In contrast to HCM, DCM is characterized by left ventricular dilation, myocyte death, fibrosis, and systolic dysfunction [26, 29]. However, it still remains unclear how these disease mutations impact key structural changes in the myosin ATPase cycle and how specific structure-function defects lead to disease phenotypes.

The following two paragraphs are paraphrased from published work [4]. The atomic structures of the myosin motor domain from both muscle and non-muscle myosin in several species ranging from *Dictyostelium* to humans show a conserved structural fold [30]. The myosin motor consists of four structural domains each connected by flexible linkers, an N-terminal 25 kDa domain, an upper and lower 50 kDa domain, and a 20 kDa C-terminal domain (Fig. 47A) [31]. Allosteric coupling between and within these domains coordinates ATP binding and hydrolysis in the active site to structural changes in the actin-binding region associated with actin binding/dissociation. In addition, the resetting of the lever arm for force generation (recovery stroke) and the force-generating structural isomerization of the lever arm (power stroke) are coordinated by amplifying small structural changes in the active site with large conformational changes in the converter/lever arm [32] (Fig. 47A&B). Specific allosteric pathways in the myosin motor have been proposed based on high resolution structural studies of myosin in different nucleotide states [33] and mutational structure-function studies [34]. However, many of these hypothesized pathways have not been examined with techniques that can directly examine conformational changes in real-time and examine the impact of specific point mutations on myosin mechanochemistry. Myosin V is an exemplary model for examining key structural changes and defining important allosteric pathways because there is high resolution structural information of many of the structural states in the myosin V ATPase pathway [35]. Additionally, many biochemical and biophysical studies have revealed important details about the mechanochemical cycle [36-38]. Thus, introducing mutations in crucial amino acid residues and examining how structural changes are altered in real

time will allow for a complete understanding of how point mutations can disrupt key allosteric pathways and specifically impair motor function.

Mutations in the converter domain of MYH7 (human β-cardiac myosin, M2β) have been linked to multiple opposing phenotypes. Specifically, R723G and F764L are both located in the converter domain (Fig. 47B) of human cardiac myosin, with R723G causing HCM while F764L causes DCM [39, 40]. The converter domain communicates structural changes between the lever arm and motor domain during mechanochemical cycling, thus, we hypothesized that mutations in this region would alter the movement of the lever arm in unique ways. Using an extremely high resolution FRET system developed by our labs, we examined the structural dynamics of the lever arm during the ATPase cycle in WT myosin V and the converter domain mutants R712G and F750L that are analogous to the HCM/DCM mutations in human M2β. This work emphasizes a powerful strategy of directly examining the impact of mutations on key structural changes to allow for determining how structural changes perturb motor function. This study presents direct evidence that mutations in the converter domain can uniquely alter lever arm rotation, which ultimately leads to the impaired ability to adapt to external load, describing a mechanistic explanation for the resulting disease phenotype. Our work also highlights important allosteric pathways in myosin for the communication between the active site and force generating lever arm.

1.2 FLUORESCENCE SPECTROSCOPY AND FRET: STRUCTURAL KINETICS

To track the dynamics of myosin's lever arm domain, we labeled myosin at two specific locations using fluorescent dyes (Fig. 1F-G). The two fluorophores were selected such that

the emission spectrum of one (the donor, AF488) overlaps with the excitation spectrum of the other (the acceptor, Cy3). By exploiting a quantum mechanical dipole-dipole coupling phenomenon called FRET (Förster Resonance Energy Transfer), these two fluorophores (with a characteristic distance R_0, dependent on the spectral overlap of the fluorophores chosen) function as a molecular "ruler" sensitive to nanometer length scales, R [41].

$$\text{FRET} = \frac{1}{1 + \left(\frac{R}{R_0}\right)^6} \qquad \text{[Eq. 1]}$$

Our lab has designed and built the high-throughput spectrometers and software to combine the spatial resolution (of time-resolved FRET) with temporal resolution (using a series of laser pulses)[42]. We use a stopped-flow for biochemically-initiated reactions and a pulsed laser and high-throughput detector capable of sub-millisecond acquisition [10]. This combination allowed us to make the first direct, real-time measurements of myosin's force generating structural isomerization, the power stroke (Fig. 1E) [43].

The non-radiative energy transfer between the donor fluorophore and the acceptor fluorophore is best visualized by a Jablonski diagram (Fig. 2A). This diagram illustrates the electronic and vibrational energy levels, as well as the electron transitions that correspond to the absorbance of a photon and the emission of a photon by electrons within each molecule. The rate of energy transfer (k_T) depends on the distance between fluorophores (R) and the decay time of the excited state of the donor fluorophore (k_D) (Fig. 2A). The "R^{-6}" dependence, of the energy transfer, results in a FRET-efficiency curve, where 50% energy transfer occurs at a characteristic distance, R_0, that depends on the fluorophores choses (Fig. 2B). This FRET-efficiency curve shows the dependence of energy transfer on donor-acceptor separation (R). FRET detects changes in fluorescence

that correspond to structural transitions, as illustrated on myosin during the powerstroke (Fig. 2B, inset). FRET can be used to quantify binding events, such as fluorescently-labeled ATP binding to fluorescently-labeled myosin (Fig. 2C). With saturating fluorescent-ATP mixed with fluorescent-myosin, a steady-state spectral emission plot shows a decrease of donor intensity (vertical green bar, 520 nm, Fig. 2D) and an enhancement in acceptor intensity, due to this energy transfer (565 nm, Fig. 2AD) [39]. In addition to binding, FRET—serving as a molecular ruler—is also utilized to detect intermolecular distance changes. The second reaction scheme illustrates the application of FRET to detect structural changes (Fig. 2E). The short laser pulse in the absence of fluorescent molecules has a characteristic shape known as the instrument response function or IRF (Fig. 2F, gray). In the presence of a sample containing a FRET-pair, the time-resolved fluorescent decay is markedly slower (Fig. 2F, red and green). In the data shown, a biochemically-initiated stopped flow mix resulted in a 27% increase in total integrated intensity with time. The change in the exponential decay lifetime of that fluorescent waveform corresponds to a distance change. In Fig. 2G, I have modeled that fluorescence decay change—which results from a structural change—as an exchange of myosin molecules between two discrete lever arm-orientations, each corresponding to known X-ray crystallography structures. A pulsed laser is used, and the acquisition of 500 or more waveforms reveals dynamic structural changes in real time (Fig. 2H). Each waveform is independently best-fit to a two-Gaussian distance distribution, revealing the structural dynamics of myosin's lever arm domain in real-time (Fig. 2I)[44].

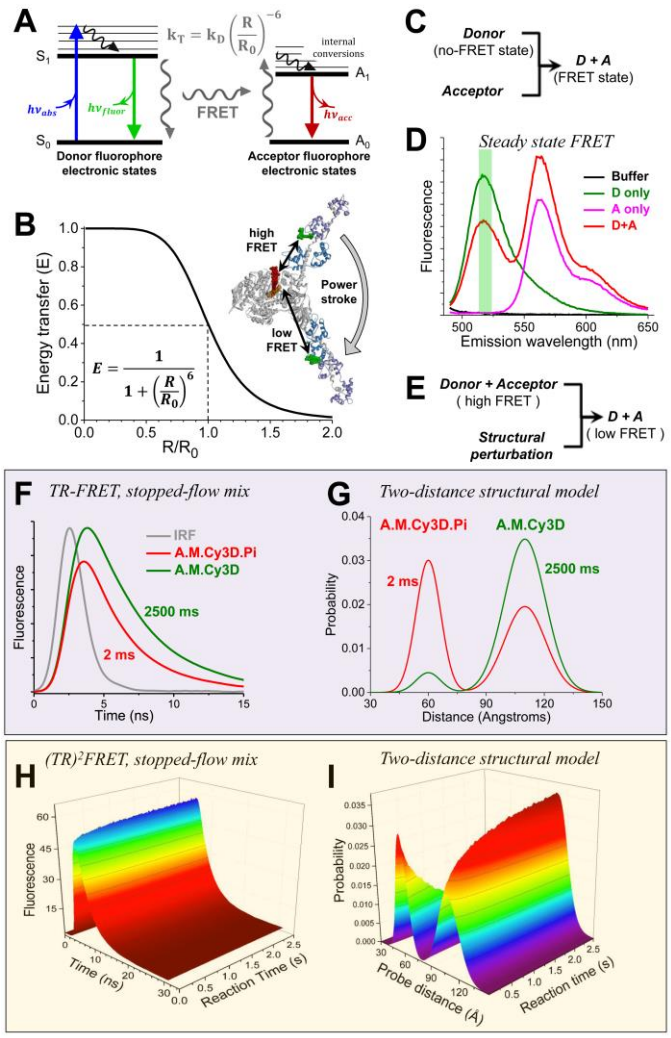

Fig. 2. FRET: steady-state, time-resolved, and transient time-resolved
(**A**) Jablonski diagram illustrating the electronic and vibrational energy levels and electron transitions corresponding to the absorbance of a photon and the emission of a photon by the donor or acceptor. The rate of energy transfer (k_T) depends on the distance between fluorophores (R) and the decay time of the excited state of the donor fluorophore (k_D). (**B**) FRET-efficiency curve showing the dependence of energy transfer on donor-acceptor separation (R). FRET detects changes in fluorescence that correspond to structural transitions, as illustrated on myosin during the powerstroke (inset; PDB: 1B7T, 1DFL). Adapted from [2] (**C**) One possible reaction scheme illustrating the use of FRET to detect binding events. Adapted from [1] (**D**) Steady-state spectral emission of a donor fluorophore (AlexaFluor 488 labeled myosin), an acceptor fluorophore (Cy3-labeled ATP), and the combination of the donor and acceptor. Excitation at 473 nm and the band-pass filter used is shown as a green band. Note the decrease in the donor emission peak when FRET is occurring[1]. (**E**) A second reaction scheme illustrating a second application of FRET to detect structural changes. (**F**) A 2.0 ns FWHM laser pulse (IRF) and the evolving time-resolved fluorescent decay of a biochemically-initiated stopped flow mix showing a 27% increase in total integrated intensity over time. The change in lifetime of that fluorescent decay corresponds to a mole fraction shift (**G**) in the two distances present (simplest and best-fit model). (**H**) A series of 500 acquisitions over 2500 ms, where the fluorescent lifetimes shown in E are the first and last in the series. (**I**) The evolving distance distributions from 500 independent mole fraction fits of the fluorescent lifetimes shown in G. Figures from:[2]. Last four subpanels adapted from [2]

Utilizing a myosin V construct, in collaboration with the Chris Yengo Lab at Penn State, we developed a site-directed FRET labeling scheme that does not rely on fluorescently labeled ATP. Myosin V was labeled on the N-terminus (NT) and on exchanged calmodulin bound on the lever arm, nearest the catalytic head (called the first IQ domain, a portion of the lever arm of the myosin heavy chain) (Fig. 3B) [4]. This labeling scheme allowed us to characterize the myosin lever-arm orientation in the absence of nucleotide (apo state), and several other states. The transient time-resolved FRET waveforms reveal substantial changes in fluorescence lifetime for various biochemical states of myosin V (Fig. 3A). This expressed protein is fluorescently labeled at the N-terminus (NT) with FlAsH and the ELC with the non-fluorescent quencher QSY. The changes to the donor fluorescence occur because of FRET, and the changing distance of the acceptor molecule, relative to the donor, in each biochemical state (Fig. 3C). The four biochemical states shown include apo myosin (M), actomyosin-ADP (A.M.D), myosin in the presence of saturating ADP (M.D), and myosin in presence of saturating ATP, which is quickly hydrolyzed to ADP.P_i, with the P_i remaining bound for a relatively long time before dissociating (M.D.Pi). The best-fit mole fractions shown in the bar graph (Fig. 3) correspond to the lifetime changes shown in Fig. 3A. In Fig. 3D-N five transient time-resolved experiments shown, both the fluorescence intensity changes during the biochemical mixes (D, F, H, J, L), and then every waveform's lifetime, independently fit to a two-distance model corresponding to the two lever arm positions. These experiments directly detect in real-time, the structural kinetics of myosin (E, G, I, K, M). For all of the five structural transients, the short-distance, pre-powerstroke state (M*) transient is shown (**Fig. 3**N). This subpanel illustrates the precision and reproducibility of $(TR)^2$FRET.

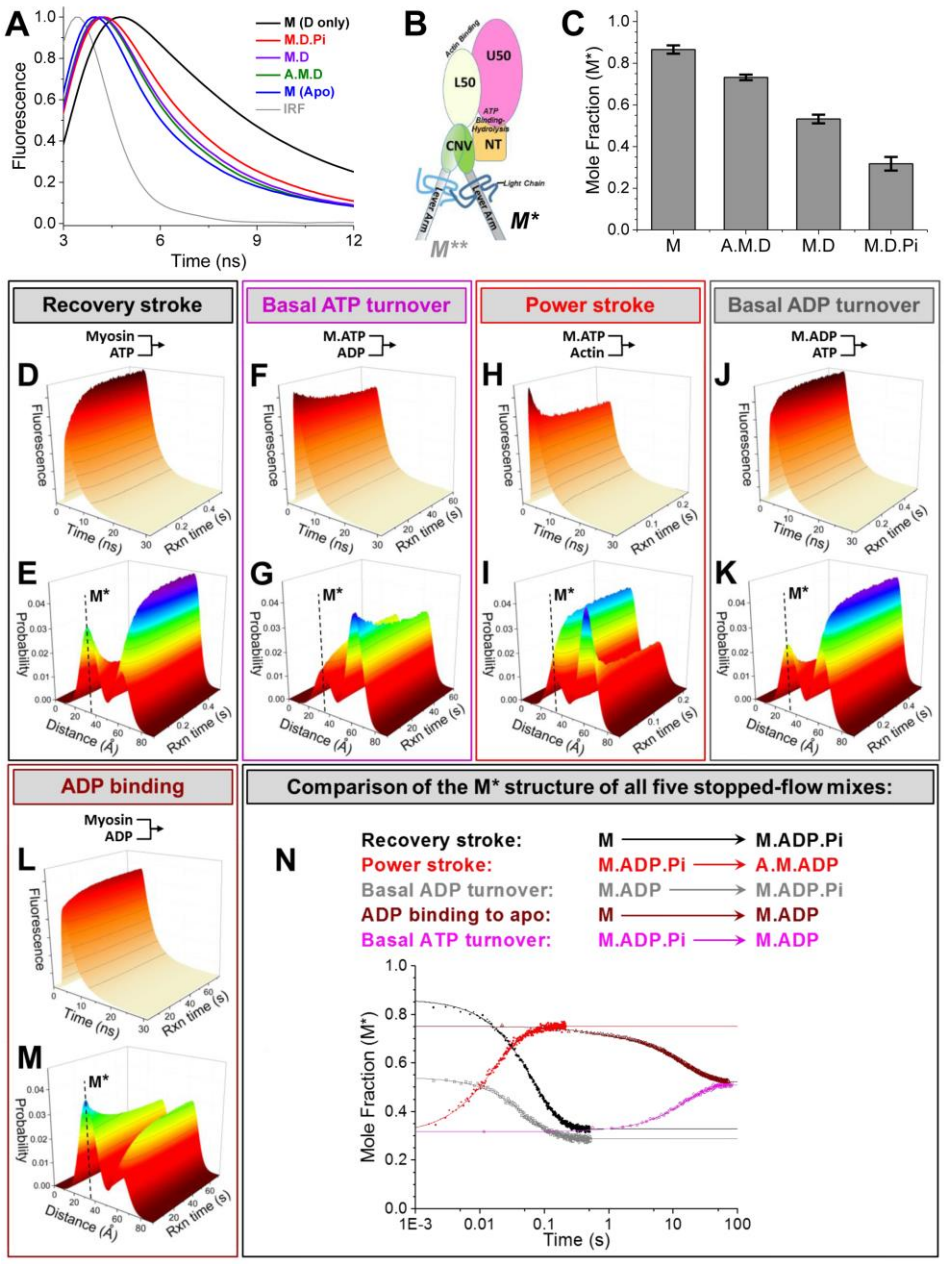

Fig. 3. Transient time-resolved FRET is a powerful tool to study structural kinetics
(A) Normalized fluorescent decays of various biochemical states of myosinV. (B) Cartoon of the myosin catalytic domain. This expressed protein was fluorescently labeled at the N-terminus (NT) with FlAsH and the ELC with the non-fluorescent quencher QSY. (C) Fit mole fractions corresponding to the lifetime changes shown in A. (D-M) Transient time-resolved FRET fluorescent waveforms acquired every 0.2 ms. The change in peak fluorescent intensity is evident in the waveforms (D, F, H, J, L), and every waveform's lifetime was independently fit for the mole fraction change, depicted in the evolving distance distributions of E, G, I, K, and M. (N) The short-distance pre-powerstroke state (M*) transient from each distance distribution is shown. Note the trends in mole fraction distributions corresponding each biochemical state. Figures from:[4]. All subpanels adapted [4].

1.3 SMALL-MOLECULE EFFECTORS TARGETING MYOSIN

The following paragraphs are paraphrased from my published work[2].

Heart failure is the leading cause of mortality in the United States[45]. A central characteristic of heart failure is a loss in cardiac contractility[46] resulting from a range of molecular factors: the inability of the sarcoplasmic reticulum to sequester Ca^{2+}, dysfunction of excitation-contraction coupling, altered myocardium metabolism, changes in the levels of gene expression, and mutations in sarcomeric proteins[47]. Treatments for heart failure include lifestyle changes, surgeries, medical devices, heart transplant, renin-angiotensin and β-adrenergic modulators, and inotropes that increase contractility. Despite these current interventions, life expectancy remains low: half of the patients diagnosed with heart failure die within five years[45].

Omecamtiv mecarbil (OM) is a small-molecule β-cardiac myosin effector in phase III clinical trials for the treatment of systolic heart failure[48]. OM was discovered from a high-throughput ATPase activity screen, from compounds identified in calcium-regulated and thin-filament-activated, ventricular cardiac myosin [16]. A high-resolution X-ray crystal structure[49] and a photo-reactive cross-linking study[16] both suggest that OM binds near the interface of several of myosin's key, conserved structural elements: the 7-stranded β-sheet, the C-terminus of the relay-helix, the SH1-helix, and the interface between the N-terminal and converter domains. Movements in these elements are coupled to the weak-to-strong actin-binding transition, rotation of the myosin light-chain domain, actin-induced phosphate and ADP release, and subsequently to force generation[6]. A number of studies have characterized OM's effect[16, 17, 49-53], and the structural basis for how OM alters force generation in the heart is likely due to a stalling of the

powerstroke[2, 54]. OM also selectively activates cardiac ryanodine receptors (RyR2) but not the skeletal isoform (RyR1)[55]. OM is in two on-going phase III trials, GALACTIC-HF and METEORIC-HF, with expected completion dates in 2021[56].

Drugs designed to treat heart failure and cardiomyopathies often have unwanted side-effects[51]. *In vivo*, OM causes a significant and clinically desirable increase to cardiac output—the volume of blood ejected from the heart per minute—a characteristic that makes the effector an ideal candidate for the treatment of systolic cardiomyopathies [48]. OM, a putative systolic heart failure therapeutic, increases and prolongs cardiac contractility, and unlike other heart failure drugs, does not perturb intracellular calcium regulation associated with contraction (Fig. 4A-B, data from [16]). Thus, by targeting myosin, OM decreases the risk to patients found in other inotropes, including the development of cardiac arrhythmias, vasodilation, hypotension, increased heart rates, and several others[51]. OM accelerates phosphate release from the myosin nucleotide-binding pocket [16, 17], and because lever arm rotation is coupled to phosphate release, we hypothesized that OM should also accelerate lever arm rotation and initiation of the powerstroke. We tested this hypothesis using $(TR)^2$FRET (Chapter 3).

In addition to OM, a second major cardiac myosin effector is also in clinical trials, mavacamten[9]. The hypertrophic cardiomyopathy mutation R403Q results in enlarged, diseased hearts with significant fibrosis (lower right, arrows). Heterozygous mice with the R403Q mutation that were administered mavacamten (mava) do not display the disease phenotype, indicating the drug prevents deleterious remodeling of the myocardium (Fig. 4C-D, data from [9]). A significant portion of my graduate research has been devoted to characterizing the molecular mode-of-action of these and other cardiac myosin effectors.

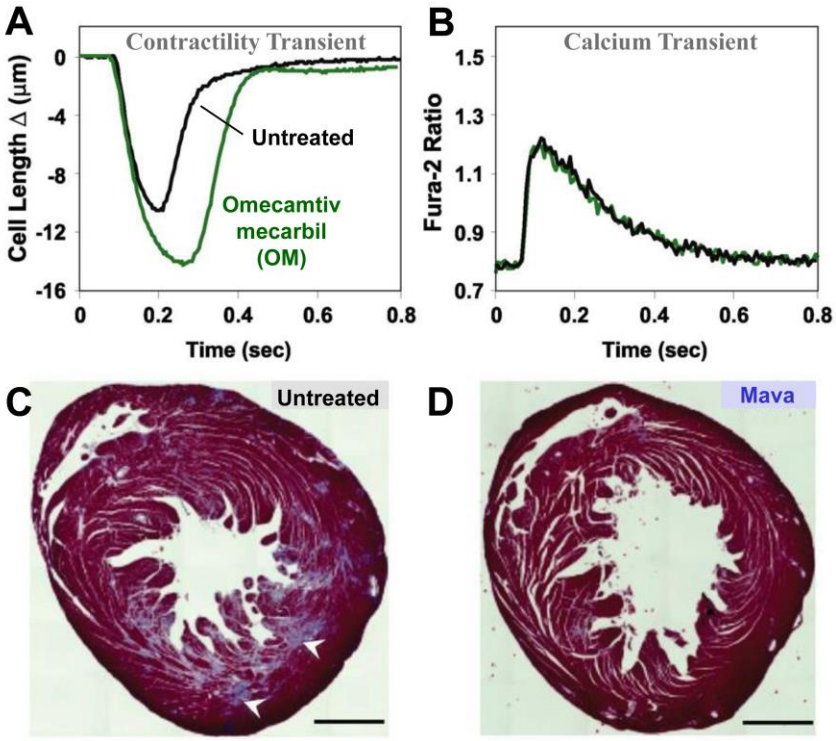

Fig. 4. Putative heart failure (OM) and cardiomyopathy (mava) therapeutics that bind cardiac myosin show promise.

(A-B) The putative systolic heart failure therapeutic omecamtiv mecarbil (OM) increases and prolongs cardiac contractility, and unlike other heart failure drugs, does not perturb intracellular calcium regulation associated with contraction, subpanels adapted from [16]. *AAAS grants permission for the use of figures in print and electronic versions of a dissertation or thesis.[57]* (C-D) The hypertrophic cardiomyopathy mutation R403Q results in enlarged, diseased hearts with significant fibrosis (lower right, arrows). Animals with the R403Q mutation that were administrered mavacamten (mava) do not display the disease phenotype, indicating the drug prevents deleterious remodeling of the myocardium, subpanels modified from [9]. *Springer-Nature grants permission to reproduce material from its journals as part of another publication or entity*[58]. The molecular mode of action on cardiac myosin for each small-molecule effector I have studied in detail and discuss in Chapters 3-4.

1.4 AUTO-INHIBITION OF TWO-HEADED MYOSIN AND THE SUPER-RELAXED STATE (SRX)

The following paragraphs are paraphrased from my published work [3].

Hypertrophic cardiomyopathies, abbreviated HCM, represent one of the most common classes of genetic disease, affecting 1 in 500 people [59]. HCM is hypothesized to result from cardiac hyper-contractility, left ventricular wall thickening, and decreased left ventricular ejection volumes [8]. So, direct inhibition of force generation by cardiac myosin is hypothesized to be a potential treatment [9]. Mavacamten (mava), previously called Myk461, is a small-molecule allosteric inhibitor of cardiac myosin in clinical trials for the treatment of HCM [9]. Mava tightly binds cardiac myosin in the presence of adenosine triphosphate (ATP) and inhibits steady-state actin-activated and actin-independent (basal) ATPase cycling and calcium regulated ATPase activity in detergent-permeabilized cardiac myofibrils [9, 60]. Mava inhibits the kinetics of rigor actin-binding and the kinetics of actin-activated phosphate release [60]. It has also been shown to decrease *in vitro* actin filament sliding velocity in the motility assay [60], and to inhibit force generation in skinned cardiac preparations from mouse HCM models [9], and decrease cardiac output in live feline hearts [61]. Mava's effect on cardiac contractility was hypothesized to primarily result from its inhibition of actin-activated phosphate release, the thermodynamic step in the mechanochemical cycle of myosin that is most-tightly coupled to force generation [60].

Our lab, building on studies of one- and two-headed soluble myosin fragments, also hypothesized that Mava may stabilize an auto-inhibited state of two-headed cardiac myosin in solution, analogous to the super-relaxed state (SRX) that has been observed in skinned

myocardium and skeletal muscle fibers (Fig. 5A-B, PDB: 5TBY) [62, 63]. This hypothesis was also informed by studies of blebbistatin, a myosin II inhibitor that also inhibits phosphate release and is proposed to stabilize the SRX state in skeletal and cardiac muscle[64-67].

In detergent permeabilized relaxed muscle fibers and myocardium, the SRX is defined by a large amplitude slow phase in the bi-exponential kinetics of single ATP turnover (Fig. 5E). The fast phase of this turnover is similar to ATP turnover in isolated single myosin heads, but the slow phase hypothesized to result from myosin heads that are auto-inhibited in a protein-protein interaction structural state that is folded back onto the filament backbone (Fig. 5A-B). This folded and inhibited state, called the interacting heads motif (IHM), is hypothesized to be stabilized by a number of protein-protein interactions including: contacts between the two-heads, contacts between the heads and the S2 coiled-coil domain, and contacts between the head and/or S2 and the thick-filament backbone. Myosin heads in this IHM turn-over ATP much more slowly than non-interacting heads; the cause of this biochemical signature is hypothesized to result from the structural changes of this state that affect the ATPase site and the subsequent dissociation of the ATP hydrolysis products. The required movement of the myosin light-chain binding domain and actin-binding interface[68, 69] would likely be inhibited when the heads interact with one another. The IHM is argued to be an evolutionarily conserved auto-inhibition mechanism for regulating myosin II-driven function within cells [69-72]. Electron microscopy (EM) has been used in numerous studies to suggest that the individual myosin heads in the cardiac thick filament can form the IHM state [66, 73]. However, the IHM has not been observed in purified cardiac myosin in solution without chemical cross-linking. Thus, the

structural correlates and transient kinetics of the cardiac myosin IHM state remained unknown before our characterization[3].

We tested our hypothesis, that (1) cardiac myosin is auto-inhibited by direct head-head interaction in solution and (2) that mavacamten selectively targets this head-head self-inhibition, by comparing the actin-activated and actin-independent (basal) single ATP turnover kinetics of one- and two-headed cardiac myosin fragments. We also evaluated the temperature and ionic strength dependence of ATP turnover by each of these two myosin preparations. If two-headed heavy meromyosin (HMM) forms an IHM-stabilized, auto-inhibited state then the kinetics and energetics of ATP turnover by HMM should reflect this structural formation and should be much more dependent on increasing ionic strength than single headed cardiac myosin S1 [74] while mavacamten should reduce this ionic strength dependence. The results from these experiments reveal key aspects of cardiac myosin function and of mavacamten's mode of action on myosin. A related and complementary body of work, the effect of mavacamten on two-headed cardiac myosin, is described in Anderson et al.[75]. We used transient biochemical and structural kinetics to elucidate the molecular mechanism of mavacamten. The two-headed myosin fragment exhibits distinct auto-inhibited ATP turnover kinetics compared to a single-headed fragment. Mavacamten enhances this auto-inhibition. Mava also enhances auto-inhibition of ADP release by two-headed myosin, unobserved in the absence of the putative drug. Furthermore, actin disrupts the structure of the auto-inhibited state by forcing myosin lever-arm rotation. Mavacamten slows this rotation in two-headed myosin but does not prevent it. We conclude that cardiac myosin is regulated in solution by an interaction between its two heads and propose that mavacamten stabilizes this state.

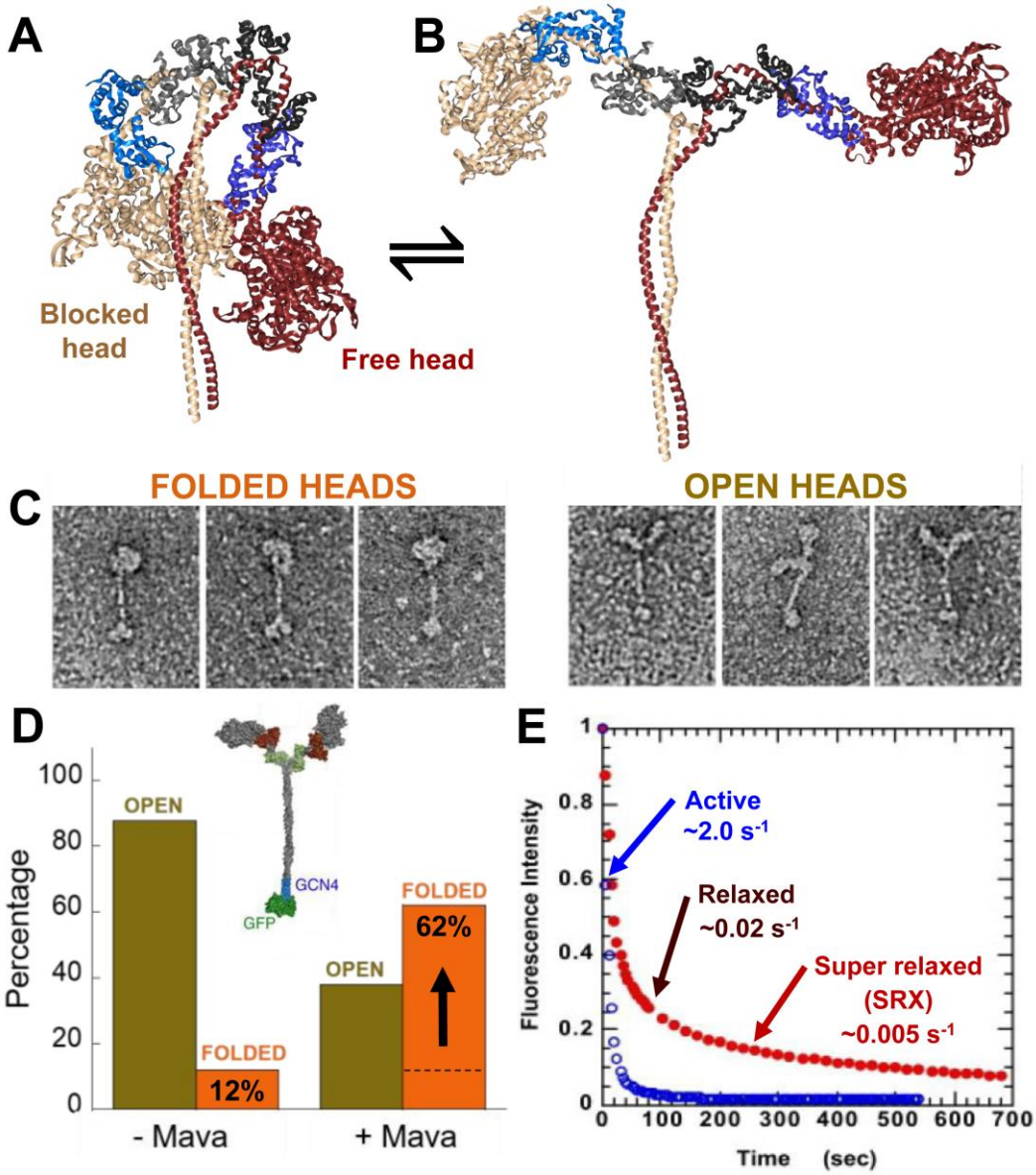

Fig. 5. A folded structural state in muscle myosin corresponds to decreased basal ATP-turnover kinetics.

(A-B) Structural model for an auto-inhibited state in two-headed myosin[3] PDB: 5TBY. Adapted from [3]. Panel (B) is constructed from (A) and is intended to represent one of many ensemble splayed-head conformations. (C) Negative-stain electron microscopy images of the heads in each state, with the folded heads being more likely in the presence of mavacamten (mava), (D); subpanels from [75]. (E) Long time-course transient biochemical data of mantATP turnover revealing a very slow fraction of myosin heads that do not readily turn-over ATP, modified from [63].

CHAPTER 2: DIRECT REAL-TIME DETECTION OF THE STRUCTURAL AND BIOCHEMICAL EVENTS IN THE MYOSIN POWER STROKE

This chapter has been adapted from the following publication:

Title: Direct real-time detection of the structural and biochemical events in the myosin power stroke

Authors: Joseph M. Muretta, John A. Rohde, Daniel O. Johnsrud, Sinziana Cornea, and David D. Thomas

Journal: Proc Natl Acad Sci U S A. 112(46): 14272–14277.

Online: November 2, 2015; ***Published:*** November 17, 2015

doi: *10.1073/pnas.1514859112;* ***PMID:*** 26578772

Permission: *for all authors of published work in PNAS, the journal grants permission "to include their articles as part of their dissertations."[76]*

2.1 CHAPTER OVERVIEW

As I was joining the Thomas Lab in 2014, our lab had recently developed a spectroscopic approach to allow us to detect angstrom-scale structural changes in several proteins using time-resolved FRET measured on the sub-millisecond time scale. This approach, transient time-resolved FRET, $(TR)^2$FRET [10, 77], allowed us to determine the structural kinetic mechanism of the force-generating myosin power stroke. The results from these experiments show that actin-induces the lever arm rotation prior to phosphate dissociation, suggesting additional complexity within myosin's kinetic cycle.

2.2 INTRODUCTION

Myosin family proteins use ATP hydrolysis to generate force and movement required for normal physiology. They drive muscle contraction, help control cell division and cellular motility, move organelles through the cytoplasm, and are important elements of the cellular mechanical-sensing machinery [5, 6]. The key to understanding how myosin and related enzymes function in cells, and how to modulate their activity to treat disease, is to determine how the protein's structural dynamics and biochemical kinetics are coupled. Though high-resolution crystal structures provide best-guess snap-shots of protein structure over a range of biochemical states, determining the physiological relevance of these snap-shots remains one of the central challenges of structural biophysics.

How myosin generates force remains debated despite more than 50 years of intense research [5, 6, 11]. The most popular current model [6, 12] proposes that after ATP hydrolysis, myosin interacts weakly with actin, and this interaction initiates an ordered series of structural and biochemical transitions that culminate in the dissociation of hydrolyzed phosphate followed by the isomerization of the actin-binding interface to a state that binds actin with nanomolar affinity and then the rotation of the myosin light-chain domain (LCD) toward the plus end of the actin filament. This rotation converts the thermodynamic energy of phosphate release and actin binding into mechanical energy that performs work. A number of results question this model, however, including spectroscopic data showing that a structural transition in the myosin relay helix, hypothesized to be coupled to LCD rotation, precedes P_i release [10] and force development precedes P_i release in muscle fibers [13].

Determining how these events take place in solution and in cells is an important question, because 1) differences in the mechanics of different myosins likely reflect differences in how the biochemical and structural transitions, described above, are coordinated [12], 2) disease-causing mutations in the myosin heavy chain should alter this coordination [14, 15], 3) recent studies show that modulating mechanochemical coupling in myosin is a viable therapeutic approach to treat myosin associated diseases [16, 17], and 4) myosin remains a model system for mechanochemical coupling in general, so what we learn about the myosin power stroke will inform work on related enzymes [11]. Understanding the coordination of actin binding, phosphate release, and LCD rotation will address each of these goals. However, direct detection of the kinetics of both LCD rotation and phosphate release, the key to understanding mechanochemical coupling in myosin, has not been achieved [12].

We have developed a spectroscopic approach that allows us to detect angstrom-scale structural changes in protein samples using time-resolved FRET measured on the sub-millisecond time scale. We call this approach, transient time-resolved FRET, $(TR)^2$FRET [10, 77], and use it to determine the structural kinetic mechanism of the myosin power stroke. The results show that actin-induces LCD rotation prior to phosphate dissociation suggesting a more nuanced interpretation of recent high-resolution crystal structures of myosins complexed with ADP and phosphate [12]. They also prompt a general model for tuning myosin force generation where the non-equilibrium distribution of pre- and post-power stroke LCD orientations, controls power output and muscle efficiency.

2.3 RESULTS

TR-FRET detects ADP- and ATP-sensitive structural states of myosin. Numerous experimental approaches have been used to investigate how myosin biochemistry is coupled to myosin structure and force generation, including high-resolution x-ray crystallography, electron microscopy, cellular mechanics, EPR, fluorescence, and single-molecule studies (reviewed in [6, 11, 78]. However, none of these approaches has directly resolved how LCD rotation is coupled to actin-induced phosphate release during the weak-to-strong actin-binding transition.

We previously examined the structural dynamics of the myosin relay helix [10, 77, 79], a conserved structural element downstream from switch-2 in myosins. The structure of this helix is allosterically coupled to interactions between switch-2 and bound ATP, ADP and hydrolyzed phosphate [68, 80]. Movement of the relay helix is hypothesized to be tightly coupled to LCD rotation [68, 80, 81]. We showed that in *Dictyostelium* myosin II, actin-binding in the presence of ATP straightens the relay helix prior to dissociation of hydrolyzed phosphate [10]. If the straight structural state of the relay helix is tightly coupled to the post-power stroke orientation of the LCD as proposed [68, 80], then, actin should LCD rotation prior to phosphate release. This hypothesis disagrees with several existing proposals [6, 12] but agrees with recent studies performed in isolated muscle fibers [13].

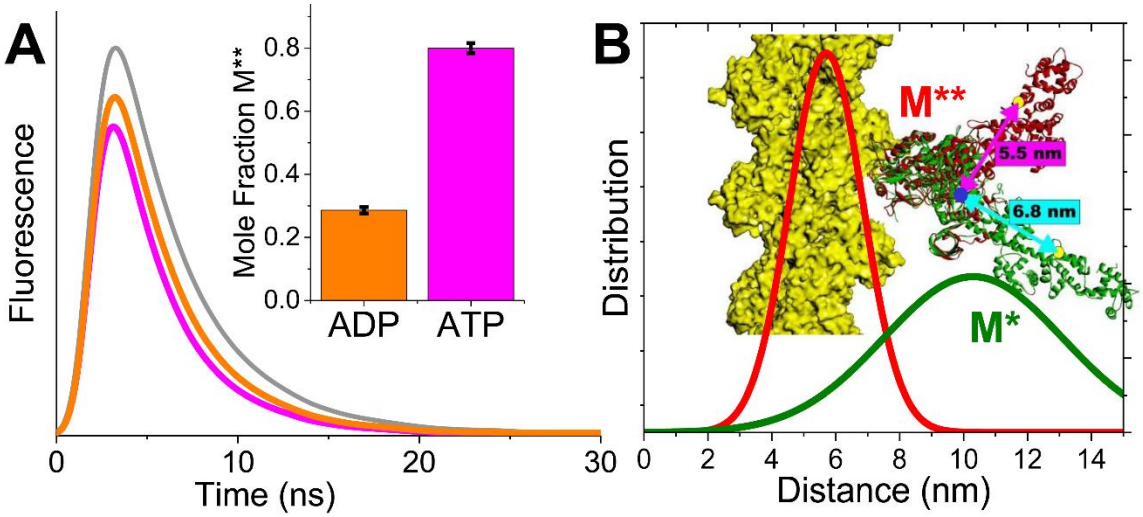

Fig. 6. Time-resolved FRET detects nucleotide-dependent LCD orientation.
(A) Representative fluorescence waveforms. Gray: donor only. Orange: donor plus acceptor, saturating Cy3-ADP. Magenta: donor plus acceptor, saturating Cy3-ATP. Inset: mole fraction of the M** structural state obtained from a two-component fit to the waveforms (n = 9, SEM). (B) Distance probability distributions from the above-mentioned fit, corresponding to the two resolved structural states (M* green line, M** red line). Cartoon depicts predicted distances from 2MYS (green ribbon, distance—cyan arrow) and 1Br1 (green ribbon, distance—magenta arrow) with modeled RLC. Actin in yellow.

To test this hypothesis directly, we designed a TR-FRET biosensor of two-headed skeletal muscle heavy-meromyosin (HMM, Fig. 6, preparation described in SI). The biosensor (Fig. 6) contains a fluorescently labeled (Alexa-488, the FRET donor) chicken-gizzard smooth muscle regulatory light-chain (cgRLC), exchanged onto skeletal muscle HMM (SI), and a fluorescent nucleotide (Cy3-ATP, the FRET acceptor) bound to the myosin nucleotide binding pocket [82-84]. We used the cgRLC because it contains a single reactive cysteine and can be exchanged efficiently with the native non-labeled RLC under conditions that do not affect ATPase activity (Fig. 9). The characterization of this construct and the validation of FRET between the probes are described in SI. Spectral overlap between the donor and acceptor gives a Förster distance (R_0) of 6.7 nm (SI). Based on high-resolution crystal structures (summarized in Table 1, PDB I.D. 2MYS [85] shown in Fig. 6 as a representative post-power stroke structure, and 1BR1 [81] with added RLC based on

homology to scallop myosin RLC structures shown as a representative pre-power stroke state) we predicted that the distance between the C-lobe of the RLC (residue C108 of the exchanged light-chain) and the Cy3 labeled ribose, will be 5.5 nm when myosin is in the pre-power stroke state and between 6.8 and 9.0 indicated by the range of predicted distances in rigor-like x-ray structures (Table 1) when myosin is in the post-power stroke state.

We measured time-resolved FRET, TR-FRET, of the labeled HMM in the presence of saturating bound Cy3-ADP or Cy3-ATP without actin Fig. 6). Data from these experiments were analyzed using programs written in MATLAB and with software used in our previous publications [10, 77] and is described in SI. The observed time-resolved fluorescence waveform of the Alexa donor probe decays faster in the presence of Cy3-ADP than when the acceptor is not present or when the samples are incubated with actin Fig. 6A). Cy3-ATP binding decreases the decay time further Fig. 6A). Thus, the donor's excited state is quenched by the presence of the fluorescent acceptors and the degree of quenching increases when the γ-phosphate is present. We fit a structure-based TR-FRET model to the observed data Fig. 10, Chapter 2 SI) and evaluated the validity of the fit based on χ^2 minimization Fig. 10), the geometry of the χ^2 error surface for each parameter in the fit Fig. 12), and the upper and lower confidence intervals for each parameter obtained from the χ^2 error surface (Table 3).

In the best-fit model, the mole fraction of two TR-FRET interprobe distance distributions depended on the nucleotide binding conditions (Fig. 6A, inset). This dependence was consistent with the structural models (Fig. 6, Table 3). ATP increased FRET compared with ADP by increasing in the mole fraction of a 5.7 nm distance

distribution (denoted M**) and decreasing a 10.3 nm distance (denoted M*, Fig. 6B inset). These distances are consistent with the expected values from the range of light-chain domain orientations seen in myosin crystal structures (Table 3). The short 5.7 nm distance state is also detected in the presence of ADP, though at a lower relative mole fraction (Fig. 6A inset). These results indicate that the LCD isomerizes between pre- and post-power stroke orientations in the presence of saturating ATP and ADP and that the γ-phosphate shifts the [M**]/[M*] equilibrium constant for this isomerization by a factor of 10 (0.4 with ADP, 4.0 with ATP). This equilibrium constant is remarkably consistent with the measured equilibrium constant for ATP hydrolysis at 20°C and 30°C in rabbit skeletal myosin S1 [86].

We measured the spectroscopic determinants of FRET including the absorbance, excitation, and emission spectra, fluorescence time-resolved anisotropy of the donor, and steady-state anisotropy of the acceptor. The spectra were measured to ensure that the overlap integral ($J(\lambda)$, Eq. 11) does not change during the ATPase cycle and the anisotropy controls were performed to estimate κ^2 and the resulting uncertainty in FRET R_0. These controls showed that the donor and acceptor absorption and excitation spectra do not change with ATP binding or with ATP hydrolysis (Fig. 11). The acceptor (Cy3) fluorescence emission is enhanced upon binding to myosin, indicating a change in quantum yield, but this does not affect FRET (Eq. 11) nor does the enhanced Cy3 emission contaminate the measured fluorescence of the donor emission detected at 520 nm (Fig. 11). The anisotropies of the probes do not change during the experiment (Table 4), and the upper and lower limits for R_0 determined from κ^2 are 6.5 nm and 8.0 nm respectively (Table 4). These limits are smaller than the magnitude of change in distance detected by structure-

based TR-FRET modeling (5.7 nm to 10.2 nm). Thus, changes in TR-FRET report changes in interprobe distance and LCD rotation.

Structural-kinetics of the power stroke detected by $(TR)^2$FRET. Armed with the biosensor described above, we performed $(TR)^2$FRET experiments during ATP binding and actin-activated single ATP turnover, to determine how the molar fractions of the resolved structural states change during the force generating weak-to-strong actin binding transition. We acquired TR-FRET waveforms every 0.2 ms after mixing in a stopped-flow device (SI). Representative waveforms during Cy3-ATP binding and the subsequent myosin recovery stroke and hydrolysis steps (Fig. 7A) and actin-activated single ATP turnover (Fig. 7B) show robust changes in TR-FRET.

We analyzed the data by first determining the total fluorescence of each sample (Fig. 7C, D), calculated by integrating the time-resolved fluorescence (TRF) waveforms over the nanosecond decay time (SI). The donor total fluorescence in the presence of acceptor provides an indication of the average energy transfer and distance between probes [87], reflecting changes in the average structural state of the protein. By fitting the TR-FRET waveforms to a structure-based model (described below), we resolved the structural states of myosin and measured the changes in their mole fractions with millisecond kinetic resolution.

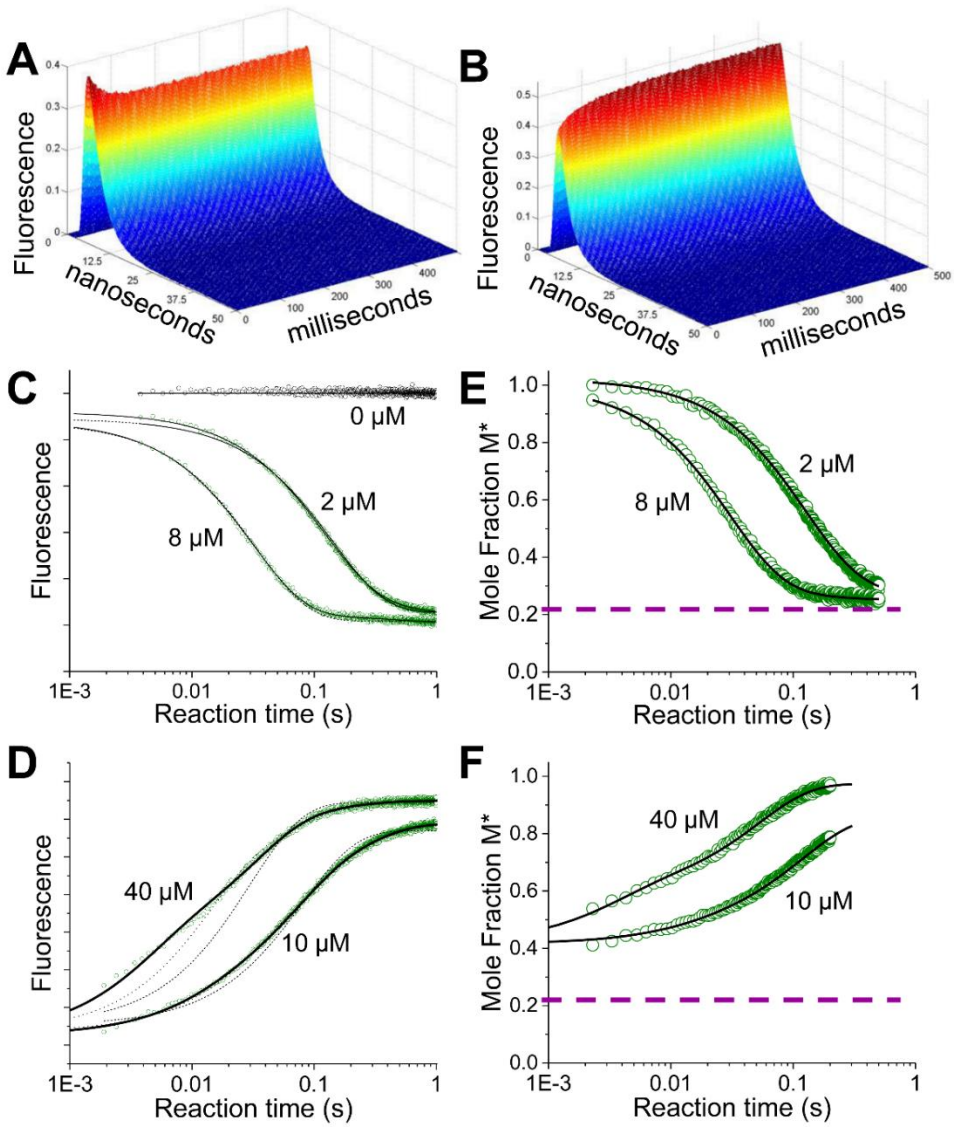

Fig. 7. $(TR)^2$FRET used to detect actomyosin structural kinetics
(A) Recovery stroke following Cy3-ATP binding: TR-FRET waveforms acquired every 0.2 ms (1 ms average shown) upon mixing 0.2 μM donor-labeled myosin HMM with 2 μM Cy3-ATP (final concentrations 0.1 μM and 1.0 μM respectively). (B) Power stroke: TR-FRET waveforms starting from the steady state of (A), after mixing with actin (40 μM post mix). (C) Total fluorescence of Alexa-488 labeled HMM mixed with [Cy3-ATP]. (D) Total fluorescence of a HMM Cy3-ATP steady-state as in C, mixed with [actin] containing 1 mM ATP. Best-fit (2-exponential for C and E and 3 exponential for panel D and F), shown as solid black line, Non fitting (dotted lines, C and D only) 1-exponential (C), and 1- and 2-exponential (D). (E) Mole fractions of M* structural state during Cy3-ATP binding determined by fitting $(TR)^2$FRET data obtained as in A, to a structural state model. (F) Mole fractions of M* structural state during the power stroke determined by fitting $(TR)^2$FRET data obtained as in B. Dotted purple line indicates M* mole fraction during steady-state ATPase cycling in the absence of actin. (n = 9). Best fit functions for C, $I(t) = 1 + 0.48e^{-8.5t} + 0.06e^{-1.9t}$ and $I(t) = 1 + 0.50e^{-32t} + 0.03e^{-1.6t}$, E, $I(t) = 1 + 0.41e^{-8.3t} + 0.06e^{-2.3t}$ and $I(t) = 1 + 0.43e^{-32t} + 0.02e^{-3.4t}$for 2 μM and 8 μM Cy3ATP respectively. Best fit functions for D, $I(t) = 1 + 0.1e^{-93t} + 1.6e^{-15t} + 0.2e^{-4.1t}$ and $I(t) = 1 + 0.3e^{-261t} + 1.5e^{-30t} + 0.06e^{-6t}$, F, $I(t) = 0.42 + 0.04e^{-81t} + 0.4e^{-8.4t}$ and $I(t) = 0.42 + 0.2e^{-314t} + 0.4e^{-20t}$ for 10 μM and 40 μM actin respectively.

Cy3-ATP binding to labeled HMM induces a single-exponential time-dependent change in the total fluorescence (Fig. 7B) of Alexa donor, consistent with Cy3-ATP binding and formation of a high-FRET state. The binding is specific and is blocked by 1 mM MgATP in the presence of excess actin (Fig. 9). The rate constant for this exponential transient increased linearly with [Cy3-ATP] (Fig. 13) and exhibited an apparent second-order rate constant of 4.0 $\mu M^{-1}s^{-1}$ and a dissociation rate constant < 0.1 s^{-1} (Table 2), consistent with the kinetics of ATP binding and ATPase cycling [82]. The pre-exponential amplitude did not change with increasing [Cy3-ATP] (Fig. 13), thus the binding saturated at concentrations the 1 μM concentration used.

We measured actin-induced structural changes by preparing a steady-state of 0.2 μM Alexa-labeled HMM with 2 μM excess Cy3-ATP in syringe A of the stopped-flow, and then mixed this steady-state complex, which is stable for 5 minutes (Fig. 9), with varied concentrations of actin (10 μM to 40 μM, final concentrations after mixing) in syringe B containing 1 mM MgATP after mixing. We added the 1 mM MgATP to prevent multiple actin-activated Cy3-ATP turnover reactions to ensure that changes in total fluorescence (Fig. 7D) reflect actin-induced changes in FRET during a single weak-to-strong transition [88] and not multiple turnovers.

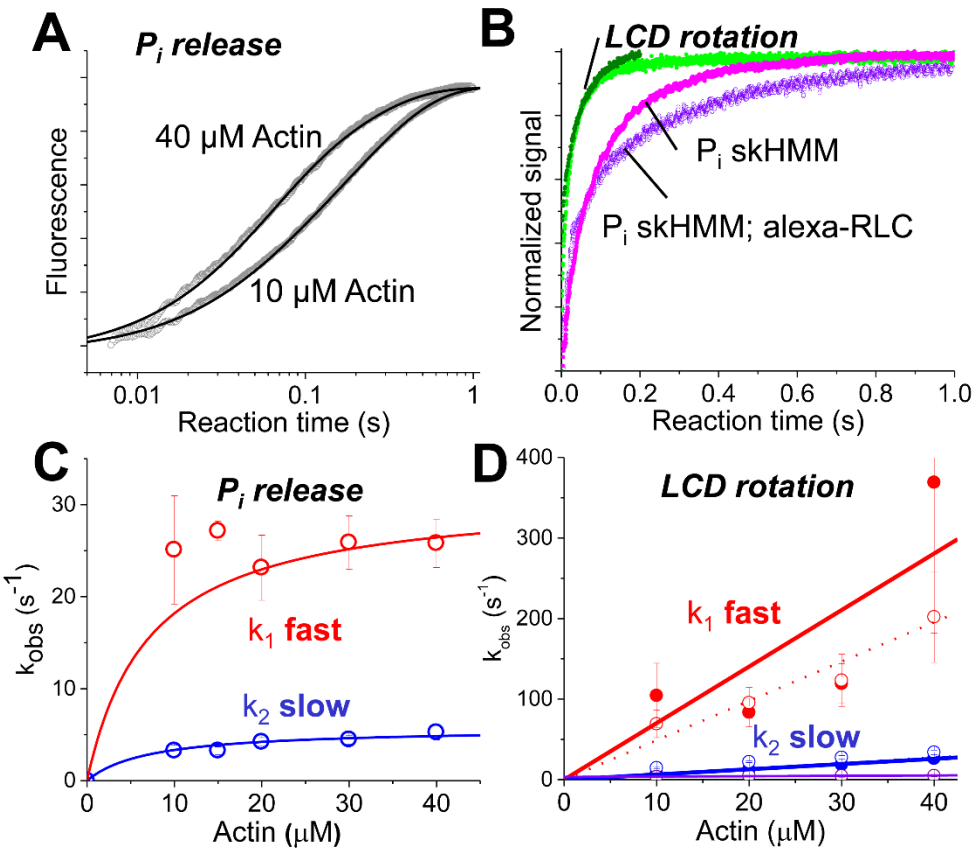

Fig. 8. Comparison of phosphate release and LCD structural kinetics
(A) Representative fluorescence of PBP after mixing 1 μM HMM containing 2 μM ATP with [actin]. Best fit functions $I(t) = 1 + 0.24e^{-20t} + 0.74e^{-4.3t}$ and $I(t) = 1 + 0.57e^{-20t} + 0.42e^{-5.3t}$ at 10 μM and 40 μM actin respectively. (B) Direct comparison between phosphate release (magenta skHMM with native RLC, purple skHMM with exchanged Alexa-RLC), total myosin fluorescence (light green), and M* mole fraction (dark green). (C) Observed rate constants for phosphate release (red, fast phase, blue, slow phase). (D) Rate constants for actin-induced LCD rotation (total fluorescence, open, M* mole fractions, solid) fit as in **Fig. 7**D,F. Triple exponential fit phase 1 red, phase 2 blue, phase 3 purple.

Actin induced an increase in total fluorescence that is best-fit to three-exponentials (Fig. 7D), consistent with a multi-step process for actin activated turnover of the Cy3-ATP and a transition from a high-FRET state, prior to actin binding, to a no-FRET state with dissociation of the Cy3 labeled acceptor at the end of the reaction transient. The slowest phase exhibited a rate constant of 3.4 s^{-1} (Fig. 8D) and was less than 10% of the total amplitude (Fig. 13) consistent with slow flux through actin-bound ATP hydrolysis [86].

The observed rate constants for the dominant phases (phase-1, red symbols, and phase-2, blue symbols, in Fig. 8D) of the actin activated fluorescence transients, increased linearly with increasing [actin] with a rate constant at 40 μM actin of 200 s^{-1} and 34 s^{-1} respectively (Table 3). The amplitudes of the pre-deadtime increase in M*, increased linearly with increasing actin (Fig. 13). This is consistent with the expected K_d > 100 μM for weak actin-binding states of myosin that contain either ATP or post-hydrolysis ADP and phosphate in the nucleotide binding pocket. The amplitudes of the actin-induced exponential transitions that occur after the rapid pre-deadtime phase did not change with increasing actin (Fig. 13). This indicates that the partitioning between each exponential phase after mixing is determined by the equilibrium constants for the recovery-stroke and ATP hydrolysis in the absence of actin and that the multi-exponential character of the transient represents flux through a linear or branched kinetic mechanism after the formation of the actomyosin collision complex.

The kinetics of phase 1 during the actin-induced FRET transients, were distinct from and faster than, both actin-induced Cy3-ATP and mant-ATP turnover (Fig. 9) while phase 2 (35 s^{-1} at 40 μM actin) is identical to the maximum turnover rate constants in Fig. 9. This indicates that phase 1 of the actin-induced change in FRET reflect structural transitions that precede ADP release after the myosin binds actin.

Structure-based TR-FRET modeling reveals the structural-kinetics and thermodynamics of the power stroke. We determined the structural underpinnings for the changes in FRET described above by fitting a structure-based FRET model (described in SI) to the $(TR)^2$FRET waveforms. The best-fit model was selected by χ^2 minimization

(Fig. 10), evaluated by the geometry of χ^2 error surface (Fig. 12), and the error surface confidence intervals (Fig. 12).

The best-fit model reveals two distinct populations of interprobe distance distributions, indistinguishable from those in Fig. 6. These distributions (M* and M** in Table 3), are in apparent equilibrium under steady-state ATPase cycling conditions, with a [M**]/[M*] K_{eq} of 4 consistent with measurements of the ATP hydrolysis reaction equilibrium constant [86]. The mole fraction of the M* and M** states exchanged in an exponential manner during Cy3-ATP binding (Fig. 7E) and actin-activated turnover (Fig. 7F) with the M* fraction decreasing during ATP binding from 1.0 to 0.2 (Fig. 7E) and increasing during actin-activated turnover from 0.2 to 1.0 (Fig. 7F). During actin-activated turnover, the M* fraction increased from 0.2 to ~0.4 within the dead-time of the stopped-flow mix, indicating that the initial stages of LCD rotation occur on the μs time-scale. This pre-dead time change is uncertain in the total fluorescence signal depicted in Fig. 7D after normalization, due to uncertainty in the total fluorescence at the start of the transient, but is well resolved when the time-resolved fluorescence of the waveforms is analyzed directly as the time resolved lifetime is independent of the total concentration of the sample and thus independent to the ~10% variation in total fluorescence between successive stopped flow mixes. We fit the observed time-dependence after mixing (2 ms onward) of the M* mole fraction with 1, 2, and 3 exponential functions, as described for the total-fluorescence transients in Fig. 7D. The observed rate constants from these fits (Fig. 8D) were indistinguishable from those obtained by fitting the total fluorescence transients. Thus the changes in total fluorescence reflect exponential time-dependent changes in the mole fractions of M* and M** structural states identified by the structure based TR-FRET

model. Because the structure-based model identifies the mole fractions of the M* and M** structural states, it reveals the apparent equilibrium constants separating the states during ATP binding and actin-activated single ATP turnover—these are not resolved in the analysis of total fluorescence. These equilibrium constants directly reveal the structural-kinetic mechanism of the myosin power stroke during weak-to-strong actin binding transition. This analysis showed that actin-induces the increase in the M* mole fraction, at 40 μM [actin] from 0.2 before formation of the weak-binding actomyosin interface, to 0.38 in the pre-dead-time phase, then to 0.53 at the completion of phase 1, 0.95 at the completion of phase 2, and 1.0 at the completion of phase 3, each corresponding to an increase in the apparent M*/M** equilibrium constant from 0.25, to 0.63, to 1.13, to 19, to >100.

Actin-initiated phosphate release is slower than the power stroke. We compared the structural kinetics of the myosin power stroke, described above, with the kinetics of actin-activated phosphate release using fluorescent labeled phosphate binding protein (SI) [86]. The observed rate constant for actin-activated phosphate release (Fig. 8, Table 2) increased hyperbolically with increasing [actin], with a $K_{0.5}$ of 8 μM and a maximum rate constant of 31 s^{-1} (Fig. 8C) for skHMM with the native RLC and 38 s^{-1} for skHMM with the exchanged Alexa labeled cgRLC. These results, at 6 mM ionic strength, are consistent with previous reports at a lower ionic strength, 1.2 mM [86] that predict 120 s^{-1} at 25°C, and 12 mM that showed 10 s^{-1} [89] at 10°C. Direct comparison of FRET and P_i release transients at 40 μM actin (Fig. 8B) and the apparent rate constants for the fast phase of each process, 30-40 s^{-1} for P_i release and >350 s^{-1} for the M* mole fraction (Fig. 8D and Table 2) shows that LCD rotation precedes biochemical dissociation of inorganic phosphate in skeletal muscle myosin.

Blebbistatin and vanadate block actin-induced LCD rotation. To test the structural and biochemical requirements for actin-induced changes in LCD orientation, we performed experiments similar to those in Fig. 7, in the presence of saturating blebbistatin or saturating vanadate. Both reagents are potent inhibitors of the weak-to-strong actin binding transition and actin-activated phosphate release. We incubated the labeled HMM with either blebbistatin (10 μM to 100 μM) and excess Cy3-ATP, or vanadate (10 μM to 1 mM) and excess Cy3-ADP, and then mixed these complexes with varied [actin]. We analyzed the results from experiments performed in the presence of blebbistatin by evaluating the total fluorescence—blebbistatin itself is fluorescent having a longer lifetime than the Alexa donor and interferes with the TR-FRET data fitting. Blebbistatin did not prevent Cy3-ATP binding (Fig. 14A, magenta) but did prevent actin-induced increases in fluorescence (Fig. 14A, purple) and slowed Cy3-ATP turnover in the absence of actin as well (Fig. 14B), consistent with blebbistatin binding and inhibition of ATPase cycling. We analyzed experiments performed with vanadate by fitting the TR-FRET waveforms to a structure-based model. Mixing 100 μM vanadate with labeled HMM in the presence of excess Cy3-ADP, slowly stabilizes the M** state (Fig. 14D) and prevents the actin-induced M**-to-M* transition on the 0-1 second time-scale (Fig. 14C). At longer times, actin weakens vanadate binding and drives nucleotide exchange with non-labeled ATP included in the actin syringe (Fig. 14D), evident by the [vanadate] dependence of the observed transients. These results indicate that actin does not induce LCD rotation when these inhibitors are bound.

Structural-kinetics modeling of FRET confirms that actin initiates LCD rotation prior to phosphate dissociation. We modeled the LCD structural-kinetics by

fitting three different structural kinetic mechanisms to the P_i release and the M* and M** transients acquired during ATP binding and actin-induced ATP turnover (Fig. 15). In mechanism (Eq. 24, Chapter 2.6), actin binding is followed by phosphate release and then LCD rotation, in mechanism 2 (Eq. 25 SI), actin binding is followed by reversible rotation of the LCD, and then P_i release and in mechanism 3 (Eq. 26 SI), mechanism 1 and 2 are combined into a branched pathway. The χ^2 from these fits showed that mechanisms 2 and 3 fit the data (Fig. 15) while mechanism 1 exhibits a χ^2 nearly 10 times greater than either mechanism 2 or 3 and does not fit the data.

2.4 DISCUSSION

Our results show that actin can induce rotation of the myosin LCD before dissociation of hydrolyzed P_i. This finding contradicts the popular model in which LCD rotation follows P_i release [6, 12]. The best-fit structural modeling of the TR-FRET (Fig. 6) and $(TR)^2$FRET (Fig. 7) waveforms reveals the structural, thermodynamic, and kinetic underpinnings of the actin-induced LCD rotation, showing that the LCD partitions between two orientations under steady-state ATPase cycling conditions. The first structural state (M*, LCD oriented down in Fig. 6) is indicated by an interprobe distance distribution centered at 10.3 nm (Table 1), consistent with rigor-like crystal structures predicting distances between 6.8 nm and 9.0 nm (PDB I.D. 2MYS is 6.8 nm). The second structural state, (M**, LCD oriented up in Fig. 6) is indicated by an interprobe distance distribution centered at 5.7 nm, consistent with the predicted pre-power stroke orientation of the LCD based on the 1Br1 crystal structure homology model (5.5 nm). Actin binding shifts the M*/M** distribution toward the M* state prior to P_i release, 0.25 to 6.3 as determined by kinetic modeling (Table 2). Thus the apparent $\Delta\Delta G$ at 25°C associated with this distribution change is 8.0 kJ/mol,

greater than the thermal background (2.4 kJ/mol) but much lower than the energy available from ATP hydrolysis (50 KJ/mol). Once the LCD has rotated, phosphate release is accelerated to 30-40 s^{-1} under our experimental conditions (6 mM ionic strength). P_i release is predicted to be faster at 1.2 mM ionic strength [86] and slower at 12 mM [89] presumably reflecting the ionic strength dependence of actomyosin binding. After P_i release, the M*/M** ratio is > 100 and myosin is trapped in the post-power stroke structural state until ATP rebinds.

Relation to high-resolution structural studies. Recent crystallographic studies [12] propose a detailed structural mechanism for actin-induced phosphate dissociation from myosin. In this work, the authors concluded that: 1) actin induces the transit of phosphate from the active site, down a phosphate release pathway, toward the inner actin-binding cleft, prior to phosphate dissociation; and 2) this transit follows switch-2 opening but precedes LCD rotation and the weak-to-strong actin binding transition. Our results are consistent wih the first conclusion but do not support the second as we clearly resolve LCD rotation prior to P_i dissociation and formation of the strong binding interface, which forms more slowly than P_i release [12].

The authors of that study[12] reach these conclusions by showing that phosphate can bind to the phosphate-release tube when the LCD is in the pre-power stroke orientation but not the post-power stroke orientation. An alternate interpretation, supported by the data presented in that study, is that phosphate does not bind to the release tube when myosin is in the post-power stroke crystal state because the binding is too weak. This interpretation is consistent with our data, with our previous FRET studies performed on the myosin relay helix [10], with tryptophan fluorescence studies performed in the absence of actin [68],

with studies performed on skinned muscle fibers [13] and with optical trapping studies showing the single molecule force develops faster than P_i release [90].

Coordination of LCD rotation with switch-2 opening. Though the LCD rotates prior to P_i dissociation from myosin, blebbistatin and vanadate inhibit the actin-activated M**-to-M* transition in the LCD (Fig. 14). Crystal structures of myosin bound by blebbistatin with ADP and vanadate [91] or ADP and vanadate without blebbistatin [92] show switch-2 in a closed conformation. Furthermore, spectroscopic studies suggest that blebbistatin [93] and vanadate [79] stabilize the closed state of switch-2 in the presence of ADP without P_i or P_i analogs. Thus switch-2 is likely predominantly closed in the presence of blebbistatin and vanadate, and because actin-induced LCD rotation is inhibited by both, we infer that the power stroke requires acceleration of switch-2 opening just as predicted by previous studies [10, 68] and by crystallographic models [12, 81].

Light-chain domain rotation and the power stroke. ATP-driven molecular motors, myosin included, couple the chemical energy of ATP hydrolysis with structural transitions that sustain pN scale forces and thus perform mechanical work. The force-velocity dependence and subsequent power output of these proteins are determined by their structural kinetic mechanism operating over a range of non-equilibrium and steady-state biochemical conditions. This mechanism defines the distribution of structural states during ATPase cycling, how these states evolve with time, and how they respond to strain.

LCD rotation is one of the primary determinants of force, velocity, and power output in myosins as it acts as an energy transducing lever-arm that converts changes in structure into work. Based on kinetic modeling (Fig. 15 and Table 2), we find that the apparent in Gibbs free energy change for LCD rotation prior to P_i release is low, -4.5

KJ/mol suggesting that non-equilibrium diffusion through the transition state is driven by the down-stream kinetics of P_i release rather than the free energy change of the transition itself. Thus, this result predicts that power is generated by LCD rotation, not as the result of the free energy change of the rotation, but because after the LCD diffuses from the M** to M* state, phosphate release inhibits the reversal of the transition, while simultaneously facilitating the formation of the strong actin-binding interface. This mechanism is analogous to a thermally activated "ratchet" that is driven by the energetics and kinetics of actin-activated phosphate dissociation. It will be interesting to test this hypothesis in conjunction with high-speed single-molecule laser trap experiments [90] and in high-resolution muscle fiber mechanics studies [13] to determine how the apparent equilibrium constant for LCD rotation is coupled to load and the development of muscle force.

Lastly, our results are nicely consistent with the long-held proposal, first made by Huxley and Simmons in 1971, that the myosin power stroke occurs in at least two thermodynamically distinct steps, a fast elastic transition followed by a slower viscoelastic transition [94]. As discussed above, the >500 s^{-1} actin-induced LCD rotation that we observe is highly reversible with a predicted change in free energy of -4.5 $KJmol^{-1}$, only 2 times greater than thermal background at the temperature of our experiments (25°C). The later stages in the FRET detected LCD rotation are consistent with the kinetics and energetics of phosphate release, which exhibits a much larger change in free energy and less readily reversed. Reversibly LCD rotation is consistent with the elastic process observed by Huxley and Simmons [94], while the slower, less reversible phase in our data, is consistent with the viscoelastic processes.

2.5 CONCLUSIONS

We have used $(TR)^2$FRET and transient phosphate release assays to determine the coordination of LCD rotation and actin-induced dissociation of hydrolyzed P_i in fast skeletal muscle myosin. The detection of nanosecond-resolved TR-FRET in real time during the millisecond-resolved biochemical transient allowed direct and quantitative measurement of the mole fraction of pre- and post-power stroke LCD structural states and thus the transient state distribution of these states during the critical actin-activated power stroke. The major change in Gibbs free energy is associated with phosphate release and the weak-to-strong actin binding transition and not the large structural reorientation of the LCD. These results provide direct and vivid insight into one of the most enigmatic aspects of myosin enzymology. Our work also serves as an important primer for future studies of other enzymes such as kinesins, dyneins, small GTPases, nucleotide polymerases, and kinases, where questions regarding the coupling of allosteric structural and biochemical transitions remain unanswered.

2.6 SUPPLEMENTAL METHODS AND INFORMATION

Methods

Protein purification and labeling.

Myosin: Skeletal myosin (rabbit) was purified as described by Margossian et al., [95] and stored at -20^{o}C in 10 mM Tris, 600 mM KCl with 50 % glycerol. Prior to digestion with chymotrypsin, the frozen myosin was dialyzed into 20 mM Tris pH 7.0, 30 mM KCl, centrifuged to sediment the resulting myosin filaments and then dissolved in 20 mM Tris pH 7.0, 0.6M KCl, 2 mM $MgCl_2$. We then digested the dissolved myosin with α-chymotrypsin (*Sigma-Aldrich*, 0.025 mg/ml final concentration) for 10 minutes at 25^{o}C

followed by addition of pefabloc (*Roche*, 5 mM final concentration) and then dialyzed the reaction into either 20 mM Tris pH 7.0, 30 mM KCl, and 2 mM $MgCl_2$, for storage on ice prior to experiments or into 20 mM Tris pH 7.0, 30 mM KCl, and 2 mM $MgCl_2$ followed by desalting into 10 mM Tris pH 7.0 with 150 mM Sucrose prior to snap freezing in liquid nitrogen for storage at -80^{o}C.

RLC: The chicken gizzard smooth muscle myosin regulatory light chain with a single reactive cysteine at position 108 was expressed in *E. coli*. as described in our previous work [96] and purified by inclusion body isolation followed by ion exchange chromatography [96]. We labeled the purified cgRLC with 5 molar excess of Alexa-488 (*Invitrogen*) overnight at 4^o C and then removed free dye by gel filtration chromatography. The labeled RLC was snap frozen in liquid nitrogen and stored at -80^{o}C. Labeling efficiency was 100% determined by the molar extinction coefficient of the Alexa dye and the measured RLC protein concentration, determined by the Bradford assay using a BSA standard.

Actin: Actin was purified from rabbit skeletal muscle by acetone dehydration followed by extraction into ice cold water as described in our previous work [97] and then polymerized in 10 mM Tris pH 7.5, 3 mM $MgCl_2$, 0.5 mM ATP and stored on ice prior to use. For phosphate release experiments, the F-actin was stabilized with stochiometric excess of phalloidin (*Sigma Aldrich*), followed by 24 h dialysis (3 buffer changes) into 10 mM Tris pH 7.0 with 2 mM $MgCl_2$.

Protein and dye concentration: The Bradford protein concentration assay utilizing a known BSA protein standard was used throughout this study to determine protein concentrations. Reagents for this assay were purchased from *Biorad*. The extinction

coefficient for the Alexa-488 dye is 73,000 at 495 nm, and for Cy3 is 136,000 at 570 nm, per manufacturers specifications.

Exchange: We exchange the Alexa labeled RLC onto HMM by combining the two proteins (3 molar excess RLC to HMM) in 50 mM Tris pH 7.5, 120 mM KCl, 2 mM DTT, 12 mM EDTA [98] and then incubated the reaction mix for 30 minutes at 30^{o}C. After the incubation, we adjusted the reaction to 12 mM $MgCl_2$ and then incubated the mixture on ice for 15 minutes followed by dialysis into 10 mM Tris pH 7.0, 30 mM KCl, 2 mM $MgCl_2$ prior to gel filtration to remove free RLC.

Buffers and solutions: All experiments, unless otherwise noted, were performed in 10 mM Tris pH 7.0, 2 mM $MgCl_2$ at 25^{o}C.

Steady-state ATPase activity. We measured actin-activated MgATPase activity using an NADH-coupled assay [88] performed at 25^{o}C in 10 mM Tris pH 7.0, 2 mM $MgCl_2$. The reaction mix contained varied [actin], and 0.2 mM NADH, 0.5 mM PEP, 2.1 mM ATP, 10 U/mL LDH, 40 U/mL PK, HMM 50-100 nM HMM. We acquired absorbance at 340 nm every 10 seconds for 120 seconds total using a Beckman-Coulter DU640B spectrophotometer.

Transient kinetics. Transient biochemical experiments with steady-state fluorescence (total fluorescence intensity) detection were performed on an *Applied Photophysics* stopped-flow spectrophotometer capable of sequential mixing experiments. The single-mix dead time for this instrument is 1.3 ms, calibrated using fluorescence enhancement of 8-hydroxyquinoline following Mg^{+2} binding under pseudo first-order kinetics conditions [99]. All buffers were filtered and then degassed for 30 minutes under high-vacuum prior to use. All stopped-flow experiments were performed at 25^{o}C maintained by a circulating

water bath. Transient time-resolved FRET (millisecond-resolved transient biochemical experiments with nanosecond-resolved fluorescence detection), $(TR)^2$FRET, was measured using a transient time-resolved fluorescence spectrophotometer [10, 42, 77]. This instrument utilizes a *Biologic USA* SFM/20 single-mix stopped-flow accessory coupled to our transient time-resolved fluorescence spectrophotometer. The dead time for the instrument was 1.8 ms, calibrated using the 8-hydroxyquinoline + Mg^{+2} control reaction [99]. For experiments mixing equilibrated myosin in the presence of 10 molar excess ATP with actin containing 1 mM MgATP, we loaded the actin into syringe A, followed by a freshly prepared 600 μL mixture of myosin + Cy3-ATP in syringe B and then immediately mixed with the actin in syringe A.

$(TR)^2$FRET: The TRF and $(TR)^2$F spectrometers, originally described in our previous work [10, 42, 77], transiently digitize the time-resolved fluorescence emission following a 1 ns laser pulse. The laser used in this study is an artisanal 473 nm microchip laser (FP2-473-3-5) with an LD-702 controller hand crafted by *Concepts Research Corporation*, in WI, operating at 5 KHz repetition frequency. Thus samples are excited every 0.2 ms. For equilibrium and steady-state biochemical conditions, 1000 replicate waveforms were signal-averaged prior to analysis. For transient time-resolved measurements acquired after rapid mixing by stopped-flow, 5 waveforms were averaged every 1 ms. Total time-resolved fluorescence was measured with the emission polarizer set to the magic angle (54.7º) or removed. For polarized time-resolved fluorescence measurements (TR-F Anisotropy), the emission polarizer was set successively to 0º, 54.7º, and 90º.

(TR)^{2}FRET Data Analysis

Total fluorescence: We determined the total fluorescence emission for FRET samples by integrating the (TR)^{2}FRET waveforms over the nanosecond decay time after subtracting the pre-trigger dark current, ~5% in amplitude compared to the maximum waveform intensity.

TR-FRET: TRF waveforms from donor and FRET-labeled samples were analyzed as described in our previous publications [10, 42, 77] Eq. 2-14, paraphrased below. The measured time-resolved fluorescence waveform, *I*(t) (Eq 1),

$$I(t) = \int_{-\infty}^{\infty} \mathrm{IRF}(t - t') \cdot F(t')dt' \qquad \text{Eq. 2}$$

is a function of the nanosecond decay time, t, and is modeled as the convolution integral of the measured instrument response function, IRF(t), and the fluorescence decay model, *F*(t). The fluorescence decay model (Eq. 3)

$$F(t) = x_{\mathrm{D}} F_{\mathrm{D}}(t) + (1 - x_{\mathrm{D}})\, F_{\mathrm{DA}}(t) \qquad \text{Eq. 3}$$

is a linear combination of a donor-only fluorescence decay function, F_{D}(t) and an energy transfer-affected donor fluorescence decay, F_{DA}(t). The donor decay F_{D}(t) is a sum of exponentials (Eq. 4)

$$F_{\mathrm{D}}(t) = \sum_{i=1}^{2} A_{\mathrm{i}}\, exp(-t/\tau_{\mathrm{i}}) \qquad \text{Eq. 4}$$

with discrete lifetime species τ_{i} and pre-exponential mole fractions A_{i}. For the Alexa-488 donor two exponentials were required to fit the observed fluorescence. The energy transfer-affected donor decay function, F_{DA}(t) (Eq. 5),

$$F_{\mathrm{DA}}(t) = \sum_{\mathrm{j}=1}^{2} X_{\mathrm{j}} \cdot T_{\mathrm{j}}(t) \qquad \text{Eq. 5}$$

is a sum over multiple structural states (j) with mole fractions X_j, represented by FRET-affected donor fluorescence decays $T_j(t)$. The increase in the donor decay rate (inverse donor lifetime) due to FRET is given by the Förster equation

$$k_{Ti} = k_{Di}(R/R_{0i})^{-6}, \text{ where} \quad \text{Eq. 6}$$

$$k_{DAi} = k_{Di} + k_{Ti}, \text{and} \quad \text{Eq. 7}$$

$$k_{Di} = 1/\tau_i \quad \text{Eq. 8}$$

We modeled TR-FRET assuming that each structural state j (Eq. 5) corresponds to a Gaussian distribution of interprobe distances, $\rho_j(R)$:

$$T_j(t) = \int_{-\infty}^{\infty} \rho_j(R) \cdot \sum_{i=1}^{3} A_i \, exp\left(\frac{-t}{\tau_i} \cdot \left[1 + \left(\frac{R_{0i}}{R}\right)^6\right]\right) dR \quad \text{Eq. 9}$$

$$\rho_j(R) = \frac{1}{\sigma_j\sqrt{2\pi}} \exp\left(\frac{-\left[R - R_j\right]^2}{2\sigma_j^2}\right) \quad \text{Eq. 10}$$

$$\sigma_j = \text{FWHM}_j/\left(2\sqrt{2\ln 2}\right) \quad \text{Eq. 11}$$

As with our previous work [10, 42, 77] , R_{0i} is calculated according to Eq. 11 from the spectral overlap integral, J, the orientation-sensitive term κ^2, the refractive index n, and the donor quantum yield Q_{Di} (Eq. 12-14). $\langle Q_D \rangle$ was measured as 0.91 ± 0.01, by comparison to a quinine sulfate fluorescence standard in 50 mM H_2SO_4 at 25ºC according to Eq. 15 (1, 4).

$$R_{0i} = 9780[J(\lambda)\kappa^2 n^{-4} Q_i]1/6 \quad \text{Eq. 12}$$

$$Q_{Di} = \langle Q_D \rangle \cdot \tau_i / \langle \tau \rangle \quad \text{Eq. 13}$$

$$\langle \tau \rangle = \frac{\sum_{i=1}^{3} A_i \tau_i}{\sum_{i=1}^{3} A_i} \quad \text{Eq. 14}$$

$$\langle Q_D \rangle = Q_S \cdot \left(\frac{F_D(\lambda)}{A_D(\lambda)}\right) \Big/ \left(\frac{F_S(\lambda)}{A_S(\lambda)}\right) \quad \text{Eq. 15}$$

Together, the donor fluorescence (A_i, τ_i) and distance terms (R_j, σ_j) in our analysis were shared globally between all waveforms containing FRET-labeled samples. R_j and σ_j were allowed to vary between 0.5 nm and 15.0 nm. The average Alexa-488/CY3 R_0, (6.7 nm in this study) was determined according to Eq. 12-15. The distance-dependent terms R_j (Eq. 10) and σ_j (Eq. 11) define unique structural states of the LCD. The mole fraction terms X_j were allowed to vary independently in each waveform. Thus, changes in X_j reflect changes in the relative populations of the structural states (j) as the biochemical state is varied under equilibrium, steady-state, or transient conditions.

We determined the number of donor lifetimes (*i*) and structural states (*j*) that are present in each sample by fitting a set of models with the number of donor lifetime states, *i* increasing from 1 to 4, and the number of structural states, *j*, increasing from 1 to 4. For each model we test a distribution of energy transfer rates, with σ_j allowed to vary, as well as discrete energy transfer rates where $\sigma \rightarrow 0$. The final model ($i_{max} = 2$, $j_{max} = 2$, $\sigma > 0$) was determined by evaluating the dependence of the minimized χ^2 on the number of free parameters in the global model and by the resolution of the χ^2 error surface support plane with a confidence intervals of 67%.

TR-F anisotropy: We analyzed time-resolved fluorescence anisotropy as described in our previous work [10, 42, 77] according to Eq. 16-19. The fluorescence lifetime and anisotropy terms are fit globally to the time-resolved fluorescence waveforms acquired with the emission polarizer set at 0°, 90°, and 54.7°. We varied the number of fluorescence lifetimes, τ_i, (Eq. 16-18) and rotational correlation times, τ_{Ri}, (Eq. 19) applied to each biochemical condition.

$$F(54.7°,\ t) = \sum_{i=1}^{3} A_i\, exp(-t/\tau_i) \qquad \text{Eq. 16}$$

$$F\ (0°, t) = F(54.7°,\ t) \cdot [1 + 2r(t)]/3 \qquad \text{Eq. 17}$$

$$F(90°, t) = F(54.7°,\ t) \cdot [1 - 2r(t)]/3 \qquad \text{Eq. 18}$$

$$r(t) = r_\infty + r_i\, exp(-t/\tau_{Ri}) \qquad \text{Eq. 19}$$

As described previously, the Alexa-488 donor is best described by a 2-exponential fluorescence decay (i = 2). A single-exponential anisotropy function was sufficient to describe the diffusion of each lifetime. We assumed that each of the Alexa-488 lifetimes experience the same global motion and thus are described by the same anisotropy function. Fitting to independent anisotropy functions did not reveal notable differences in anisotropy between the two lifetime states. The total anisotropy, r_o, was calculated according to Eq. 20.

$$r_0 = \frac{\int_{-\infty}^{\infty} F(54.7°,\ t) \cdot r(t)dt}{\int_{-\infty}^{\infty} F(54.7°,\ t)dt} \quad \text{Eq. 20}$$

$$\langle d_P^x \rangle = \sqrt{r_{0P}/r_f} \quad \text{Eq. 21}$$

$$\langle \kappa^2 \rangle_{min} = \left(\frac{2}{3}\right) \cdot \left(1 - \frac{\langle d_D^x \rangle + \langle d_A^x \rangle}{2}\right) \quad \text{Eq. 22}$$

$$\langle \kappa^2 \rangle_{max} = \left(\frac{2}{3}\right) \cdot \left(1 + \langle d_D^x \rangle + \langle d_A^x \rangle + 3\langle d_D^x \rangle \langle d_A^x \rangle\right) \quad \text{Eq. 23}$$

$$R_{min,max} = [(3/2) \cdot \langle \kappa 2 \rangle_{min,max}]^{1/6} \cdot R(\kappa 2 = 2/3) \quad \text{Eq. 24}$$

We used the total anisotropy to calculate the probe depolarization factors,d_p^x, (Eq.21), with the anisotropy of a rigid assembly of probes, r_f,.of 0.4. The maximum and minimum values of the orientation sensitive term κ^2 were calculated according to Eq. 22 and Eq. 23 and the resulting maximum and minimum range for the average R_0 according to Eq. 24.

Convolution integral and optimization: Nonlinear optimization was performed in software described in previous papers [10, 42, 77] and in Matlab using the fmincon optimizer. The TRF models, described above were convolved with the measured instrument response function using a numerical integration routine obtained from the David

D. Thomas Laboratory at the University of Minnesota or in Matlab using the "filter" function.

Error support plane analysis. We determined the upper and lower confidence intervals for fit parameters using strategies adapted from Beecham [100, 101] and Johnson [101]. (1) Optimization was performed on global data sets containing donor and donor + acceptor labeled samples acquired over a range of biochemical conditions to determine the best-fit parameter values according to the Eq. 2-24. (2) The dependence of the fit χ^2 on variations in each parameter was determined and the upper and lower 67% confidence intervals estimated as the range of values for each parameter that sustains less than a 67% increase in the minimized χ^2.

Transient kinetics of phosphate release. We detected dissociation of inorganic phosphate from myosin using phosphate-binding protein (PBP) labeled with MDCC[89]. Reagents for the expression or PBP were provided by Dr. Howard White [86]. The purification and characterization of phosphate-binding protein (PBP) was performed as described in our previous work [10]. For experiments measuring the kinetics of actin-activated phosphate dissociation, MDCC-PBP (10 μM) was included in all syringes, along with phosphate mop [86, 88, 89], which is added to remove contaminating free phosphate present in buffers, samples, and the stopped-flow instrument.

Cy3-ATP: We purchased the Cy3-ATP and Cy3-ADP used in this study from *Jena Bioscience*. These reagents are > 95% pure by the manufacturer's specifications.

The absorbance, excitation, and emission spectra of the Alexa-488 donor and Cy3-ATP nucleotides, do not change during ATPase cycling. We measured the absorbance, excitation, and emission spectra of the Alexa-488 donor labeled myosin and the Cy3

nucleotides used in this study over a range of biochemical conditions. The photophysical properties of the Alexa donor did not change with the biochemical condition of the sample (Fig. 11). The Cy3 nucleotides used in this study undergo a well-documented increase in fluorescence when they bind to the nucleotide binding pocket of myosin [82-84]. We verified that this change does not reflect a change in the absorbance extinction coefficient of the Cy3 probe (Fig. 11). Furthermore, the fluorescence enhancement detected upon binding is solely associated with a change in quantum yield (Fig. 11) as the normalized excitation spectra (Fig. 11) are identical for Cy3-nucleotides in solution or Cy3-ADP or Cy3-ADP.Vanadate bound by saturating excess of HMM (Fig. 11). These controls indicate that the spectral overlap between the donor Alexa probe and the bound Cy3 nucleotides does not change when the nucleotides bind, nor is the spectral overlap dependent on the ATP hydrolysis state, thus the average R_0, which we determined to be 6.7 nm, does not change during ATPase cycling.

Cy3 fluorescence does not contaminate the measured Alexa-488 signal. Any Cy3 emission that passes through the 520 nm band-pass filter (*Semrock*) used to isolate the Alexa-488 emission in our experiments would affect the interpretation of TR-FRET and the structural kinetics modeling. Thus, we verified that even in the presence of 10 molar excess Cy3-ATP or Cy3-ADP, the Cy3-emission that passes through the 520 nm band pass filter as the result of direct excitation by the 473 nm laser or by excitation via FRET, is not significant (Fig. 11).

Time-resolved fluorescence anisotropy and κ^2. We determined that the time-resolved anisotropy of the Alexa donor is not sensitive to the biochemical state of the myosin and the anisotropy of the Cy3-ATP bound to myosin is the same as Cy3-ADP and Cy3-ATP

(Table 4) and thus does not change during the weak-to-strong actin-binding transition. Furthermore, the Alexa donor, which exhibits a nanosecond fluorescence lifetime, rotates with a correlation time on the nanosecond time-scale (Table 4), and the maximum and minimum uncertainties in R_0 resulting from the uncertainty of κ^2, (Eq. 20-24) were 6.5 and 8.0 respectively. This indicates that the measured FRET is primarily dependent on the distance between the probes and not a change in probe orientation. Thus TR-FRET between the labeled RLC and Cy3-nucleotides, detects the rotation of the LCD.

Kinetics Simulations: We used KinTek Explorer [101-103] to model the structural kinetics of LCD rotation and phosphate release. Mole fractions of the M** and M* states after mixing with varied [Cy3-ATP] or 2 μM Cy3-ATP and then varied [Actin], and released [P_i] were modeled by simultaneously fitting either kinetic mechanisms 1 (Eq. 25) , 2 (Eq. 26), or 3 (Eq. 27) in KinTek Explorer. We evaluated the fit χ^2 (Fig. 15) to determine which mechanism best describes the observed data. The χ^2 from mechanism 1 (Fig. 15) was 8 times greater than mechanism 2 despite having the same degrees of freedom. Mechanism 3, which allows for both the phosphate first and the power stroke first pathways, did not improve the χ^2 despite increased model complexity. This analysis demonstrates that the phosphate first mechanism does not describe the data.

$$M^0 + ATP \overset{K_1}{\leftrightarrow} M^*T \overset{K_2}{\leftrightarrow} M^{**}DP + A \overset{K_3}{\leftrightarrow} AM^{**}DP \overset{k_{+4}}{\rightarrow} AM^{**}D + P \overset{K_5}{\leftrightarrow} AM^*D \overset{K_6}{\leftrightarrow} AM^0 + D \quad \text{Eq. 25}$$

$$M^0 + ATP \overset{K_1}{\leftrightarrow} M^*T \overset{K_2}{\leftrightarrow} M^{**}DP + A \overset{K_3}{\leftrightarrow} AM^{**}DP \overset{K_4}{\leftrightarrow} AM^*DP \overset{k_{+5}}{\rightarrow} AM^*D + P \overset{K_6}{\leftrightarrow} AM^0 + D \quad \text{Eq. 26}$$

$$\begin{array}{l} M^0 + ATP \overset{K_1}{\leftrightarrow} M^*T \overset{K_2}{\leftrightarrow} M^{**}DP + A \overset{K_3}{\leftrightarrow} AM^{**}DP \overset{k_{+4}}{\rightarrow} AM^{**}D + P \\ \qquad\qquad\qquad\qquad\qquad\qquad\qquad\qquad K_5 \updownarrow \qquad K_6 \updownarrow \\ \qquad\qquad\qquad\qquad\qquad\qquad\qquad\qquad k_{+7} \qquad K_8 \end{array} \quad \text{Eq. 27}$$

$$AM^{*}DP \rightarrow AM^{*}D + P \leftrightarrow AM^{0} + D$$

Table 1. Predicted TR-FRET distance distribution center
Determined by measuring the distance between the α-carbon of residues homologous to chicken gizzard smooth muscle myosin RLC C108, and the 2' oxygen of bound or modeled ADP ribose in the pre-power stroke and rigor like crystal structures. For 1Br1, the scallop RLC was modeled onto the smooth muscle myosin heavy-chain. Estimate uncertainties +/- 1.0 nm assuming 0.5 nm probe linkers.

State	Distance (PDB)	Lower Estimate	Upper Estimate
Pre-Power	5.5 (1Br1)	4.5	6.5
Rigor-Like	6.8 (2MYS)	5.8	7.8
""	7.5(1DFL)	6.5	8.5
""	8.5(1DFK)	7.5	9.5
""	9.0(1KQM)	8	10
""	8.4(1KK7)	7.4	9.4

Table 2. Steady-state and transient kinetics

Steady-state activities as determined in Fig. 9, observed transient structural kinetics from Fig. 8 and modeled structural kinetics from kinetic modeling in Fig. 15.

Steady-state ATPase			
	Unlabeled	**Labeled**	
$V_{max(actin)}$	$12.9 \pm 0.5\ s^{-1}$	$13.4 \pm 0.6\ s^{-1}$	
$K_{m(actin)}$	$22.0 \pm 2.0\ \mu M$	$22.2 \pm 2.3\ \mu M$	
Basal	$0.01 \pm 0.005\ s^{-1}$	$0.01 \pm 0.005\ s^{-1}$	
Transient Biochemical and Structural Kinetics			
Transition	**forward**	**reverse**	$K_{(app)}$
ATP Binding	$4.0\ \mu M^{-1}\ s^{-1}$	$< 0.1\ s^{-1}$	$K_{(app)} < 25$ nM
P_i Release acto-skS1	$35\ s^{-1}$	—	—
P_i Release acto-skHMM	$35\ s^{-1}$	—	—
P_i Release acto-skHMM(smRLC)	$38\ s^{-1}$	—	—
Weak Actin Binding	$7.0\ \mu M^{-1}\ s^{-1}$		$> 100\ \mu M$
Actin-induced LCD rotation pre-dead time	$> 1000\ s^{-1}$		0.6
Actin-induced LCD rotation (phase-1)	$> 500\ s^{-1}$		1.1
Actin-induced LCD rotation (phase-2)	$35\ s^{-1}$		19
Actin-induced LCD rotation (phase-3)	$3\ s^{-1}$		—
Modeled Structural Kinetics			
Transition	**forward**	**reverse**	K_{eq}
ATP Binding	$3.9 \pm 0.03\ \mu M^{-1}\ s^{-1}$	< 0.1	< 25 nM
Recovery/Hydrolysis	$294 \pm 36.8\ s^{-1}$	$109 \pm 14.2\ s^{-1}$	2.7
Weak Actin Binding	$15.8 \pm 5.5\ \mu M^{-1}\ s^{-1}$	$1200 \pm 400\ s^{-1}$	135 μM
LCD Rotation	$689 \pm 33\ s^{-1}$	$109 \pm 3.9\ s^{-1}$	6.3
Pi Release	$17.9 \pm 0.14\ s^{-1}$	—	—
ADP Release	$>1000\ s^{-1}$	—	—

Table 3. Time-Resolved fluorescence lifetime parameters
For donor and donor + acceptor labeled HMM at 25°C. Upper and lower 67% confidence bounds determined from χ^2 support plane error analysis (described in SI Methods).

Parameter	Best-Fit	Lower Bound	Upper Bound
Donor only			
Amplitude τ_1	0.81	0.80	0.81
$\tau_{1\ (ns)}$	3.86	3.85	3.87
Amplitude τ_2	0.19	0.20	0.19
$\tau_{2\ (ns)}$	1.49	1.45	1.54
Distance distributions			
R1 (nm)	5.7 ±0.007	5.52	5.96
FWHM 1 (nm)	2.7 ±0.05	2.04	2.92
R2 (nm)	10.3 ±0.09	10.06	10.63
FWHM 2 (nm)	6.6 ±0.21	5.06	8.22

Table 4. Time-Resolved anisotropies and correlation times
For Alexa-488-Labeled HMM of Cy3-nucleotides bound to excess non-labeled HMM at 25˚C.

	Biochemical State			
Alexa-488	**Apo**	**ATP/ADP.P_i**	**ADP**	**Actin**
Initial Anisotropy	0.31 ± 0.01	0.31 ±0.01	0.31 ±0.01	0.29 ±0.01
Correlation Time (ns)	2.02 ±0.23	1.66 ± 0.36	2.12 ± 0.22	1.59 ± 0.23
Final Anisotropy	0.16 ± 0.005	0.16 ± 0.006	0.16 ± 0.004	0.15 ± 0.004
r_o	0.29	0.30	0.29	0.27
Cy3-ATP	**Apo**	**ATP/ADP.P_i**	**ADP**	**Actin**
r_o	—	0.33 ±0.01	0.33 ±0.01	—
Cy3-ADP	**Apo**	**ATP/ADP.P_i**	**ADP**	**Actin**
r_o	—	0.33 ± 0.01	0.33 ± 0.01	—
κ^2_{min}	0.57	0.57	0.57	0.58
κ^2_{max}	2.02	2.04	2.02	1.98
$R_{0\ min}$	6.54	6.54	6.54	6.54
$R_{0\ min}$	8.03	8.03	8.03	8.03

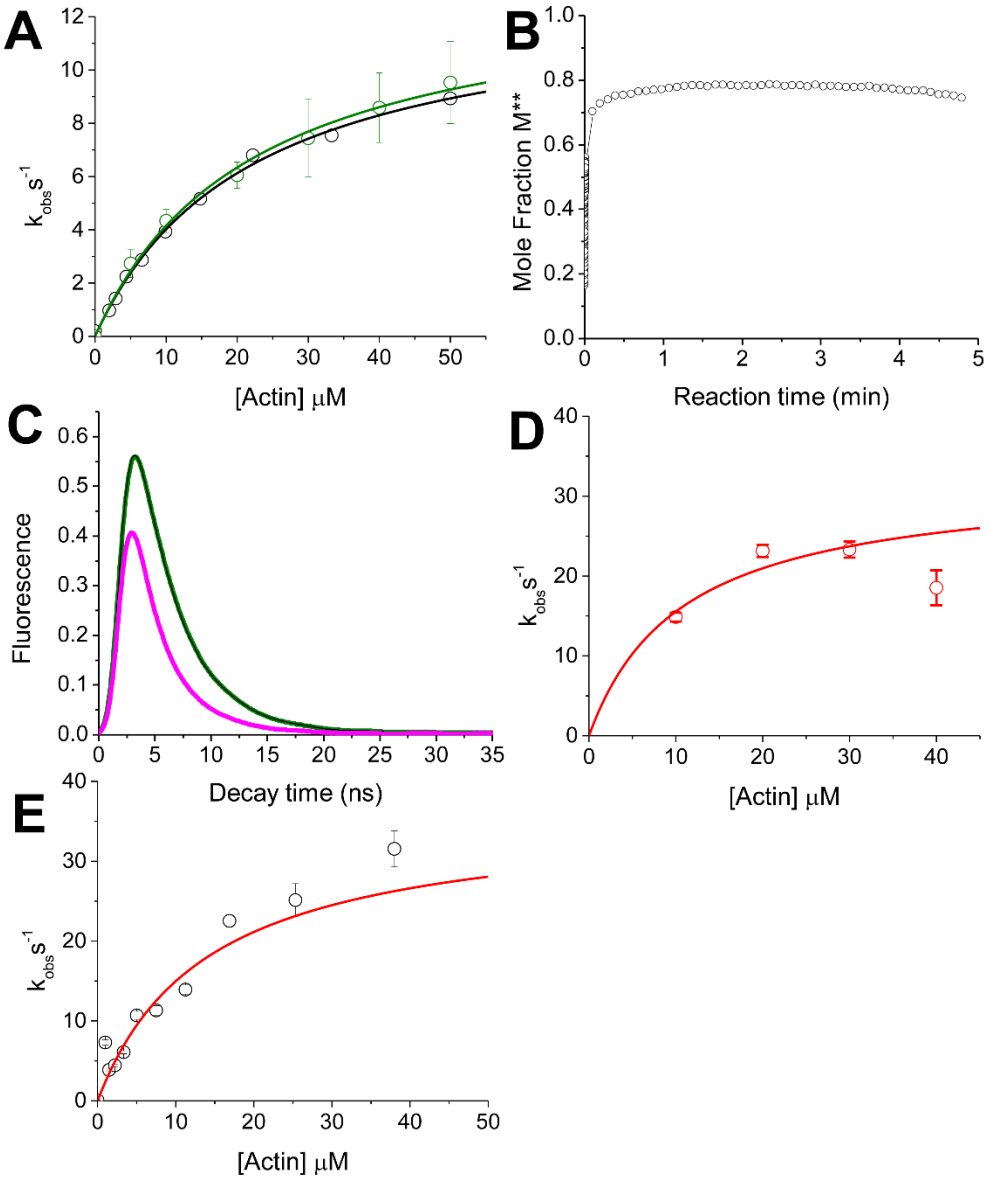

Fig. 9. Steady-state actin-activated ATPase, nucleotide binding and actin-activated turnover (A) Steady-state ATPase activity of Alexa-488 labeled HMM (green, best-fit function, $ATPase = 13.4\,[Actin]/(22 + [Actin])$ and non-labeled HMM (black, $ATPase = 12.9\,[Actin]/(22 + [Actin])$). (B) Steady-state stability of the Alexa-HMM:Cy3ATP complex under conditions used in this study. The Cy3-ATP dependent M** state is stable for more than 2 minutes after mixing 0.1 μM HMM with 2 μM (10 molar excess) Cy3-ATP. (C) Representative TR-FRET waveforms under steady-state ATPase cycling as in B, in the presence (green) or absence (magenta) of actin or in the absence of Cy3-ATP (black). (D and F) Actin-activated single-turnover with Cy3-ATP (D, best-fit function, $k_{obs} = 32.0\,[Actin]/(10 + [Actin])$) or mant-ATP (E, best-fit function, $k_{obs} = 35.0\,[Actin]/(14 + [Actin])$). N = 3, errors calculated as SEM of replicate experiments.

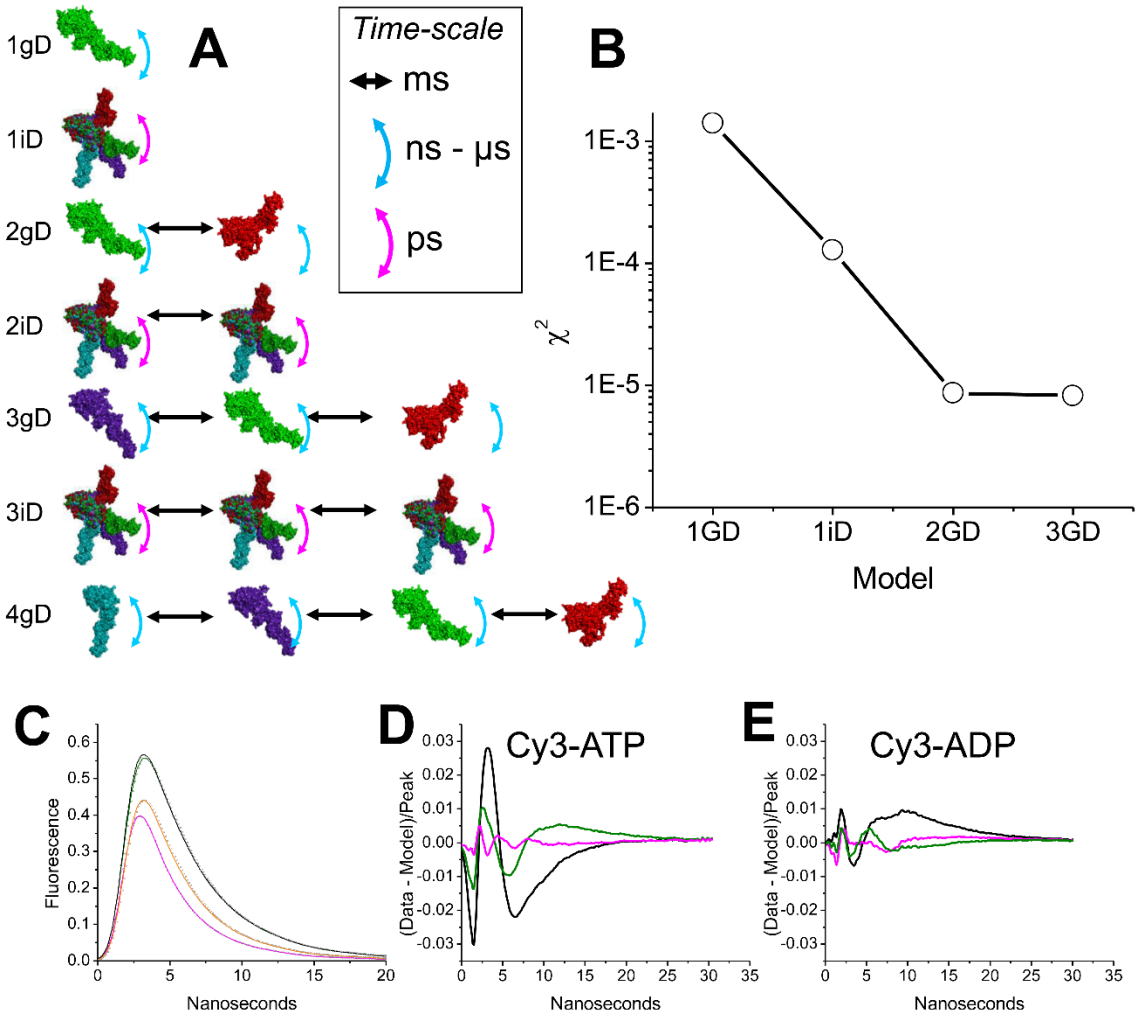

Fig. 10. Structure-based TR-FRET model validation

(A) Models tested in this study are noted by the number of distance distributions (1, 2, 3, 4) the dependence of the center and width of the distribution on the biochemical conditions (g, global center and width shared over all biochemical states, i, independent center and width allowed to vary over all biochemical states) . Thus 2gD (the best-fit model in this study) is a model with 2 global distance distributions with the center and width of the distributions common to all biochemical states. In the 2gD model, changes in TR-FRET reflect changes in the mole fractions for each distance distribution as described in Eq. 5. In the independent models (1iD, 2iD, 3iD) the continuous variation of distance distributions indicates conformational exchange on the picosecond to nanosecond timescale (magenta arrow indicated in panel A inset box), while in the global models (1gD, 2gD, 3gD, 4gD), the distance distribution center and width do not vary and exhibit µs motion (blue arrow indicated in panel a inset box). Linear black arrows indicate structural transitions occurring on the millisecond time scale. (B) χ^2 for models tested in this study. Increasing the model complexity beyond 2gD does not improve the fit. (C). Typical waveforms obtained under equilibrium or steady-state biochemical conditions. HMM Alexa-488 donor only (black), HMM Alexa-488 + Cy3-ATP mixed with Actin + 1 mM ATP (green, indistinguishable from donor), HMM Alexa-488 + saturating Cy3-ADP (orange), HMM Alexa-488 + saturating Cy3-ATP (magenta). Data shown as open symbols, 2GD best-fit model shown as lines. (D and E) Residuals (data –model): HMM Alexa-488 + saturating Cy3-ATP (D) or Cy3-ADP (E) for 1gD (black), 1iD (green), or 2gD (magenta) models.

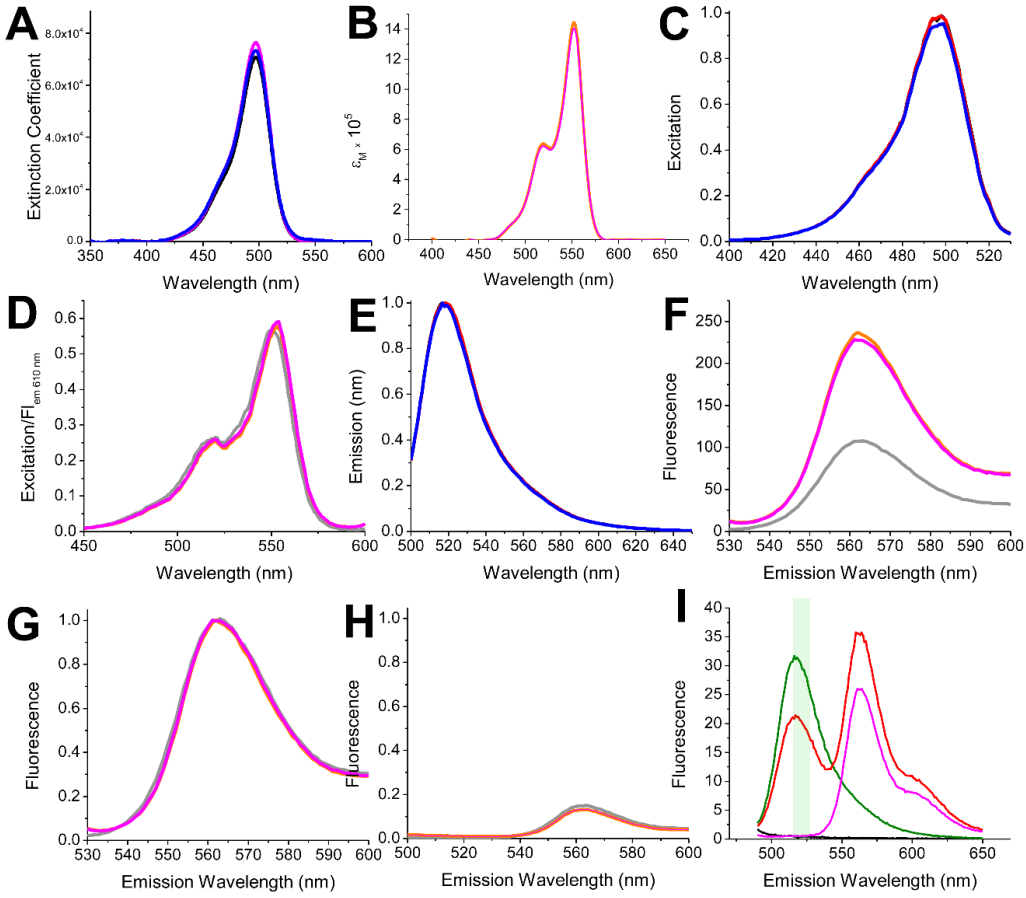

Fig. 11. Absorbance, excitation, and emission spectra of fluorescent probes
(A) Absorbance molar extinction coefficient of Alexa-488 labeled HMM (black) or in the presence of excess MgATP (magenta), or actin (blue) showing that the absorbance spectra of the donor does not change with nucleotide of actin binding. Differences in peak absorbance are within the error of sample preparation (5%), and background subtraction. (B) Absorbance molar extinction coefficient of Cy3-ADP (orange) or Cy3-ADP.Vanadate (magenta) bound to non-labeled HMM showing that the absorbance of the acceptor does not change with binding to myosin. (C) Excitation spectra of samples in panel a, monitoring emission at 550 nm showing that the excitation spectra does not change with biochemical state. (D) Excitation spectra of Cy3-ADP in solution (grey) or bound (orange) to HMM or Cy3-ADP.Vanadata bound (magenta) to HMM showing that the excitation spectra of the acceptor does not change with biochemical state. (E). Emission spectra of Alexa-488 labeled HMM samples from panel a showing that the donor fluorescence emission does not change with biochemical state. (F) Emission spectra of Cy3-ADP or Cy3-ADP.Vanadate excited at 520 nm in the absence (grey) or presence (orange and magenta respectively) of HMM showing that the acceptor undergoes an increase in quantum yield with binding, but that the emission does not change with the ATP hydrolysis state. (G) Data in (F) normalized to emission peak showing that the shape of the acceptor emission spectra do not change. (H) Emission spectra as in (G) upon excitation at 473 nm to check for direct excitation of the Cy3 by the 473 nm laser used in this study. (I) Emission spectra of 0.2 μM donor-labeled HMM (green), 0.2 μM donor-labeled HMM with 2 μM Cy3-ATP, or Cy3-ATP alone (red) upon excitation at 473 mM. The fluorescence of the bound acceptor does not contribute to the 520 nm detection window (green box) used to monitor donor emission.

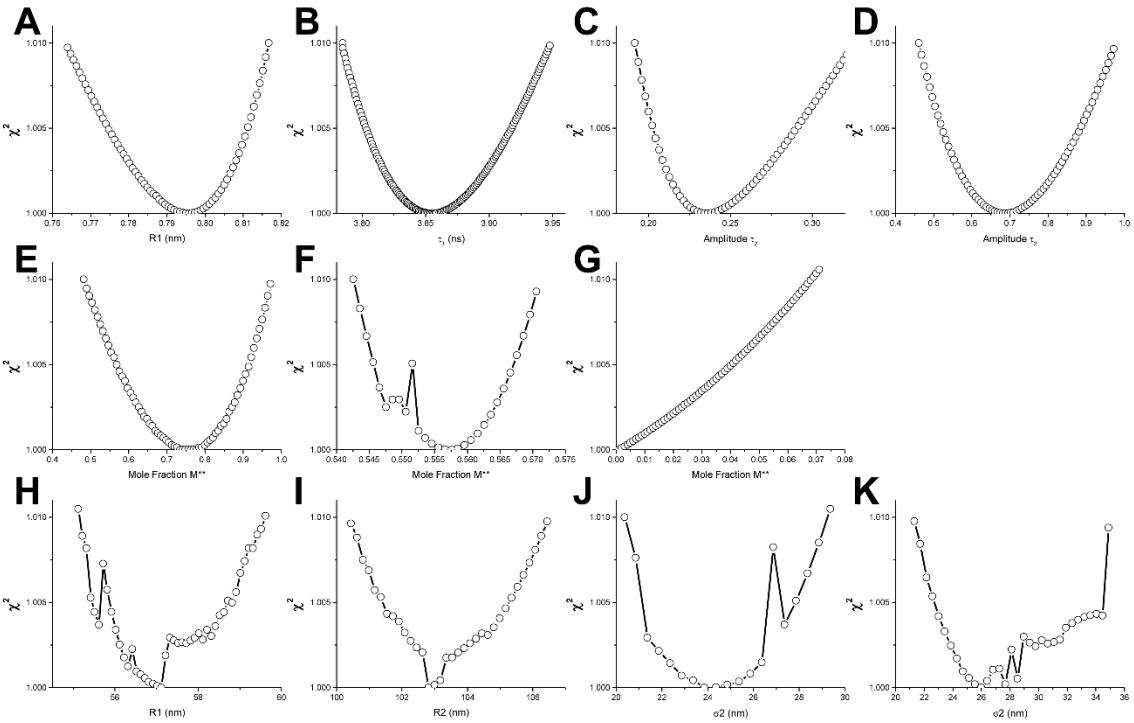

Fig. 12. Representative confidence interval (67%) support plane for best-fit parameters
Each fit represents the dependence of the fit's χ^2, on variation in fit parameters within the 67% confidence interval. Upper and Lower bounds in Table 3 and Table 4 determined from the width of the error surfaces. (A) Donor time-resolved fluorescence τ_1 pre-exponential factor, (B) τ_1 lifetime, (C) τ_2 pre-exponential factor, or (D) τ_1 lifetime. The M** mole fraction (E) under steady-state ATPase cycling conditions, (F) at the start of the actin-induced power stroke or (G) after completing the power stroke. (H) M** distance distribution center, (I) M* distance distribution center, (J) M** FWHM, (K) M* FWHM. Error plane computed as described in SI.

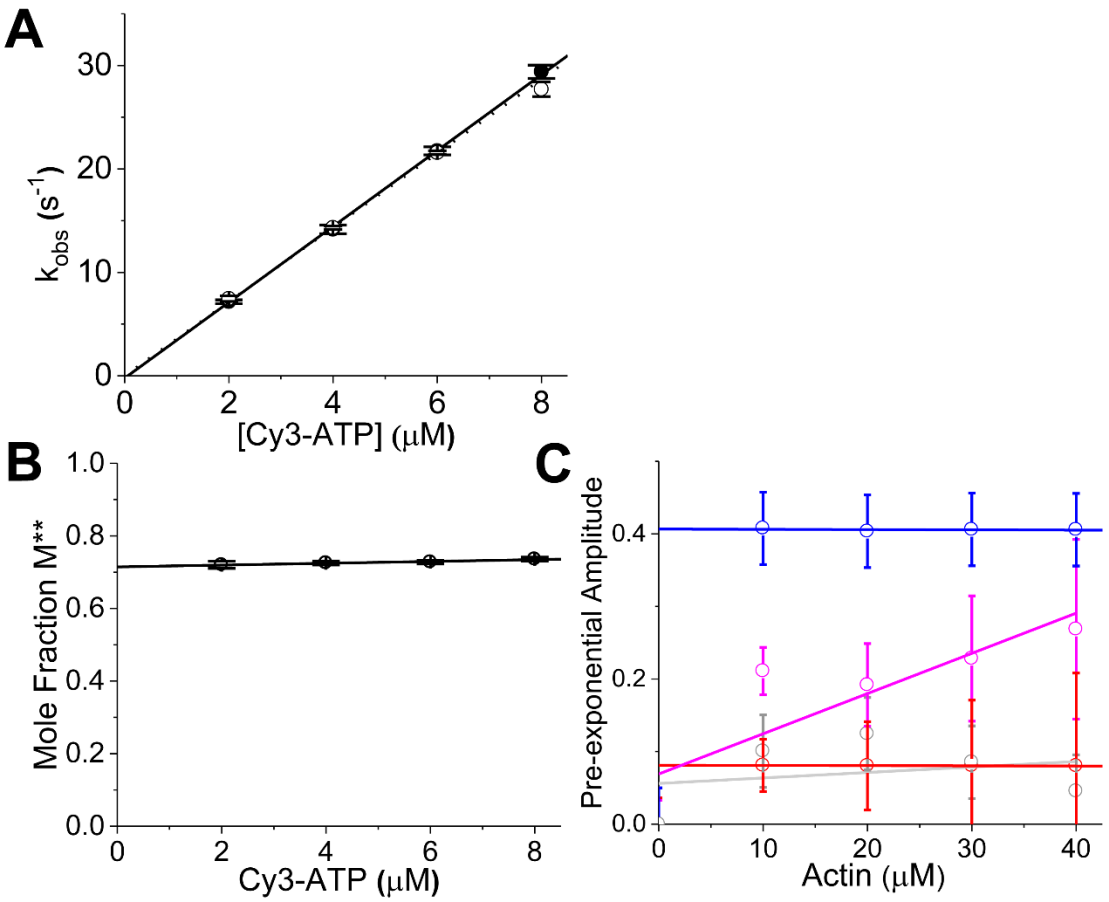

Fig. 13. Supplemental observed kinetics for transient changes in FRET measured
(A) Observed rate constants for Cy3-ATP binding, determined as described in Fig. 7, total fluorescence transients (open symbols, dotted lines), mole fraction M* transients (solid symbols, solid lines). (B) Pre-exponential amplitudes for M* mole fraction transients during Cy3-ATP binding described in Fig. 7. (C) Pre-exponential amplitudes for 3 exponential fits of M* transients described in Fig. 7 during the actin induced power stroke, pre-dead time rapid equilibrium (magenta), phase 1 (red), phase 2 (blue), 3.4 $^{s-1}$ slow phase (grey).

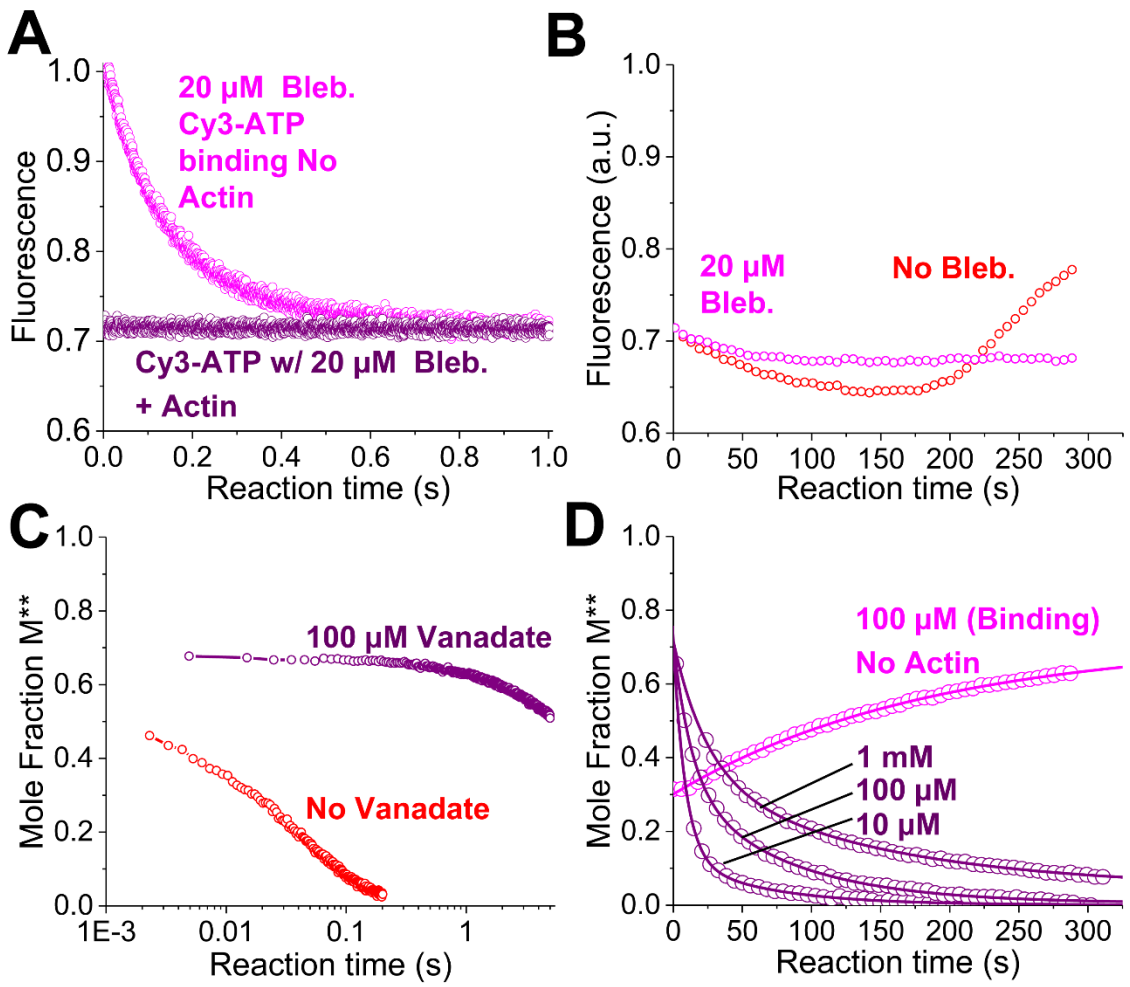

Fig. 14. Blebbistatin and vanadate inhibit LCD rotation
(**A**) Standardized total fluorescence after mixing 0.2 μM donor-labeled HMM and 20 μM blebbistatin with 2 μM Cy3-ATP (magenta) and then with 40 μM Actin (purple). (**B**) Standardized total fluorescence after mixing 0.2 μM donor-labeled HMM, in the presence (magenta) or absence (red) of 20 μM blebbistatin, with 2 μM Cy3-ATP. (**C**) M** mole fraction obtained from $(TR)^2$FRET after mixing 0.2 μM donor-labeled HMM with 2 μM Cy3-ATP (red) or 2 μM Cy3-ADP and 100 μM Vanadate with actin (40 μM post-mix, purple). (**D**) M** mole fraction after mixing 0.2 μM donor-labeled HMM and 2 μM Cy3-ADP with 100 μM vanadate (magenta) or with 40 μM actin and varied [vanadate] (purple). Solutions contained 2 mM $MgCl_2$, 10 mM Tris (pH 7.5), 25 C.

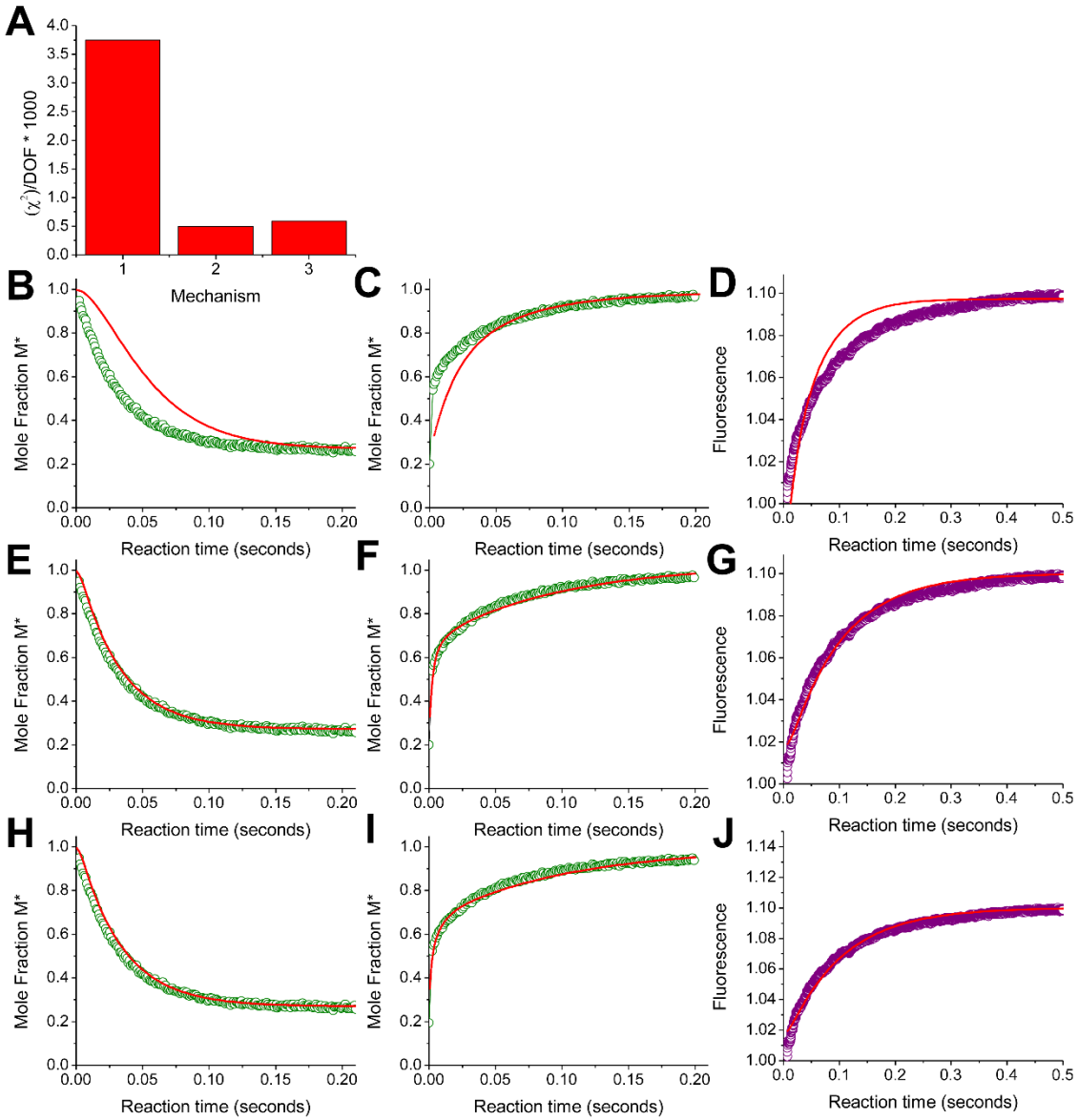

Fig. 15. Global structural kinetics modeling of the power stroke and phosphate release
(**A**) χ^2 for global kinetic fitting of mechanism 1 (phosphate-first), 2 (power stroke first), or 3 (branched) to mole fraction and phosphate release data using KinTek Explorer (SI). (**B-D**) Comparison of data (symbols) and fit (red line) for mechanism-1 fitting, mechanism-2 (**E-G**), or mechanism-3 (**H-J**). (**B, E, H**) Mole fraction M* during ATP binding driven recovery/hydrolysis phase in the absence of actin (data obtained as described in a, 8 μM Cy3-ATP shown). (**C, F, I**) Mole fraction M* during actin-induced single ATP turnover (data obtained as described in Fig. 7, 40 μM actin shown). (**D, G, J**) Phosphate release detected by fluorescence of phosphate binding protein during actin-induced single ATP turnover (data obtained as described in Fig. 8, 40 μM actin shown).

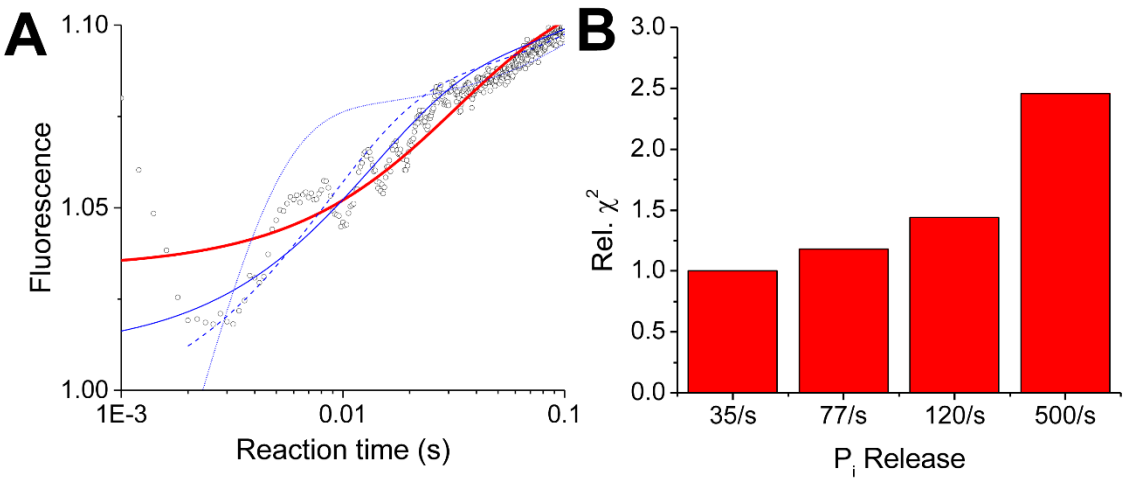

Fig. 16. Sensitivity analysis of phosphate release observed rate constant
(**A**) Phosphate release detected with mdcc-PBP after mixing with 40 μM [actin] as performed in Fig. 3. Data fit with $I(t) = y0 + A1\ e^{-k1\ t} + A2\ e^{-k2\ t}$ fixing k1 at 35 s^{-1} (red line), 77 s^{-1} (solid blue line), 120 s^{-1} (dashed blue line), 500 s^{-1} (dotted blue line). (**B**) Reduced χ^2 normalized to best fit reduced χ^2.

CHAPTER 3: A HEART FAILURE DRUG CHANGES THE MECHANOENZYMOLOGY OF THE CARDIAC MYOSIN POWERSTROKE

This chapter has been adapted from the following publication:

Title: Heart failure drug changes the mechanoenzymology of the cardiac myosin powerstroke

Authors: John A. Rohde, David D. Thomas, and Joseph M. Muretta

Journal: Proc Natl Acad Sci U S A. 114(10): E1796–E1804.

Online: February 21, 2017; ***Published:*** March 7, 2017

doi: *10.1073/pnas.1611698114****; PMID:*** 28223517

Permission: *for all authors of published work in PNAS, the journal grants permission "to include their articles as part of their dissertations."[76]*

3.1 CHAPTER OVERVIEW

Omecamtiv mecarbil (OM) is a small-molecule β-cardiac myosin effector in clinical trials for the treatment of systolic heart failure. Using $(TR)^2$FRET, we discovered that OM binding stabilizes the pre-powerstroke structural state of cardiac myosin—consistent with kinetic studies [17]. It also causes the powerstroke to occur at a slower rate, and after a notable lag of more than 10 ms, a lag not observed in the dissociation of ATP's hydrolyzed phosphate, which is a step in the kinetic cycle of cardiac myosin that was thought to precede the powerstroke. This inhibition suggests the accumulation of an actin-bound structural state of myosin that does not undergo a normal powerstroke. This hypothesis was recently

supported by the Ostap lab using three-bead optical trapping to investigate the effect of omecamtiv mecarbil [54].

3.2 INTRODUCTION

Heart failure is the leading cause of mortality in the United States [45]. A primary defect in heart failure is a loss in cardiac contractility [46] resulting from a range of molecular factors: the sarcoplasmic reticulum's inability to sequester Ca^{2+}, dysfunction of EC-coupling, altered metabolism, changes in gene expression levels, and mutations in sarcomeric proteins [47]. Treatments for heart failure include lifestyle changes, surgeries, medical devices, heart transplant, renin-angiotensin and β-adrenergic modulators, and inotropes that increase contractility. Despite these interventions, life expectancy remains low, and half of the patients diagnosed with heart failure, die within five years [45].

Omecamtiv mecarbil (OM) is a small-molecule β-cardiac myosin effector in clinical trials for the treatment of systolic heart failure. OM was developed from lead compounds identified in a high-throughput calcium-regulated and thin-filament-activated, ventricular cardiac myosin ATPase activity screen [16]. A high-resolution X-ray crystal structure [49] and a photo-reactive cross-linking study [16] both suggest that OM binds near the interface of several of myosin's key, conserved structural elements: the 7-stranded β-sheet, the C-terminus of the relay-helix, the SH1-helix, and the interface between the N-terminal and converter domains. Movements in these elements are coupled to the weak-to-strong actin-binding transition, rotation of the myosin light-chain domain, actin-induced phosphate and ADP release, and subsequently to force generation [6]. Despite a number of

recent studies however [16, 17, 49-53], the structural basis for how OM alters force generation in the heart remains enigmatic.

Mechanically active myosins all use changes in the Gibbs free energy associated with myosin binding to actin, ATP, ADP, and inorganic phosphate (P_i), to drive force-generating structural transitions, most notably a lever-arm rotation of the light-chain domain (LCD). This rotation, termed the powerstroke, converts the free energy liberated from ATP hydrolysis under non-equilibrium cellular conditions, into mechanical work (11, 12). The powerstroke is coupled to actin-activated release of hydrolyzed phosphate, ADP release, and myosin's weak-to-strong actin-binding transition. Structural changes in the myosin nucleotide-binding pocket following actin binding are hypothesized to initiate these transitions, and thus initiate force generation (11, 12). OM accelerates phosphate release from the nucleotide-binding pocket [16, 17], and because LCD rotation is coupled to phosphate release, we hypothesized that OM should also accelerate LCD rotation and initiation of the powerstroke.

We tested this hypothesis using transient time-resolved FRET, abbreviated $(TR)^2$FRET, and transient biochemical kinetics. $(TR)^2$FRET utilizes subnanosecond time-resolved fluorescence, measured repeatedly and with high signal-to-noise, every 0.1 to 0.2 ms, during the transient phase of a biochemical rapid-mixing experiment (12, 13). The resulting time-resolved fluorescence waveforms, 10,000 to 5,000 per second, are independently fit by a structure-based model, revealing the pre-steady-state distribution of nanosecond-resolved structural states detected by FRET, and thus how these states evolve over time during the biochemical transient. This approach has revealed the structural kinetics of the recovery-stroke of *Dictyostelium discoideum* myosin II [77], the

powerstroke and its coordination with phosphate release in both *Dictyostelium discoideum* myosin II [10] and fast skeletal muscle myosin II [1], the recovery and powerstroke in mouse myosin V [104], and the structural kinetics of kinesin family members [105, 106]. Here we apply this technology to answer an important question in molecular cardiology: does OM accelerate the actin-activated powerstroke, as suggested by its effect on phosphate release?

Strikingly, our results disproved our initial hypothesis: though OM binding stabilizes the pre-powerstroke structural state of cardiac myosin—consistent with kinetic studies [17]—it simultaneously causes the powerstroke to occur more than 10 ms after dissociation of ATP's hydrolyzed phosphate. This inhibition suggests the accumulation of an actin-bound structural state of myosin that does not undergo a normal powerstroke. We discuss these effects in detail below.

3.3 RESULTS

Time-resolved FRET detects ADP- and ATP-sensitive structural states of cardiac myosin. We used time-resolved FRET [87] and transient time-resolved FRET (12, 13) to determine if OM changes the orientation of the ventricular cardiac myosin LCD in the absence of actin. Previous kinetics studies on porcine ventricular cardiac myosin showed that OM shifts the apparent equilibrium constant for ATP hydrolysis toward the post-hydrolysis ADP.P_i biochemical state [17]. The orientation of the myosin LCD is coupled to hydrolysis, so OM should alter LCD orientation. To test this hypothesis, we first developed a time-resolved FRET (TR-FRET) based assay to measure LCD orientation in ventricular myosin. Our previous work inspired this assay [1]: We attached the fluorescent donor Alexa Fluor 488 (AF488) to the myosin regulatory light-chain domain and then

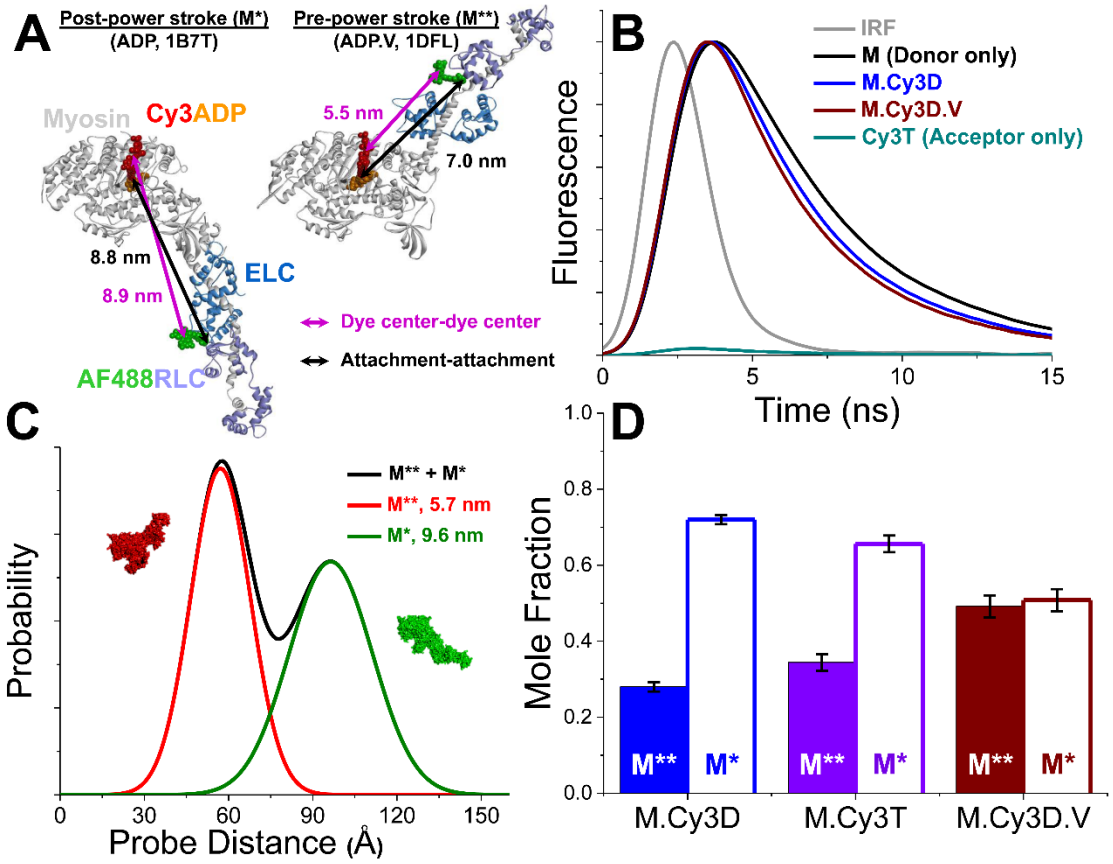

Fig. 17. Time-resolved FRET detects nucleotide-dependent LCD orientation
(A) Predicted distances between the donor (C_α of C108 on the exchanged cgRLC) and acceptor (2′/3’-O of nucleotide ribose), based on post-powerstroke (left, PDB 1B7T, 8.9 nm brown arrow) and pre-powerstroke (right, PDB 1DFL, 5.5 nm brown arrow) structural models (similar to 2MYS and 1BR1 respectively). For simplicity, single-headed myosin S1 is depicted, although all experiments were performed on double-headed HMM. (B) Representative normalized fluorescence waveforms: Instrument response (gray), donor only (black), Cy3-ADP (blue), Cy3-ADP + vanadate (burgundy), non-labeled HMM with bound Cy3-ATP acceptor (cyan). (C) M** (red) and M* (green) structural state obtained from the best fit two structural state model of waveforms in B. (D) Mole fractions of M** (closed bars) and M* states (open bars) in panel C, (n = 9, SEM). M.Cy3T (purple) from transient stopped-flow experiments in Fig. 18. Solutions contained 2 mM $MgCl_2$, 10 mM Tris (pH 7.5), 25 ºC.

incubated the labeled myosin with fluorescent nucleotides 2’/3’-O-(2-aminoethyl-carbamoyl)-adenosine-5’-tri/di-phosphate, (Cy3-ATP, Cy3-ADP, or Cy3-ADP with vanadate).

We prepared the AF488 labeled bovine ventricular cardiac HMM as described in SI Methods (Chapter 3.6). The donor AF488 probe, attached to the C-lobe of an exchanged

RLC in the HMM, exhibited normal ATPase activity (Fig. 24). The spectral overlap between the AF488 donor and Cy3 acceptor gives a Förster distance (R_0) of 6.7 nm [1], and based on high-resolution crystal structure models of pre- and post-powerstroke structural states (examples shown in Fig. 17A, post-powerstroke, PDB: 1B7D, pre-powerstroke, 1DFL), we predicted that the distance between the C-lobe of the RLC and the Cy3-labeled nucleotide ribose would change with LCD rotation and this change would detect the powerstroke. We used a single-cysteine recombinant chicken gizzard RLC, highly homologous to bovine RLC, for these studies because it contains a single cysteine for labeling, and can be exchanged efficiently onto the bovine heavy chain under mild conditions that preserve ATPase activity (Fig. 24), summarized in Table 5.

We measured TR-FRET of the labeled cardiac HMM (100 nM) with either bound Cy3-ADP (20 μM, saturating at equilibrium in a 100 μL cuvette), Cy3-ATP (2.0 μM, only after rapid mixing by stopped-flow to avoid loss of bound Cy3-ATP via basal steady-state ATP turnover), or Cy3-ADP (2.0 μM, at equilibrium in a 100 μL cuvette) with excess vanadate (20 μM), all without actin (Fig. 17B), and then analyzed the resulting data as described in our previous publication [1] and in SI Methods (Chapter 3.6). The TR-FRET decays (Fig. 17B) of the labeled cardiac myosin biosensor detect Cy3-ADP, Cy3-ATP, and Cy3-ADP.vanadate binding. FRET was greater—indicated by the average time-constant for the measured time-resolved fluorescence waveforms, with saturating Cy3-ATP and Cy3-ADP.vanadate, compared to saturating Cy3-ADP. Thus the average distance between the FRET probes is shorter in the presence of the ATP's γ-phosphate or γ-phosphate analog. We observed similar results in skeletal muscle myosin [1]. TR-FRET waveforms can be modeled by well-defined structure-based functions [87] to determine if multiple interprobe

distance distributions are present in the sample (SI Methods, Chapter 3.6)—multiple populations of distance distributions reflect structural heterogeneity in the sample. We performed this analysis as described in our previous studies [1] and validated the best-fit model based on χ^2 minimization (Fig. 25) and the geometry of the χ^2 error surface evaluated by parameter perturbation (Fig. 26) [1].

The TR-FRET waveforms were best-fit by a model composed of two resolved structural states of the LCD (Fig. 17C), a short, 5.7 nm distance distribution, and a longer 9.6 nm distance distribution. The centers of these distributions are consistent with the predictions from high-resolution crystal structures (Fig. 17A). The mole fraction of each distance distribution depended on the nucleotide binding state, just as we observed for skeletal myosin HMM [1]. The mole fraction of the short-distance state (5.7 nm), termed M**, increased with Cy3-ATP binding or Cy3-ADP with excess vanadate (Fig. 17D) compared to Cy3-ADP alone. The apparent equilibrium constant ([M**]/[M*] at 25 ºC) separating the M** and M* states under steady-state ATP bound conditions was 0.7—it is 4.0 in rabbit fast skeletal muscle HMM measured under similar thermodynamic conditions [1]. The difference between the M**/M* equilibrium constant, under steady-state ATP bound conditions in the absence of actin, in skeletal muscle myosin HMM and bovine ventricular cardiac myosin HMM, is consistent with predictions of the ratio between pre-powerstroke M** and post-powerstroke M* states, 0.8, made from tryptophan fluorescence measurements reported by Liu et al. [17].

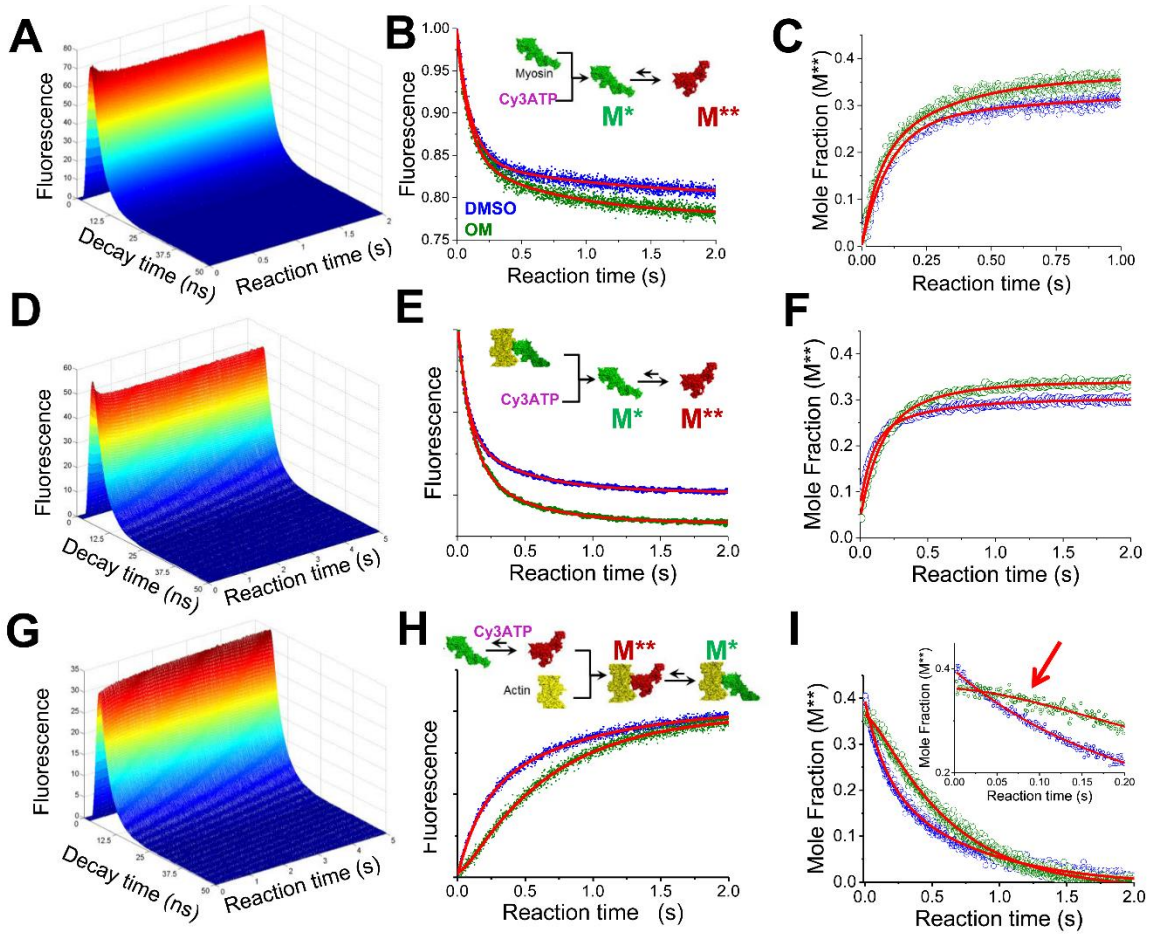

Fig. 18. $(TR)^2$FRET used to detect actomyosin structural kinetics
(A-C) Cy3-ATP binding and approach to steady-state with donor-labeled cardiac HMM, representative waveforms shown in A, total fluorescence shown in B, fits in B: $F_{DMSO} = 0.16e^{-9.4t} + 0.04e^{-0.9t} + 0.80$, $F_{OM} = 0.14e^{-10.6t} + 0.07e^{-1.3t} + 0.78$. Mole fractions of the M** state shown in C, fits in C: $M^{**}_{DMSO} = 0.339 - 0.263e^{-9.2t} - 0.073e^{-1.03t}$, $M^{**}_{OM} = 0.362 - 0.183e^{-15.2t} - 0.177e^{-3.13t}$. Experiments performed in the presence of 5 μM OM (green symbols) in assay buffer with 1% DMSO or DMSO alone (blue symbols). (D-F) Cy3-ATP binding to HMM as in A, in the presence of 20 μM Actin, total fluorescence in E, fits in E: $F_{DMSO} = 0.14e^{-13.4t} + 0.07e^{-2.2t} + 0.80$. $F_{OM} = 0.16e^{-10.3t} + 0.08e^{-2.3t} + 0.77$. Mole fraction M** in F, fits in F: $M^{**}_{DMSO} = 0.301 - 0.155e^{-11.3t} - 0.15e^{-2.09t}$, $M^{**}_{OM} = 0.338 - 0.181e^{-7.81t} - 0.116e^{-2.32t}$. (G-I) Powerstroke: TR-FRET waveforms starting from the steady state shown in A, after mixing with actin (40 μM post mix), total fluorescence in H, mole fractions of M** in I. Inset in I shows the lag phase induced by OM binding, $M^{**}_{DMSO} = 0.161e^{-6.72t} + 0.244e^{-1.37t}$, $M^{**}_{OM} = 0.4469e^{-1.76t} - 0.069e^{-10.7t}$. TR-FRET waveforms in A, C, and G, acquired every 0.2 ms (1 ms average shown). Total fluorescence in B, E, and H determined as described in SI. Mole fractions of M** structural states in C, F, and I determined by fitting $(TR)^2$FRET data obtained as in panels A, D, and G, to a global M*-M** structural state TR-FRET model described in SI. Solutions contained 2 mM $MgCl_2$, 10 mM Tris (pH 7.5), 1 % DMSO, 25 ºC. In the reaction schemes of B, E and H, M** is depicting a fraction (Fig. 17D) of molecules in this state. Data are representative of n = 9 experiments.

As we observe in skeletal myosin [1], the short 5.7 nm distance M** state is also detected when Cy3-ADP is bound at saturation, though at a lower relative mole fraction (0.28, Fig. 17D). Thus the average distance between probes is longer in the presence of ADP, and myosin spends a greater percentage of its time in a post-rigor, post-powerstroke structural state, while still periodically isomerizing to a pre-powerstroke state. This is consistent with crystallization studies showing that myosin can be crystalized in both pre- and post-powerstroke structural states in the presence of ADP [12]. Together, these results demonstrate that the ventricular cardiac myosin LCD isomerizes between pre- and post-powerstroke orientations in the presence of both Cy3-ATP and Cy3-ADP and that the γ-phosphate shifts the apparent equilibrium constant for this isomerization at 25 ºC from 0.4 with Cy3-ADP to 0.7 with Cy3-ATP and to 1.0 with Cy3-ADP.V_i.

OM stabilizes an actin-attached pre-powerstroke structural state. The FRET-based cardiac myosin biosensor allows us to correlate the structural kinetics of LCD rotation with the nucleotide binding state. We used a similar approach in our previous work to characterize ATP-induced priming of the pre-powerstroke state in fast skeletal myosin II and the actin-induced powerstroke [1]. We mixed cardiac HMM in the absence or presence of excess actin (20 μM) with varied [Cy3-ATP], all in the presence (5 μM in 1% DMSO) or absence (1% DMSO) of saturating OM and then acquired time-resolved FRET waveforms every 0.2 ms. These waveforms showed robust changes in the TR-FRET as evident by transient changes in their time-integrated total fluorescence (Fig. 18 B, E). We evaluated transient changes in the mole fraction of the M* and M** states (Fig. 18 C, F) determined by fitting the M*/M** structural state model described in Fig. 17, to the acquired data as performed in our previous work [1].

Cy3-ATP binding to HMM or HMM complexed with actin, induced a bi-exponential time-dependent change in the total fluorescence (Fig. 18 B, E) of the AF488 donor probe and the M** mole fraction (Fig. 18 C, F) in the presence and absence of 5 μM OM, consistent with Cy3-ATP binding and formation of a high-FRET state described in Fig. 17. The rate constants for this bi-exponential transient increased with [Cy3-ATP] (

Fig. **19**A, B), consistent with the characterized kinetics of cardiac myosins [107] and were not greatly affected by the drug. The apparent second-order rate constant for Cy3-ATP binding to HMM is 6.9 $\mu M^{-1}s^{-1}$ and 4.0 $\mu M^{-1}s^{-1}$ in the absence and presence of the drug respectively, and to HMM complexed with actin, 4.0 $\mu M^{-1}s^{-1}$ in both cases (Table 5, extrapolated from the hyperbolic [Cy3-ATP] dependence of the observe rate constants in

Fig. **19**. The total [M**] at steady-state in the absence of OM, extrapolated from the bi-exponential fit to the data, showed that the apparent M**/M* K_{eq} is 0.53 ± 0.03 in the absence of actin, and 0.74 ± 0.04 in the presence of actin (20 μM). OM induces a small change in the M**/M* ratio, shifting the apparent K_{eq} to 0.56 ± 0.04 in the absence of actin and 0.87 ± 0.05 in the presence of actin (20 μM) (Fig. 18). This contrasts conclusions in previous work by Liu et al. [17]. We address this contrast in the discussion.

OM prevents the actin-induced powerstroke. We measured actin-induced structural changes in the absence (1 % DMSO) and presence of OM (5 μM in 1 % DMSO) by preparing 0.2 μM AF488 labeled cardiac HMM with 2 μM excess Cy3-ATP in syringe A of the stopped-flow, and then mixing this steady-state complex, with varied concentrations of actin (10 μM to 40 μM, final concentrations after mixing) in syringe B containing 1 mM MgATP. The 1 mM MgATP prevents multiple actin-activated Cy3-ATP

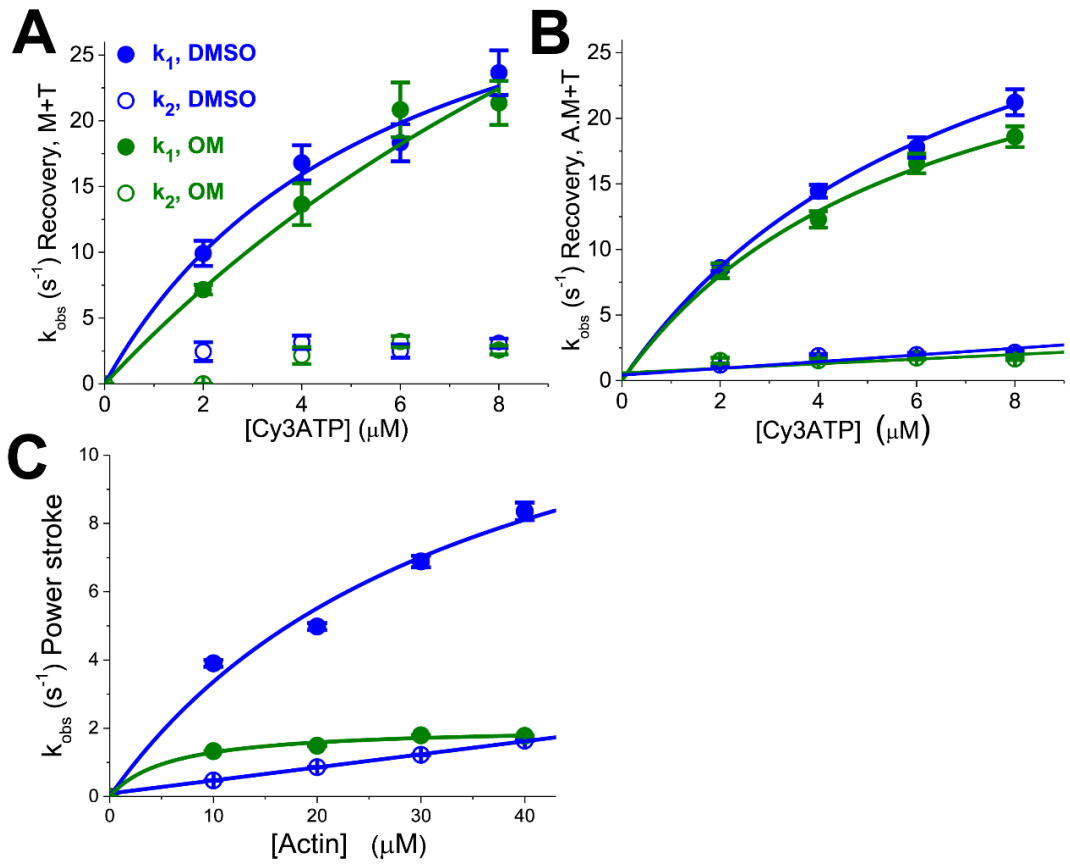

Fig. 19. Structural kinetics of ATP-driven actin detachment and actin-induced powerstroke
(A) Hyperbolic dependence between the rate constant for fast (closed circles) and slow (open circles) phases for Cy3-ATP induced M** accumulation during Cy3-ATP binding to HMM in 1% DMSO (blue) or 5.0 μM OM in 1 % DMSO (green) performed in **Fig. 18**A-C. Fits in A: $k_{1,DMSO}$ = 39 s^{-1}·[Cy3T]/(5.81μM+[Cy3T]), $k_{1,OM}$ = 75s^{-1}·[Cy3T]/(18.7μM+[Cy3T]).
(B) Data acquired during Cy3-ATP binding to HMM complexed with 20 μM Actin performed in **Fig. 18**D-F. Fits in B: $k_{1,DMSO}$ = 40.4 s^{-1}·[Cy3T]/(7.3 μM+[Cy3T]), $k_{1,OM}$ = 33.0 s^{-1}·[Cy3T]/(6.2 μM+[Cy3T]), $k_{2,DMSO}$ = 0.26 s^{-1}/μM·[Cy3T]+0.42μM, $k_{2,OM}$ = 0.18 s^{-1}/μM·[Cy3T]+0.59μM.
(C) Actin dependence of observed rate constants of the actin-induced powerstroke performed in **Fig. 18**G-I. Fits in C: $k_{1,DMSO}$ = 15.3 s^{-1}·[Actin]/(35.5μM+[Actin]), $k_{2,DMSO}$ = 0.038s^{-1}/μM·[Actin]+0.089μM, $k_{1,OM}$ = 2.05 s^{-1}·[Actin]/(5.85 μM+[Actin]). No fast phase is detected in the presence of OM. Solutions contained 2 mM $MgCl_2$, 10 mM Tris (pH 7.5), 25 ºC.

turnover reactions ensuring that the actin-induced changes in FRET (Fig. 18G-I) reflect a single weak-to-strong actin-binding transition [88].

In the absence of OM, the total fluorescence transients (Fig. 18H) and M** mole fraction transients (Fig. 18I) were best-fit by a bi-exponential function, consistent with a multi-step kinetic process. The observed rate constant for the fast phase (

Fig. 19C) increased with increasing [actin]—we modeled this increase with a hyperbola—while the slow phase did not change with increasing [actin] (

Fig. 19C). The $K_{0.5}$ for the hyperbolic dependence of the fast phase was 35.5 ± 18.1 μM and the predicted maximum rate constant was 15.3 ± 4.3 s^{-1} (Table 5). OM induced a lag phase, followed by a single-exponential actin-activated powerstroke (Fig. 18 I, inset, red arrow). This indicates that OM delays the actin-induced rotation of the LCD.

OM uncouples the powerstroke from actin-activated phosphate release. We compared the structural kinetics of the myosin powerstroke, described above, with the kinetics of actin-activated phosphate release (Fig. 20) using MDCC labeled phosphate binding protein (PBP) [86] as described in SI Methods and in our previous work [1]. OM increased the actin-activated release of hydrolyzed phosphate (Fig. 20B), consistent with previous reports (5,7). We ensured that the detected phosphate release was not affected by contaminating phosphate present in the actin by performing control experiments mixing the actin with ATP in the presence of the PBP sensor (Fig. 32). This is an important control because actin polymerization requires ATP and even after phalloidin stabilization with extensive dialysis, polymerized actin can contain significant bound phosphate. We find that rapid mixing actin by stopped-flow can trigger release of the bound phosphate (Fig. 32)—presumably reflecting sheering of longer filaments—thus we extensively dialyze the stabilized actin in the presence of the phosphate mop to remove trace amounts of bound P_i.

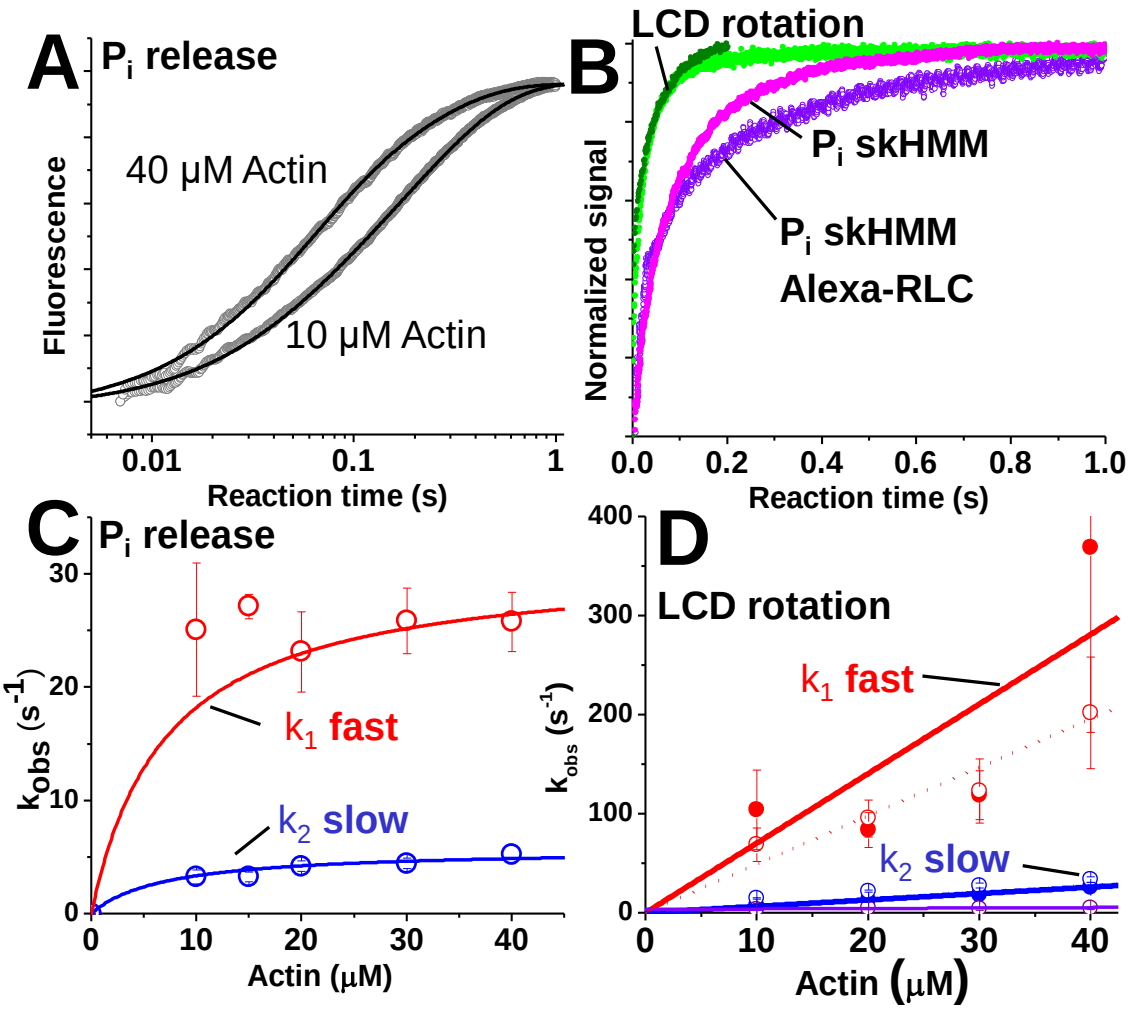

Fig. 20. Comparison of phosphate release and LCD structural kinetics.
(A) Representative fluorescence of PBP after mixing 1 μM HMM containing 2 μM ATP with [actin]. Best fit functions $I(t) = 1 + 0.24e^{-20t} + 0.74e^{-4.3t}$and $I(t) = 1 + 0.57e^{-20t} + 0.42e^{-5.3t}$at 10 μM and 40 μM actin respectively. (B) Direct comparison between phosphate release (magenta skHMM with native RLC, purple skHMM with exchanged Alexa-RLC), total myosin fluorescence (light green), and M* mole fraction (dark green). (C) Observed rate constants for phosphate release (red, fast phase, blue, slow phase). (D) Rate constants for actin-induced LCD rotation (total fluorescence, open, M* mole fractions, solid) fit as in Fig. 19D,F. Triple exponential fit phase 1 red, phase 2 blue, phase 3 purple.

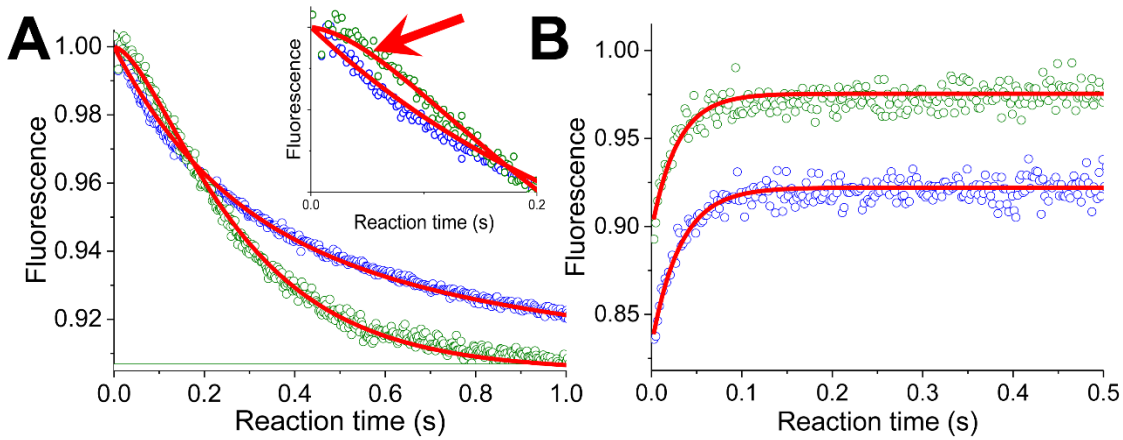

Fig. 21. Single actin-activated ATP turnover and ADP release kinetics in the presence of OM
(A) Actin-activated single turnover of mant-ATP performed by sequential mix of 1.0 μM HMM with 0.5 μM mant-ATP, aged 2 seconds and mixed with 20 μM actin and 1 mM ATP all in the presence or absence of saturating OM (post-mix concentrations). Fits in A: $F_{DMSO} = 0.899 + 0.06e^{-3.9t} + 0.04 e^{-0.71t}$, $F_{OM} = 0.905 + 0.145e^{-4.4t} – 0.05e^{-12.1t}$.
(B) ADP release kinetics measured by mixing 0.1 μM HMM bound to 10 μM actin and equilibrated with 2.0 μM Cy3-ADP mixed with 5.0 mM unlabeled ATP, in the presence or absence of saturating OM. Fits in B: $F_{DMSO} = 0.918 – 0.097e^{-31.5t}$, $F_{OM} = 0.973 – 0.080e^{-35.1t}$.

The observed rate constant for actin-activated phosphate release increased hyperbolically with increasing [actin], exhibiting a $K_{0.5}$ of 15.5 ± 6.5 μM in the 1 % DMSO and 26.1 ± 7.7 μM in the presence of 5 μM OM (Table 5). OM increased the maximum rate constant for actin-activated phosphate release from 11.6 ± 2.4 s^{-1} to 22.2 ± 3.9 s^{-1} (Table 5) consistent with previous reports [17], but in sharp contrast to the compounds effect on the powerstroke shown in (Fig. 18 G-I). Thus, OM binding to cardiac myosin inhibits the actin-induced rotation of the myosin light-chain domain, despite activating actin-induced dissociation of phosphate from the myosin surface. This suggests that the compound increases the transition state free energy separating the pre and post-powerstroke structural states of myosin and decreases the transition state free energy for phosphate release.

OM inhibits actin-activated ATP turnover but not ADP release. OM's effect on the powerstroke suggests that single ATP turnover should be slowed. We investigated this by mixing 1.0 μM cardiac HMM with 0.5 μM 2'/3'-O-N-methylanthraniloyl adenosine 5'-triphosphate (mant-ATP), a fluorescent ATP derivative that reports bound ATP directly [88], in the stopped-flow, aged the mixture for 2.0 seconds to allow hydrolysis, and then mixed the resulting steady-state with 20 μM actin similar to Fig. 18. Again, OM slowed ATP turnover in the first 100 ms of the reaction (Fig. 21), similar to the powerstroke. We verified that the single-turnover kinetics of mant-ATP and Cy3-ATP are identical (Fig. 31), thus the FRET and mant-ATP turnover experiments are comparable. We measured the kinetics of ADP release by mixing an equilibrated solution of 10 μM actin, 0.1 μM of the AF488 labeled cardiac HMM and 2.0 μM Cy3-ADP with 5.0 mM ATP (Fig. 21B) and then monitored the kinetics of Cy3-ADP dissociation by detecting FRET between the AF488 label and the Cy3 fluor as in Fig. 18. The kinetics of the resulting fluorescence transients were indistinguishable from each other, exhibiting a single-exponential rate constant of $35.1 \pm 2.2\ s^{-1}$ in the presence of DMSO and $31.5 \pm 1.5\ s^{-1}$ in OM. Thus, OM does not alter the kinetics of ADP release, consistent with previous reports [16, 17].

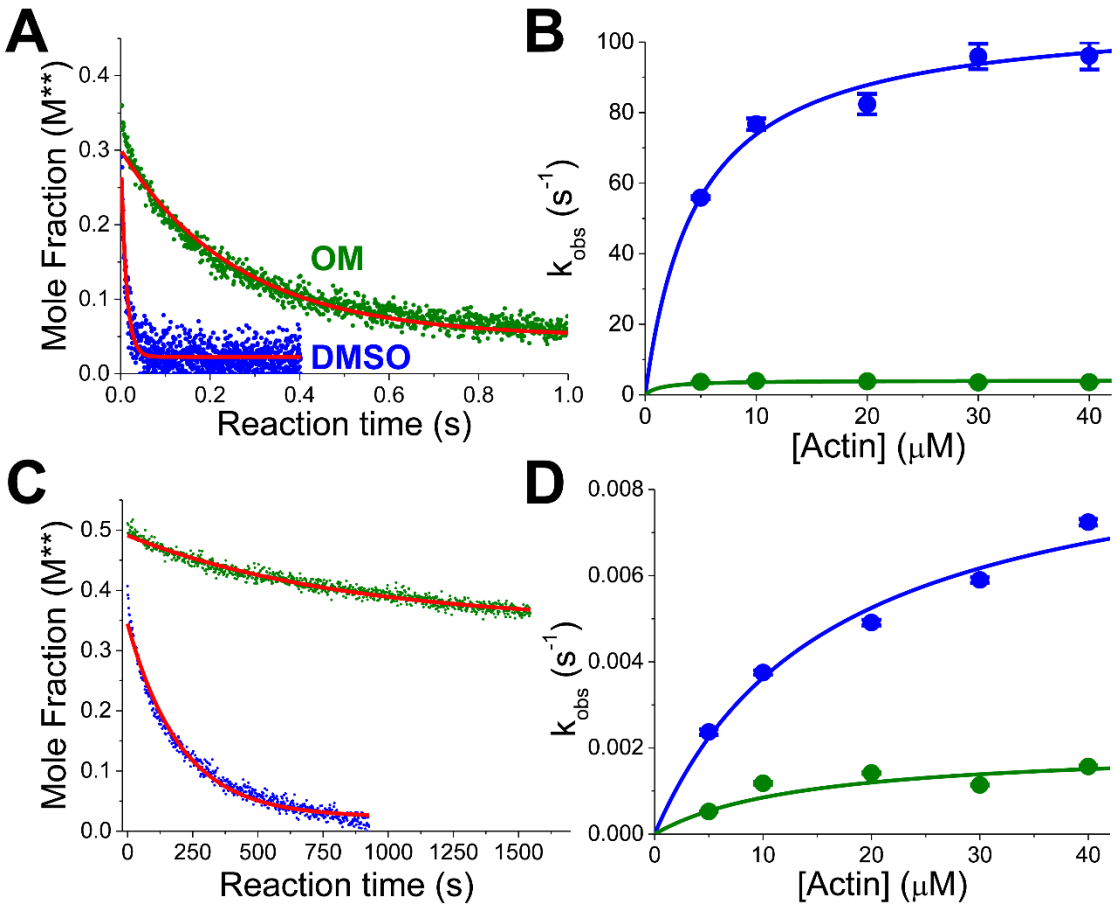

Fig. 22. OM inhibits actin-induced LCD rotation when Cy3-ADP or Cy3-ADP and vanadate are bound to HMM

(A) 0.1 μM labeled HMM and 2.0 μM Cy3-ADP were equilibrated and then mixed with 20 μM actin and 5 mM ATP in the presence (green) or absence (blue) of 10 μM OM. (B) Actin dependence of the observed rate constant obtained by fitting data in panel A to a single-exponential function over a range of actin concentrations, $k_{obs,DMSO}$ = 108.3 s^{-1}[Actin]/(4.6 μM + [Actin]), and $k_{obs,OM}$ = 4.1 s^{-1}[Actin]/(0.7 μM + [Actin]). (C) 0.1 μM HMM, 2.0 μM Cy3-ADP and 100 μM vanadate were equilibrated for 20 minutes and then mixed with 20 μM actin, 100 μM vanadate, and 5 mM ATP. (D) Actin dependence of the observed rate constant obtained by fitting data in panel D to a single hyperbolic function, $k_{obs,DMSO}$ = 9.5 x 10^{-3} s^{-1}/(16.2 μM + [Actin]) and $k_{obs,OM}$ = 2.03 x 10^{-3} s^{-1}/(14.0 μM + [Actin]).

OM slows light-chain domain rotation in the absence of ATP's γ-phosphate.

ADP binding stabilizes a small fraction of the M** structural state (Fig. 17). We investigated the effect of actin on this M** population by mixing an equilibrated solution of 0.1 μM AF488 labeled cardiac HMM and 1.0 μM Cy3-ADP with actin varied from 5.0

μM to 40 μM in the presence of 1 mM ATP. We acquired $(TR)^2$FRET waveforms as in Fig. 18 and then determined the mole fraction of M** and M* during the resulting transient. The M** mole fraction transients (Fig. 22A) were single-exponential. The rate constants for these exponentials increased hyperbolically with increasing [actin] (Fig. 22B). The $K_{0.5}$ for this increase was 4.7 ± 0.4 μM and the k_{max} was 108.3 ± 4.6 s^{-1}, three-times faster than the rate constant for ADP release detected in Fig. 21B. Thus, in the absence of OM, actin straightens the LCD before ADP is released from the ATPase site. We performed the same experiment in the presence of OM. The maximum rate constant for LCD rotation decreased to 4.1 ± 0.2 s^{-1}, a 26-fold decrease compared to the rate constant in the absence of the drug. Thus, OM inhibits LCD rotation, even in the absence of ATP's γ-phosphate.

OM inhibits actin-induced LCD rotation in the presence of both ADP and vanadate. OM's acceleration of phosphate release suggests that it changes the energetics of myosin's actin-activation. To further dissect the structural determinants for this acceleration, we evaluated the dependence of actin-induced LCD rotation on orthovanadate (V_i), a phosphate analog that binds with sub-μM affinity to myosin in the presence of ADP, and μM affinity in the presence of saturating actin and ADP. Vanadate binding stabilizes a closed structural state of the switch-2 and switch-1 loops thought to mimic a post-hydrolysis/pre-phosphate release structural configuration [92]. In our previous work investigating the powerstroke and phosphate release in skeletal myosin, we found that vanadate binding to myosin with ADP ($ADP.V_i$) prevented LCD rotation, even though LCD rotation preceded phosphate release during single ATP turnover. Thus vanadate binding traps a "locked" structural state of myosin where the LCD is prevented from rotating. We propose that this trapped state precedes the movement of phosphate away

from ADP after hydrolysis, consistent with arguments proposed by Llinas et al. [12]. We hypothesized that OM would slow the actin-activated exchange of vanadate, just as it slows actin-activated LCD rotation, given our prior hypothesized coupling between switch-2 movement and the powerstroke in skeletal myosin.

We measured the ability of vanadate to prevent the actin-induced rotation of the cardiac myosin LCD, by performing $(TR)^2$FRET experiments mixing 0.1 μM AF488 labeled cardiac HMM, 2.0 μM Cy3-ADP and 100 μM vanadate with a range of actin concentrations all containing 5.0 mM ATP. We acquired and fit the resulting waveforms as described for Fig. 18. In the absence and presence of OM, the M** mole fraction transients were single-exponential with the rate constants increasing hyperbolically with increasing actin (Fig. 22). At 100 μM vanadate, the k_{max} decreased from 0.010 ± 0.001 s^{-1} in the absence of OM to 0.002 ± 0.001 s^{-1} in the presence of the drug, a 5-fold decrease, while the [actin] $K_{0.5}$ did not change (16.2 ± 3.9 μM and 14.0 ± 4.6 μM respectively). Thus, OM slows actin-induced vanadate exchange, but does not change the affinity of actin for myosin.ADP.V_i.

The observed rate constant for actin-activated dissociation of Cy3-ADP.Vi decreases with increasing vanadate, indicating that rebinding of vanadate to actomyosin.ADP before ADP dissociation traps the complex. The [vanadate] dependence of this inhibition reflects the affinity of actomyosin.ADP for vanadate. We varied the concentration of vanadate included in the reaction (Fig. 27C), fit the resulting M** transients to single-exponential functions as in Fig. 22 and then evaluated the dependence of the observed rate constant on [V_i] (Fig. 27C). The maximum rate constant determined from these fits (as [V_i] goes to 0 μM) was 85.5 ± 1.9 s^{-1} in the absence of OM, and 8.7 ±

3.4 s^{-1} in the presence of the drug, consistent with the observed rate constant in the presence of ADP without vanadate under similar [actin] conditions (Fig. 22B). The $K_{0.5}$ for this dependence was 3.8 ± 0.1 μM in the absence of OM and 2.7 ± 1.8 μM in the presence of the drug. Thus, OM does not change the affinity of actomyosin.ADP for vanadate; it only slows exchange of vanadate with actomyosin.ADP, in contrast to OM's acceleration of phosphate release. We discuss these differences below.

3.4 DISCUSSION

In this study, we investigated how OM alters the structural kinetics of bovine ventricular cardiac myosin's force-transducing structural transition, actin-induced light-chain domain rotation—*vis-à-vi* the powerstroke. Previous kinetic studies showed that OM inhibits cardiac myosin's basal and actin-activated ATPase activity, while simultaneously increasing the apparent rate constant for actin-induced phosphate release 2-3 fold (4, 10). OM also shifts the equilibrium constant for hydrolysis toward the post hydrolysis ADP.P_i state by more than 6-fold. However, those studies do not determine which step in the ATPase cycle is slowed by the drug *in vitro*, as the measured biochemical steps are either affected to a negligible degree, or are accelerated by OM [17]; none yet examined are greatly slowed.

OM dramatically alters myosin's mechanical properties. The drug inhibits the sliding velocity of actin filaments *in vitro*—more than 20-fold [17, 50, 108], while simultaneously increasing the ensemble stall-force induced by a model for viscoelastic load in the same motility assay [50]. That study suggested that OM increases the relative amount of time that myosin spends bound to actin during its ATPase cycle *in vitro* as much as 10-fold and increased the average force generated by actin-attached cross-bridges [50],

suggesting that it increases the unimolecular force-generating capacity of single myosin molecules and the actin-binding affinity of cardiac myosin or cardiac myosin bound by ADP [109-111].

Myocardial mechanics studies reached similar conclusions [53], showing that OM increases the fraction of time cardiac myosin spends attached to actin generating force, though not nearly as much as predicted from *in vitro* motility studies [17, 50, 108]. This increase, which occurred in both mouse, enriched in the faster α-cardiac myosin isoform, and human ventricular myocardium, highly enriched in the slower β-cardiac myosin isoform, is primarily the result of a decrease in the rate constant for actin-detachment [53]. The kinetic step that limits actin detachment in these experiments was not clear, as the kinetics of ADP release in the absence of load is not altered by OM in solution (Fig. 21) [10]. Future work will be needed to determine whether OM slows ADP release when myosin is loaded. Our results showing a 25-fold decrease in the rate of actin-induced LCD rotation when ADP is bound in the presence of OM (Fig. 22), suggest that it will. They also suggest that in the presence of OM, the rate limiting step for steady-state ATPase cycling and for force development in the contracting heart is actin-induced rotation of the cardiac myosin LCD (Fig. 23).

OM also binds to skeletal myosin and inhibits the steady-state ATPase cycling (Fig. 28), albeit at higher concentrations of the drug [16]. Thus, we performed similar experiments with a skeletal myosin HMM and find that OM slows the powerstroke there as well (Fig. 28, SI Methods). This suggests that derivatives of OM that specifically bind other myosin family members—fast-skeletal myosin, smooth and non-muscle myosin II, or transport motors like myosin V, VI, VII, or X— at sub-μM concentrations, would be

potent modulators of their unique mechano-enzymologies and molecular physiology in cells.

OM slows the powerstroke but accelerates phosphate release. When we began this study, we hypothesized that OM accelerates the powerstroke as it accelerates phosphate release (Fig. 20) (Table 5) [16, 17]. Our work on fast skeletal myosin II [1], *Dictyostelium disodium* myosin II [10], and myosin V [104] all show that FRET-detected structural transitions associated with lever-arm rotation occur faster than the actin-induced dissociation of hydrolyzed phosphate. Thus we reasoned that OM's acceleration of P_i release would be accompanied by a corresponding acceleration in the powerstroke.

In the absence of OM, the observed phosphate release rate constant predicted from fitting the actin dependence of the fast phase of actin-induced phosphate dissociation from the myosin surface, is 25% slower than the predicted maximum rate constant for light-chain domain rotation detected by FRET (11.6 s^{-1} vs. 15.5 s^{-1}, Table 5). This 25% difference is comparable to the 43% difference seen in myosin V, where phosphate release is 201 s^{-1} and lever arm rotation is 352 s^{-1} [104], but much less than the 10-fold difference observed in fast skeletal myosin HMM, where phosphate release was measured at 38 s^{-1} and LCD rotation at > 500 s^{-1} [1], and in the *Dictyostelium* myosin II catalytic domain, where phosphate release was 37 s^{-1} and relay-helix straightening was > 500 s^{-1} [10].

OM increased the rate constant for actin-activated phosphate release from 11.6 ± 2.4 s^{-1} to 22.1 ± 3.9 s^{-1}; a similar change was observed by Liu et al. [17]. But rather than accelerate the powerstroke as we initially hypothesized, OM causes the force-generating lever-arm rotation to lag behind actin-activated phosphate release (Fig. 18H, I). The pre-exponential amplitude of the lag, increased hyperbolically with [OM] (Fig. 29, Methods).

The apparent $K_{0.5}$ for this increase was 25 μM (Fig. 29) compared to the reported affinity of OM binding to cardiac myosin alone, 1.6 μM [16]. This suggests that the compound must dissociate prior to LCD rotation and that OM binds more weakly to the actomyosin.ADP complex than to myosin in the absence of actin. This is reminiscent of how actin affects the affinity of myosin II for blebbistatin [112] and for vanadate in the presence of ADP [1], and is consistent with the stabilization of an actin-bound pre-powerstroke structural state. Furthermore, OM dramatically slowed actin-induced LCD rotation in our cardiac HMM sensor with either bound ADP or bound ADP.V_i (Fig. 22). This inhibited rotation precedes ADP release, as OM has no effect on the kinetics of ADP dissociation from cardiac HMM bound to actin (Fig. 21B). Thus OM's primary effect is to inhibit the actin-induced rotation of cardiac myosin's light-chain domain before and after phosphate dissociation.

The crystal structure of the catalytic domain of human cardiac myosin lacking light-chains, crystalized in a nucleotide free, near-rigor/pre-recovery/post-powerstroke-like structural state, in the presence of OM [49], suggests that OM increases the twist of myosin's critical β-sheet in the absence of nucleotide. The structure of cardiac myosin in a true pre-powerstroke state with bound OM has not been reported. Such a state, when revealed, will provide key insight into OM's mode of action. The subtle twisting of the β-sheet by OM [49] is consistent with the slight stabilization of the pre-powerstroke state shown in Fig. 18 and Fig. 27: the β-sheet is hypothesized to twist with ATP binding and subsequent closure of myosin's conserved nucleotide binding loops: switch-1, switch-2 and the P-loop. The powerstroke structural transition is coupled to the structural state of

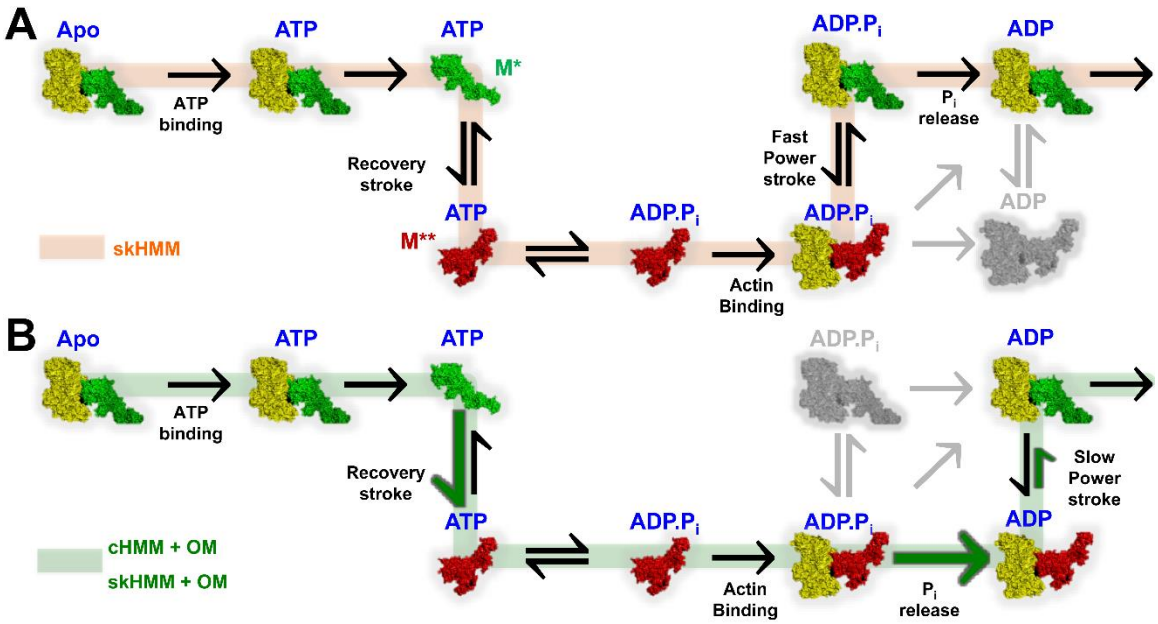

Fig. 23. Thermodynamic models for modulation of P_i release-powerstroke coupling by OM (A) The coordination of the powerstroke and P_i release in skeletal HMM (skHMM) is best fit by a powerstroke first model (orange)[1]. (B) However, cardiac HMM (cHMM) + OM and skHMM + OM accelerates P_i release, stabilizes the M** state, while introducing a lag in the powerstroke (green arrows) suggesting a phosphate-first mechanism (green line). In each case, statistical mechanics requires that off pathway states are accessible (gray).

these conserved nucleotide-binding elements and is hypothesized to correlate with β-sheet straightening, though the exact timing of this coordination has not been fully established.

OM increases the fraction of time that cardiac myosin spends bound to actin. Phosphate release is coupled to the weak-to-strong actin-binding transition. Dissociation of hydrolyzed phosphate allows the actin-binding cleft to close, switch-I to open, and Mg^{+2} and ADP to dissociate [6]. OM accelerates P_i release [16, 17], but as Fig. 18I shows, it slows down the powerstroke while having no effect on ADP release (Fig. 21). These changes would increase the amount of time that individual myosin cross-bridges spend bound to actin, consistent with cardiac myocardium experiments suggesting a 50% increase in the strong actin-binding attachment time, a 20% increase in force-generating cross-

bridge stiffness and a corresponding increase in cross-bridge mediated thin-filament activation [53].

The inhibition of the powerstroke by OM helps explain the decreased actin sliding velocity seen in the *in vitro* motility assay [17, 50, 108]. The powerstroke performs mechanical work on actin to drive filament sliding. OM inhibits powerstroke rotation, prolonging the time myosin spends bound to actin in a pre-powerstroke state after phosphate dissociates. This state binds actin more strongly than before phosphate is released as indicated by comparing the $K_{0.5}$ values for the [actin] dependent transitions measured in this study (Table 5), all of which decrease in the absence of P_i or P_i analogs. Thus the OM trapped pre-powerstroke state should act as a drag force on actin-filament sliding, just as seen in the *in vitro* motility assay [17, 50, 108]. OM lowered the [actin] $K_{0.5}$ for the actin-induced powerstroke from 35 μM to 5μM and for actin-induced LCD rotation in the presence of ADP from 5 μM to 0.7 μM (Table 5), all indicating that the drug strengthens the affinity of cardiac myosin binding to actin during force generation. This strengthened binding is consistent with a previously proposed increase in the actomyosin duty cycle [17, 50, 108] during ATPase cycling, and also with the observed increase in maximum ensemble force generation in the *in vitro* motility assay (7) as maximum force generation by myosins correlates with the energetics of actomyosin binding [109-111].

However, OM does not strengthen the actin binding affinity of ADP.phosphate bound cardiac myosin. The [actin] $K_{0.5}$ for exchange of ADP and vanadate, a kinetically stable post-hydrolysis ADP.P_i analog, was 16.2 μM and 14.0 μM in the absence and presence of OM respectively (Table 5), while the [actin] $K_{0.5}$ for actin-activated

phosphate release was increased from 15.5 μM to 26.2 μM (Table 5). The difference between the [actin] $K_{0.5}$ for myosin.ADP.V_i and the [actin] $K_{0.5}$ for phosphate release in the presence of OM, suggests that myosin is in unique structural states under the two biochemical conditions (P_i vs V_i) consistent with OM's acceleration of actin-activated phosphate disociation from the myosin surface, and slowed actin-induced vanadate exchange.

The actin-activated ATPase K_m decreases 2-fold with OM binding (Table 5), this, together with the decreased actin $K_{0.5}$ for LCD rotation after phosphate release and during actin-induced LCD rotation in the presence of ADP suggest that strong actin-binding, post-phosphate release species accumulate on actin during steady-state ATPase cycling. Consistent with this, the M** mole-fraction is increased at steady-state upon mixing cardiac HMM bound to actin with excess Cy3-ATP in Fig. 18.

The cardiac myosin powerstroke is closely coordinated with phosphate release in the absence of OM. Our previous studies of fast skeletal myosin showed that actin induces LCD rotation more than 10 times faster than phosphate dissociates from the surface of myosin [1]. In that same study, we found that LCD rotation is blocked by both blebbistatin and vanadate. Both molecules are thought to trap phosphate in the nucleotide binding site with the switch-2 loop closed [91, 92]. Together, these results suggest that switch-2 opening is required for LCD rotation, phosphate release, and the weak-to-strong actin binding transition.

Phosphate release and the powerstroke are definable molecular events. The simplest thermodynamic mechanism explaining the coordination between these events is depicted in Fig. 23. Statistical mechanics requires that the molecules of the system diffuse

over all possible paths in this mechanism—some myosin molecules will dissociate phosphate before the powerstroke (Fig. 23B), others will undergo the powerstroke before phosphate release (Fig. 23A), some will undergo both transitions simultaneously, traversing the landscape diagonally from the pre-powerstroke ADP.P_i state to the post-powerstroke ADP state.

In skeletal myosin, it is clear that the structural transition associated with LCD rotation precedes phosphate dissociation in solution and thus the orange pathway in Fig. 23A is favored. In cardiac myosin, our results show that at saturating [actin] the powerstroke occurs only 0.25 times faster than phosphate release (Table 5). This difference is similar to the 0.43-fold difference seen in myosin V and suggests that LCD rotation is more closely coordinated with actin-induced phosphate release in higher duty-ratio motors, like β-cardiac myosin and myosin V, than in low duty-ratio motors like skeletal muscle myosin. The physiological implications for the difference between the coordination of the powerstroke and phosphate release in different myosin isoforms remain to be fully determined but probably reflects the intrinsic role each protein plays in cells.

OM increases the transition state free energy for the powerstroke. OM is an allosteric inhibitor of myosin ATPase cycling (10). It is also an allosteric activator of phosphate release (5, 10) and of maximum force generation (7, 11). Our results show that OM binding induces small changes in the distribution of M* and M** states in the absence of actin (Fig. 18C). This is not what we expected based on the change in the apparent K_{eq} for ATP hydrolysis measured by Liu et al. (10). That study made two important predictions: (a) In ventricular cardiac myosin, LCD orientation, as infered from tryptophan

fluorescence—a proxy for the M** state in most myosins [113]—is not tightly coupled to hydrolysis. (b) OM binding causes a large change in the M**/M* K_{eq} as indicated by its affect on tryptophan fluorescence. In that study, OM binding shifts the apparent K_{eq} for the hydrolysis of ATP by myosin from 2.7 to 6.8, while it shifts the apparent M**/M* K_{eq} estimated from tryptophane fluorescence, from 0.77 to 3.98 (10). Our FRET measurements show a much smaller change in the K_{eq} for LCD priming, 0.52 to 0.56 in the absence of actin (Fig. 18), and 0.74 to 0.87 in the presence of actin—essentially no change, much less than predicted by Liu et al. (10). The Eyring-Polanyi transition state model [114] predicts these changes in K_{eq} should not alter the ms-resolved kinetics of the protein.

The dramatic effect that OM has on the kinetics of the powerstroke structural transition, in the presence of ATP (Fig. 18), ADP (Fig. 22A), and ADP.V_i (Fig. 22C), show that the primary affect of the compound on the LCD is to increase the transition state Gibbs free energy seperating the pre- and post-powerstroke orientations of the LCD, most notably when bound to actin, after phosphate dissociates. In the high-resolution structure published by Winkelmann et al. [49], OM makes important contacts with multiple structural elements that move with respect to one another during the powerstroke and thus, by binding these elements, OM should slow or even prevent LCD rotation, just as we observe.

3.5 CONCLUSIONS

We have investigated the actin-induced structural kinetics of cardiac myosin's light-chain domain during the powerstroke, in order to determine how OM modulates the coordination between the phosphate release biochemical step and the force-generating rotation of the myosin LCD. Our results reveal a previously unknown aspect of OM's mode of action: the small molecular therapeutic changes the coordination between phosphate

release and the powerstroke and inhibits the powerstroke by increasing the transition state free energy for actin-induced LCD rotation. These results provide novel molecular insight into OM's diverse range of effects in patients and *in vitro* biochemical studies.

3.6 SUPPLEMENTAL INFORMATION AND METHODS

Supplemental Methods: Protein purification and labeling

Myosin: Bovine cardiac myosin was purified based on procedures based on Margossian et al. [95], modified with suggestions made by Dr. Josh E. Baker and Travis Stewart (University of Nevada, Reno, personal communication). Cow hearts were obtained on wet ice from *Pel-Freez*. The entire purification process was performed in a 4 ºC cold room. The left ventricle was dissected, processed with an electric meat grinder, washed four times with homogenization buffer (40 mM Imidazole pH 7.2, 2 mM $MgCl_2$, 0.1% PMSF) in a ratio of 1 part burger by mass, to 3 parts buffer by mass, and filtered after each wash through cheesecloth. The rinsed burger was spun in an SLA3000 *Sorvall* rotor at 3000 rpm for 5 min at 4 ºC, washed twice more in homogenization buffer, and spun again in an SLA3000 *Sorvall* rotor at 3000 rpm for 5 min at 4 ºC. Myosin was then extracted under high salt conditions from the burger for 15 min using a modified *Guba Straub* buffer containing: 300 mM KCl, 150 mM potassium mono-/dibasic phosphate buffer (KPi) pH 6.4, 5 mM $MgCl_2$, 2 mM ATP, 2 mM DTT, 1 mM EGTA, and 0.1 % PMSF, and then spun at 3000 rpm for 5 minutes at 4 ºC. We collected the final supernatant, again filtered through cheese cloth. The supernatant was diluted 1:10 with cold (4 ºC) H_2O by gently pouring into a large bucket containing the water followed by gentle stirring with a plastic serological pipet. This mixture was covered with aluminum foil or plastic wrap and allowed to sit for 2-4 hours while filaments formed. The filaments settle to the bottom of the bucket in a flocculent layer. The filaments will not

sediment if the pH is 7.0 or higher. We avoid disturbing the mixture while the filaments sediment. Once the filaments have settled, we remove the excess liquid by siphoning. We then collect the remaining precipitant and spin it in a SLA3000 *Sorvall* rotor, at 10,000 rpm for 20 min at 4 ºC. The resulting pellets were collected and dissolved in a minimal volume of suspension buffer (1 M KCl, 60 mM KPi pH 6.7, 20 mM EDTA, 2 mM DTT), then dialyzed overnight with two buffer exchanges in: 0.6 M KCl, 25 mM KPi pH 6.7, 2 mM DTT. The following day the dialyzed myosin was diluted in an equal volume of cold H_2O and mixed gently for 30 min, then centrifuged in a Ti45 *Beckman* rotor at 18,800 rpm for 1 hour at 4 ºC. The supernatant was mixed in a 1:15 ratio with cold H_2O and allowed to sit for 2-4 hours for precipitation of filaments. The precipitant was again collected, spun, suspended, and dialyzed in 0.6 M KCl, 25 mM KPi pH 7.0, 2 mM DTT. A final clarification centrifugation was performed as in Day 2. The purified myosin is then brought to 150 mM sucrose and drip frozen in 30 μL to 50 μL droplets in liquid N_2 and stored at -80 ºC.

HMM digestion: Myosin prepared as described above was thawed and brought to 2 mM $MgCl_2$ in its freezing buffer before digestion to HMM with α-chymotrypsin (*Sigma-Aldrich*, 0.025 mg/ml final concentration) for 10 minutes at 25 ºC, followed by addition of pefabloc (*Roche*, 5 mM final concentration) and then dialyzed into either 10 mM Tris pH 7.5, 2 mM $MgCl_2$ for storage on ice prior to experiments or into 10 mM Tris pH 7.5, 2 mM $MgCl_2$ followed by desalting into 10 mM Tris pH 7.0 with 150 mM sucrose prior to snap freezing in liquid nitrogen for storage at -80ºC.

The digested HMM was purified by Q-sephadex, anion-exchange chromatography. The column was equilibrated in 10 mM Tris pH 8.0 at 4.0 C, the digested myosin loaded and then eluted in a gradient of 0-300 mM KCl, 10 mM Tris pH 8.0, over 300 mL at 1.5

mL/min, collecting 4 mL fractions (AKTA Prime Plus, GE). Fractions were evaluated by SDS-Page and those containing intact HMM without contaminants, pooled for experiments.

RLC: Chicken gizzard regulatory light chain with a single reactive cysteine at position 108 was expressed in *E. coli*. as described in our previous work [96] and purified by inclusion body isolation followed by ion exchange chromatography [96]. We labeled the purified cgRLC with 5 molar excess of Alexa Fluor 488 (*Invitrogen*) overnight at 4^{o} C and then removed free dye by gel filtration chromatography. The labeled RLC was snap frozen in liquid nitrogen and stored at -80^{o}C. Labeling efficiency was 100% determined by the molar extinction coefficient of the AF488 dye and the measured RLC protein concentration, determined by the Bradford assay using a BSA standard. The cgRLC shares high sequence similarity to the endogenous bovine cardiac RLC, that is lacking a cysteine.

Actin: Actin was purified from rabbit skeletal muscle by acetone dehydration followed by extraction into ice cold water as described in our previous work [97] and then polymerized in 10 mM Tris pH 7.5, 2 mM $MgCl_2$, 0.5 mM ATP and stored on ice prior to use. For phosphate release experiments, the F-actin was stabilized with a 1:1.3 stochiometric excess of phalloidin (*Sigma Aldrich*), followed by 48 h dialysis (3 buffer changes) into 10 mM Tris pH 7.0 with 2 mM $MgCl_2$. Apyrase (*Sigma Aldrich*) was added at 0.005 U/mL and P_i MOP containing 0.1 mM 7-methylguanosine (*Sigma Aldrich*) and 0.05 U/mL PNPase (*Sigma Aldrich*) was added four or more hours before using.

Protein and dye concentration: The Bradford protein concentration assay utilizing a known BSA protein standard was used throughout this study to determine protein concentrations. Reagents for this assay were purchased from *Biorad*. The extinction

coefficient for the AF488 dye is 73,000 at 495 nm, and for Cy3 is 136,000 at 570 nm, per the manufacturer's specifications.

Exchange: We exchanged the AF488-labeled RLC onto HMM by combining the two proteins (3 molar excess RLC to HMM) in 50 mM Tris pH 7.5, 120 mM KCl, 2 mM DTT, 12 mM EDTA [98] and then incubated the reaction mix for 30 minutes at 30^{o}C. After the incubation, we adjusted the reaction to 12 mM $MgCl_2$ and then incubated the mixture on ice for 15 minutes followed by dialysis into 10 mM Tris pH 7.0, 30 mM KCl, 2 mM $MgCl_2$ prior to gel filtration to remove free RLC.

Buffers and solutions: All experiments, unless otherwise noted, were performed in 10 mM Tris pH 7.5, 2 mM $MgCl_2$ at 25 ºC.

Chemicals: Omecamtiv Mecarbil (abbreviated OM, CK-1827452) was purchased from *Selleckchem*, Catalog No. S2623 and dissolved in DMSO prior to use. ATP (Adenosine 5'-triphosphate disodium salt hydrate, Grade 1 >99 %) and ADP (Adenosine 5'-diphosphate sodium >95 %) were purchased from *Sigma Aldrich*. Mant-ATP (2'-(or-3')-O-(N-methylanthraniloyl) adenosine 5'-triphosphate, trisodium salt) was purchased from *Thermo Fisher Scientific*. All other chemicals where purchased from *Sigma Aldrich*.

Steady-state ATPase activity: We measured the actin-activated MgATPase activity of the purified cardiac myosin HMM using an NADH-coupled assay [88] performed at 25 ºC in 10 mM Tris pH 7.5, 2 mM $MgCl_2$. The reaction mix contained varied [actin], and 0.2 mM NADH, 0.5 mM PEP, 2.1 mM ATP, 10 U/mL LDH, 40 U/mL PK, HMM (200 nM). We acquired absorbance at 340 nm every 10 seconds for 120 seconds total using a Beckman-Coulter DU640B spectrophotometer.

Transient kinetics: Transient biochemical experiments with steady-state fluorescence (total fluorescence intensity) detection were performed on an *Applied Photophysics* stopped-flow spectrophotometer capable of sequential mixing experiments. The single-mix dead time for this instrument is 1.3 ms, calibrated using fluorescence enhancement of 8-hydroxyquinoline following Mg^{+2} binding under pseudo first-order kinetics conditions [99]. All buffers were filtered and then degassed for 30 minutes under high-vacuum prior to use. All stopped-flow experiments were performed at 25 ºC maintained by a circulating water bath.

Transient time-resolved FRET (millisecond-resolved transient biochemical experiments with nanosecond-resolved fluorescence detection), TR^2FRET, was measured using a transient time-resolved fluorescence spectrophotometer [10, 42, 77]. This instrument utilizes a *Biologic USA* SFM/20 single-mix stopped-flow accessory coupled to our transient time-resolved fluorescence spectrophotometer. The dead time for the instrument was 1.8 ms, calibrated using the 8-hydroxyquinoline + Mg^{+2} control reaction [99]. For experiments mixing equilibrated myosin in the presence of 10 molar excess ATP with actin containing 1 mM MgATP, we loaded the actin into syringe A, followed by a freshly prepared 600 μL mixture of myosin + Cy3-ATP in syringe B and then immediately mixed with the actin in syringe A.

Single-turnover experiments with mant-ATP and Cy3-ATP were performed with a sequential stopped flow. For mant-ATP: excitation at 280 nm and detection through a 400 nm long-pass filter. For Cy3-ATP: excitation at 540 nm and detection through a 600 nm long-pass filter.

Total fluorescence: The total fluorescence transients from $(TR)^2$FRET experiments was determined as described in our pervious publications [1].

FRET: Time-resolved FRET (TR-FRET) and transient time-resolved FRET $(TR)^2$FRET were performed and analyzed as described in our previous publications [1] with the correction that equation 17 in that work should read, $F(90°, t) = F(54.7°,\ t) \cdot [1 - r(t)]/3$ rather than, $F(90°, t) = F(54.7°,\ t) \cdot [1 - 2r(t)]/3$. Time-resolved fluorescence photophysical parameters measured in this study are summarized in **Table 6**.

Transient kinetics of phosphate release: We detected dissociation of inorganic phosphate from myosin using phosphate-binding protein (PBP) labeled with MDCC [89]. Howard White generously provided bacterial stocks for the expression of PBP [86]. The purification and characterization of phosphate-binding protein (PBP) was performed as described in our previous work [1]. For experiments measuring the kinetics of actin-activated phosphate dissociation, MDCC-PBP (10 μM) was included in all syringes, along with phosphate mop [86, 88, 89], which is added to remove contaminating free phosphate present in buffers, samples, and the stopped-flow instrument. Extreme care was taken to ensure that actin, which can contain significant amounts of hydrolyzed phosphate, was both nucleotide and phosphate free—we speculate that f-actin can release hydrolyzed phosphate when sheared in a stopped-flow device, that is otherwise not removed by the phosphate mop. This in turn can lead to artificially fast phosphate release transients which are easily detected in control experiments mixing all components except myosin.

Table 5. Steady-state and transient kinetics, cardiac

Steady-state ATPase		
	0 mM KCl (Unlabeled)	**0 mM KCl (Labeled)**
$V_{max(actin)}$	3.44 ± 0.14 s^{-1}	2.57 ± 0.11 s^{-1}
$K_{m(actin)}$	61 ± 4 μM	57 ± 7 μM
Basal ATPase	0.020 ± 0.009 s^{-1}	0.012 ± 0.006 s^{-1}
	DMSO, 0 mM KCl (Unlabeled)	**5 μM OM, 0 mM KCl (Unlabeled)**
$V_{max(actin)}$	3.58 ± 0.58 s^{-1}	1.76 ± 0.07 s^{-1}
$K_{m(actin)}$	66 ± 13 μM	35 ± 2 μM
Basal ATPase	0.033 ± 0.010 s^{-1}	0.007 ± 0.005 s^{-1}
	25 mM KCl, (Unlabeled)	**25 mM KCl (Unlabeled)**
$V_{max(actin)}$	2.71 ± 0.16 s^{-1}	1.33 ± 0.27 s^{-1}
$K_{m(actin)}$	83 ± 5.9 μM	180 ± 50 μM
Basal ATPase	0.035 ± 0.013 s^{-1}	—
Transient Biochemical and Structural Kinetics		
Transition	**DMSO**	**5 μM OM**
ATP binding to acto-HMM	4.0 μM^{-1} s^{-1}	4.0 μM^{-1} s^{-1}
Myosin.ADP.P binding to actin	0.7 μM^{-1} s^{-1}	0.8 μM^{-1} s^{-1}
P_i release acto-HMM	11.6 ± 2.4 s^{-1}	22.1 ± 3.9 s^{-1}
P_i release acto-HMM $K_{0.5}$ [actin]	15.5 ± 6.5 μM	26.2 ± 7.7 μM
ATP-induced LCD rotation	40.4 ± 1.7 s^{-1}	32.9 ± 3.2 s^{-1}
ATP-induced LCD rotation $K_{0.5}$ [Cy3-ATP]	7.34 ± 0.46 μM	6.21 ± 1.08 μM
Actin-induced LCD rotation (powerstroke)	15.3 ± 4.3 s-1	2.07 ± 0.10 s^{-1}
Actin-induced LCD rotation $K_{0.5}$ [actin] (powerstroke)	35.5 ± 18.1 μM	5.62 ± 1.07 μM
ATP-induced ADP release from actomyosin	35.1 ± 2.2 s^{-1}	31.5 ± 1.5 s^{-1}
Actin-induced LCD rotation (ADP)	108.3 ± 4.6 s^{-1}	4.1 ± 0.2 s^{-1}
Actin-induced LCD rotation (ADP)	4.7 ± 0.4 μM	0.7 ± 0.9 μM
Actin-induced ADP.Vi exchange	0.0095 ± 0.0010 s^{-1}	0.0020 ± 0.0004 s^{-1}
Actin-induced ADP.Vi exchange	16.2 ± 3.9 μM	14.0 ± 4.6 μM
Transition	**MantATP**	**Cy3-ATP**
Single-turnover, sequential mix (k_1)	5.1 ± 0.7 s^{-1}	6.4 ± 1.9 s^{-1}
Single-turnover, sequential mix ($K_{1.0.5}$)	7.3 ± 2.3 μM	15.8 ± 8.6 μM
Single-turnover, sequential mix (k_2)	1.4 ± 0.7 s^{-1}	0.7 ± 0.1 s^{-1}
Single-turnover, sequential mix ($K_{2.0.5}$)	16.2 ± 11.2 μM	4.0 ± 1.5 μM

Table 6. Time-Resolved fluorescence lifetime parameters, cardiac
For donor and donor + acceptor labeled HMM at 25 ºC. Upper and lower 67% confidence bounds determined from χ^2 support plane error analysis, extensively described in [1].

Parameter	Best-Fit	Lower Bound	Upper Bound
Donor only			
Amplitude τ_1	0.784	0.780	0.788
τ_1 (ns)	3.85	3.836	3.867
Amplitude τ_2	0.216	0.193	0.246
τ_2 (ns)	0.684	0.637	0.732
Distance distributions			
R_1 (nm)	5.7	5.6	5.9
$FWHM_1$ (nm)	2.9	2.6	3.4
R_2 (nm)	9.6	9.2	10.7
$FWHM_2$ (nm)	3.7	3.2	4.3
Mole Fraction			
M** (ADP.V)	0.40	0.39	0.41

Supplemental Figures

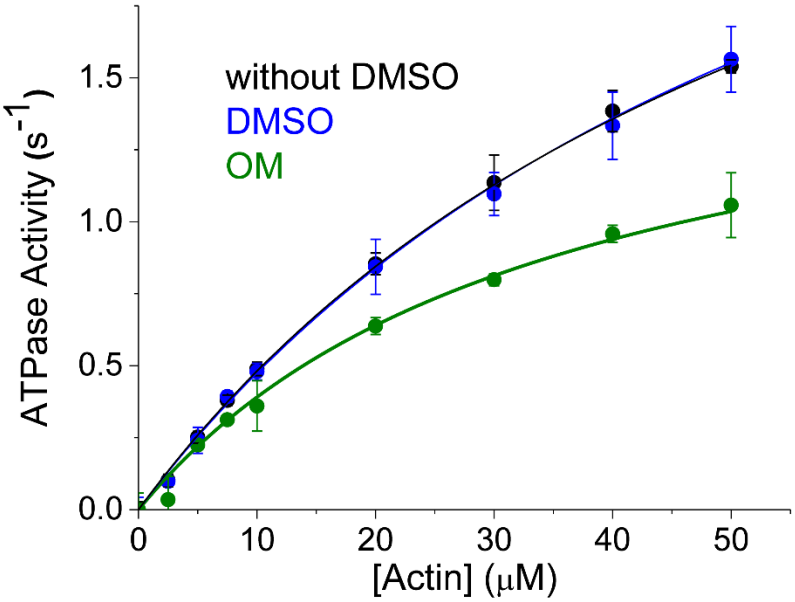

Fig. 24. Actin-activated, NADH-coupled ATPase assay
Bovine HMM (black), with 1% DMSO (blue), and with 5 μM OM in 1% DMSO (green). Basal ATPase rates (0 μM actin) were subtracted from each set of eight [actin] and fit to a single hyperbola. n = 9 experiments ± SEM.

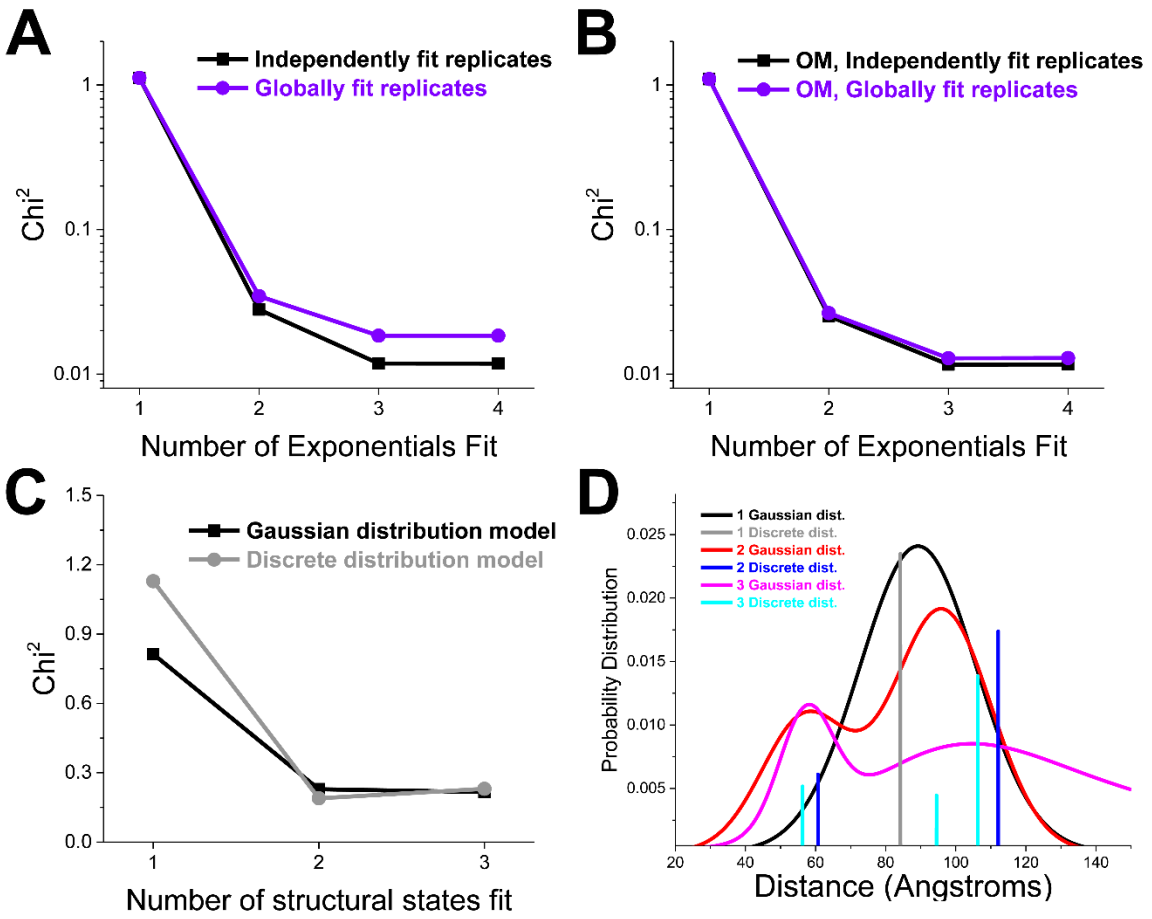

Fig. 25. Model-testing to determine the time-resolved fluorescence decay function for the AF488 donor used in this study and the structural state model

(A) Model testing was performed on donor-only sample replicates (AF488-HMM) for both independently (black) and globally constrained data sets (purple). Two exponentials for AF488 were then used to fit the donor-only and donor + acceptor (FRET) samples. (B) The drug OM does not affect the number of lifetimes of the AF488 donor fluorophore, two exponentials were used to fit the donor only and FRET samples in the presence of OM. (C) Data sets containing a range of biochemical conditions were fit globally by a time-resolved FRET models with 1, 2, or 3 structural states, both discrete-distance (gray) and Gaussian-distance distribution (black) models were tested by χ^2 optimization. The Gaussian models reflect probe and protein disorder, and prevent over-fitting of the data. (D) Visualization of the three discrete and three Gaussian structural state models obtained in panel C.

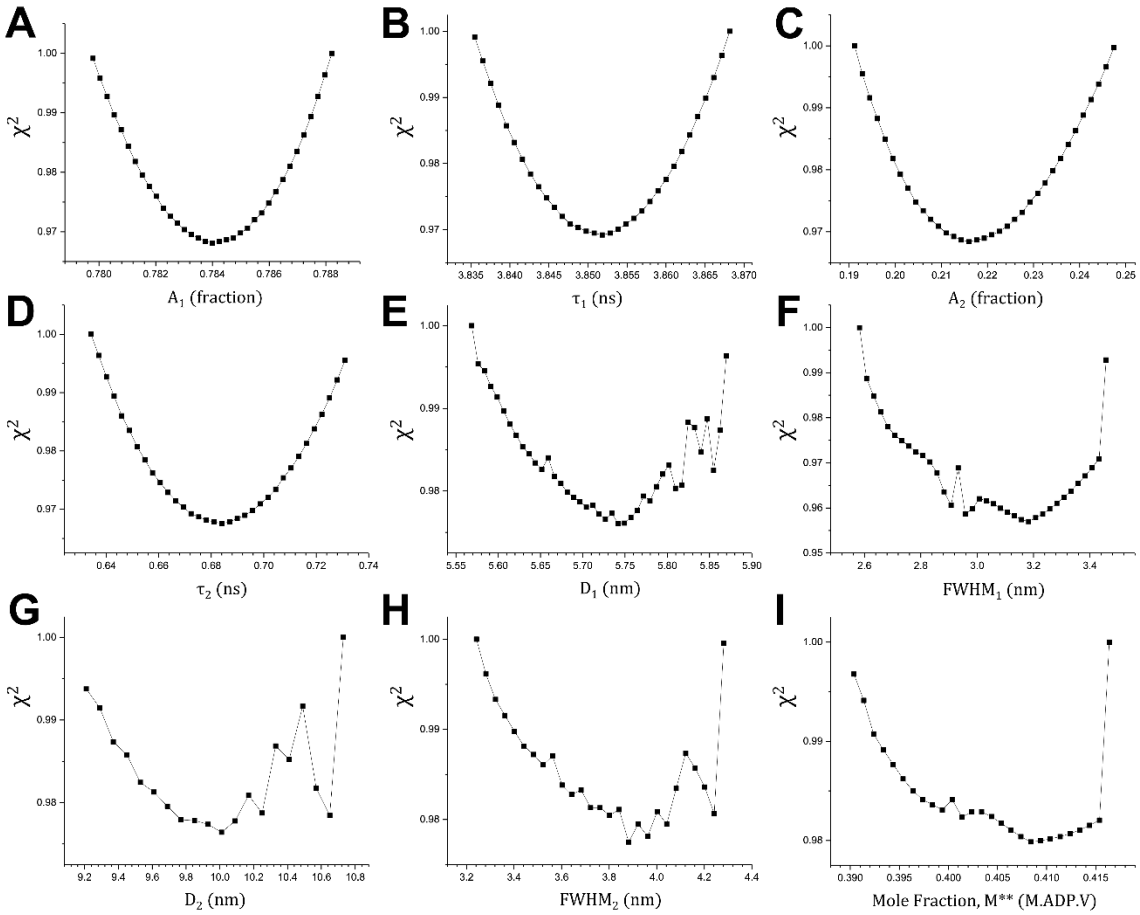

Fig. 26. Surface plane error analysis of key photophysical, structural state, and thermodynamic parameters during fitting

(A-D) The two exponential fit parameters of the donor-only fluorophore: A_1, τ_1, A_2, τ_2. (E-H) Structural state parameters of two Gaussian distance distribution model. (I) Mole fraction of M** for myosin.ADP.vanadate biochemical condition with two Gaussian distance distribution model.

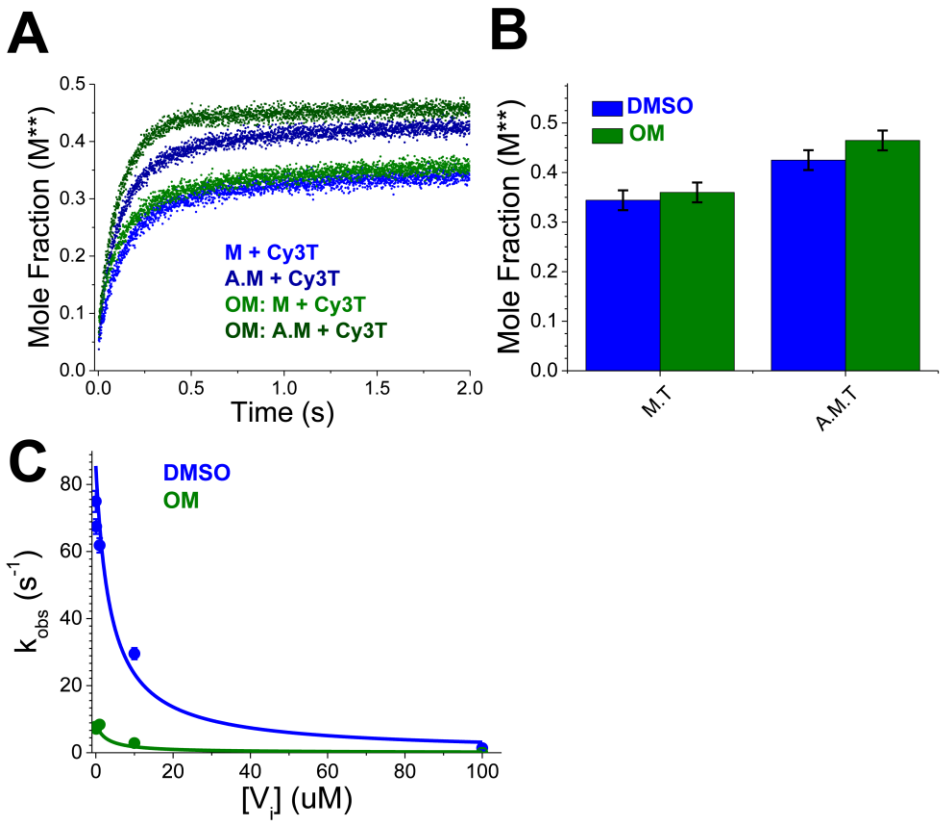

Fig. 27. OM increases the mole fraction of M structural states under steady-state Cy3-ATP bound conditions, and slows the actin-activated nucleotide exchange of Cy3-ADP.V with ATP**

(A) Structural kinetics of Cy3-ATP binding to cardiac myosin or cardiac myosin bound to actin and approach to steady-state in the absence (blue) or presence (green) of OM. (B) Steady-state distribution of M** as developed in panel A. (C) Rapid mixing AF488-HMM.Cy3-ADP.$[V_i]_{varied}$ + Actin & $[V_i]_{varied}$ at a single phalloidin-stabilized actin concentration of 20 μM. $k_{obs,DMSO}$ = (85.5 s^{-1})/(1+$[V_i]$/3.8μM) and $k_{obs,OM}$ = (8.7 s^{-1}) (1+$[V_i]$/2.6μM). Solutions contained 10 μM PiBP, PiMOP [SI Methods], 2 mM $MgCl_2$, 10 mM Tris (pH 7.5), 25 ºC. Error bars are SEM of 3 independent experiments.

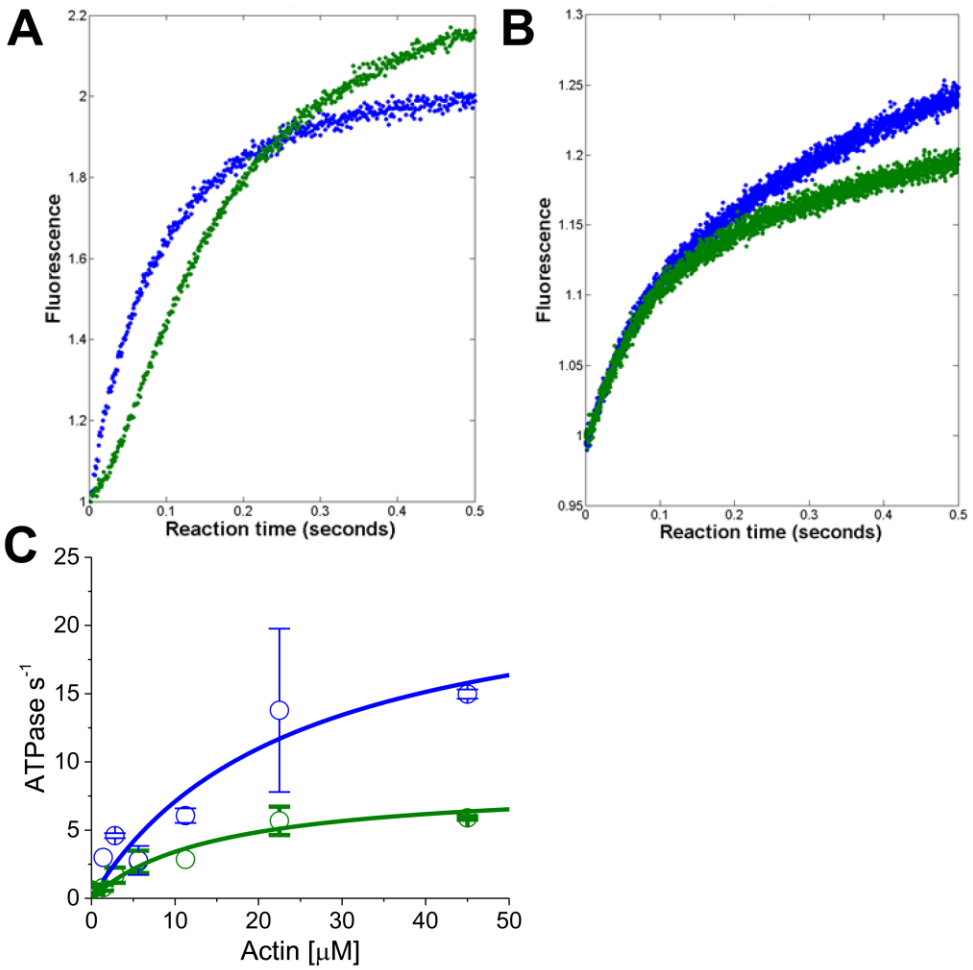

Fig. 28. OM delays the powerstroke in skeletal myosin HMM and inhibits steady-state ATPase cycling

(A) The powerstroke in skeletal myosin HMM, as described in [1], detected in the presence of 1 % DMSO (blue) or 100 μM OM (green). Omecamtiv induces a lag, similar to its effect on cardiac myosin observed in **Fig. 18**. (B) Phosphate release kinetics by skeletal myosin HMM in A, detected by MDCC-PBP in the presence or absence of OM. Solutions contained 10 μM PiBP, PiMOP [SI Methods], 2 mM $MgCl_2$, 10 mM Tris (pH 7.5), 20 C. (C) Steady-state ATPase cycling in the presence and absence of 100 μM OM.

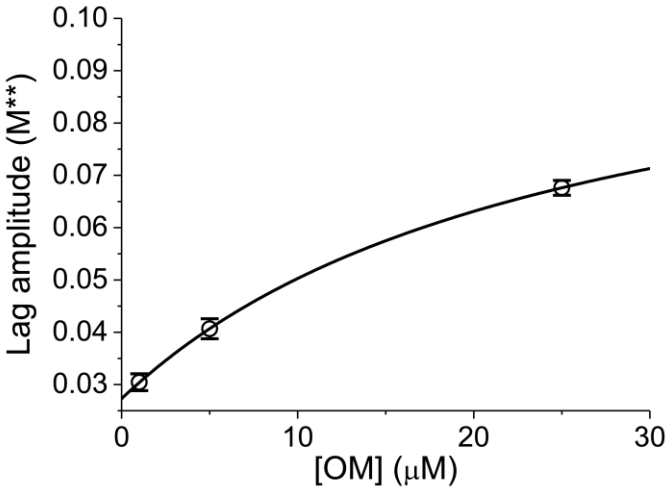

Fig. 29. Amplitude of the [OM]-dependent lag phase in Fig. 18.
Error bars represent standard error of the fit.

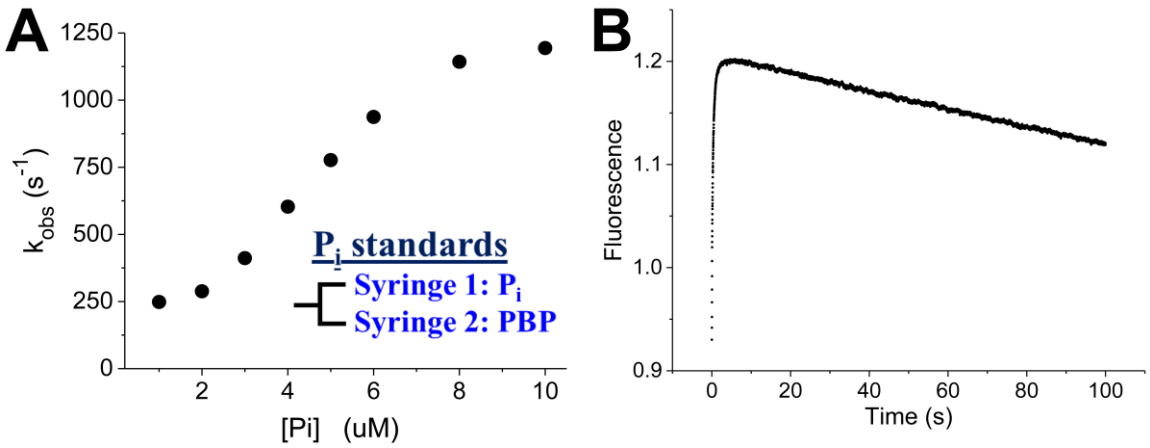

Fig. 30. Characterization of MDCC-PBP
(A) Standard curve of inorganic P_i (SigmaAldrich) and MDCC-PBP mixed in a stopped-flow, excited at 425 nm and detection through a 482/25 nm Semrock BrightLine bandpass filter. Maximum rate constants detectable by the sensor are much faster than those detected in this study. (B) Long time course detection showing the PiMOP (7-methylguanosine, PNPase) removing the P_i from the MDCC-PBP (linear decreasing transient) demonstrates the clearance of contaminating P_i from the stopped-flow and from buffers upon inclusion of the PiMOP.

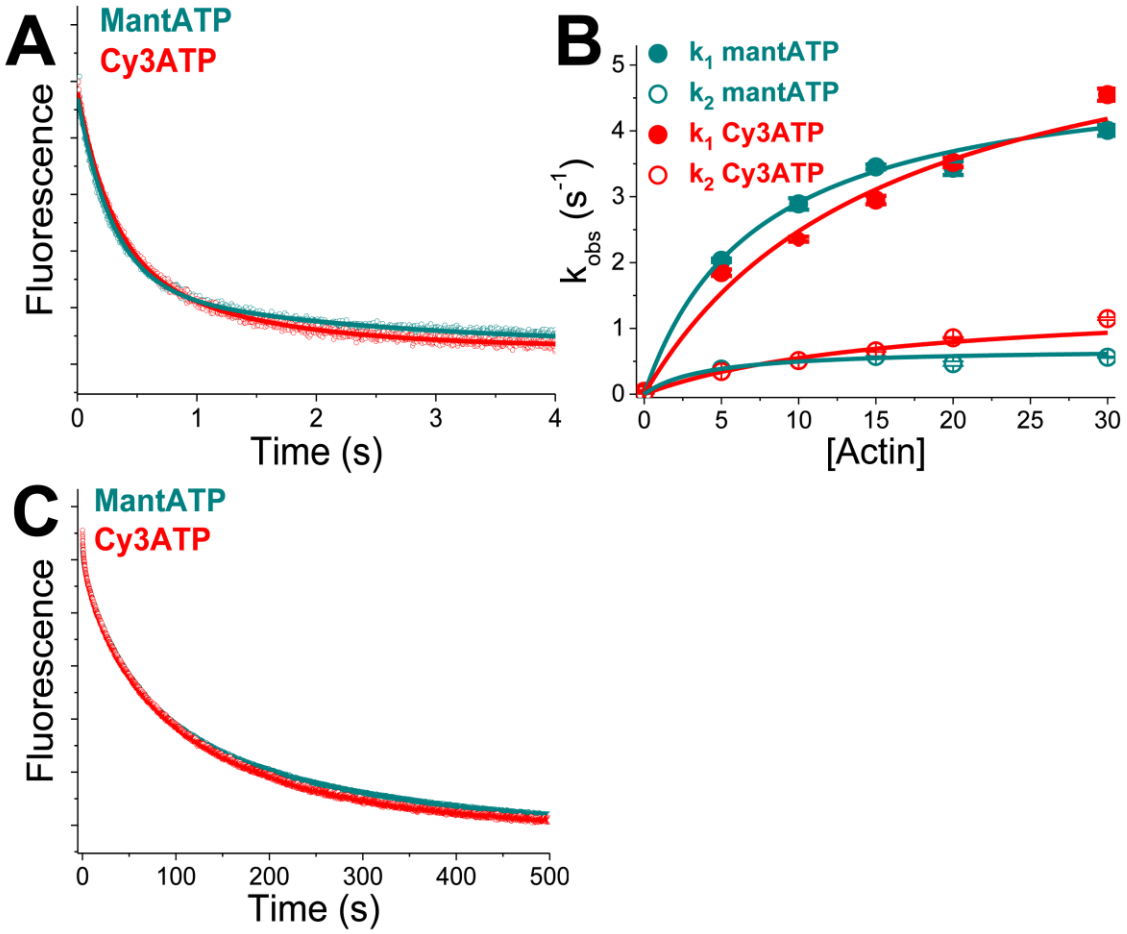

Fig. 31. Single-turnover experiments by sequential mix
All experiments performed with 1.0 μM HMM with either 0.5 μM mantATP or 0.5 μM Cy3-ATP and 20 μM, aged 2.0 s, then mixed with either 10 μM actin (A), a range of actin concentrations (B) with single hyperbolic fit parameters in SI table, or in the absence of actin (C).

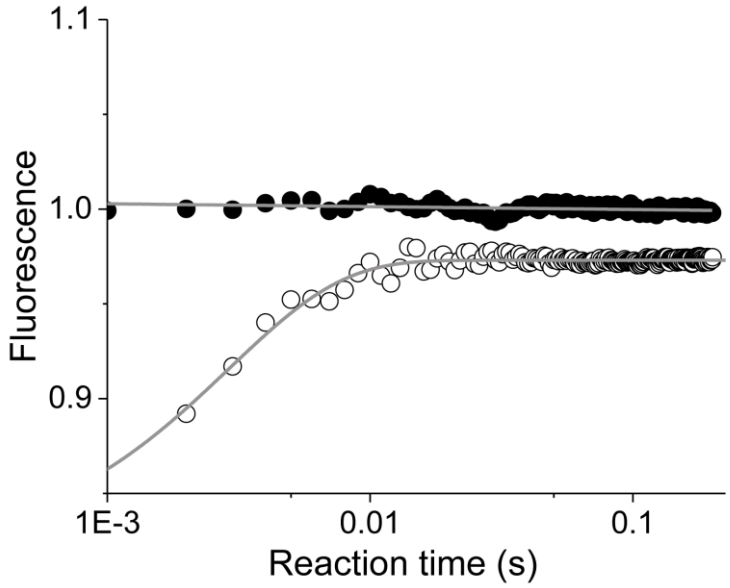

Fig. 32. Phosphate release by actin after stopped-flow mixing in the absence of myosin
Closed circles, phosphate free actin used in , open circles, actin containing trace μM phosphate.

CHAPTER 4: MAVACAMTEN STABILIZES AN AUTO-INHIBITED STATE OF TWO-HEADED CARDIAC MYOSIN

This chapter has been adapted from the following publication:

Title: Mavacamten stabilizes an autoinhibited state of two-headed cardiac myosin

Authors: John A. Rohde, Osha Roopnarine, David D. Thomas, and Joseph M. Muretta

Journal: Proc Natl Acad Sci U S A. 115(32): E7486–E7494.

Online: July 17, 2018; ***Published:*** August 7, 2018

doi: 10.1073/pnas.1720342115; ***PMID:*** 30018063

4.1 CHAPTER OVERVIEW

In this publication I characterized the molecular mode-of-action of a small-molecule effector, mavacamten, that binds cardiac myosin and was designed to treat hypertrophic cardiomyopathies (HCM). In additional to time-resolved FRET experiments, I also performed transient kinetics experiments to characterize the actin-independent (basal) ATP-turnover rate of the cardiac HMM in the presence and absence of mavacamten. To our surprise, the HMM showed distinct basal turnover kinetics that differed from single-headed S1 myosin. Thus, this study presents results on two discoveries: an auto-inhibited state exists in two-headed HMM that is largely absent in single-headed S1, as well as the further stabilization of the auto-inhibited state when HMM is bound by mavacamten.

4.2 INTRODUCTION

Familial hypertrophic cardiomyopathies, abbreviated HCM, represent one of the most common classes of genetic disease, affecting 1 in 500 people[59]. HCM is hypothesized to result from cardiac hyper-contractility[8]. Direct inhibition of force generation by cardiac myosin is thus a putative treatment[9]. Mavacamten (mava), previously termed Myk461, is a small-molecule allosteric inhibitor of cardiac myosin that shows promise in preclinical and clinical trials for the treatment of HCM[9]. Mava binds with sub-micromolar affinity to cardiac myosin in the presence of adenosine triphosphate (ATP) and inhibits steady-state actin-activated and actin-independent (basal) ATPase cycling and calcium regulated ATPase activity in permeabilized cardiac myofibrils[9, 60]. Mava also inhibits the kinetics of rigor actin-binding as well as the kinetics of actin-activated phosphate release[60]. It decreases *in vitro* actin filament sliding velocity in the actomyosin motility assay[60], decreases force generation by skinned cardiac preparations from mouse HCM models[9], and decreases cardiac output in live feline hearts[61]. Mava's effect on cardiac contractility is hypothesized to follow from its inhibition of actin-activated phosphate release, the kinetic step most-tightly coupled to force generation [60].

Because mava changes the kinetics of actin-activated phosphate release, we hypothesized that it may also stabilize an auto-inhibited state of two-headed cardiac myosin in solution, analogous to the super-relaxed state (SRX) observed in skinned myocardium and skeletal muscle fibers[62, 63]. This hypothesis was prompted by studies of blebbistatin, a myosin II inhibitor which also inhibits phosphate release and is proposed to stabilize the SRX state in skeletal and cardiac muscle[64-67].

In permeabilized relaxed muscle and myocardium, the SRX is defined by the bi-exponential kinetics of single ATP turnover. The fast phase of this turnover is similar to ATP turnover in isolated single myosin heads (S1, Fig. 33A), while the slow phase is thought to reflect myosin heads that are auto-inhibited in a structural state that is folded back onto the filament backbone. The folded state, termed the interacting heads motif (IHM) is hypothesized to be stabilized by a number of protein-protein interactions including contacts between the two-heads, contacts between the heads and the S2 coiled-coil, and contacts between both the heads and the S2 coiled-coil, and the thick-filament backbone. Myosin heads in the IHM are hypothesized to turn over ATP much more slowly than non-interacting heads, because the structural changes in the ATPase site that are required for dissociation of the ATP hydrolysis products, require movement of the myosin light-chain binding domain and actin-binding interface[68, 69] and movement of these elements should be prevented when the heads interact. The IHM is hypothesized to be an evolutionarily conserved auto-inhibition mechanism for controlling myosin II driven motility in cells[69-72]. Electron microscopy (EM) studies suggest that the individual myosin heads in the cardiac thick filament can form the IHM state[66, 73]. However, the IHM has not been observed in purified cardiac myosin in solution without chemical cross-linking. Thus, the structural correlates and transient kinetics of the cardiac myosin IHM state remain unknown.

We tested the hypothesis that cardiac myosin is auto-inhibited by direct head-head interaction in solution and that mavacamten selectively targets this intrinsic inhibition by comparing the actin-activated and actin-independent (basal) single ATP turnover kinetics of single and two-headed bovine ventricular cardiac myosin fragments. Based on the results

from those experiments, we evaluated the temperature and ionic strength dependence of ATP turnover by these same myosin preparations. We reasoned that if the two-headed heavy meromyosin (HMM) forms an IHM-driven, auto-inhibited state, then the energetics of ATP turnover by HMM should reflect this formation and should be much more dependent on increasing ionic strength than single headed cardiac myosin S1[74] and mavacamten should reduce this ionic strength dependence. The results from these experiments reveal key aspects of cardiac myosin function and of mavacamten's mode of action on this critical protein. A related and complementary body of work is described in Anderson et al.[75] and PNAS, in revision.

4.3 RESULTS

The steady-state actin-activated ATPase k_{cat} of two-headed cardiac myosin HMM is lower than single-headed S1. We prepared soluble myosin fragments for this study as described in our prior work [2] by isolating cardiac myosin from the left ventricles of bovine hearts, digesting the isolated myosin with α-chymotrypsin (Fig. 33B, Lane 2) and purifying the soluble, digested fragments by both size-exclusion and anion-exchange FPLC as described in the SI (Chapter 4.6). Fractions containing two-headed heavy meromyosin (HMM) or the single-headed S1 fragment lacking the regulatory light-chain binding domain and the S2 coiled-coil domain were separated and dialyzed into assay buffers as indicated for each experiment (Fig. 33B, Lanes 3,5). We verified that the purified HMM and S1 were fully intact and did not contain contaminating cardiac actin by gel electrophoresis (Fig. 33B, Lane 4).

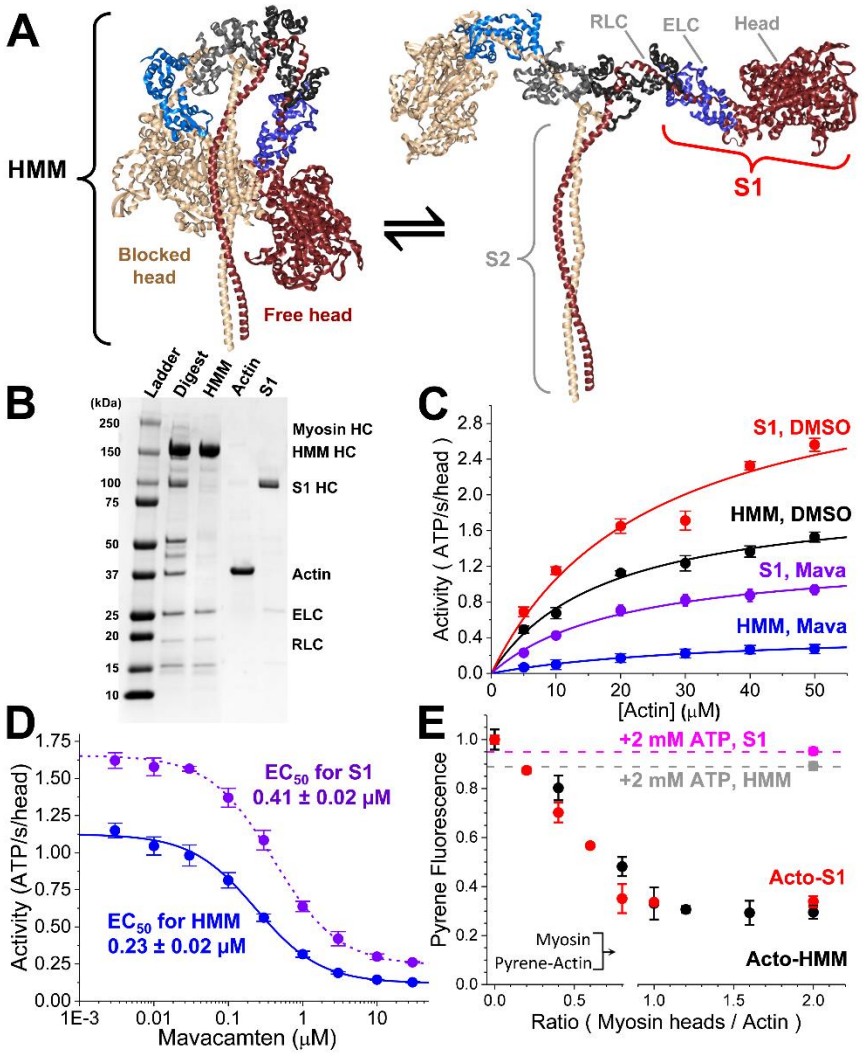

Fig. 33. Steady-state ATPase activity of purified cardiac myosin fragments, HMM and S1
(**A**) Proposed structural isomerization of HMM between a sequestered interacting-heads motif (IHM, PDB: 5TBY, left) and splayed heads (right). (**B**) SDS-PAGE gel, stained with coomassie, demonstrating the purification of α-chymotryptic-digested HMM and S1 myosin fragments, removing contaminating actin. HC = heavy chain of myosin, ELC = essential light chain, RLC = regulatory light chain. (**C**) Steady-state, actin-activated ATPase activity of 0.2 μM S1 with DMSO (red) or 10 μM mavacamten (Mava, purple), 0.2 μM HMM with DMSO (black) or 10 μM mava (blue). $Activity_{S1,DMSO}$ = (3.6 ± 0.4 s^{-1})*[Actin]/((24.4 ± 7.4 μM) + [Actin]). $Activity_{HMM,DMSO}$ = (2.02 ± 0.12 s^{-1})*[Actin]/((17.6 ± 2.8 μM) + [Actin]). $Activity_{S1,Mava}$ = (1.35 ± 0.08 s^{-1})*[Actin]/((20.6 ± 3.1 μM) + [Actin]) . $Activity_{HMM,Mava}$ = (0.48 ± 0.04 s^{-1})*[Actin]/((35.3 ± 6.3 μM) + [Actin]). Replicates of n=6 for each actin concentration ± SEM. (**D**) Mavacamten is a potent inhibitor of 0.2 μM HMM and S1 during actin-activated, steady-state ATPase cycling, [Actin] = 20 μM. Replicates of n=4 ± SEM. (**E**) Varied [S1] from 0-2.0 μM, and varied [HMM] from 0-1.0 μM (0-2.0 μM heads) mixed with 1.0 μM pyrene-labeled actin. Final concentrations listed. The HMM and S1 used in this study releases from pyrene-labeled actin with addition of 2.0 mM ATP, F_{S1} = 0.95 ± 0.1 (magenta), F_{HMM} = 0.89 ± 0.02 (grey). Replicates of n=4 ± SEM. All experiments performed in 10 mM Tris, pH 7.5 at 25 °C, 2 mM $MgCl_2$, and 1.0 mM (1,4-dithiothreitol) DTT, unless otherwise noted.

We evaluated the functional activity of the purified myosin fragments by measuring actin-activated ATPase activity over a range of actin concentrations using the NADH-coupled ATPase assay[88] (Fig. 33C). Single hyperbolic fits to the actin concentration-dependence of ATPase activity showed that the k_{cat} for the S1 fragment is 3.6 ± 0.4 s^{-1} compared to 2.02 ± 0.12 s^{-1} for cardiac HMM from the identical preparation ($p \leq 0.0035$, throughout this manuscript, measurement statistics and statistical significance are tabulated in Table 7). Thus, dimerization of the myosin heads reduces the maximum rate of actin-activated ATPase cycling (Fig. 33A,C).

We verified that the mavacamten preparation (synthesized by EAG Laboratories, verified by mass spectrometry and NMR spectroscopy, described in the SI, Chapter 4.6) inhibits cardiac myosin as demonstrated in prior reports [9] (Fig. 33C,D). Mavacamten potently inhibited the steady-state ATPase cycling of HMM, decreasing the k_{cat} from 2.02 ± 0.12 s^{-1} to 0.48 ± 0.04 s^{-1} ($p \leq 0.001$), a (4.21 ± 0.43)-fold reduction, and shifting the K_m from 17.6 ± 2.8 μM to 35.3 ± 6.3 μM ($p \leq 0.05$), a two fold increase. The actin-activated ATPase k_{cat} of S1 was inhibited from 3.6 ± 0.4 to 1.35 ± 0.08, a (2.70 ± 0.34)-fold reduction. The enhanced inhibition of the actin-activated k_{cat} of HMM compared to S1 is significant ($p \leq 0.03$). The enhanced inhibition of HMM compared to S1 is reflected in the compounds apparent EC_{50} for inhibition of actin-activated ATPase cycling measured at 20 μM actin (near the K_m) which was 0.23 ± 0.02 μM for HMM compared to 0.41 ± 0.02 μM for S1 ($p \leq 0.001$).

We determined that both purified myosin fragments freely and equivalently bind to actin in the absence of ATP and dissociate from actin upon the addition of 2.0 mM ATP by equilibrating varying concentrations of HMM or S1 myosin with a fixed concentration

of pyrene-labeled actin (Fig. 33E). The fluorescence of pyrene-labeled actin is linearly proportional to the binding of individual myosin heads to actin [88]. The fluorescence decreased linearly with an increase in the [myosin heads]/[actin] equilibration stoichiometry (Fig. 33E), reaching a maximum at 1:1 stoichiometry with a 70% fluorescence quench, as expected [88]. The quench of pyrene fluorescence by HMM or S1 was identical indicating that both heads of the HMM freely bind actin to a similar degree as S1 heads. The binding is nearly entirely disrupted to 0.89 ± 0.02 or 0.95 ± 0.01 respectively, with the addition of 2.0 mM magnesium ATP (MgATP), and the remaining strongly bound myosin heads are consistent with the expected 5-10% duty-ratio of cardiac myosin estimated in other studies [8]. Thus, the S1 and HMM are functional as ATP incubation increases pyrene-actin fluorescence and the reduced actin-activation seen in the HMM does not reflect "dead" or non-functional myosin heads which do not detach from actin.

Mavacamten inhibits transient actin-activated single ATP turnover more for two-headed cardiac HMM than for single-headed S1. We investigated the transient kinetics of actin-activated single ATP turnover by cardiac myosin HMM and S1 using fluorescently-labeled ATP, mant-ATP (2'- or 3'-O-[N-methylanthraniloyl] adenosine 5'-triphosphate). We mixed the purified myosin fragments by stopped-flow with fluorescent mant-ATP, aged the sample for 2.0 seconds to allow for ATP binding and hydrolysis, and then mixed the resulting steady-state sample with increasing concentrations of actin in the presence of 2.0 mM MgATP. The fluorescence of mant-ATP is enhanced when bound by myosin, and the dissociation of mant-ADP after a single kinetic cycle results in a fluorescent decay (Fig. 34A,D).

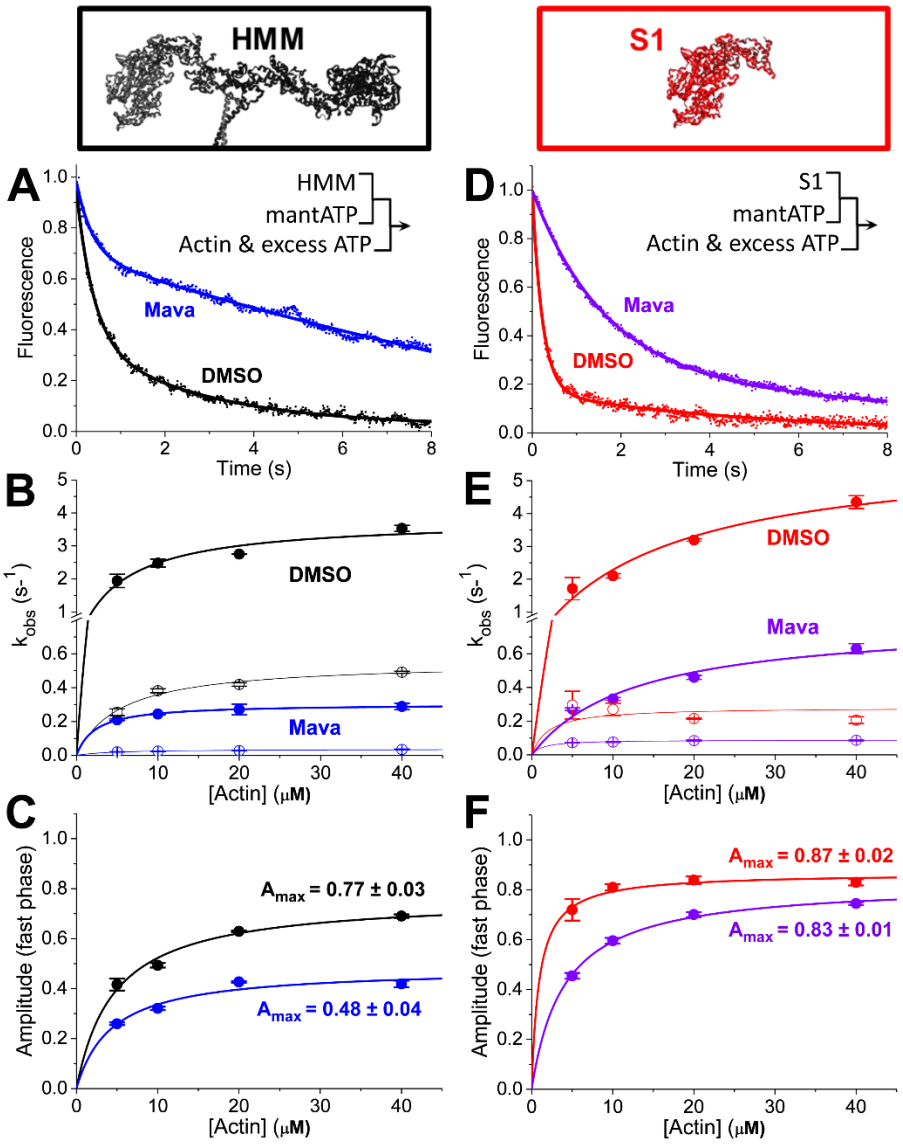

Fig. 34. Actin-activated single ATP turnover

(**A**) 0.1 μM HMM (DMSO control in black, 30 μM mavacamten in blue), mixed with 2.0 μM mant-ATP and 10 μM actin and 2.0 mM MgATP by sequential stopped flow. Pre-mix concentrations listed. Sequential stopped-flow mix schematic is inset. (**B-C**) Two-exponential fits showing rates and amplitudes with varied [actin]. HMM data is shown in the left column of plots; S1 data is shown in the right column of plots. (**D**) 0.2 μM S1 (DMSO in red, 30 μM mavacamten in violet), mixed with 2.0 μM mant-ATP and 10 μM actin and 2.0 mM MgATP by sequential stopped flow. (**E-F**) Two exponential fits showing rates and amplitudes, with varied [actin]. Replicates of n=6 ± SEM, Table 7.

The actin-activated single ATP turnover fluorescent transients were best fit by a bi-exponential time-dependent function consistent with previous published studies of actin-activated ATP turnover by cardiac myosin preparations, Fluorescence = $A_{fast} \cdot \exp(-k_{fast} \cdot t) + A_{slow} \cdot \exp(-k_{slow} \cdot t)$ [17]. We evaluated the actin dependence of the two rate constants (k_{fast} and k_{slow}) and the normalized amplitudes (A_{fast} and A_{slow}) for each phase in the presence or absence of mavacamten (Fig. 34). The fast phase (closed circles) reflects the release of ATP from a primed, post-hydrolysis, myosin.ADP.P_i state ready to undergo actin-activation, while the slow phase (open circles) reflects actin-dependent release from states which are activated more slowly[2, 17]. Importantly, the fast and slow phases are both faster than basal single ATP turnover in the absence of actin (presented in Fig. 35). The maximum observed rate constant for the fast phase of actin-activated ATP turnover was larger for S1 (5.97 ± 0.80 s^{-1}) than for HMM (3.80 ± 0.33 s^{-1}, $p < 0.05$). Mavacamten inhibited the maximum observed rate constant for the fast phase of actin-activated ATP turnover to 0.80 ± 0.11 s^{-1} in S1 and 0.30 ± 0.01 s^{-1} in HMM. The maximum observed rate constant for the slow phase was reduced from 0.28 ± 0.04 s^{-1} to 0.089 ± 0.002 s^{-1} in S1 (a 3-fold inhibition), and from 0.55 ± 0.03 s^{-1} to 0.04 ± 0.01 in HMM (a 14-fold inhibition). Thus, in HMM the slow phase of ATP turnover is significantly more inhibited than in S1 ($p \leq 0.0001$). In the absence of mavacamten, the amplitude of the slow phase of actin-activated single ATP turnover is larger in HMM than in S1 (Fig. 34C,F). At saturating actin concentrations, mavacamten decreased the amplitude of the fast phase in HMM (0.48 ± 0.04) but not in S1 (0.83 ± 0.01, $p \leq 0.0001$, S1 compared to HMM, Fig. 34C,F). The primary difference between S1 and HMM is the presence of the RLCs and S2 coiled-coil domain, and the dimerization of two myosin heads (Fig. 33A). This dimerization allows

the two heads to directly, and allosterically, interact with each other. Head-head interactions play critical roles in regulating actin-activation in other myosin II family members [69]. The selective effect of mavacamten on the amplitudes in HMM but not S1 at saturating concentrations of actin indicates that mavacamten stabilizes a state in HMM which occurs infrequently in S1.

Mavacamten inhibits basal single ATP turnover and basal ADP release in two-headed cardiac HMM differently than in single-headed S1. We investigated the differences between S1 and HMM in the absence of actin by examining the effects of mavacamten on the kinetics of basal single ATP turnover and basal ADP release. We mixed 0.4 μM S1 or 0.2 μM HMM—identical concentrations of ATP-binding heads—with either 4.0 μM mant-ATP (Fig. 35A-E) or 4.0 μM mant-ADP (Fig. 35F-J) and then measured nucleotide release after mixing with 2.0 mM MgATP. Mavacamten's effect on ADP release was previously measured in S1 but not in HMM (Fig. 35G) [60].

We analyzed the kinetics of nucleotide exchange in these experiments by fitting the data to a bi-exponential function. Basal ATP turnover by HMM was distinct from the ATP turnover kinetics measured in S1 (Fig. 35A-C, black and red traces and bars) exhibiting two distinct kinetic phases. HMM's slow phase has an amplitude of 0.55 ± 0.04, significantly more than in S1, 0.17 ± 0.04 (Fig. 35C). The rate constant for the fast and slow phase of basal single ATP turnover are very similar in HMM and S1 (Fig. 35 D, E, I, J: compare black and red bars). The rate constants we observed for the fast and slow phases of basal single ATP turnover are 0.02-0.03 s^{-1} and 0.005-0.008 s^{-1} respectively (Table 7), notably similar to the rate constants for bi-exponential mant-ATP turnover kinetics

detected in permeabilized myocardium where the auto-inhibited SRX state has been described [63].

Mavacamten inhibited the rate constants for basal single ATP turnover in both HMM and S1 preparations to a similar degree (Fig. 35D, E, I, J: blue and violet bars). However, as with the actin-activated single ATP turnover experiments in Fig. 34, the amplitude of the slow phase of basal single ATP turnover is significantly increased by mavacamten in HMM, more than in S1 (Fig. 35C: compare black and blue to red and violet) ($p \leq 0.0001$).

The kinetics of ADP release are very similar in HMM and S1 in the absence of mavacamten (Fig. 35F-J: compare black and red traces and bars). As with ATP turnover, ADP release is inhibited more by mavacamten in HMM (Fig. 35F,G: compare blue and violet traces). This increased inhibition reflects stabilization of a slow phase for ADP dissociation that is greatly enhanced from a mole fraction of 0.37 ± 0.02 to 0.62 ± 0.02 (Fig. 35F,H: compare black and blue traces and bars). The fast and slow rate constants for ADP release are similar in S1 and HMM (Fig. 35I,J: black and red bars). But unlike in HMM, in S1, mavacamten does not affect the amplitude of the slow phase of ADP dissociation (Fig. 35H, red, violet). These results further support the hypothesis that the structural kinetics of HMM are distinct from those of S1, and mavacamten stabilizes the slow phase of nucleotide turnover.

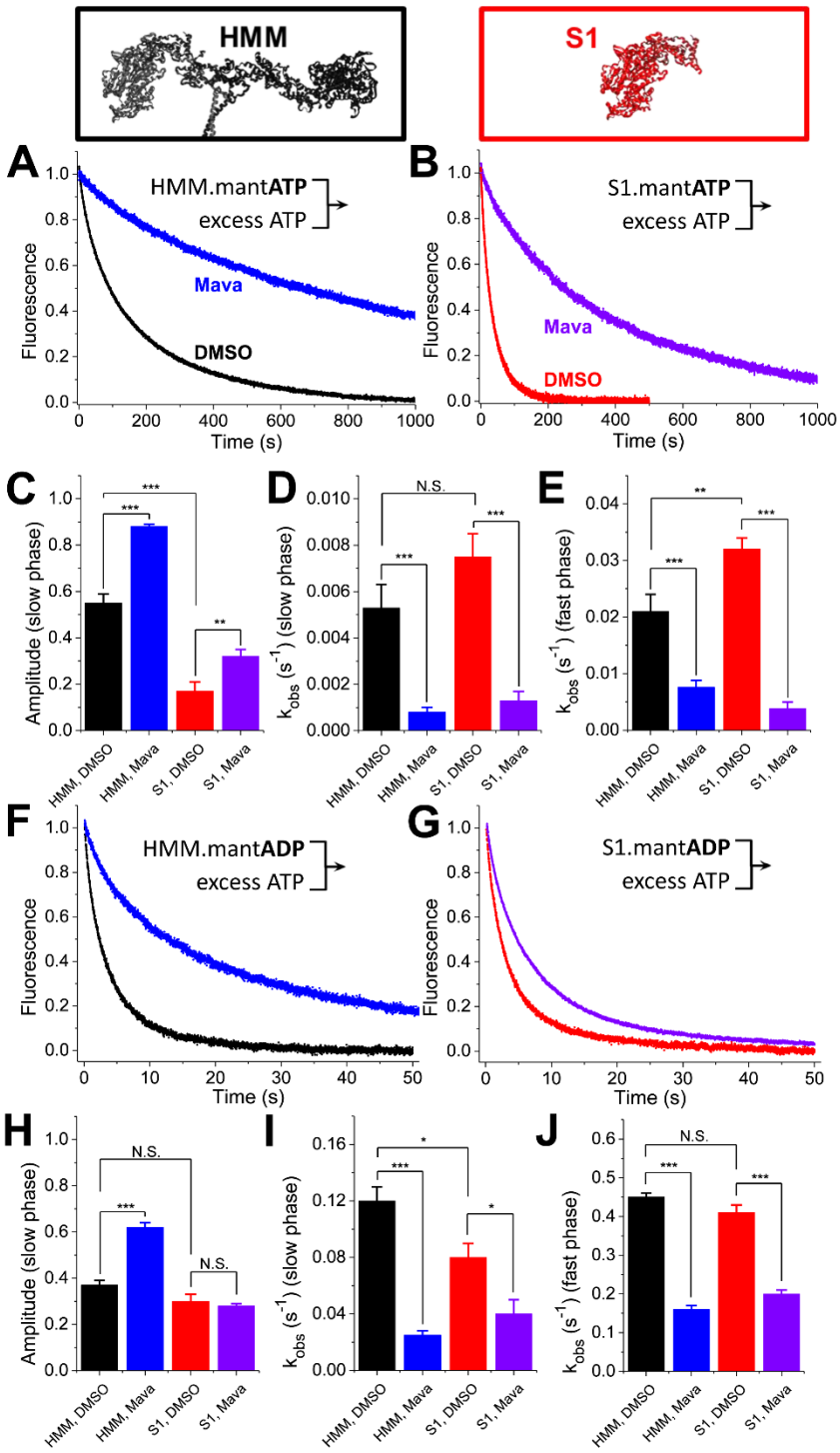

Fig. 35 Basal nucleotide exchange in the absence of actin

(**A**) Basal single ATP turnover by stopped-flow mix of 0.2 μM HMM or (**B**) 0.4 μM S1, mixed with 4.0 μM mant-ATP, then chased with 2.0 mM MgATP. Blue and violet traces indicate 30 μM mavacamten. (**C-E**) Amplitudes and rates of the two-exponential fits of A and B. (**F**) Basal single ADP dissociation from HMM or (**G**) S1, mixed with 4.0 μM mant-ADP then chased with 2.0 mM MgATP. (**H-J**) Amplitudes and rates of the two-exponential fit of F and G. Replicates of n = 9, ± SEM. Two-exponential fits reported in Table 7.

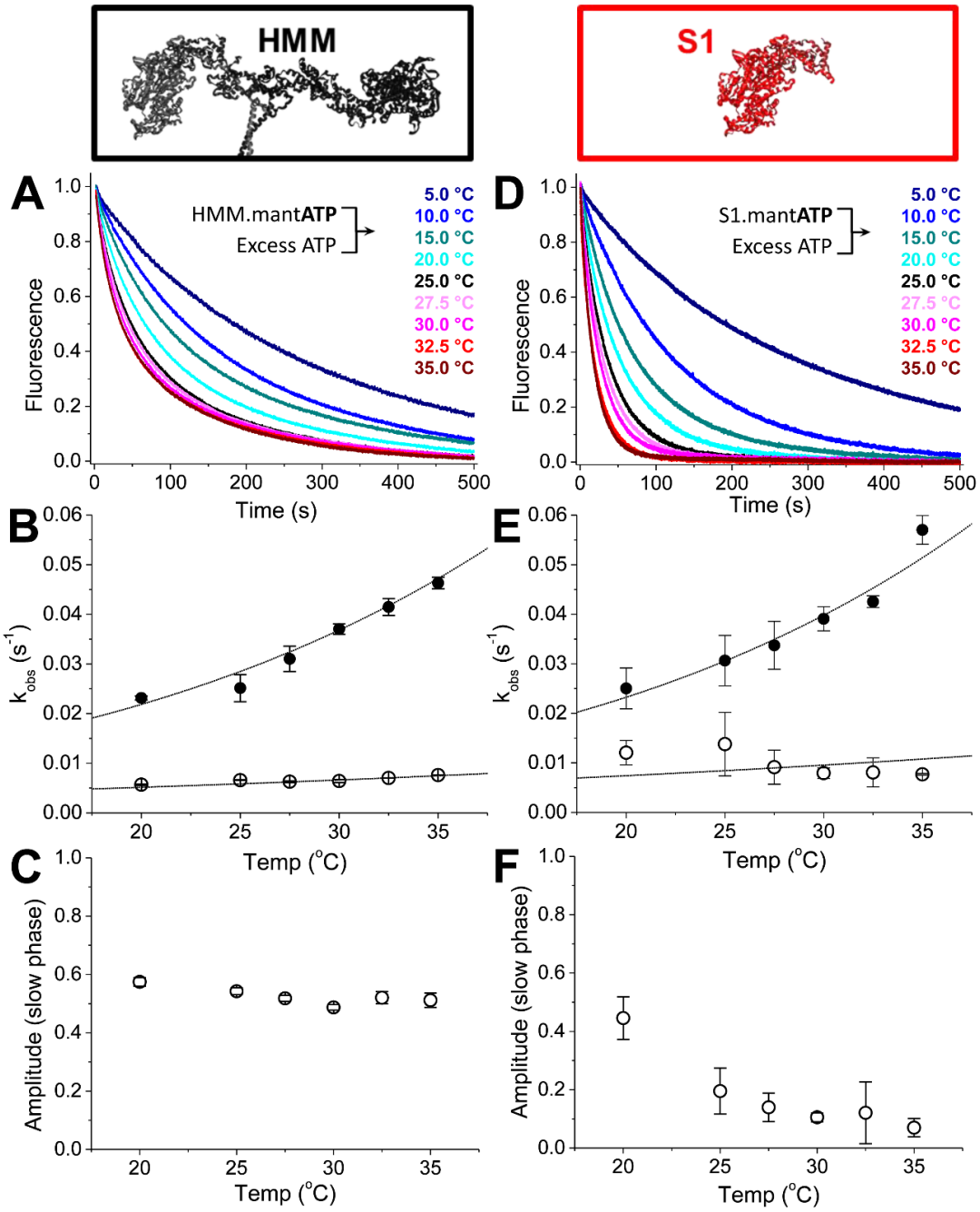

Fig. 36. Temperature dependence of basal single ATP turnover
(**A**) 0.4 µM HMM, or (**D**) 0.8 µM S1, mixed with 8.0 µM mant-ATP, then mixed with 2.0 mM MgATP. These data were fit to a two-exponential function. (**B**) The rates for HMM were fit to the Erying equation: k_{fast} = T*exp(–[35.3 kJ/mol]/RT + 5.3) $s^{-1}K^{-1}$, k_{slow} = T*exp(–[15.9 kJ/mol]/RT – 4.3) $s^{-1}K^{-1}$, with temperature T in Kelvin. Fast phase closed circles; slow phase open circles. (**C**) The amplitudes of the slow phases depicted in A. (**E**) The rates from the two-exponential fit for S1 were also fit to the Erying equation: k_{fast} = T*exp(–[30.9 kJ/mol]/RT + 3.6) $s^{-1}K^{-1}$, k_{slow} = T*exp(–[15.1 kJ/mol]/RT – 3.9) $s^{-1}K^{-1}$. (**F**) The amplitudes of the slow phases depicted in D. Replicates of n = 4 for each temperature, ± SEM.

The energetics of basal single ATP turnover in two-headed cardiac HMM are distinct from that of single-headed S1. We evaluated the biophysical determinants underlying the difference between S1 and HMM described in Fig. 35 by examining the temperature dependence of basal single ATP turnover in the absence of actin and in the absence of mavacamten. We performed these experiments identically to those in Fig. 35 over a range of temperatures (5.0 to 35 °C), analyzing the resulting basal single ATP turnover transients by fitting a bi-exponential function to the data. The results from these experiments are summarized in Fig. 36. The kinetics of basal single ATP turnover were distinctly bi-exponential above 15 °C; we focused our analysis above this temperature (Fig. 35B,C,E,F). The rate constants for the fast phase of ATP turnover increased with increasing temperature in both HMM and S1 and the temperature dependence for the increase in k_{fast} and k_{slow} was nearly identical for the two proteins (Table 7). Fitting to the Eyring equation (given in Table 7) provides apparent transition state enthalpy ($\Delta H^{\ddagger}_{app}$) and a collection of terms associated with the transition state entropy ($\Delta S^{\ddagger}_{app}$). For both HMM and S1, the fast rate constant of basal single ATP turnover (k_{fast}) has a larger, endothermic $\Delta H^{\ddagger}_{app}$ than the slow rate constant (Table 7). In addition, for both HMM and S1, k_{fast} has a positive $\Delta S^{\ddagger}_{app}$ while the k_{slow} has a negative, $\Delta S^{\ddagger}_{app}$. This suggests that k_{fast} and k_{slow} (Fig. 36B, E) are distinct biophysical processes exhibiting unique transition state energetics and are rate-limited by unique biochemical or biophysical transitions.

The temperature dependence for the amplitudes of basal single ATP turnover (Fig. 36C,F) were also distinct between S1 and HMM samples. In S1, increasing temperature from 20 to 35 °C dramatically decreased the amplitude of k_{slow} from 0.45 ± 0.07 to 0.07 ± 0.03 (Fig. 36F) while in HMM the amplitude only decreased from 0.57 ± 0.01 to 0.51 ±

0.02 (Fig. 36C). Thus, near physiologic temperatures (35 °C) the slow phase of basal single ATP turnover is significantly more abundant in HMM than in S1 ($p \leq 0.0001$). Temperature stability is consistent with the biochemically sequestered SRX state observed in permeabilized muscle fibers [62], and the ordered state of the myosin thick filament observed by fluorescence polarization [115], and X-ray diffraction [116-118], all of which are stabilized by increasing temperature.

Increasing ionic strength activates two-headed cardiac HMM but not S1. Previous studies showed an isolated S2 coiled-coil domain fragment of human cardiac myosin interacts at low-ionic strength with an isolated S1 fragment and with a two-headed HMM truncated at the second heptad of the S2 coiled-coil domain; and an EM study showed the IHM is disrupted in myosin II homologues by increasing ionic strength [69, 74]. We therefore examined the ionic strength dependence of basal single ATP turnover in S1 and HMM at 25 °C increasing the concentration of potassium chloride (KCl) from 0 mM to 100 mM. The results from these experiments are depicted in Fig. 37. Increasing ionic strength accelerated basal ATP turnover by HMM (Fig. 37A-C) but had little effect on S1 (Fig. 37E-G). We fit bi-exponential functions to the resulting transients. The k_{fast} and k_{slow} rate constants for basal ATP turnover did not change with increasing ionic strength in HMM (Fig. 37B), or in S1 (Fig. 37F). The ionic strength dependence of turnover by HMM, reflected an increase in the amplitude of the fast phase and a decrease in the amplitude of

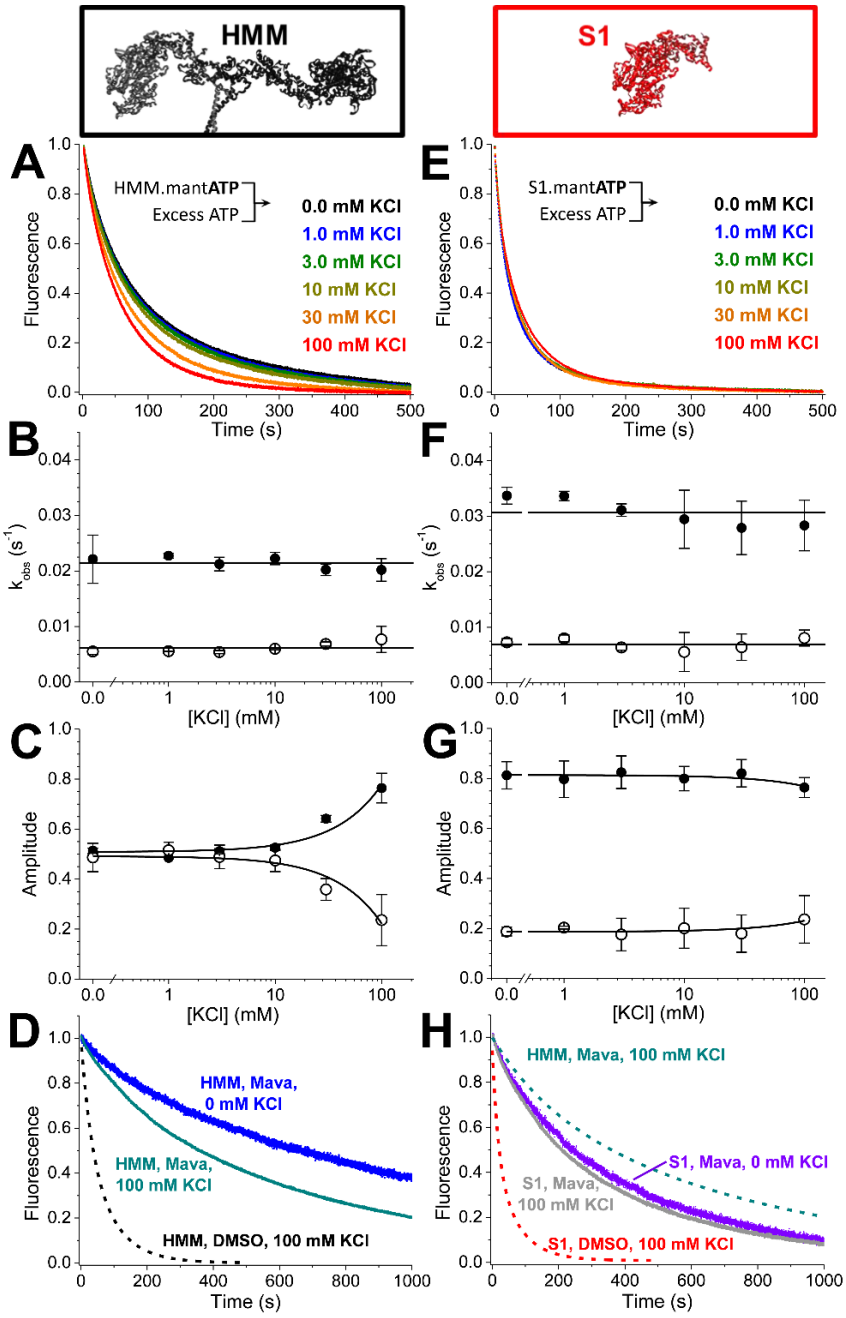

Fig. 37. Ionic strength dependence of basal ATP turnover
(**A**) 0.4 µM HMM, or (**E**) 0.8 µM S1, mixed with 8.0 µM mant-ATP, then mixed with 2.0 mM MgATP. Data best fit to two exponentials. (**B**) The rates of HMM's basal mant-ATP turnover are relatively constant over these [KCl] with average value depicted as a horizontal line. Closed circles represent the fast phase; open circles the slow phase. (**C**) The amplitude of the fast phase increases with increasing [KCl] (closed circles fast phase; open circles slow phase). Linear fits to show trends. (**D**) In the presence of mavacamten, HMM is sensitive to increasing ionic strength (blue to dark cyan). (**F-G**) The rates and amplitudes of S1's basal mant-ATP turnover are relatively constant. Linear fits to show trends. (**H**) S1 in the presence of mavacamten is insensitive to changes in [KCl] (violet to grey), consistent with S1 in the absence of mavacamten (E). Replicates of n = 4 for each [KCl], ± SEM. Fits reported in Table 7.

the slow phase while in S1, the amplitudes did not change. At 100 mM KCl, the amplitude of the fast and slow phases of turnover were similar in HMM and S1 (Fig. 37C, G). These data suggest that the transition between fast- and slow-ATP turnover kinetics states exchange in solution, and that the energetics of this exchange are dependent on charge-charge interactions that are disrupted with increasing ionic strength.

We also examined the ionic strength dependence of HMM's auto-inhibited state in the presence of mavacamten by performing basal single ATP turnover under 100 mM KCl or no KCl conditions (Fig. 37D). Increasing ionic strength to 100 mM KCl partially relieved mavacamten's inhibition on ATP turnover in HMM but not in S1, indicating that the mavacamten-stabilized state in HMM is specifically ionic strength dependent (Fig. 37H). Notably, however, at 100 mM KCl and saturating mavacamten, ATP-turnover by HMM is still slower and distinctly bi-exponential compared to the turnover by S1 (Fig. 37H: compare dashed cyan to gray).

Actin disrupts the auto-inhibited state of two-headed cardiac HMM. Results in Fig. 35 show that in the absence of actin half of the myosin ATPase sites in HMM turnover ATP more slowly than in S1. This population is stable with increasing temperature (Fig. 36) and is disrupted by increasing ionic strength (Fig. 37), both of which suggest formation of an auto-inhibitory protein-protein interaction interface. Furthermore, in the presence of mavacamten, the steady-state ATPase k_{cat} (Fig. 33 and Table 7) and the fast and slow rate constants for actin-activated single ATP turnover (Fig. 34) are faster than the same kinetics in the absence of actin (Fig. 35). This indicates that actin still activates ATP turnover and ATPase cycling in the presence of saturating mavacamten. Together, these observations

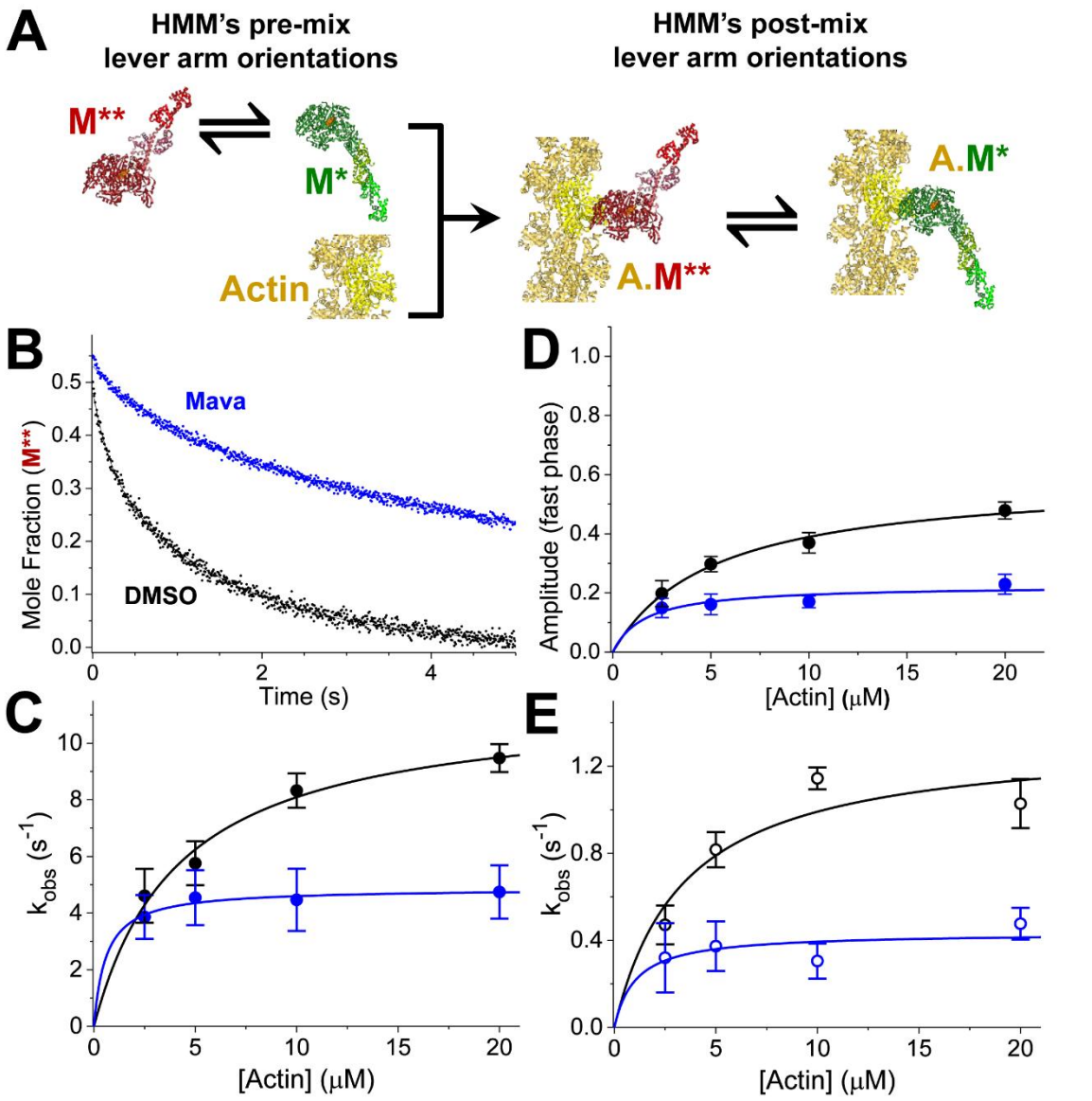

Fig. 38. Mavacamten inhibits lever arm rotation in HMM during actin-activation, detected with $(TR)^2$FRET

(**A**) Stopped-flow mix of fluorescently-labeled myosin with actin, to detect FRET between the lever arm and catalytic domain of cardiac HMM during the actin-activated powerstroke. An equilibrium of structural states for myosin (green, red) are depicted before and after stopped-flow mixing. Fluorophores are located on the RLC and nucleotide. S1 shown for simplicity, HMM used. (**B**) Mole fraction of the M** pre-powerstroke structural state (red), detected with $(TR)^2$FRET. Structural transients are fit to two exponentials. (**C**) Observed rate constants for the fast phase of the actin-activated powerstroke over a range of [Actin]. $k_{obs,fast,DMSO}$ = $11.5s^{-1}$[Actin]/(4.2μM+[Actin]), $k_{obs,fast,Mava}$ = $4.9s^{-1}$[Actin]/ (0.6μM+[Actin]). (**D**) Amplitude of the fast phase: $A_{fast,DMSO}$ = 0.59[Actin]/(5.1μM+[Actin]), $A_{fast,Mava}$ = 0.23[Actin]/ (1.6μM+[Actin]). (**E**) Slow phase: $k_{obs.slow,DMSO}$ = $1.3s^{-1}$[Actin]/(3.4μM+[Actin]), $k_{obs,slow,Myk461}$ = $0.4s^{-1}$[Actin]/(1.0μM+[Actin]). Replicates of n = 6 biochemically independent mixes, each averaging 6-10 shots, two separate preparations of cardiac HMM, error bars represent ± SEM.

suggest that actin interaction relieves the auto-inhibition present in HMM, even when mavacamten is bound. We reasoned that if the enhanced inhibition of HMM by mavacamten results from a folded, IHM-like structural state, then the structural dynamics of the two light-chain binding domains of the HMM dimer, which are presumably prevented from moving when HMM is in the IHM state, should be altered, compared to when the HMM is not in the IHM. We tested this hypothesis by using transient time-resolved FRET, $(TR)^2$FRET, to measure these dynamics directly in response to actin-activation.

We followed the strategy outlined in our prior work to perform these experiments [2]. We labeled the cardiac myosin regulatory light-chain (RLC) with the AlexaFluor-488 fluorescent probe on a single engineered cysteine residue, replacing the native valine at position 105 in the bovine cardiac RLC sequence. We then exchanged the labeled RLC onto purified cardiac HMM to obtain donor-labeled HMM. Expression and purification of the RLC, labeling, and light-chain exchange were performed identically to our prior study and are described in detail in that paper and outlined in the SI (Chapter 4.6) [2]. We confirmed that neither the exchange nor the attachment of the fluorescent labels perturb the auto-inhibited state by measuring basal single ATP turnover (Fig. 41).

We measured actin-initiated changes in light-chain domain (lever-arm) orientation by equilibrating the donor labeled HMM with 20-molar excess Cy3-ATP. The Cy3-ATP binds and is hydrolyzed by the myosin. When bound, the Cy3 fluorescent probe is a FRET acceptor to the Alexa488 probe and thus we obtained FRET-labeled cardiac HMM. FRET between the labeled RLC and the Cy3-ATP reports on the orientation of the myosin light-chain binding domain [2] (Fig. 33A, bound by the ELC and RLC). While binding of the

Cy3-ATP stabilizes a pre-powerstroke structural state of the light-chain binding domain, actin stabilizes the post-powerstroke state during the phosphate release/powerstroke phase and prior to the dissociation of the hydrolyzed Cy3-ADP. Cy3-ATP stabilization of the pre-powerstroke state is reflected in a decrease in the time-resolved fluorescence lifetime of the AlexaFluor-488 donor probe and the powerstroke is reflected in the actin-initiated increase in the lifetime (Fig. 42) [2].

We mixed the Cy3-ATP/Alexa488-HMM complex with increasing concentrations of actin containing excess 2 mM MgATP by stopped-flow (Fig. 38A) and acquired time-resolved fluorescence waveforms every 1.0 millisecond during the resulting actin-induced single ATP turnover transient (Fig. 42). We analyzed the changes in the time-resolved fluorescence decay using a two-distance, structure-based model as in our prior study [2]. The structural states obtained from fitting this model to the data, summarized in Table 7, were indistinguishable from our previous results. The center and widths of pre and post-powerstroke like structural states where not changed by mavacamten under the conditions of our experiments (Fig. 44) and were therefore treated as global parameters in the structural model with control samples containing DMSO. We used the same approach in our prior work investigating the effect of omecamtiv mecarbil on the cardiac myosin powerstroke [2]. From this analysis, we obtain the structural kinetics of the lever-arm rotation in response to actin-activation (Fig. 38C, Table 7).

In the absence of mavacamten, actin drives lever-arm rotation and the resulting millisecond time-scale mole-fraction transients for each structural state (pre-powerstroke short distance or post-powerstroke long distance) obtained from fitting the two-state model to the data, are best fit to bi-exponential functions (Fig. 38C-E, Fig. 42). The fast phase

reflects lever-arm rotation of myosin heads that are primed for activation (Fig. 38C) while the slow phase reflects the equilibration of other HMM species, less readily activated by actin (Fig. 38E).

The maximum observed rate constant for the fast phase of actin-activated lever-arm rotation is 11.5 ± 0.8 s^{-1}, and the maximum observed rate constant for the slow phase of actin-activated lever-arm rotation is 1.3 ± 0.2 s^{-1}. These rate constants are significantly faster than the fast and slow rate constants for actin-activated single ATP turnover (Fig. 34) indicating that actin binding by the two populations of myosin is followed by FRET-detected lever-arm rotation, followed by ADP release. Saturating mavacamten significantly reduced these rate constants to 4.9 ± 0.2 s^{-1} ($p < 0.0001$) and 0.43 ±0.08 s^{-1} ($p < 0.001$).

We compared the effect of mavacamten on the observed rate constants for actin-activated lever-arm rotation (Fig. 38) to the rate constants for basal single ATP turnover (Fig. 35). At saturating mavacamten and actin, the fast phase of the powerstroke is 23 ± 3% of the total structural transient and is 16-fold faster than the fast phase of basal ATP turnover in the presence of mavacamten (Fig. 38C, D; Fig. 35E). The slow phase of the powerstroke is 77 ± 3% of the transient and is 12-fold faster than the slow phase of basal ATP turnover in the presence of mavacamten (Fig. 38E; Fig. 35D). Because both rate constants for the structural change induced by actin are faster than the fastest phase of basal ATP turnover in the absence of mavacamten, we conclude that actin is able to bind the mavacamten-inhibited HMM, and to trigger lever-arm rotation in both the fast and slow basal turnover populations. Thus, actin interaction triggers the disruption of the auto-inhibited state of cardiac HMM that mavacamten otherwise stabilizes (Fig. 35). We also

note that actin-activation triggers turnover of all bound Cy3-ATP in the presence of mavacamten, though with slower kinetics than in the absence of the compound. Thus, mavacamten does not permanently trap cardiac myosin in an inhibited state.

Several steps of the cardiac myosin ATPase cycle are not affected by mavacamten. Additional transient stopped-flow kinetics experiments utilizing $(TR)^2$FRET showed that the ATP-induced recovery stroke is not substantially altered by mavacamten (Fig. 43), nor are ATP-binding to myosin or actomyosin, ADP release from actomyosin, myosin dissociation from actomyosin, or the apparent equilibrium constant for ATP hydrolysis measured by acid-quench (Fig. 45, Table 7). Mavacamten's effects on other steps in myosin's ATPase cycle, such as phosphate release and actin association in the ADP state, have been reported previously[60]. We summarize the kinetics steps in the cardiac myosin ATPase cycle that mavacamten inhibits in Fig. 40 and discuss the implications for these changes below.

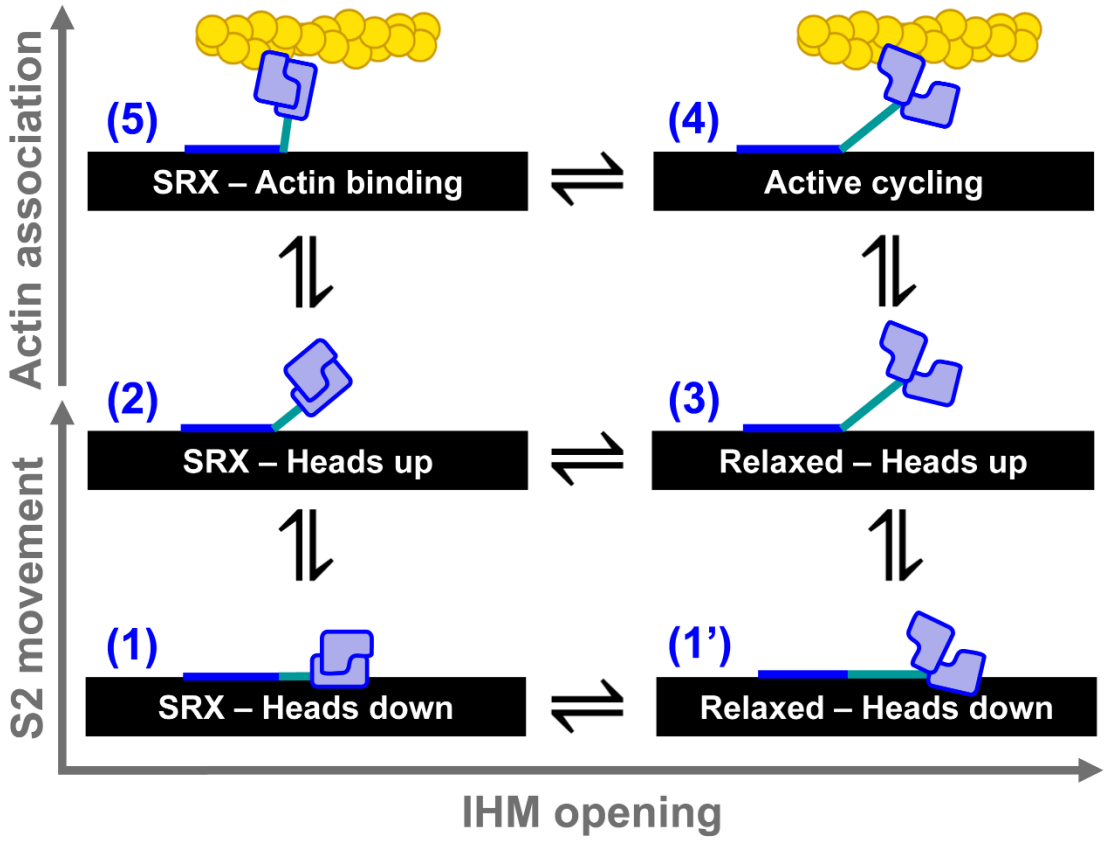

Fig. 39. Structural model for thick filament regulation
(1) Electron microscopy data supports an interacting-heads motif folded back against the thick filament (black). (1') The heads may open while the S2 is on the thick filament. (2) Hypothesized state based on our detection of an SRX-like state in HMM. (3) Relaxed myosin with heads splayed and ready to interact with actin. (4) Active actomyosin cycling. (5) Hypothesized state based our detection of actin accelerating the auto-inhibited basal ATP turnover of HMM, and thus likely unfolding the IHM.

4.4 DISCUSSION

Regulated activation of the cardiac myosin thick filament is a critical determinant of contraction in the heart. This regulation contributes to the Frank-Starling relationship, a fundamental correlate of cardiac performance[119]. It may also contribute to heart diseases [74, 120]. Activation of cardiac thick filaments is hypothesized to be controlled by an evolutionarily-conserved mechanism where the heads of each myosin dimer fold back and

interact with the dimer's S2 coiled-coil domain and the underlying surface of the thick filament[69]. This structural state, termed the interacting heads motif, has been observed in relaxed muscle [115, 116, 121], in isolated thick filaments, and purified myosin preparations including glutaraldehyde cross-linked cardiac myosin in the presence of the myosin II inhibitor blebbistatin [67, 69, 122, 123].

Previous muscle fiber studies revealed a population of myosin ATPase sites with dramatically inhibited ATP turnover kinetics compared to isolated myosin S1 analyzed *in vitro* [62, 63, 124]. This population is termed the super-relaxed state (SRX). The SRX biochemical state is hypothesized to result from the formation of the IHM structural state[125] however, their biochemical and structural correlates remain enigmatic. Our results show that an SRX-like biochemical state, indicated by auto-inhibited ATP turnover, forms in solution at low ionic strength in the presence of ATP and that this state correlates with changes in the biochemical and structural kinetics of actin-activation. This conclusion is based on measured differences between the biochemical kinetics of single-headed cardiac myosin S1 and two-headed HMM.

The steady-state ATPase experiments in Fig. 33 and the transient, actin-activated, single ATP turnover studies in Fig. 34 demonstrate that key biochemical differences exist between cardiac S1 and HMM. These differences are indicative of head-head mediated auto-inhibition seen in highly regulated two-headed smooth muscle myosins[126, 127] and suggest the compound may target the same allosteric pathway as RLC phosphorylation. In HMM, mavacamten stabilizes the slow phase of ATP turnover in the presence (Fig. 34C) and absence of actin (Fig. 35A). It also slows actin-independent ADP release to a greater extent in HMM. These changes indicate that interactions between the two-heads of the

HMM dimer are stabilized by the compound and that this stabilization slows the rate limiting kinetics of ATP-turnover and ADP dissociation (Fig. 35F-H). We hypothesize that this reflects an increase in the transition state free energy for opening of the phosphate release pathway and nucleotide-binding pocket in the absence of actin—these transitions limit phosphate and ADP release respectively. Furthermore, the compound's lower binding affinity for HMM compared to S1, indicated by its EC_{50} for steady-state ATPase cycling (Fig. 33 and Table 7), shows that the two-headed myosin adopts a structural state that preferentially binds mavacamten.

The temperature and ionic strength dependence studies in Fig. 36 and Fig. 37 support the conclusion that the rate limiting kinetics for ATP-turnover in the absence of actin are distinct in HMM compared to S1 and reflect the formation of a large protein-interaction interface. The disruption by increasing ionic strength and stability at higher temperatures are consistent with HMM's two heads interacting in an IHM like state. Formation of the IHM involves putative ionic interactions [74] and the slow ATP-turnover phase, which we hypothesize correlates with head-head interaction, is disrupted by increasing ionic strength. Stabilization of the slow phase at physiologic temperature is consistent with structural studies in intact muscle that also show slowed ATP turnover and thick-filament ordering at increasing temperature. Importantly, mavacamten stabilizes the auto-inhibited state of two-headed HMM in the presence of physiological ionic strengths (Fig. 37D,H) and thus we expect a similar result in the heart. Recent work suggests this may be the case[75].

Mavacamten changes the structural kinetics of actin-activation, consistent with its stabilization of a pre-existing auto-inhibited state. This conclusion is reflected by the

compound's inhibition of actin-activated lever-arm rotation in Fig. 38. The slowest phase of actin-activated lever arm rotation is significantly faster than the fastest phase of mavacamten-saturated basal ATP-turnover by HMM (Fig. 35A, C-E). This is an important result that indicates actin-interaction triggers structural changes in HMM that disrupt the auto-inhibited state and mavacamten binding slows, but does not prevent these structural changes.

Based on these results, we propose a mechanism for actin-activation of the single myosin molecules in the cardiac thick filament (Fig. 39). In this mechanism, auto-inhibited myosin heads transition from a folded IHM state that is docked on the thick-filament backbone (state 1) to an IHM state with S2 extended off the filament backbone (state 2). The IHM heads then "open" (state 3) and become available for actin-activation (state 4). Thus, myosin in the IHM can be actin-activated by following the pathway (1) ↔ (2) ↔ (3) ↔ (4) (Fig. 39). Alternatively, actin interaction accelerates IHM head opening if one of the heads—we hypothesize the free IHM head[69] (Fig. 33A)—weakly interacts with available myosin binding sites on the actin thin-filament (state 5 in Fig. 39) and subsequently undergoes a structural transition that disrupts the IHM state. Thus, activation can also proceed via the pathway (1) ↔ (2) ↔ (5) ↔ (4). This second, actin-activated pathway is supported by our biochemical and structural kinetics data and also depicted in the myosin ATPase cycle in Fig. 40. The "SRX – Heads up" state (2) is likely present in muscle fibers because we have observed it in tissue-purified HMM, and it is stable at physiological temperatures (Fig. 36). This state is weakened at physiological ionic strengths (Fig. 37), indicating that additional protein-protein interactions are likely required for its full stabilization in the cardiac sarcomere. Similar arguments were made in a

previous paper based on head-to-S2 binding experiments performed by microscale thermophoresis[74]. We predict that in muscle fibers, mavacamten will shift the apparent equilibrium between the Relaxed heads, to the IHM heads occupied in state (1) and (2). Recent work shows this may occur [75].

In solution, we propose that mavacamten saturated HMM follows the pathway through states (1) ↔ (2) ↔ (5) ↔ (4), actin accelerates ATP-turnover compared to basal turnover. This conclusion is based on the observation that the slowest phases of lever-arm rotation detected by $(TR)^2$FRET is substantially faster than the fastest phase of mavacamten inhibited ATP-turnover in the absence of actin. The transition between state 1 and state 2 is likely to play an important role in muscle. This transition, is hypothesized to be controlled by interactions with myosin-binding protein-C and passive strain on the thick filament [128, 129]. Thus, structural studies in intact muscle will be critical for fully understanding the compounds mode of action in the heart.

4.5 CONCLUSIONS

We have detected a biochemically auto-inhibited state in tissue-purified cardiac HMM. The kinetics and energetics of this state are consistent with the SRX observed in permeablized myocardium and thus we argue that the SRX state can be detected in solution. Mavacamten stabilizes this state, revealing a new mechanism for a drug's inhibition of two-headed cardiac myosin that was not previously seen in studies of single headed myosin. Actin interaction is able to disrupt the auto-inhibited state and accelerate the rate-limiting structural transition of head-head splaying that limits ATP turnover in HMM. Thus, weak interaction with actin and cardiac myosin can disrupt auto-inhibition, indicating that how the auto-inhibited myosin heads are tethered to the thick-filament

backbone in muscle is critical. Mechanisms likely regulating this tethering include cardiac myosin RLC phosphorylation[130], binding of myosin-binding protein-C to the HMM portion of intact myosin in the thick filament [124], thick-filament mechano-sensing[131], and small molecules[132].

4.6 SUPPLEMENTAL INFORMATION AND METHODS

Steady-state ATPase activity: The actin-activated MgATPase activity of purified cardiac myosin HMM or S1 was measured using an NADH-coupled assay [88] performed at 25 ºC in 10 mM Tris pH 7.5, 2 mM $MgCl_2$ with 1.0 mM DTT. The reaction mix contained 0.2 μM HMM or 0.4 μM S1, varied [actin], and 0.2 mM NADH, 0.5 mM PEP, 2.1 mM ATP, 10 U/mL LDH, 40 U/mL PK, HMM (200 nM). We acquired absorbance at 340 nm every 10 seconds for 120 seconds total using a Beckman-Coulter DU640B spectrophotometer.

Transient kinetics: Transient biochemical experiments with steady-state fluorescence detection (total fluorescence intensity) were performed on an *Applied Photophysics* stopped-flow spectrophotometer capable of single-mix and sequential-mix experiments with water bath temperature control. All experiments performed at 25 °C unless otherwise stated. The single-mix dead time for this instrument is 1.3 ms. All buffers were filtered and then degassed for 30 minutes under high-vacuum prior to use.

Single ATP turnover experiments with mant-ATP were performed with both sequential and single stopped flow mixes. Samples were excited at 280 nm with a Xe lamp and monochromator, and detected through a 400 nm long-pass filter.

Statistics and error analysis: Individual, representative traces shown throughout the manuscript depict the average of 6-10 shots of the stopped-flow. All experiments were performed in replicates of n = 4 to 9, and as biochemically independent experiments. Three

separate preparations of cardiac HMM from separate bovine myocardia obtained unfrozen from Pel-Freez Biologicals contributed to the experiments throughout this manuscript; error bars represent ± SEM. The student's t-test was used to determine statistical significance of measured parameters, tabulated in Table 7.

A complete discussion of all methods, including the extraction, digestion, purification and expression of the proteins utilized in this study, the steady-state and transient kinetics methodologies, and $(TR)^2$FRET data acquisition and analysis are included in the SI (Chapter 4.6).

Protein purification and labeling

Myosin: Bovine cardiac myosin was purified following procedures based on Margossian et al. [95]. Cow hearts were obtained on wet ice from *Pel-Freez.* The entire purification process was performed in a 4 ºC cold room. A thorough description is given in our previous publications [2].

HMM digestion: Myosin prepared as described in Rohde et al. [2] was thawed and brought to 2 mM $MgCl_2$ in its freezing buffer before digestion to HMM with α-chymotrypsin (*Sigma-Aldrich*, 0.025 mg/ml final concentration) for 10 minutes at 25 ºC, followed by addition of pefabloc (*Roche*, 5 mM final concentration) and then dialyzed into 10 mM Tris pH 7.5 with 2 mM $MgCl_2$ and then purified by Q-sephadex ion-exchange chromatography. The column was equilibrated in 10 mM Tris pH 8.0 at 4.0 C, the digested myosin loaded and then eluted in a gradient of 0-300 mM KCl, 10 mM Tris pH 8.0, over 300 mL at 1.5 mL/min, collecting 4 mL fractions (AKTA Prime Plus, GE). Fractions were evaluated by SDS-Page and those containing intact HMM without contaminants, pooled for experiments. The pooled HMM was dialyzed into buffers utilized for each experiment.

RLC: Expression, labeling and storage of recombinant Bovine ventricular regulatory light chain with a single engineered cysteine at position 105, is described in our previous work [2].

Actin: Actin was purified from rabbit skeletal muscle by acetone dehydration followed by extraction into ice cold water as described in our previous work [97] and then polymerized in 10 mM Tris pH 7.5, 2 mM $MgCl_2$, 0.5 mM ATP and stored on ice prior to use. Prior to use, the F-actin was stabilized with a 1:1.3 stochiometric excess of phalloidin (*Sigma Aldrich*), followed by 48 h dialysis (3 buffer changes) into 10 mM Tris pH 7.0 with 2 mM $MgCl_2$.

Protein and dye concentration: The Bradford protein concentration assay utilizing a known bovine serum albumin (BSA) protein standard was used throughout this study to determine protein concentrations. Reagents for this assay were purchased from *Biorad*. The extinction coefficient for the AF488 dye is 73,000 at 495 nm, and for Cy3 is 136,000 at 570 nm, per the manufacturer's specifications.

Exchange: We exchanged the AF488-labeled RLC onto HMM by combining the two proteins (4.5 molar excess RLC to HMM) in 50 mM Tris pH 7.5, 120 mM KCl, 2 mM DTT, 12 mM EDTA [98] and then incubated the reaction mix for 30 minutes at 30^{o}C. After the incubation, we adjusted the reaction to 12 mM $MgCl_2$ and then incubated the mixture on ice for 15 minutes followed by dialysis into 10 mM Tris pH 7.0, 30 mM KCl, 2 mM $MgCl_2$ prior to gel filtration to remove free RLC.

Buffers and solutions: All experiments, unless otherwise noted, were performed in 10 mM Tris pH 7.5, 2 mM $MgCl_2$ at 25 ^{o}C.

Chemicals: Mavacamten (Myk-461) was custom synthesized by EAG Laboratories; purity was >97% by proton nuclear magnetic resonance (^{1}H NMR) and 99.36% by liquid chromatography/mass spectrometry (LC/MS). ATP (Adenosine 5'-triphosphate disodium salt hydrate, Grade 1 >99 %) and ADP (Adenosine 5'-diphosphate sodium >95 %) were purchased from *Sigma Aldrich*. Mant-ATP (2'-(or-3')-O-(N-methylanthraniloyl) adenosine 5'-triphosphate, trisodium salt) was purchased from *Thermo Fisher Scientific*. All other chemicals where purchased from *Sigma Aldrich*.

Steady-state ATPase activity: We measured the actin-activated MgATPase activity of the purified cardiac myosin HMM using an NADH-coupled assay [88] performed at 25 ºC in 10 mM Tris pH 7.5, 2 mM $MgCl_2$. The reaction mix contained varied [actin], and 0.2 mM NADH, 0.5 mM PEP, 2.1 mM ATP, 10 U/mL LDH, 40 U/mL PK, HMM (200 nM). We acquired absorbance at 340 nm every 10 seconds for 120 seconds total using a Beckman-Coulter DU640B spectrophotometer.

Transient kinetics: Transient biochemical experiments with steady-state fluorescence (total fluorescence intensity) detection were performed on an *Applied Photophysics* stopped-flow spectrophotometer capable of sequential mixing experiments with water bath temperature control. All experiments performed at 25 °C unless otherwise stated. The single-mix dead time for this instrument is 1.3 ms, calibrated using fluorescence enhancement of 8-hydroxyquinoline following Mg^{+2} binding under pseudo first-order kinetics conditions [99]. All buffers were filtered and then degassed for 30 minutes under high-vacuum prior to use.

Transient time-resolved FRET (millisecond-resolved transient biochemical experiments with nanosecond-resolved fluorescence detection), $(TR)^2$FRET, was

measured using a transient time-resolved fluorescence spectrophotometer [10, 42, 77]. This instrument utilizes a *Biologic USA* SFM/20 single-mix stopped-flow accessory coupled to our transient time-resolved fluorescence spectrophotometer. The dead time for the instrument was 1.8 ms, calibrated using the 8-hydroxyquinoline + Mg^{+2} control reaction [99]. For experiments mixing equilibrated myosin in the presence of 10 molar excess ATP with actin containing 1 mM MgATP, we loaded the actin into syringe A, followed by a freshly prepared 600 μL mixture of myosin + Cy3-ATP in syringe B and then immediately mixed with the actin in syringe A.

Single-turnover experiments with mant-ATP were performed with a sequential stopped flow. For mant-ATP: excitation at 280 nm and detection through a 400 nm long-pass filter.

Pyreneiodoacetimide (PIA) labeled actin was prepared as described in [133]. Pyrene-actomyosin association in the absence of nucleotide, pyrene-actomyosin dissociation in the presence of 50-molar excess of unlabeled actin, and ATP-induced dissociation of actomyosin was performed as described in [88].

Hydrolysis of ATP: We detected free phosphate in solution as described in [134]. 12.5 μM cardiac HMM (25 μM heads) was manually mixed with 20 μM ATP (Sigma-Aldrich), allowed to incubate for 5.0 seconds and quenched with 0.6 M perchloric acid, and detected with malachite green as described in [135]. Experiments were performed at room temperature, 22-23 °C.

Time-resolved fluorescence resonance energy transfer (TR-FRET) and transient TR-FRET, $(TR)^2$FRET: Fit parameters of the two-distance model are given in Table 7 and a detailed description of data fitting is described in Rohde et al. [2].

(TR)^{2}FRET: The TRF and (TR)^{2}F spectrometers, originally described in our previous work [10, 42, 77], transiently digitize the time-resolved fluorescence emission following a 1 ns laser pulse. The laser used in this study is an artisanal 473 nm microchip laser (FP2-473-3-5) with an LD-702 controller hand crafted by *Concepts Research Corporation*, in WI, operating at 5 KHz repetition frequency. Thus samples are excited every 0.2 ms. For equilibrium and steady-state biochemical conditions, 1000 replicate waveforms were signal-averaged prior to analysis. For transient time-resolved measurements acquired after rapid mixing by stopped-flow, 5 waveforms were averaged every 1 ms. Total time-resolved fluorescence was measured with the emission polarizer set to the magic angle (54.7^o) or removed.

(TR)^{2}FRET Data Analysis

Total fluorescence: We determined the total fluorescence emission for FRET samples by integrating the (TR)^{2}FRET waveforms over the nanosecond decay time after subtracting the pre-trigger dark current, ~5% in amplitude compared to the maximum waveform intensity.

TR-FRET: TRF waveforms from donor and FRET-labeled samples were analyzed as described in our previous publications [10, 42, 77] Eq. 25-38, paraphrased below. The measured time-resolved fluorescence waveform, *I*(t) (Eq 25),

$$I(t) = \int_{-\infty}^{\infty} \mathrm{IRF}(t - t') \cdot F(t')dt' \qquad \text{Eq. 25}$$

is a function of the nanosecond decay time, t, and is modeled as the convolution integral of the measured instrument response function, IRF(t), and the fluorescence decay model, *F*(t). The fluorescence decay model (Eq. 26)

$$F(t) = x_{\mathrm{D}} F_{\mathrm{D}}(t) + (1 - x_{\mathrm{D}})\, F_{\mathrm{DA}}(t) \qquad \text{Eq. 26}$$

is a linear combination of a donor-only fluorescence decay function, $F_D(t)$ and an energy transfer-affected donor fluorescence decay, $F_{DA}(t)$. The donor decay $F_D(t)$ is a sum of exponentials (Eq. 27),

$$F_D(t) = \sum_{i=1}^{2} A_i \, exp(-t/\tau_i) \qquad \text{Eq. 27}$$

with discrete lifetime species τ_i and pre-exponential mole fractions A_i. For the Alexa-488 donor two exponentials were required to fit the observed fluorescence. The energy transfer-affected donor decay function, $F_{DA}(t)$ (Eq. 28),

$$F_{DA}(t) = \sum_{j=1}^{2} X_j \cdot T_j(t) \qquad \text{Eq. 28}$$

is a sum over multiple structural states (j) with mole fractions X_j, represented by FRET-affected donor fluorescence decays $T_j(t)$. The increase in the donor decay rate (inverse donor lifetime) due to FRET is given by the Förster equation

$$k_{Ti} = k_{Di}(R/R_{0i})^{-6}, \text{ where} \qquad \text{Eq. 29}$$

$$k_{DAi} = k_{Di} + k_{Ti}, \text{and} \qquad \text{Eq. 30}$$

$$k_{Di} = 1/\tau_i \qquad \text{Eq. 31}$$

We modeled TR-FRET assuming that each structural state j (Eq. 28) corresponds to a Gaussian distribution of interprobe distances, $\rho_j(R)$:

$$T_j(t) = \int_{-\infty}^{\infty} \rho_j(R) \cdot \sum_{i=1}^{3} A_i \, exp\left(\frac{-t}{\tau_i} \cdot \left[1 + \left(\frac{R_{0i}}{R}\right)^6\right]\right) dR \qquad \text{Eq. 32}$$

$$\rho_j(R) = \frac{1}{\sigma_j\sqrt{2\pi}} \exp\left(\frac{-\left[R - R_j\right]^2}{2\sigma_j^2}\right) \qquad \text{Eq. 33}$$

$$\sigma_j = \mathrm{FWHM}_j / \left(2\sqrt{2\ln 2}\right) \quad \text{Eq. 34}$$

As with our previous work [10, 42, 77] , R_{0i} is calculated according to Eq. 35 from the spectral overlap integral, J, the orientation-sensitive term κ^2, the refractive index n, and the donor quantum yield Q_{Di} (Eq. 26-28). $\langle Q_D \rangle$ was measured as 0.91 ± 0.01, by comparison to a quinine sulfate fluorescence standard in 50 mM H_2SO_4 at 25°C according to Eq. 28 (1, 4).

$$R_{0i} = 9780[J(\lambda)\kappa^2 n^{-4} Q_i]1/6 \quad \text{Eq. 35}$$

$$Q_{Di} = \langle Q_D \rangle \cdot \tau_i / \langle \tau \rangle \quad \text{Eq. 36}$$

$$\langle \tau \rangle = \frac{\sum_{i=1}^{3} A_i \tau_i}{\sum_{i=1}^{3} A_i} \quad \text{Eq. 37}$$

$$\langle Q_D \rangle = Q_S \cdot \left(\frac{F_D(\lambda)}{A_D(\lambda)}\right) \Big/ \left(\frac{F_S(\lambda)}{A_S(\lambda)}\right) \quad \text{Eq. 38}$$

Together, the donor fluorescence (A_i, τ_i) and distance terms (R_j, σ_j) in our analysis were shared globally between all waveforms containing FRET-labeled samples. R_j and σ_j were allowed to vary between 0.5 nm and 15.0 nm. The average Alexa-488/CY3 R_0, (6.7 nm in this study) was determined according to Eq. 25-28. The distance-dependent terms R_j (Eq. 23) and σ_j (Eq. 24) define unique structural states of the LCD. The mole fraction terms X_j were allowed to vary independently in each waveform. Thus, changes in X_j reflect changes in the relative populations of the structural states (j) as the biochemical state is varied under equilibrium, steady-state, or transient conditions.

We determined the number of donor lifetimes (i) and structural states (j) that are present in each sample by fitting a set of models with the number of donor lifetime states, i increasing from 1 to 4, and the number of structural states, j, increasing from 1 to 4. For each model we test a distribution of energy transfer rates, with σ_j allowed to vary, as well as discrete energy transfer rates where $\sigma \rightarrow 0$. The final model ($i_{max} = 2$, $j_{max} = 2$, $\sigma > 0$) was determined by evaluating the dependence of the minimized χ^2 on the number of free parameters in the global model and by the resolution of the χ^2 error surface support plane with a confidence intervals of 67%.

Table 7. Steady-state and transient kinetics, mavacamten
HMM and 1% DMSO, S1 and 1% DMSO, HMM and 10 μM Mava, S1 and 10 μM Mava.
Student's T-Test reporting: N.S. for $p > 0.05$, ***** for $p \leq 0.05$, ****** for $p \leq 0.01$, ******* for $p \leq 0.001$. N.C. for not compared.

Experiment, Parameters	**Myosin fragment, ± DMSO or Mava**		**Stat. signif.**
HMM steady-state, actin-activated NADH-coupled ATPase	**HMM, DMSO**	**HMM, Mava**	
k_{cat} (s^{-1}), *n=6, Error of 3 fit hyperbolas.*	2.02 ± 0.12	0.48 ± 0.04	***
$K_{0.5,Actin}$ (μM)	17.6 ± 2.8	35.3 ± 6.3	*
Mavacamten EC_{50} (μM), *n=4*	N/A	0.23 ± 0.02	N.C.
S1 steady-state, actin-activated NADH-coupled ATPase	**S1, DMSO**	**S1, Mava**	
k_{cat} (s^{-1}), *n=6, Error of 3 fit hyperbolas.*	3.64 ± 0.41	1.35 ± 0.08	***
$K_{0.5,Actin}$ (μM)	24.4 ± 7.4	20.6 ± 3.1	N.S.
Mavacamten EC_{50} (μM)	N/A	0.41 ± 0.02	N.C.
HMM steady-state, basal NADH-coupled ATPase	**HMM, DMSO**	**HMM, Mava**	
Activity (s^{-1}), *Repli.: n=3, Error: ± SEM.*	0.016 ± 0.005	0.003 ± 0.001	*
S1 steady-state, basal NADH-coupled ATPase	**S1, DMSO**	**S1, Mava**	
Activity (s^{-1}) , *Repli.: n=3, Error: ± SEM.*	0.028 ± 0.007	0.006 ± 0.002	**
HMM steady-state pyrene-actin quenching	**Acto-HMM**	**Acto-S1**	
Normalized fluorescence (A.U.), *n=4, Error: ± SEM.*	0.29 ± 0.03	0.34 ± 0.02	N.S.
S1 steady-state pyrene-actin quenching	**ActoHMM+ATP**	**ActoS1 + ATP**	
Normalized fluorescence (A.U.), *n=4, Error: ± SEM.*	0.89 ± 0.02	0.95 ± 0.01	*
HMM actin-activated single-turnover of mant-ATP	**HMM, DMSO**	**HMM, Mava**	
k_{fast} (s^{-1}), *n=6, Error of 3 hyperbolic fits.*	3.80 ± 0.33	0.30 ± 0.03	***
$K_{0.5,Actin}$ (μM)	5.3 ± 1.7	2.3 ± 0.5	N.S.
k_{slow} (s^{-1})	0.55 ± 0.03	0.037 ± 0.007	***
$K_{0.5,Actin}$ (μM)	5.4 ± 1.1	4.7 ± 1.5	N.S.
A_{fast}, fraction (A.U.)	0.77 ± 0.03	0.48 ± 0.04	**
Mavacamten EC_{50} (μM)	N/A	0.36 ± 0.08	N.C.
S1 actin-activated single-turnover of mant-ATP	**S1, DMSO**	**S1, Mava**	
k_{fast} (s^{-1}), *n=6, Error of 3 hyperbolic fit.*	5.97 ± 0.80	0.80 ± 0.11	**
$K_{0.5,Actin}$ (μM)	16.1 ± 5.0	12.6 ± 4.2	N.S.
k_{slow} (s^{-1})	0.28 ± 0.04	0.089 ± 0.002	**
$K_{0.5,Actin}$ (μM)	2.7 ± 0.9	1.3 ± 0.3	N.S
A_{fast}, fraction (A.U.)	0.87 ± 0.02	0.83 ± 0.01	N.S

HMM basal single-turnover of mant-ATP	**HMM, DMSO**	**HMM, Mava**	
k_{fast} (s^{-1}), *n=9, Error: ± SEM.*	0.021 ± 0.003	0.0076 ± 0.0012	***
k_{slow} (s^{-1})	0.0053 ± 0.0010	0.0008 ± 0.0002	***
A_{slow}, fraction (A.U.)	0.55 ± 0.04	0.88 ± 0.01	***
S1 basal single-turnover of mant-ATP	**S1, DMSO**	**S1, Mava**	
k_{fast} (s^{-1}), *n=9, Error: ± SEM.*	0.032 ± 0.002	0.0038 ± 0.0012	***
k_{slow} (s^{-1})	0.0075 ± 0.0010	0.0013 ± 0.0003	***
A_{slow}, fraction (A.U.)	0.17 ± 0.04	0.32 ± 0.03	**
HMM basal single-turnover of ATP, chased with mant-ATP	**HMM, DMSO**	**S1, DMSO**	
k_{fast} (s^{-1}), *n=6, Error: ± SEM.*	0.028 ± 0.005	0.025 ± 0.002	N.S.
k_{slow} (s^{-1})	0.0039 ± 0.0011	0.0045 ± 0.0006	N.S.
A_{slow}, fraction (A.U.)	0.81 ± 0.02	0.27 ± 0.03	***
AF488-RLC-HMM basal single-turnover of mant-ATP	***HMM***	**AF488-HMM**	
k_{fast} (s^{-1}), *n=9 for HMM, n=4 for AF488-HMM, Error: ± SEM.*	*0.021 ± 0.003*	0.011 ± 0.002	N.S.
k_{slow} (s^{-1})	*0.0053 ± 0.0010*	0.0037 ± 0.0007	N.S.
A_{slow}, fraction (A.U.)	*0.55 ± 0.04*	0.47 ± 0.03	N.S.
HMM basal mant-ADP release	**HMM, DMSO**	**HMM, Mava**	
k_{fast} (s^{-1}), *n=9, Error: ± SEM.*	0.45 ± 0.01	0.16 ± 0.01	***
k_{slow} (s^{-1})	0.12 ± 0.01	0.025 ± 0.003	***
$Amplitude_{slow}$, fraction (A.U.)	0.37 ± 0.02	0.62 ± 0.02	***
S1 basal mant-ADP release	**S1, DMSO**	**S1, Mava**	
k_{fast} (s^{-1}), *n=9, Error: ± SEM.*	0.41 ± 0.02	0.20 ± 0.01	***
k_{slow} (s^{-1})	0.08 ± 0.01	0.04 ± 0.01	*
$Amplitude_{slow}$, fraction (A.U.)	0.30 ± 0.03	0.28 ± 0.01	N.S.
Basal mant-ATP turnover, temperature dependence **Erying equation:** $\mathbf{k = T \cdot e^{\left(\frac{-\Delta H^{\ddagger}}{RT} + b\right)}, R = 8.314(10^{-3}) kJ \cdot K^{-1} \cdot mol^{-1}}$	**HMM**	**S1**	
Fast phase: $\Delta H^{\ddagger}$ (kJ/mol), *n=4, Error of fit.*	35.3 ± 1.5	30.9 ± 3.3	N.S.
Fast phase: b, constants and $\Delta S^{\ddagger}$ (dimensionless)	5.3 ± 0.6	3.6 ± 1.4	N.S.
Slow phase: $\Delta H^{\ddagger}$ (kJ/mol)	15.9 ± 1.3	15.1 ± 8.9	N.S.
Slow phase: b, constants and $\Delta S^{\ddagger}$ (dimensionless)	-4.3 ± 0.5	-3.9 ± 3.7	N.S.
$Amplitude_{slow}$, fraction at 35 °C (A.U.) , *n=4, Error: ± SEM.*	0.51 ± 0.03	0.07 ± 0.03	***
Basal mant-ATP turnover, KCl dependence	**HMM**	**S1**	

Average k_{fast} (s^{-1}), *n=4, Error: ± SEM.*	0.022 ± 0.001	0.031 ± 0.002	**
Average k_{slow} (s^{-1})	0.0062 ± 0.0004	0.0069 ± 0.0013	N.S.
$Amplitude_{slow}$, fraction at 100 mM KCl (A.U.), *Error of fit.*	0.23 ± 0.10	0.24 ± 0.09	N.S.
Basal mant-ATP turnover, 100 mM KCl and 10 μM Mava	**HMM**	**S1**	
k_{fast} (s^{-1}), *n=4, Error: ± SEM.*	0.0037 ± 0.0008	0.0049 ± 0.0005	N.S.
k_{slow} (s^{-1})	0.0009 ± 0.0001	0.0011 ± 0.0002	N.S.
A_{slow}, fraction (A.U.)	0.59 ± 0.03	0.46 ± 0.02	*
Powerstroke, $(TR)^2$FRET, fluorescently-labeled RLC	**HMM, DMSO**	**HMM, Mava**	
Actin-induced lever arm rotation (s^{-1}), *n=6, Error of 3 fits.*	11.49 ± 0.81	4.87 ± 0.17	**
Actin-induced rotation, $K_{0.5,Actin}$ (μM)	4.20 ± 0.89	0.6 ± 0.2	*
Slow phase, lever arm rotation (s^{-1})	1.33 ± 0.24	0.43 ± 0.08	*
Slow phase, $K_{0.5,Actin}$ (μM)	3.42 ± 2.05	1.0 ± 1.3	N.S.
Maximum fit Amplitude, fast phase (normalized)	0.59 ± 0.04	0.23 ± 0.03	**
Maximum fit Amplitude, $K_{0.5,Actin}$ (μM)	5.1 ± 0.8	1.6 ± 1.0	N.S.
Distance Distribution, $(TR)^2$FRET	**HMM, DMSO**	**HMM, Mava**	
M** (Distance 1), *n=28, Error is avg. surface plane error.*	6.54 ± 0.55	Globally-fit	
FWHM 1 (nm)	1.87 ± 0.62	"	
M* (Distance 2) (nm)	10.53 ± 1.15	"	
FWHM 2 (nm)	2.20 ± 0.82	"	
Donor-only fluorescence, AF488, $(TR)^2$FRET	**HMM, DMSO**	**HMM, Mava**	
τ_1 (ns), *n=12, Error is avg. surface plane error.*	3.791 ± 0.008	Globally-fit	
A_1 (A.U.)	0.645 ± 0.029	"	
τ_2 (ns)	0.493 ± 0.011	"	
Pyrene-A.M diss. (50x unlabeled-actin chase)	**HMM, DMSO**	**HMM, Mava**	
k_1 (s^{-1}), *n=6, Error: ± SEM.*	0.052 ± 0.004	0.052 ± 0.006	N.S.
A_1, fraction (A.U.)	0.23 ± 0.01	0.24 ± 0.01	N.S.
k_2 (s^{-1})	0.0071 ± 0.0001	0.0075 ± 0.0001	*
Mant-ATP binding Myosin	**HMM, DMSO**	**HMM, Mava**	
k_1 (s^{-1}), *n=3, Error: ± SEM.*	24.3 ± 0.8	29.0 ± 1.0	*
A_1, fraction (A.U.)	0.69 ± 0.01	0.77 ± 0.02	*
k_2 (s^{-1})	1.42 ± 0.6	1.75 ± 0.9	N.S.
Mant-ATP binding Actomyosin	**HMM, DMSO**	**HMM, Mava**	
k_1 (s^{-1}), *n=6, Error: ± SEM.*	309 ± 110	143 ± 22	N.S.

A_1, fraction	0.27 ± 0.01	0.28 ± 0.02	N.S.
k_2 (s^{-1})	25.6 ± 0.9	20.9 ± 0.7	**
A_2, fraction	0.63 ± 0.02	0.61 ± 0.01	N.S.
k_3 (s^{-1})	6.4 ± 2.4	1.8 ± 0.3	N.S.
Mant-ADP release from actoHMM, chased with ATP	**HMM, DMSO**	**HMM, Mava**	
k_1 (s^{-1}), *n=6, Error:* ± *SEM.*	66.8 ± 0.8	64.5 ± 2.3	N.S.
A_1, fraction	0.93 ± 0.01	0.92 ± 0.01	N.S.
k_2 (s^{-1})	2.4 ± 0.4	2.4 ± 0.3	N.S.
Recovery stroke, $(TR)^2$FRET	**HMM, DMSO**	**HMM, Mava**	
Fast phase, ATP-induced lever arm rotation, k_{cat} (s^{-1})	58.5 ± 11.7	42.1 ± 4.7	N.S.
ATP-induced lever arm rotation $K_{0.5}$ [Cy3ATP] (μM)	10.4 ± 3.2	8.3 ± 1.5	N.S.
Slow phase, k_{cat} (s^{-1})	1.97 ± 0.38	1.24 ± 0.20	N.S.
Slow phase $K_{0.5}$ [Cy3ATP] (μM)	1.56 ± 0.93	1.29 ± 0.70	N.S.
Mavacamten EC_{50} (μM)	N/A	27.5 ± 4.7	N.C.
Steady state hydrolysis	**HMM, DMSO**	**HMM, Mava**	
[P_i] / [ATP] (no units), *n=6, Error:* ± *SEM.*	0.62 ± 0.03	0.55 ± 0.01	N.S.

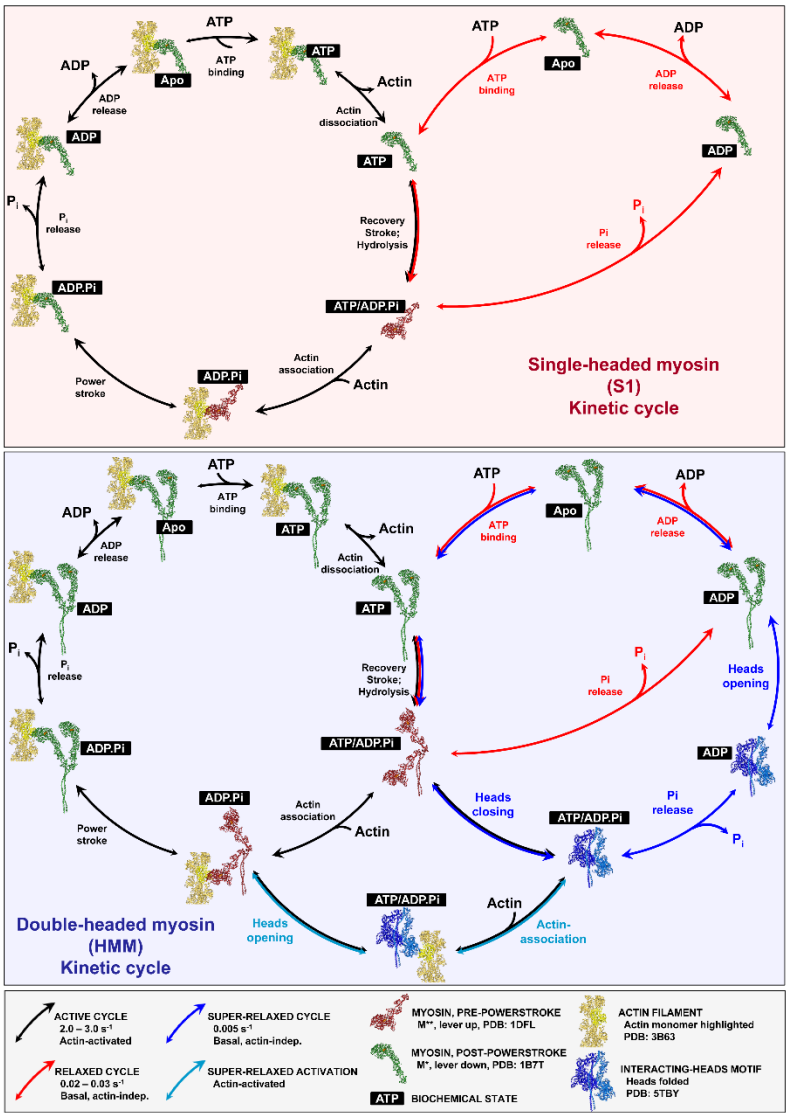

Fig. 40. Summary of predominant kinetic steps navigated by cardiac myosin in the presence of excess ATP

(**Top**) Kinetic steps navigated by a single S1 head during actin-independent (red arrows) or actin-activated (black arrows) ATPase cycling. (**Bottom**) Kinetic steps navigated by an individual HMM head of the HMM dimer during actin-independent (red arrows), actin-activated (black arrows) ATPase cycling. Steps associated with auto-inhibition in the absence or actin (blue arrows). Activation of auto-inhibited HMM by actin indicated by light blue arrows. Myosin's dominant thermodynamic states indicated as defined in the figure legend. For HMM, the scheme denotes the activity of a single head. The second head's thermodynamic state is not considered in the model. The mavacamten sensitive steps include structural transitions associated with lever-arm movement and phosphate release after ATP hydrolysis, structural changes in the nucleotide-binding pocket associated with ADP release in the absence of actin, and isomerization to an auto-inhibited structural state hypothesized to result from the interacting heads motif (open-to-closed transition).

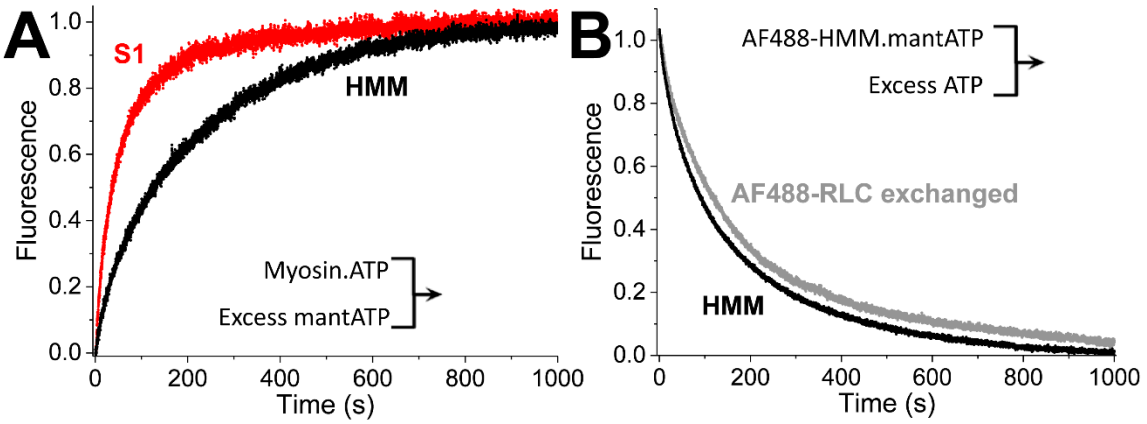

Fig. 41. Basal ATP turnover controls: Myosin.ATP mixed with mant-ATP; basal turnover with exchanged light chain

(**A**) To ensure the mant-nucleotide was not inducing non-physiological phenomenon in the basal mant-turnover experiments, we performed the inverse mix: incubating 0.4 μM S1 or 0.2 μM HMM with 4.0 μM ATP and then mixed with 400 μM mant-ATP. HMM remains biphasic, unlike S1. (**B**) Fluorescently-labeled and exchanged-on RLC, used in $(TR)^2$FRET experiments, did not disrupt the SRX-like basal ATP turnover of HMM. The same bi-phasic behavior was observed. Fits reported in Table 7.

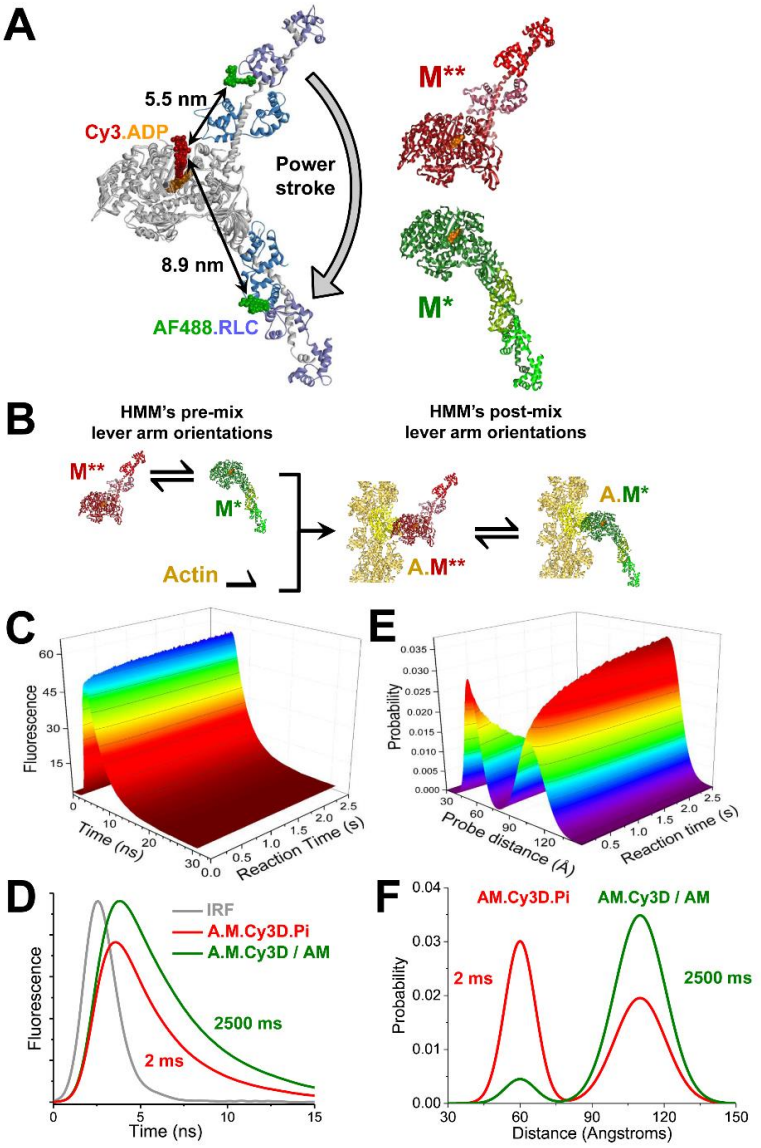

Fig. 42. Light-chain domain rotation data acquisition and analysis with (TR)^{2}FRET
(**A**) Fluorescently-labeled HMM, dyes modeled on perpendicular to the protein surface, PDB: 1B7T, 1DFL. Donor fluorophore is AlexaFluor488-RLC and acceptor fluorophore is Cy3-ATP. Distances represent dye center-dye center. Powerstroke occurs from the lever-up pre-powerstroke state (red myosin S1 cartoon, lever up) to the lever-down post-powerstroke state (green myosin S1 cartoon, lever down). S1 depicted for simplicity, HMM used. (**B**) Stopped-flow mix of myosin with actin, to detect FRET between the lever arm and catalytic domain of cardiac HMM. Equilibrium of structural states of myosin with fluorescently-labeled and exchanged-on RLC with excess fluorescent Cy3-ATP, mixed with actin, detecting the depletion of the lever-up M** structural state (red). (**C**) 2000 time-resolved FRET waveforms were acquired with 125 picosecond resolution. Each waveform results from after excitation with a 5000 Hz pulsed laser, acquired following stopped-flow mixing of 0.1 μM AF488-labeled cardiac HMM equilibrated with 2.0 μM Cy3-ATP, mixed with 20 mM Actin containing 1.0 mM ATP, depicting a total integrated fluorescence intensity change of 27% for the DMSO control shown. (**D**) The first and last time-resolved fluorescent waveforms shown in C. Laser pulse (IRF) is shown in gray. (**E**) Global two-distance fit to each acquired waveforms in C, depicting a mole fraction change of 0.49 for DMSO. Every waveform detected in C was fit to this two-distance model (SI Methods). (**F**) First and last two-distance fit shown in E.

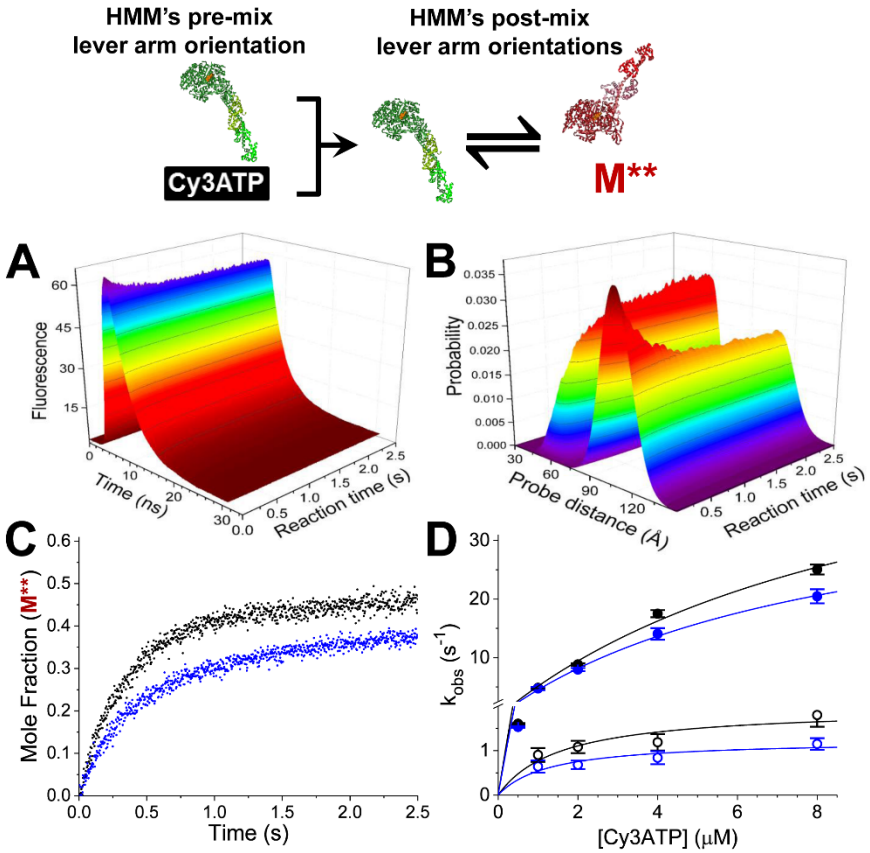

Fig. 43. Recovery stroke detected with (TR)^{2}FRET.
(**A**) Transient time-resolved FRET waveforms acquired after mixing 0.1 μM AF488 labeled cardiac HMM with 2.0 μM Cy3-ATP, depicting a total integrated fluorescence intensity change of 25% for DMSO. Reaction mixed represented above; S1 shown for simplicity. (**B**) Global two-distance structural state model was fit to each acquired waveforms in A, depicting a mole fraction change of 0.46. (**C**) Plotted mole fraction of the M**, lever-up, post-recovery stroke structural state at 2.0 μM Cy3ATP in the absence (black) or presence (blue) of 10 μM Myk461. While our fluorescent labeling scheme is likely detecting inter-head FRET, our analysis of the power stroke and recovery stroke has focused on the rate of fluorescence change and not the structural resolution of these measurements. The distance distributions of our two-distance fits were unchanged in the presence or absence of mavacamten, and the mole fraction of myosin molecules in a pre- and post-powerstroke state were consistent in the presence and absence of mavacamten as well. These observations suggest inter-head FRET is a small contribution to the FRET changes we observe because mavacamten had no detectable effect on the fluorescence lifetimes associated with the various biochemical states in these stopped-flow experiments. (**D**) Observed rate constant for the recovery stroke over a range of nucleotide concentrations. $k_{obs1,DMSO}$ = 58.5s^{-1}[ATP]/(10.4μM+[ATP]), $k_{obs1,Myk461}$ = 42.1s^{-1}[ATP]/ (8.3μM+[ATP]), $k_{obs2,DMSO}$ = 1.9s^{-1}[ATP]/(1.6μM+[ATP]), $k_{obs2,Myk461}$ = 1.2s^{-1}[ATP]/(1.3μM+[ATP]).

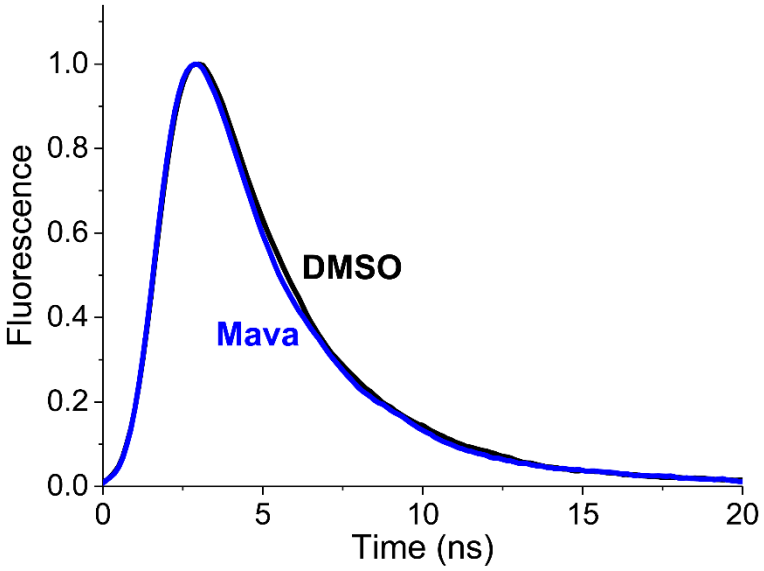

Fig. 44. Mavacamten does not change TR-FRET between AF488 labeled cardiac HMM with 2.0 μM Cy3-ATP

TR-FRET measured as described in **Fig. 43** in the absence of actin and presence of 30 μM mavacamten. The difference between the average lifetimes of the depicted waveforms is 80 picoseconds +/- 10 picoseconds.

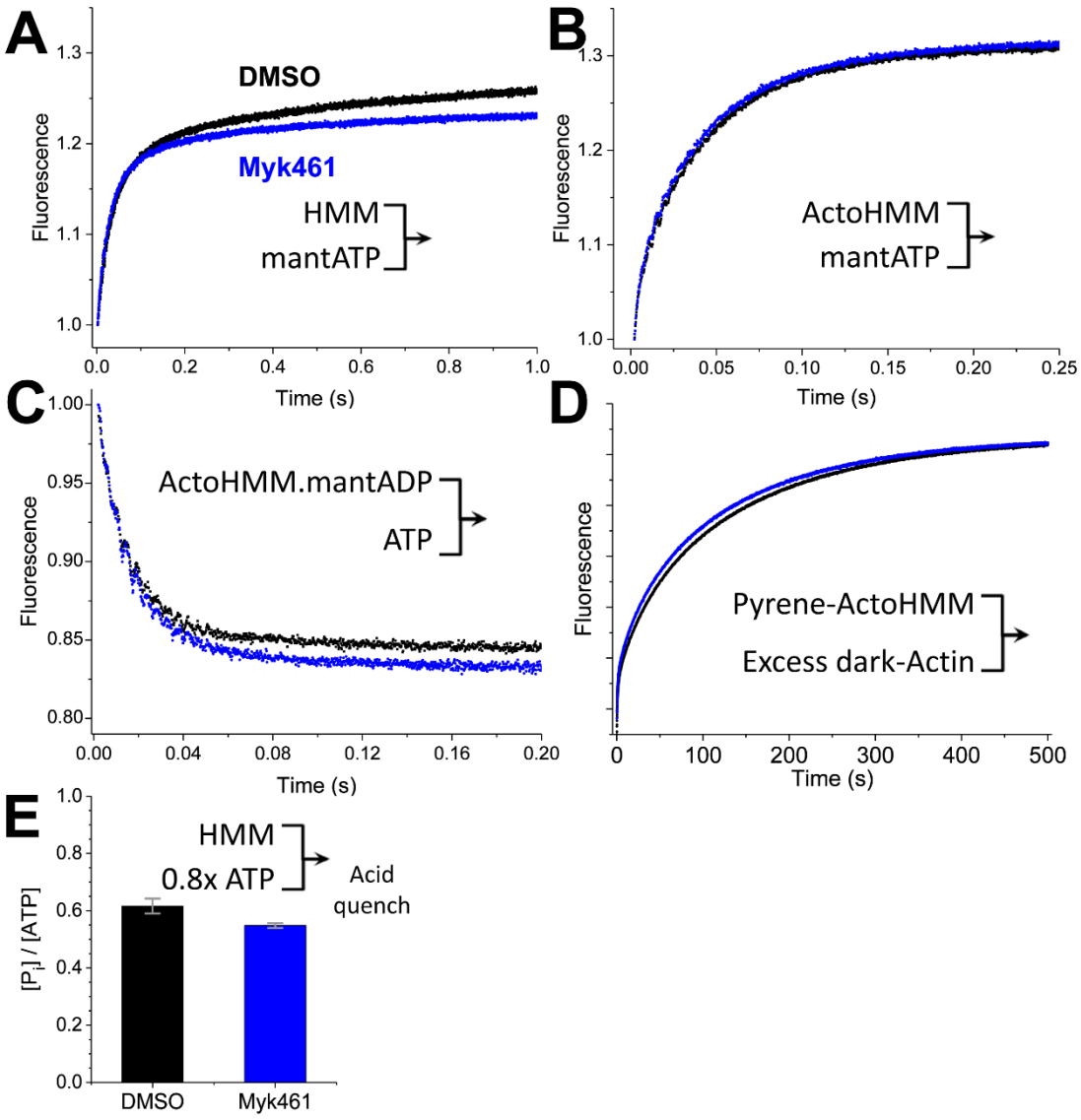

Fig. 45. Mavacamten does not change the kinetics of several steps in the myosin ATPase cycle

(**A**) Mant-ATP binding to HMM. 2.0 μM mant-ATP binding to 0.1 μM HMM in the presence of 1% DMSO (black) or 5.0 μM Myk461 dissolved in DMSO (blue). (**B**) Mant-ATP binding actoHMM. 2.0 μM mant-ATP binding pre-incubated 5.0 μM actin and 0.1 μM HMM. Observed rate constants given in Table 7. Individual, representative mixes with transients from the average of 6-10 shots of the stopped flow. Two exponential fit and error bars shown in Table 7 from n = 6 mixes, ± SEM. (**C**) ADP dissociation detected with 5.0 μM actin, 0.1 μM HMM and 2.0 μM mant-ADP chased with 2.0 mM non-fluorescent ATP. Black is DMSO control, blue is 5.0 μM Myk461. Observed rate constants reported in Table 7, ± SEM from n = 6 mixes. (**D**) Actomyosin dissociation detected with incubation of 1.5 μM pyrene-actin and 0.4 μM HMM mixed with 20 μM unlabeled-actin. Black trace is DMSO, blue is 5.0 μM Myk461. Observed rate constants reported in Table 7 ± SEM from n =6. (**E**) Hydrolysis detected with malachite green following acid quench with perchloric acid. 12.5 μM two-headed HMM was mixed with 20 μM ATP (5:4 stoichiometry) and incubated for 5.0 s, then quenched with 0.6 M perchloric acid and detected with malachite green. The concentration of P_i was determined with a standard curve.

CHAPTER 5: CONVERTER DOMAIN MUTATIONS IN MYOSIN ALTER THE STRUCTURAL KINETICS AND MOTOR FUNCTION

This chapter has been adapted from the following publication:

Title: Converter domain mutations in myosin alter structural kinetics and motor function

Authors: Laura K. Gunther*, John A. Rohde*, Wanjian Tang*, Shane D. Walton, William C. Unrath, Darshan V. Trivedi, Joseph M. Muretta, David D. Thomas and Christopher M. Yengo (* co-first authors)

Journal: The Journal of Biological Chemistry. 294, 1554-1567.

Online: December 5, 2018; ***Published:*** February 1, 2019

doi: 10.1074/jbc.RA118.006128

Permission: *for all authors of published work in JBC, the journal permits "Appending a reprinted article to a Ph.D. dissertation."[136]*

5.1 CHAPTER OVERVIEW

In a collaboration between the David D. Thomas lab at the University of Minnesota and the Chris M. Yengo lab at Penn State, this study focused on two mutations found in the converter domain of human MYH7 (β-cardiac myosin, "M2β") that have been linked to opposing phenotypes. R723G and F764L are both located in the converter domain (Fig. 47B) of human cardiac myosin, but while R723G causes hypertrophic cardiomyopathy (HCM), F764L causes dilated cardiomyopathy (DCM) [39, 40]. Since the converter domain is proposed to communicate structural changes between the lever arm and motor

domain during the catalytic cycle, we proposed that mutations in this region will differentially alter the movement of the lever arm. Using an extremely high resolution FRET system developed by our lab, we have examined the dynamics of the lever arm during the ATPase cycle in WT myosin V, as well as for the converter domain mutants R712G and F750L that are analogous to the HCM/DCM mutations in M2β. This study highlights a powerful approach of directly examining the impact of mutations on key structural changes to determine how structural impairments disrupt motor function. Specifically, this study presents direct evidence that mutations in the converter domain can differentially alter lever arm rotation which ultimately leads to the impaired ability to adapt to external load.

5.2 INTRODUCTION

Myosins are molecular motors that generate force by utilizing a highly conserved ATPase cycle [137]. Myosin motors perform diverse cellular functions including cytokinesis, cell adhesion, organelle transport, cell polarization, and muscle contraction [138, 139]. The structure of the myosin molecule is broadly divided into head, neck, and tail regions. The head contains the catalytic domain, which is conserved across the myosin superfamily and is responsible for ATP hydrolysis and actin binding. Depending on the myosin isoform, the neck contains a variable number of IQ motifs that serve as binding sites for light chains (e.g. calmodulin) and is also referred to as the lever arm domain. Force is generated as a result of the lever arm swinging at key points in the ATPase cycle, and it is the converter domain that communicates structural changes between the lever arm and the catalytic domain. Recently, the converter domain has been highlighted as a hot spot for point

mutations in cardiac myosin associated with inherited cardiomyopathies, indicating the importance of this region in mediating mechano-chemical coupling in all myosin motors [22].

Hypertrophic cardiomyopathy (HCM) is an extremely prevalent inherited heart disease, affecting approximately 1 in 200 individuals [23]. HCM is also the most common cause of sudden cardiac death in young people [24]. Clinically, HCM is characterized by left ventricular hypertrophy, myocyte disarray, fibrosis, and diastolic dysfunction [25-27]. Furthermore, the characteristic left ventricular hypertrophy is associated with increased contractility. Dilated cardiomyopathy (DCM) affects approximately 1 in 2500 individuals, and is the most common cause of heart failure in young adults [28]. In contrast to HCM, DCM is characterized by left ventricular dilation, myocyte death, fibrosis, and systolic dysfunction [26, 29]. However, it still remains unclear how these disease mutations impact key structural changes in the myosin ATPase cycle and how specific structure-function defects lead to disease phenotypes.

The atomic structure of the myosin motor domain from both muscle and non-muscle myosin and various species from *Dictyostelium* to humans has revealed a conserved structural fold [30]. The myosin motor consists of four structural domains each connected by flexible linkers, an N-terminal 25 kDa domain, an upper and lower 50 kDa domain, and a 20 kDa C-terminal domain (Fig. 47A) [31]. Allosteric coupling between these domains allows for coordination of ATP binding and hydrolysis in the active site with structural changes in the actin binding region associated with actin binding/dissociation. In addition, the priming of the lever arm for force generation (recovery stroke) and the force generating structural changes in the lever arm (power stroke) are coordinated by amplifying small

structural changes in the active site with large conformational changes in the converter/lever arm [32] (Fig. 47A&B). Specific allosteric pathways in the myosin motor have been proposed based on high resolution structural studies of myosin in different nucleotide states [33] and mutational structure-function studies [34]. However, many of these hypothesized pathways have not been examined with techniques that can directly examine conformational changes in real-time and examine the impact of specific point mutations on myosin mechanochemistry. Myosin V is an exemplary model for examining key structural changes and defining important allosteric pathways because there is high resolution structural information of many of the structural states in the myosin ATPase pathway [35]. Additionally, many biochemical and biophysical studies have revealed important details about the mechanochemical cycle [36-38]. Thus, introducing mutations in crucial amino acid residues and examining how structural changes are altered in real time will allow for a complete understanding of how point mutations can disrupt key allosteric pathways and specifically impair motor function.

Interestingly, mutations in the converter domain of MYH7 (β-cardiac myosin, "M2β") have been linked to opposing phenotypes. Specifically, R723G and F764L are both located in the converter domain (Fig. 47B) of human cardiac myosin, R723G causes HCM while F764L causes DCM [39, 40]. Since the converter domain is proposed to communicate structural changes between the lever arm and motor domain during the catalytic cycle, we proposed that mutations in this region will differentially alter the movement of the lever arm. In addition, communication between the converter domain and the active site is thought to be a mechanism for mediating the sensitivity of the myosin ATPase cycle to external load. Using an extremely high resolution FRET system developed

by our lab, we have examined the dynamics of the lever arm during the ATPase cycle in WT myosin V, as well as for the converter domain mutants R712G and F750L that are analogous to the HCM/DCM mutations in M2β. Although, the mutations will not likely have same impact on M2β as they do in myosin V, this study highlights a powerful approach of directly examining the impact of mutations on key structural changes to allow for determining how structural impairments disrupt motor function. Specifically, this study presents direct evidence that mutations in the converter domain can differentially alter lever arm rotation which ultimately leads to the impaired ability to adapt to external load. Our work also highlights important allosteric pathways in myosin that allow for communication between the active site and force generating lever arm.

5.3 RESULTS

Expression and purification of myosin V constructs. We examined the motor function, biochemical, and structural properties of myosin V 1IQ containing the N-terminal tetracysteine motif (MV) expressed in the baculovirus system as described [140-143]. To examine the impact of the mutations on the steady-state kinetic, transient kinetic, and motile properties we co-expressed MV with wild type calmodulin. For the studies in which we examined the lever arm swing during the recovery and power stroke by FRET we exchanged QSY-labeled calmodulin (T110C) during the purification procedure and labeled the N-terminal tetracysteine site with FlAsH (MV NTF:QSY-CaM) [142]. A non-calmodulin exchanged MV was labeled with FlAsH and served as a donor only control. Each of the protein preparations had similar yields/purity and fluorescence labeling efficiencies as previously reported [142].

Impact of the mutations on steady-state motor properties. We first examined the impact of the R712G and F750L mutations on myosin motor properties. The actin-activated ATPase assay was examined in 3-4 protein preparations and revealed that the mutations only had a minor impact on the steady-state ATPase kinetics. The ATPase activity was plotted as function of actin concentration and fit to a Michaelis-Menten equation (Fig. 55, Table 8). The K_{ATPase}, actin concentration at which ATPase is one-half maximal, was unchanged in both mutants compared to WT. The maximum rate of ATPase (k_{cat}) was slightly increased (10%) in the F750L mutant but unchanged in the R712G mutant.

We examined the in vitro motility assay under unloaded conditions in six different protein preparations. The average velocity of 2-3 videos and more than 30 filaments from each video was determined and the overall average and standard deviation of all of the preparations was found to be similar in WT, R712G, and F750L (395±19, 401±17, 399±11 nm/sec, respectively) .

In two protein preparations we examined loaded in vitro motility by determining the sliding velocity in the presence of increasing amounts of a tethering load (Fig. 48). The tethering load was produced by a MV mutant (G440A) that can bind actin with a high affinity even in the presence of saturating ATP [144]. The advantage of using a mutant myosin as a tether is that its size and therefore interaction with the actin filament on the motility surface is identical to that of the active myosin. We found that the velocity and number of stuck filaments for both R712G and F750L was more sensitive to the presence of tethering loads. The average velocity, percent stuck filaments, and average velocity of moving filaments was plotted as a function of the fraction of G440A MV present

([G440A]/[Total MV]) (Fig. 48A-C). In the presence of 20% or more G440A MV the average sliding velocity was reduced approximately two fold more than WT in both mutants (WT = 226±20, R712G=98±37, F750L=143±12 nm/s) (Fig. 48A). A similar trend was observed by examining the percent stuck filaments (Fig. 48B). We also examined the velocity of only the moving filaments by eliminating the stuck filaments from the analysis and found that there was little difference in the velocity as a function of load in all 3 constructs (Fig. 48C).

Transient kinetic analysis. We performed transient kinetic analysis of key steps in the MV ATPase cycle using established methods [144-147]. The conserved actomyosin ATPase pathway (Fig. 46) was used to model the transient kinetic studies with the actin bound equilibrium constants represented by a prime and the dominant pathway outlined within the box. The transient and steady-state kinetic results are summarized in Table 8.

The rate of ATP binding and maximum rate of ATP hydrolysis in the absence of actin was monitored by examining the increase in tryptophan fluorescence (1 μM MV) at varying ATP concentrations (Fig. 49). The fluorescence transients were fit to a single exponential function and the rate constants were hyperbolically dependent on ATP concentration (Fig. 49A). At concentrations less than 50 μM ATP the rate constants were linearly dependent on ATP concentration and allowed us to determine the second-order binding constant for ATP binding, which was unchanged in both mutants compared to WT. However, the maximum rates of the tryptophan fluorescence transients were 20% faster in the F750L mutant and 40% slower in the R712G mutant (Fig. 49B), indicating a change in the apparent rate constant for ATP hydrolysis.

We also examined the rate of ATP-induced dissociation of actomyosin using pyrene labeled actin (0.25 μM MV: 0.25 μM pyrene actin) (Fig. 49C). We found that the rate of pyrene fluorescence increase as a function of ATP concentration was best fit to a two exponential function. The slow phase was approximately 10% of the fluorescence signal and independent of ATP concentration ($k_{obs} \sim 20s^{-1}$). The fast phase of the fluorescence transient was hyperbolically dependent on ATP concentration and allowed us to determine the equilibrium constant for the initial rapid-equilibrium interaction between ATP and actomyosin (K_{1T}) and the maximum rate of transition into the weak binding states (k_{+2T}). We found there was little difference in K_{1T} and k_{+2T} for the 3 constructs.

The rate constants for actin-activated phosphate release were measured by mixing MV (0.5 μM) with substoichiometric ATP (0.45 μM) and then mixing with varying actin concentrations in the presence of phosphate binding protein (5 μM, MDCC-PBP) (Fig. 50A&B). The fluorescence transients were best fit by a single exponential function (phosphate burst) followed by a linear or slow exponential phase (Fig. 50A). The phosphate burst rate constant was hyperbolically dependent on actin concentration for WT and R712G, while F750L displayed a linear dependence on actin concentration (Fig. 50B). The actin concentration required to reach one-half maximal phosphate release was increased more than 2-fold by the F750L mutant but unchanged by the R712G mutant. The maximum rate of phosphate release was increased more than 40% in the R712G mutant, and while it was not determined in the F750L mutant the rate constants measured at 30 μM actin were similar to WT.

The rate constants for ADP release from acto-MV were determined by mixing a complex of MV, *mant*ADP, and actin (0.25 μM, 5 μM, 0.5 μM, respectively) with excess

ATP (1 mM) (Fig. 50C&D). The *mant* fluorescence decrease for most transients followed a single exponential function with some transients displaying a slow fluorescence decrease that was less than 10% of the signal (Fig. 50C). There was an increase (23%) in the *mant*ADP release rate constant in the F750L mutant while the R712G was similar to WT. We also measured the *mant*ADP release rate constant as a function of temperature and observed that the F750L mutant maintained a faster *mant*ADP release rate constant at all temperatures, while the Eyring plots yielded a similar energy of activation for all three constructs ($\Delta H \sim 80\text{-}82$ kJ·mol^{-1}) (Fig. 50D).

Structural kinetics of lever arm swing. In our previous work we established a method of measuring the movement of the lever arm during the recovery and power stroke steps using FRET between FlAsH labeled at the N-terminus and the non-fluorescent acceptor QSY-labeled at T110C on calmodulin of the first IQ motif [142]. In the current work we performed similar measurements in the R712G and F750L mutant and compared these results to repeated measurements of WT MV.

The rate constants for the movement of the lever arm during the recovery stroke were monitored by mixing MV NTF:QSY-CaM (0.25 μM) with varying concentrations of ATP (data represents 3-4 protein preparations) (Fig. 51). The fluorescence transients were best fit by a one or two exponential function (Fig. 51A). The fast phase of the fluorescence transient was hyperbolically dependent on ATP concentration (Fig. 51B) while the slow phase (5% or less of the fluorescence signal) was also hyperbolically dependent on ATP concentration (Fig. 51C). We found that compared to WT, the R712G mutant reduced the maximum rate constant of the fast recovery stroke (25%) while the F750L had a 2-fold

increase in the maximum rate constant of the recovery stroke. The slow phase of the recovery stroke was unchanged in the two mutants compared to WT.

The lever arm swing during the power stroke was measured with a sequential mix stopped-flow experiment (Fig. 52) (similar conditions to the phosphate release experiments in Fig. 50A&B). We first mixed MV NTF:QSY-CaM (0.25 μM) with sub-stoichiometric ATP (0.2 μM) and allowed the reaction to age (10s) and then mixed with varying concentrations of actin. The resulting fluorescence transients were best fit by a three exponential function (Fig. 52A). The fluorescence decrease contained a fast phase (k_{+PWF}, fast power stroke) and slow phase (k_{+PWS} slow power stroke) that were both dependent on actin concentration. The relative amplitudes of the fast/slow phase were similar in the WT and two mutants (fast phase 85-90% of the fluorescence transients at 40 μM actin). We also observed a very slow fluorescence increase in many of the fluorescence transients that was similar at all actin concentrations (k_{obs}~0.1-0.3 s^{-1}). The actin-dependence of the fast power stroke was similar in both mutants and WT (Fig. 52B). Also, the maximum rate of the slow power stroke in both mutants was found to be not significantly different from WT MV (Fig. 52C).

Structural dynamics of the lever arm. In order to examine the impact of the converter mutations on the distribution of structural states of the lever arm in each nucleotide state, we performed transient time-resolved FRET [$(TR)^2$FRET] (Fig. 53, Fig. 56, Table **9**, Table 10). In addition, $(TR)^2$FRET allows interpretation of the fast and slow phase amplitudes observed in the total fluorescence studies. This approach utilizes nanosecond resolved time-resolved fluorescence of the donor probe (TR-FRET) to follow changes in the structural state of the donor+acceptor labeled protein acquiring individual

time-resolved fluorescence waveforms every 0.1 millisecond follow rapid mixing by stopped flow. A detailed description of the acquired data and instrumentation is described in previous work [1, 77]. We analyzed the resulting data as described in those studies, fitting a structure based model to each data set.

Our results revealed that both mutants and WT MV could be fit to a model in which there are two structural states of the lever arm, a pre-power stroke state (M**) and a post-power stroke state (M*). Neither mutation impaired the distance or distance distribution profile of the pre- and post-power stroke states as a function of nucleotide (Table 10, Fig. 57). Interesting, the R712R mutation caused a shift in the mole fraction of structural states which demonstrated an increase in the population of the post-power stroke conformation in the strong actin-binding nucleotide states (AM.ADP and AM) (Table 10, Fig. 58). In contrast, the F750L mutation decreased the mole fraction of the post-power stroke conformation in the ADP states (AM.ADP and M.ADP). In the M.ADP.Pi state there was no difference in pre- and post-power stroke mole fractions when comparing R712G to WT, while the F750L mutant had a slight increase in the post-power stroke conformation in this state suggesting the mutations do not dramatically alter the equilibrium constant for hydrolysis (K_H).

We examined the structural kinetics of the recovery stroke with $(TR)^2$FRET (Fig. 53A&B) and found similar results to the other stopped-flow FRET studies (Fig. 51). We observed fluorescence transients (fluorescence intensity and lifetime) that were best fit by a two exponential function. The maximum rate of the fast phase of the recovery stroke was enhanced 2-fold in F750L (891±141 s^{-1}) while it was reduced 35% in R712G (266±6 s^{-1}) compared to WT (408±10 s^{-1}) (Fig. 53B). The structural kinetics of the power stroke were

examined with a single mix experiment, in which MV and ATP were mixed with actin and ADP to induce a single turnover, as previously described [1]. We observed a single exponential function at each actin concentration and the rate constants were linearly dependent on actin concentration. The rate constants of the power stroke were likely an average of the fast and slow phases we observed in our sequential mix stopped flow experiments. The slopes of the linear dependence of the power stroke rate constant on actin concentration were slightly higher for the F750L mutant (4.3±0.4 $\mu M^{-1} \cdot s^{-1}$) and slightly lower for the R712G mutant (2.3±0.1 $\mu M^{-1} \cdot s^{-1}$) compared to WT (3.3±0.2 $\mu M^{-1} \cdot s^{-1}$). Overall, the $(TR)^2$FRET results demonstrate the mutants dramatically changed the recovery stroke but did not induce major changes in the power stroke, which is similar to what we observed in our stopped-flow FRET studies.

5.4 DISCUSSION

The structural mechanism of actomyosin-based force generation has been studied with many different structural and biophysical methods. One crucially important question that remains, is how disease associated mutations alter conserved allosteric pathways and how can therapies be designed to correct these impairments. Myosin V is one of the best studied myosin motors and thus is thought to be an excellent model to investigate conserved allosteric pathways. In the current study we investigate two mutations in the converter domain of myosin V and found that they both impair motor-based force generation. We demonstrate how these mutations disrupt the structural kinetics of lever arm rotation during the recovery and power strokes as well as how they alter other steps in the myosin ATPase cycle. We conclude that disruption in the allosteric pathway that coordinates structural changes in the lever arm with changes in the nucleotide binding

pocket can impair the ability of myosin to adapt to external loads. The mutations do not change the intrinsic structure of the pre- and post-power stroke states based on $(TR)^2$FRET measurements but they do alter the rate and equilibrium constants associated with the transition between these two structural states. Our results have implications for understanding how conserved communication pathways in myosin can be altered by disease associated mutations.

Impact on mechanosensitivity. Myosin motors and other motor proteins have the unique ability to alter their catalytic cycle in the presence of external loads [148]. This feature was demonstrated in early studies of muscle contraction which found a decrease in heat production (myosin ATPase activity) when muscle contracts against a higher load (Fenn effect) [149]. Thus, myosins working within a contractile unit can fine tune their mechanical properties by altering their load dependent kinetics (e.g. slowing the detachment rate at higher loads to increase the time myosin is attached to actin). The structural mechanism of myosin mechanosensitivity has been investigated in recent studies using x-ray crystallography and cryo-electron microscopy (Cryo-EM) which demonstrated different conformations of the lever arm in nucleotide-states that are thought to play a crucial role in mediating force production [150-153]. The two converter mutants we investigated in the current study demonstrated little difference in unloaded sliding velocity but displayed increased sensitivity to external loads examined with load-dependent mixed motor motility assays (Fig. 48). It is expected that the tethering load would cause the myosin to slow the ADP release rate constant and thus slow the detachment and sliding velocity. Interestingly, the converter mutants were not able to overcome the tethering loads as well as WT MV, while the sliding velocity of moving filaments was indistinguishable

from WT. Thus, when the converter mutants experienced higher tethering loads they displayed the largest and most robust differences in mechanosensitivity compared to WT MV. The ADP-release rate constant typically correlates well with unloaded in vitro motility, while in the case of the F750L mutant the increased ADP-release rate constant (k'_{+D}) did not lead to a corresponding increase in unloaded sliding velocity. However, the changes in the slow power stroke (k'_{PWS}) and/or ADP isomerization ($k'_{D'}$) steps may contribute to the overall detachment rate. It is possible that the mutants reduce ensemble force (F_E) which is the product of intrinsic force (f), duty ratio (r), and the number of myosin motors (N) working in the contractile unit ($F_E = f \times r \times N$) [25]. Kinetic simulations did not reveal a major change in duty ratio in either mutant compared to WT (Table 11 and Fig. 61). However, the duty ratio simulations did not take into account the impact of load in the individual rate constants. It is conceivable that the mutants impair intrinsic force, which was observed in several converter mutants in human M2β associated with HCM [154]. The number of force generating myosin motors in a contractile unit could be changed by altering the hydrolysis equilibrium constant (K_H) but since we observed only minor changes in the mole fraction values of the pre- and post-power stroke state conformation in the M.ADP.Pi state (Table 10) we argue that this is unlikely. A final possibility is that the R712G and F750L mutants have impaired strain dependent detachment which has been shown to be crucial for myosin motors to adapt to different loads [148, 155]. Interestingly, both the R712G and F750L mutant demonstrate alterations in the actomyosin.ADP states, which are known to be critical for strain dependent ADP release. Compared to WT, the R712G mutant displays an increase in the post-power stroke conformation while the F750L

mutant displays a decrease in the post-power stroke conformation in the AM.ADP state. In addition, F750L demonstrates an altered ADP release rate constant (k'_{+D}).

It was previously determined that mutations in the converter domain can impair the stiffness of a myosin head and thus alter its force generating properties without altering cross-bridge kinetics [156-158]. Studies of the R723G mutation in human M2β, which corresponds to R712G in MV, found an increase in the rigidity of the strongly bound myosin heads which led to a 1.3 fold increase in force per myosin head [158]. Interestingly, the increased stiffness did not alter maximum velocity or the rate of force redevelopment. Another study found that the F764L mutation in mouse alpha cardiac myosin resulted in decreased ATPase and in vitro motility but no change in ensemble force [159, 160]. Thus, the current work highlights that mutations can have different effects in different myosin isoforms and it is important to evaluate their impact on both unloaded and loaded myosin mechanochemistry.

Impact of converter mutations on the recovery stroke. Overall, our results demonstrate that the mutations do not alter the conformation of the pre- and post-power stroke states, as the distance and distance distributions of these two states are identical (Table 9). However, the mutations do alter the mole fractions of the pre- and post-power stroke structural states (Table 10). The shift in the mole fractions indicates that the mutation alters the free energy difference between the pre- and post-power stroke states while the change in the recovery stroke rate constant indicates an impact on the activation energy associated with the structural transition. The recovery stroke is an important determinant of the number of myosin motors in an ensemble that are primed to generate force (N). In addition, the rate constant of the recovery stroke can alter the duty ratio by

altering the period of time a myosin motor remains in the weakly bound states. We find that the F750L mutation increases the recovery stroke rate constant two-fold and this correlates well with the increase in the maximum rate of ATP hydrolysis measured by tryptophan fluorescence. Thus, the mutation lowers the activation energy associated with the transition from the post- to pre-power stroke states. The region where F750 is located has been identified as site of hydrophobic interactions between the converter domain, SH1-SH2 helix, and rely helix/loop [31, 161]. As depicted in Fig. 54A, this pathway allows for communication between the lever arm and active site because the relay helix extends into the nucleotide binding pocket and is connected to the switch II region which participates in ATP binding/hydrolysis. The formation of the pre-power stroke state is driven by a change in the relay helix from a straight to a bent conformation, which then causes a repositioning of the converter/lever arm domain into the pre-power stroke conformation [162]. A salt-bridge that forms between the converter and relay loop is thought to be important for communication. In addition, hydrophobic interactions between the relay helix region and the converter domain play a particularly important role, and F750 is a highly conserved converter domain residue (Fig. 54C) that has been proposed in structural and molecular modeling studies to be crucial [162]. The leucine that replaces the phenylalanine at this position likely reduces the hydrophobic surface because of the loss of the bulky aromatic side chain that interacts with other hydrophobic residues (e.g. Y477, F698, P699, I749, F751). However, the substitution of leucine at this position appears to improve the efficiency of this structural transition, possibly because a smaller hydrophobic side chain allows a more rapid reorganization of the hydrophobic cluster. A recent study that mutated a nearby residue R778K in non-muscle myosin IIC

(R762 in MV) found a 50% increase in the maximum rate of ATP hydrolysis indicating this region is important for tuning the recovery stroke which is coupled to formation of the hydrolysis competent state [163]. Other studies in insect flight muscle found that mutations that disrupt the converter-relay interactions have a major impact on myosin and muscle function [164, 165]. Thus, modulating the charge-charge and hydrophobic interactions in the relay/converter interface can alter the recovery stroke kinetics.

The R712G mutation causes a reduction in the recovery stroke rate constant and shifts the mole fraction of structural states to favor the post-power stroke conformation in the strong actin-binding states (M, AM.D, and M.D). The R712 residue is not well conserved in myosins (Fig. 54C) and is located at the region of the converter that is in close proximity to the light chain bound to the first IQ motif. Furthermore, we found that in many myosin structures the region of the converter near R712 is often in close proximity to charged residues on the essential light chain (Fig. 54C&D). Thus, R712 may form charge-charge interactions with light chain residues (e.g. D118, E119 and E120 in CaM) which could stabilize the pre-power stroke state (see Fig. 62). Studies in myosin V demonstrated that altering the light chain associated with the first IQ motif can impact the ATP hydrolysis rate and equilibrium constant [166]. Interestingly, myosin Vc has a naturally occurring glycine at the 712 site and it was found to have a reduced maximum rate of ATP hydrolysis compared to myosin Va [167]. We evaluated the correlation between the maximum rate of ATP hydrolysis ($k_{+H} + k_{-H}$) and the number of potential complementary charges between the converter domain and essential light chain in different myosin isoforms (Fig. 54). We found that myosins with a positively charged amino acid at the corresponding position to R712 which allows for a potential interaction with at least one other negatively charged

residue on the ELC tend to have a faster ATP hydrolysis rate constant while those that have no charge or a negative charge at the R712 position have a slower ATP hydrolysis rate constant (Fig. 54B). In the highly mechanosensitive Myo1b, an insert in the converter domain called the WPH motif (nearby the corresponding R712 residue) was found to directly interact with calmodulin [151]. Thus, our results suggest that interactions between the converter and essential light chain are important for fine tuning the recovery stroke rate constant and may play a role in mechanosensitivity.

Impact of converter mutations on the power stroke. Compared to the recovery stroke the converter mutations had less of an impact on the power stroke. A possible explanation is that the allosteric coupling pathway (active site-relay helix-converter-lever) is crucial for the recovery stroke while other unknown allosteric pathways are important for the power stroke. In our previous work we found that the there is a fast structural change in the lever arm that occurs upon myosin binding to actin in the M.ADP.Pi state, which is closely followed by phosphate release and then a slow power stroke that occurs before ADP release [142]. Although there has been considerable controversy, a recent review article describes a unifying theme for how actin activates the power stroke based on much of the current data available [33]. The authors suggest that actin binding triggers a rapid structural change in the active site that opens up the phosphate release tunnel allowing phosphate to enter the tunnel and the fast power stroke to occur. The observed rate of phosphate release measured in solution is slower because dissociation of phosphate from the exit tunnel and binding to the phosphate binding protein is being monitored. There is a second power stroke which occurs during the transition between actomyosin.ADP states which was identified in structural studies of

smooth muscle myosin, myosin V, myosin IB [150, 153, 168]. Kinetic simulations demonstrate that the power stroke and phosphate release transients are best fit by a fast power stroke (k_{+PWF}) followed by rapid phosphate release (k_{+Pi}) (Fig. 59 and Fig. 60). However, we cannot rule out that phosphate release and the fast power stroke occur simultaneously, since phosphate may remain in the exit tunnel for a period of time before being released into solution and detected by the phosphate binding protein. We find that the converter mutants do not disrupt the fast power stroke associated with the phosphate release step and no significant differences were observed in the slow power stroke that occurs during the transition between actomyosin.ADP states (Table 8). The actin-dependence of phosphate release is also similar in the mutants and WT (see Table 11 and Fig. 52C). Overall, the observed transient kinetic parameters do not alter the steady-state ATPase activity, as the K_{ATPase} and k_{cat} are not dramatically altered from WT. Interestingly, altering the slow power stroke rate constant may alter the period of time myosin spends in the force generating actomyosin.ADP states which is thought to be an important determinant of the myosin duty ratio. For example, a reduction in the slow power stroke rate constant could be accompanied by a faster ADP release rate constant (k'_{+D}) which overall results in little change in duty ratio.

5.5 CONCLUSIONS

The current study demonstrates direct evidence for an allosteric pathway in myosin associated with positioning the lever arm in the pre- and post-power stroke states. We find that the mutations disrupt ensemble force, likely by altering intrinsic force or strain dependent detachment. We highlight the importance of key residues and interactions in the allosteric pathway and identify potentially new mechanisms for positioning the force

generating lever arm. Our work highlights that mutations in this key allosteric pathway can change the kinetics of the recovery and power stroke as well as the equilibrium between the pre- and post-power stroke states. In addition, our studies demonstrate that point mutations can alter the rate and equilibrium constants that control the population of structural states without altering the overall conformation of the lever arm. Thus, therapies designed to shift the equilibrium between major structural states may be effective at rescuing the structural impact of the disease mutations. Our work provides a basis for future studies designed to examine the impact of disease mutations on key structural changes as a method of determining the mechanism of motor impairment and potential for therapeutic strategies to correct specific impairments.

5.6 SUPPLEMENTAL INFORMATION AND METHODS

Experimental procedures

Reagents. Reagents used for all experiments were commercially available and of the highest purity. ATP and ADP stocks were freshly prepared from powder and their concentrations were measured by absorbance at 259nm (ε_{259} = 15,400 $M^{-1}cm^{-1}$). The non-fluorescent acceptor QSY-9 and pyrene iodoacetamide were purchased from Invitrogen (Carlsbad, CA). FlAsH dye was a generous gift from Roger Tsien and Stephen Adams at the University of California, San Diego. The fluorescently labeled phosphate binding protein (MDCC-PBP) [86] was a generous gift from Howard White (Eastern Virginia Medical School). The 2'-deoxy-ADP and 2'-deoxy-ATP labeled with N-Methylanthraniloy at the 3'-ribose position (*mant*ADP and *mant*ATP, respectively) were purchased from Jena Biosciences.

Protein Construction, Expression, and Purification. A chicken myosin V (MV) construct containing a single IQ motif (residues 1-792) was used for this study. This construct was further modified to add a tetracysteine motif (CCPGCC) to the extreme N-terminus in order to label with FlAsH, and to add a C-terminal FLAG tag (DYKDDDDK) for purification as described previously [140, 169]. The two converter domain mutations, R712G and F750L, were separately introduced into this construct. All constructs were coexpressed with chicken calmodulin in the baculovirus system. MV R712G, MV F750L, and WT MV were labeled with FlAsH as described previously. A single cysteine (T110C) was introduced into calmodulin (CaM) for site-specific labeling with the non-fluorescent acceptor QSY-9. During purification, the MV constructs were stripped of native calmodulin and QSY-9 labeled CaM was exchanged onto the lever arm at the single IQ motif [142]. Actin was purified from rabbit skeletal muscle by the acetone powder method [170] and labeled with pyrene actin when necessary [171]. All experiments were performed in KMg50 TCEP buffer (10mM imidazole-HCl, 50mM KCl, 1mM EGTA, 1mM $MgCl_2$, 1mM TCEP) at pH 7.0, 25°C.

***In vitro* Motility.** *In vitro* motility measurements were carried out as described previously [141-143]. Briefly, MV WT, R712G, MV F750 were attached to a nitrocellulose coated coverslip using anti-cMYC antibody (Invitrogen). The coverslip surface was blocked with 1 $mg \cdot ml^{-1}$ BSA. Motility was initiated by adding activation buffer that consisted of 0.35% methylcellulose, 1 $mg \cdot ml^{-1}$ BSA, 2 mM ATP, 20 units ml^{-1} pyruvate kinase, 2.5 mM phosphoenolpyruvate, and 10 µM calmodulin. An oxygen scavenging system consisting of 1 mg $ml^{-1} \cdot$glucose, 0.1 $mg \cdot ml^{-1}$ glucose oxidase and catalase was used to prevent photobleaching. Time-lapse images of the motility of rhodamine-phalloidin labeled F-actin

filaments were recorded in 2s intervals for 4 minutes using a Nikon TE2000 microscope. The loaded in vitro motility assay was performed as described above except different amounts of the non-hydrolyzing strong actin binding mutant (G440A) [144] [172] were mixed with MV (amount of MV remained constant at 0.4 μM, while G440A MV was varied between 0 and 0.2 μM) and added to the flow cell. The sliding velocities were determined using the program FAST [50], which allowed determining the total number of filaments moving and the velocity of each moving filament. The velocities of the moving filaments were binned and fit to a Gaussian function to determine the average velocity and standard error at each condition. A student t test was performed to determine significant differences between WT and the two mutants.

Steady-state ATPase measurements. We performed actin-activated ATPase measurements of MV NT constructs (0.1 μm) as a function of actin concentration (0. 2.5, 5, 10, 20, 30 μm) using the NADH coupled assay [140-143, 173]. Experiments were performed in an Applied Photophysics (Surrey, UK) stopped flow at 25 °C for a 200 second period. A standard curve of known ADP concentrations was used to determine the relationship between the NADH absorbance and ADP concentration. The ATPase rate was plotted a function of actin concentration and fit to the Michaelis Menten equation to determine the maximum ATPase rate (k_{cat}) and actin concentration as which the ATPase activity is one-half maximal (K_{ATPase}). Data from several protein preparations was used to determine the average ATPase rate (±SD) at each actin concentration. A student t test was performed to determine significant differences between WT and the two mutants.

Transient kinetic measurements. Measurements of the individual steps in the myosin ATPase cycle were examined using an Applied Photophysics stopped flow with a

1.2 ms dead-time at 9.3 nm band pass. The *mant*ATP or *mant*ADP fluorescence was examined by exciting intrinsic protein fluorescence at 290 nm and examining the *mant* emission with a 395 nm long pass filter. Pyrene-actin fluorescence was examined by exciting at 365 nm and measuring the emission with a 395 nm long pass filter. To examine tryptophan fluorescence an excitation of 290 nm and 320 nm long pass emission filter was used. To examine MDCC-PBP an excitation of 380 nm and 395 nm long pass emission filter was used. We examined the FRET signal with the FlAsH-QSY donor/acceptor pair by exciting FlAsH at 488 nm and examining the emission with a 515 nm long-pass filter (since QSY is non-fluorescent). A student t test was performed to determine significant differences between WT and the two mutants ($n \geq 3$ separate protein preparations).

Transient time resolved FRET. Transient time-resolved FRET (0.2 millisecond-resolved transient biochemical experiments with 125 picosecond-resolved fluorescence decay detection), $(TR)^2$FRET, was measured using a transient time-resolved fluorescence spectrophotometer [10, 42, 77]. This instrument utilizes a *Biologic USA* SFM/20 single-mix stopped-flow accessory coupled to a transient time-resolved fluorescence spectrophotometer. The dead time for the instrument is 1.8 ms, calibrated using the 8-hydroxyquinoline + Mg^{+2} control reaction [99].

Recovery stroke experiments (post-mix concentrations): 50-80 nM MV.FlAsH-CaM.QSY was mixed with 0 – 1.0 mM ATP. Power stroke experiments: 50-80 nM MV.FlAsH-CaM.QSY and 5.0 μM ATP was mixed with 0 – 40 μM actin and 5.0 mM ADP. Biochemical mixes were prepared with 600 μL per syringe and shot at 40 μL per syringe for acquisition. 10 – 12 shots were averaged for each biochemical mix, with replicates of n = 3 to 6.

Time-resolved FRET transients for WT, F750L, and R712G donor-only labeled samples in n=12 were globally fit to obtain amplitudes and lifetimes for the donor-only fluorescence (Table 11). These parameters were used to fit a distance-dependent FRET model. 1-, 2-, and 3-distance models were tested, with the best fit obtained using a two Gaussian distance distribution (Table **9**), corresponding to pre- and post-power stroke structural states, extensively discussed in our earlier work [1]. Each biochemical mix, containing 500+ waveforms acquired after excitation of the sample from the pulsed laser, were then globally fit to this two-Gaussian structural model, allowing the mole fractions of the two states to vary. Reported errors estimates reflect the 67% confidence interval for each parameter determined by error plane analysis with all parameters allowed to vary, as described in previous publications (31).

Table 8. Summary of steady-state and transient kinetic results

[a]**Steady-State ATPase Values, (±SD) n=4**	**WT**	**R712G**	**F750L**
v_0 (s^{-1})	0.09±0.11	0.04±0.03	0.07±0.05
k_{cat} (s^{-1})	9.4±0.3	8.9±0.7	*10.3±0.5
K_{ATPase} (μM)	2.4±0.4	2.6±0.7	1.8±0.5
Rate/Equilibrium Constants (±SE)	**WT**	**R712G**	**F750L**
[b]ATP Binding/Hydrolysis (Myosin)			
$K_{1T}k_{+2T}$ (μM·s^{-1})	1.5 ± 0.1	1.4 ± 0.1	1.5 ± 0.1
$k_{+H} + k_{-H}$ (maximum rate, s^{-1})	397 ± 46	230 ± 23	484 ± 25
[c]ATP Binding (Actomyosin)			
$1/K'_{1T}k'_{+2T}$ (μM·s^{-1})	1.6 ± 0.2	1.7 ± 0.2	1.6 ± 0.2
k'_{+2T} (s^{-1})	660 ± 50	699 ± 46	631 ± 34
[d]Recovery Stroke, n=3-4			
$k_{+H} + k_{-H}$ (maximum rate, s^{-1})	290 ± 8	*219 ± 14	**596 ± 44
[e]Actin-activated Phosphate Release, n=3			
k_{+Pi} (maximum rate)	206 ± 35	269 ± 69	181 ± 56
[d]Power Stroke, n=3			
$K_{Actin}*k_{PWF}$ (actin conc. dependence, μM·s^{-1})	7.9 ± 0.5	8.1 ± 0.6	7.3 ± 0.6
k_{+PWF} (maximum rate, s^{-1})	≥276	≥288	≥314
k_{+PWS} (maximum rate, s^{-1})	78 ± 33	109 ± 75	38 ± 12
Actomyosin ADP Release			
[f]k'_{+D} (s^{-1})	26.9 ± 0.4	25.3 ± 0.3	33.0 ± 0.6

[a]Steady-state ATPase measurements
[b]Intrinsic tryptophan fluorescence
[c]Pyrene actin
[d]FRET
[e]MDCC-PBP fluorescence
[f]*mant*ADP fluorescence
*p<0.05, **p<0.01

Table 9. Transient time-resolved FRET ((TR)^{2}FRET) parameters

Determined by simultaneous fitting a two-Gaussian distance distribution model to power stroke and recovery stroke data. Error estimates are ±67% confidence interval determined by error plane analysis.

	Post-power stroke Gaussian (M*)		**Pre-power stroke Gaussian (M**)**	
Construct	**D_1**	**$FWHM_1$**	**D_2**	**$FWHM_2$**
WT	3.56 ± 0.48	2.64 ± 0.93	6.89 ± 0.20	1.33 ± 0.68
R712G				
F750L				
All parameters were fit globally.				

Table 10. Mole fractions of MV lever in the post-power stroke (M*) state
Mole fractions determined by simultaneous fitting a two-Gaussian distance distribution model to powerstroke and recovery stroke data. Error estimates are ±67% confidence interval determined by error plane analysis.

	Construct		
Nucleotide State	**WT**	**R712G**	**F750L**
M	0.73 ± 0.04	0.87 ± 0.02 ***	0.74 ± 0.03 *N.S.*
A.M.D	0.68 ± 0.03	0.73 ± 0.01 ***	0.60 ± 0.03 ***
M.D	0.43 ± 0.04	0.53 ± 0.02 ***	0.40 ± 0.02 *
M.D.Pi	0.33 ± 0.03	0.32 ± 0.03 *N.S.*	0.37 ± 0.03 **
Statistical significance, comparing to WT: comparing each of the four nucleotide states of R712G or F750L to the corresponding nucleotide state in WT. For each nucleotide state for each construct, n ≥ 12. N.S.: p ≥ 0.05. *: p < 0.05. **: p < 0.01. ***: p < 0.001.			

	Construct		
Nucleotide State	**WT**	**R712G**	**F750L**
M	0.73 ± 0.04	0.87 ± 0.02	0.74 ± 0.03
A.M.D	0.68 ± 0.03 **	0.73 ± 0.01 ***	0.60 ± 0.03 ***
M.D	0.43 ± 0.04 ***	0.53 ± 0.02 ***	0.40 ± 0.02 ***
M.D.Pi	0.33 ± 0.03 ***	0.32 ± 0.03 ***	0.37 ± 0.03 ***
Statistical significance, comparing to M: comparing the last three nucleotide states (A.M.D, M.D, and M.D.Pi) to the M nucleotide state, within each single construct. For each nucleotide state for each construct n ≥ 12. N.S.: p ≥ 0.05. *: p < 0.05. **: p < 0.01. ***: p < 0.001.			

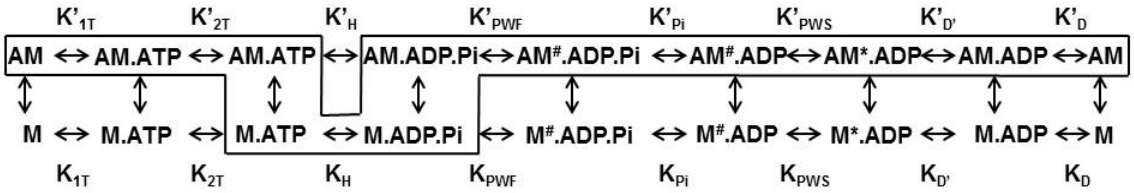

Fig. 46. Myosin V kinetic pathway in the structural and biochemical reaction space

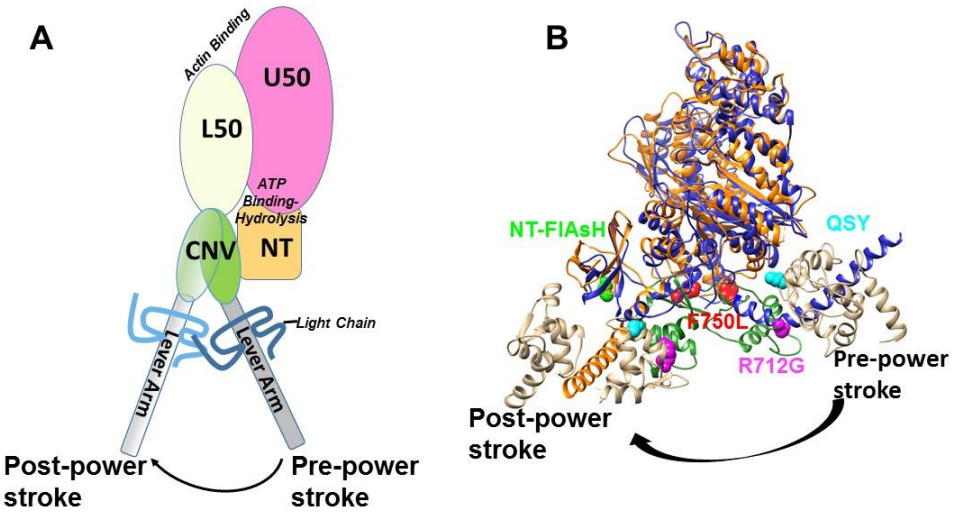

Fig. 47. Structural model of converter mutations in myosin V
A) Diagram of the domain structure of myosin and the movement of the lever arm in the pre- and post-power stroke states (L50, lower 50 kDa domain; U50, upper 50 kDa domain; CNV, converter domain; NT, N-terminal domain). **B)** An alignment of pre- and post- power stroke state crystal structures showing the conformational change of converter/lever arm. Pre-power stroke state structure in navy (PDB ID: 1BR4), post-power stroke state structure in orange (PDB ID: 1OE9), light chain in beige, and converter domain in green.

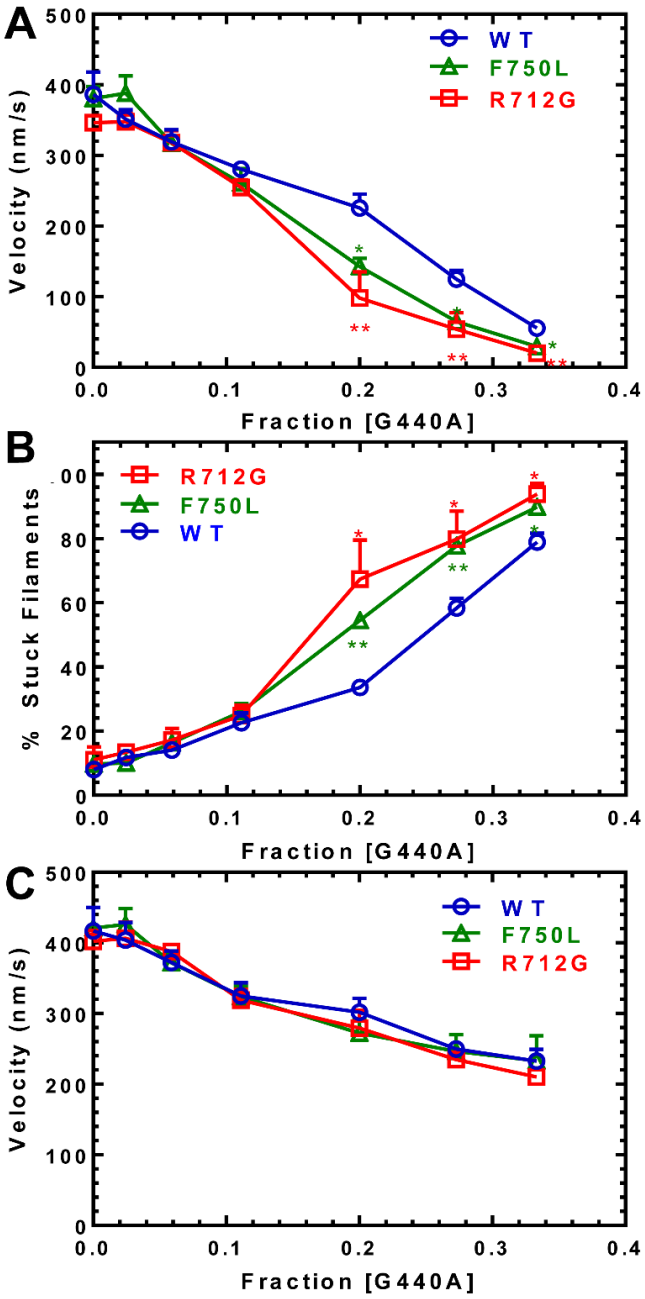

Fig. 48. *In vitro* motility sliding velocity
The sliding velocity was similar to WT for both mutants in the absence of load examined in 4 preparations (see Table 8).
The presence of G440A MV (non-hydrolyzing mutant) was used as a tethering load in the in the loaded in vitro motility assay in two preparations. A) The average velocity of all the filaments (moving and non-moving) was determined and plotted as a function of the fraction of G440A MV present relative to the total MV added to the assay. B) The number of stuck filaments was determined and plotted as a function of the fraction of G440A. C) The velocity of only the moving filaments was plotted as a function of G440A fraction. Significant differences of the mutants compared to the WT are indicated by an asterisk (*p<0.05, **p<0.005).

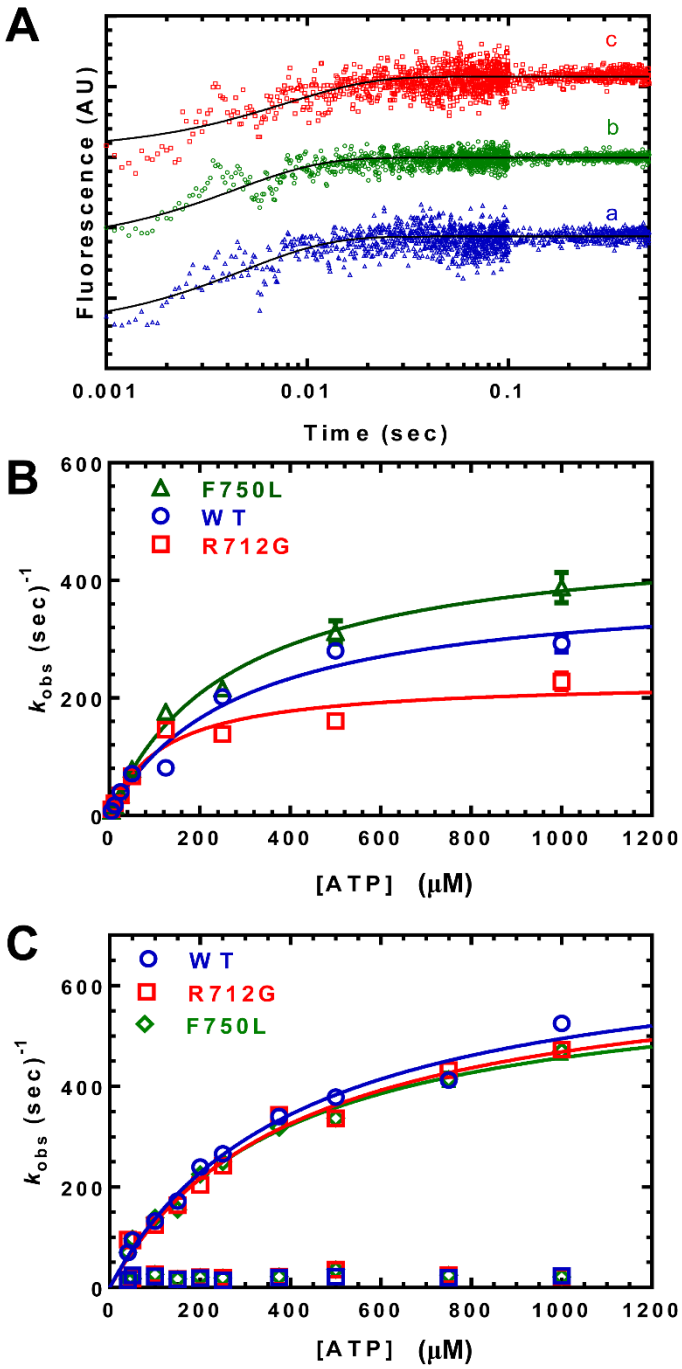

Fig. 49. ATP binding and hydrolysis

A) MV (1 µM) was mixed with varying concentrations of ATP and the tryptophan fluorescence increase was monitored as a function of time and fit to a single exponential function. **B)** The observed rate constants were hyperbolically dependent on ATP concentration. **C)** The rate of ATP-induced dissociation from pyrene actin was examined by mixing MV:pyrene actin (0.25 µM) with varying concentrations of ATP. The fluorescence transients were fit to a two exponential function with the fast phase being hyperbolically dependent on ATP concentration. The slow phase was a small component (5-10%) of the fluorescence signal and similar at each actin concentration (10-20 s^{-1}).

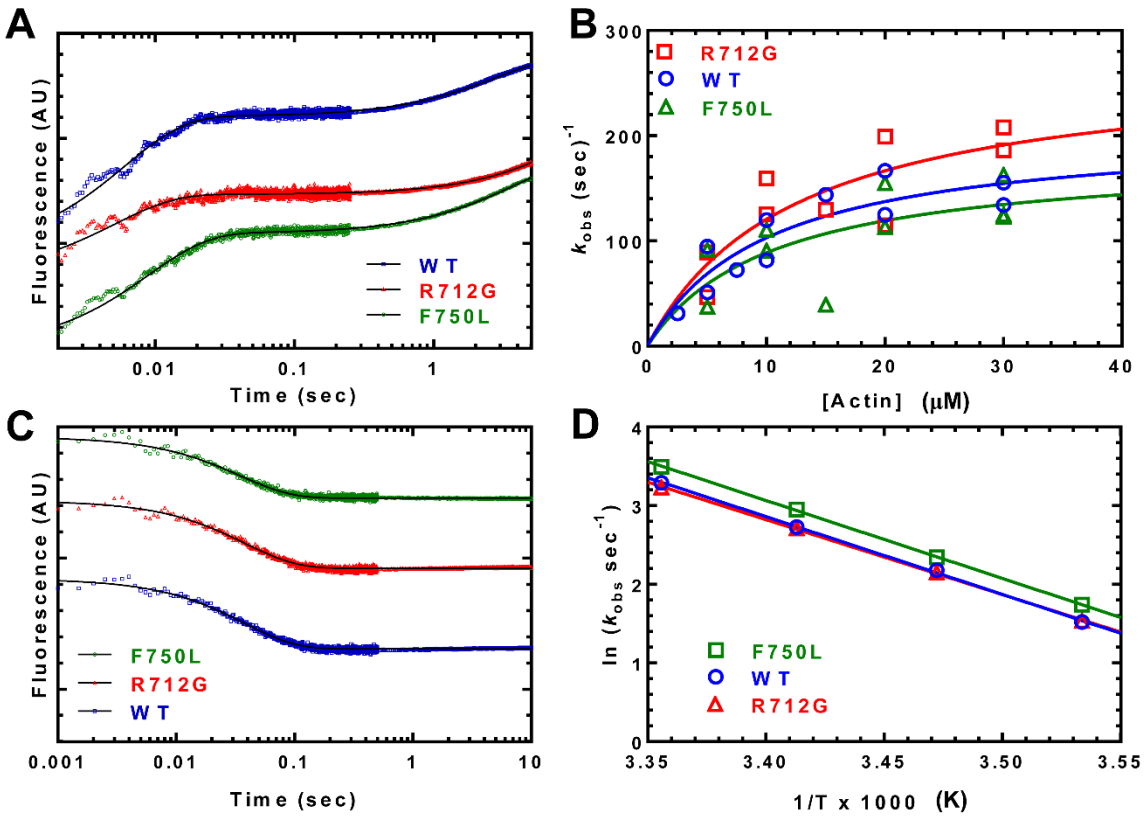

Fig. 50. Actin-activated product release

Sequential mix single-turnover experiments were performed by mixing MV with ATP, aging the reaction to form the M.ADP.Pi state (0.45 μM), and then mixing with different concentrations of actin in the presence of the phosphate binding protein (5 μM). **A)** The fluorescence transients were fit to a single exponential function (phosphate burst) followed by a linear or slow exponential rise. **B)** The phosphate release rate constants were plotted as a function of actin concentration and fit to a hyperbolic function to estimate the maximum rate of phosphate release. The F750L mutant displayed a more linear dependence on actin concentration preventing determination of the maximum rate of phosphate release. Acto-MV (0.25 μM) in presence mantADP (5 μM) was mixed with saturating ATP (1 mM) at different temperatures to determine the ADP release rate constant. **C)** The mant fluorescence transients were fit to a single exponential function at most temperatures. **D)** The Eyring plot (natural log of the ADP release rate constant as a function of inverse temperature) was fit to a linear regression.

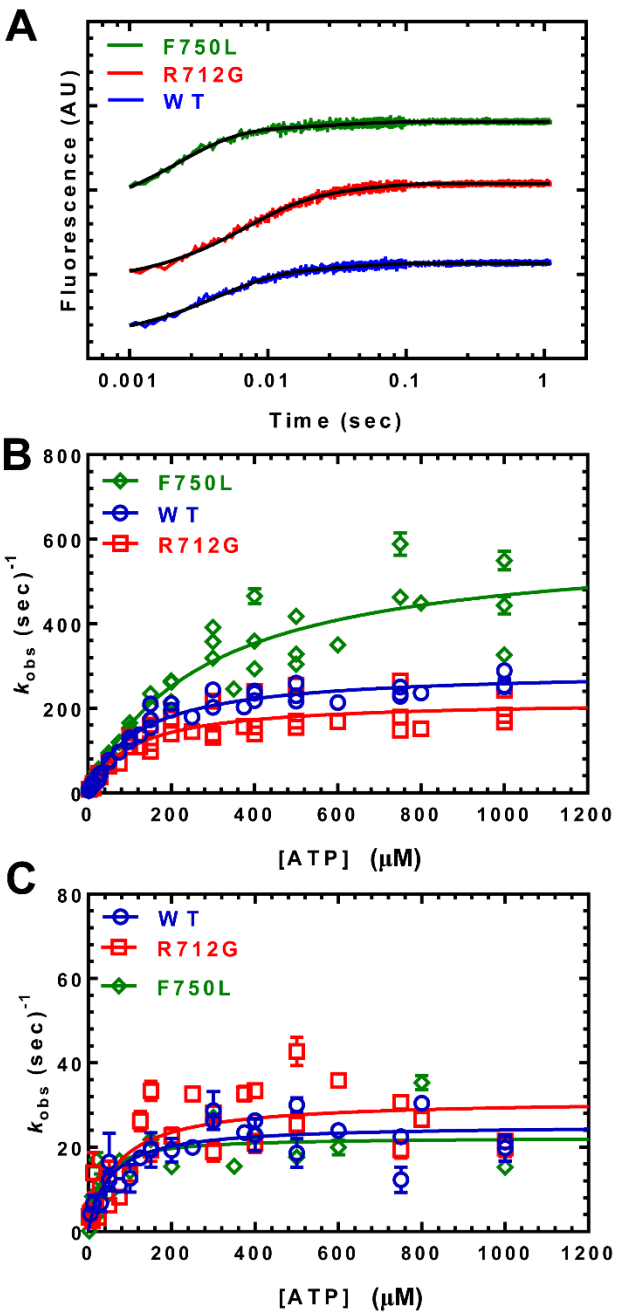

Fig. 51. Recovery stroke sequential mix time-resolved fluorescence experiments
A) 0.25µM MV FlAsH.QSY-CaM was mixed with increasing concentrations of ATP and the decrease in the FRET signal was monitored by following the increase in FlAsH fluorescence. The fluorescence transients were best fit by a two exponential function at all ATP concentrations. **B)** The fast phase (recovery stroke) was the majority of the fluorescence signal (≥90%) and was hyperbolically dependent on ATP concentration. **C)** The slow phase was also hyperbolically dependent on ATP concentration.

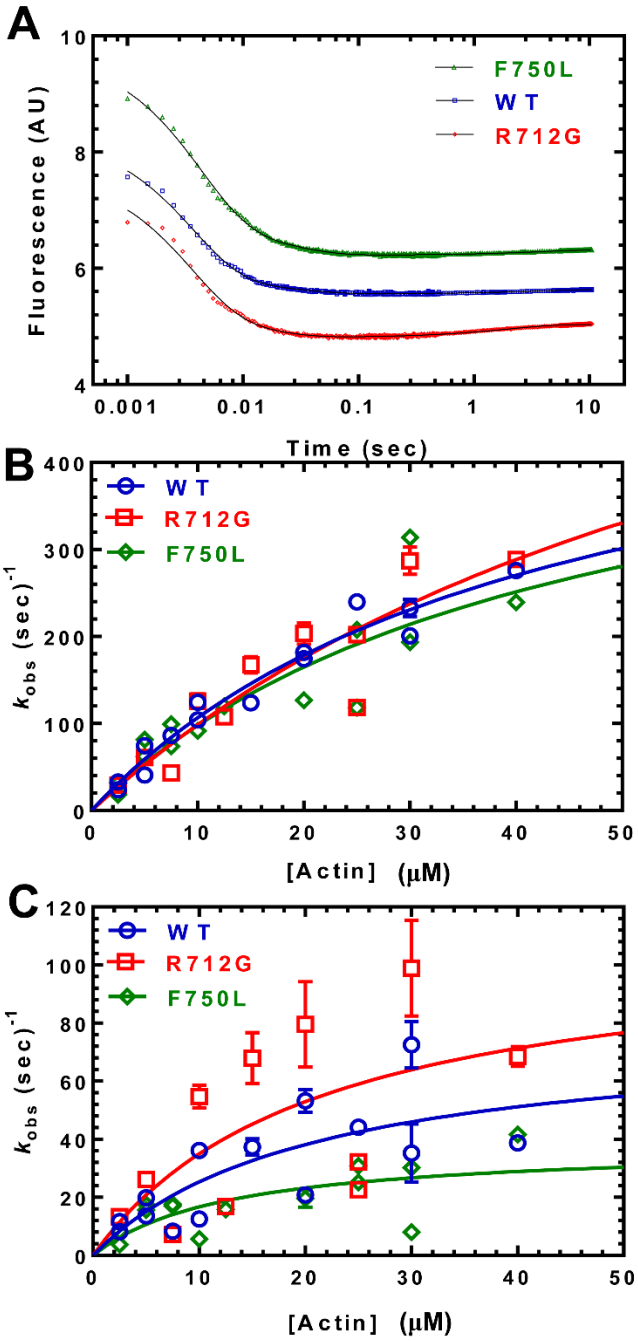

Fig. 52. Power stroke Sequential mix single-turnover experiments
Experiments were performed in which 0.25μM MV FlAsH.QSY-CaM was mixed with ATP (0.2 μM) aged for 10s and then mixed with different concentrations of actin. A) The increase in FRET was monitored by the decrease in FlAsH fluorescence and was best fit by a three exponential function. B) The fast phase of the fluorescence transients (fast power stroke) was plotted as a function of actin concentration and fit to a hyperbolic or linear function. C) The intermediate phase (slow power stroke) was hyperbolically dependent on actin concentration while the slow phase was similar at all actin concentrations.

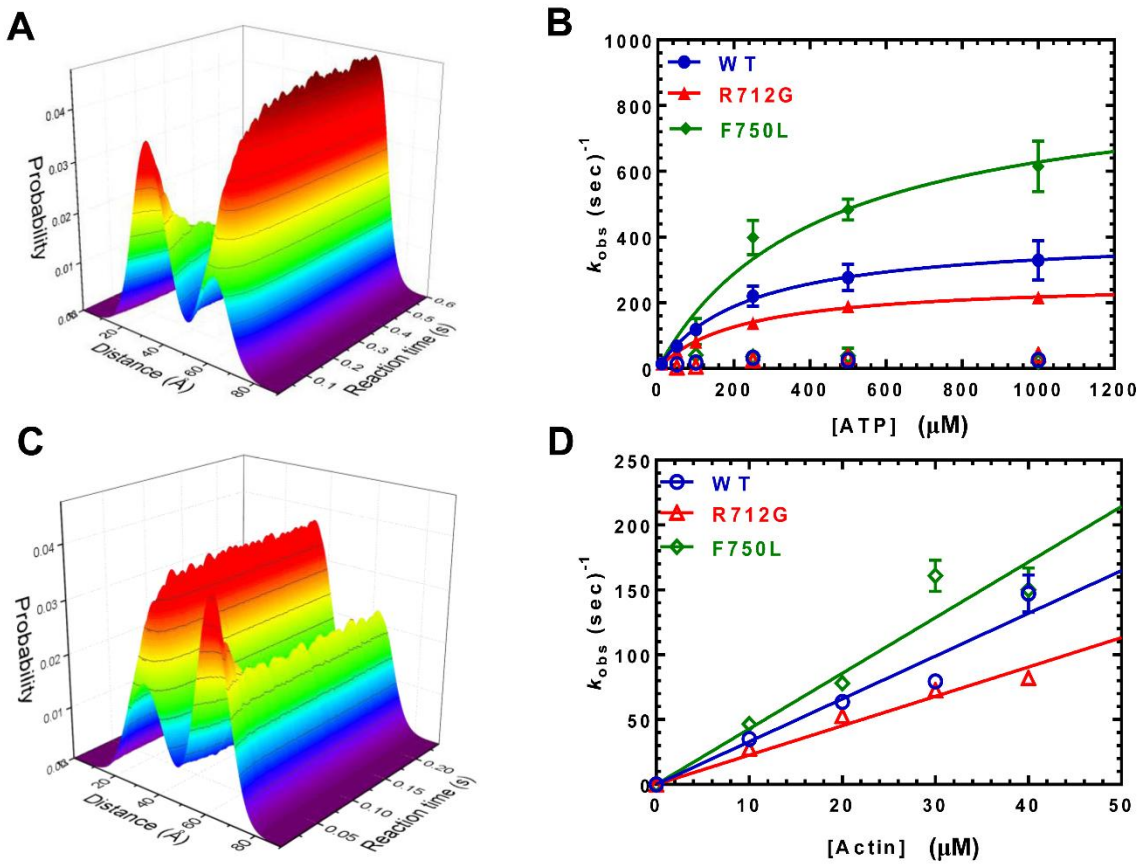

Fig. 53. Transient time-resolved FRET: time-resolved fluorescence waveform acquisition to structural kinetics

(**A**) TR^2-FRET of the recovery stroke. The fluorescence of 160 nM MV FlAsH.QSY-CaM changes upon rapid stopped-flow mixing with varying concentrations of ATP, 0.01 mM shown. Both the peak fluorescence intensity and the waveform shape changes over the reaction (rxn) time. The three-dimensional plot depicts the nanosecond-resolved waveforms (xy-plane) evolving with rxn time (z-axis). Each waveform was fit to a two-Gaussian distance distribution. The three-dimensional plot depicts each distance distribution (xy-plane) evolving with rxn time (z-axis). (**B**) The summary of rate constants from fitting the recovery stroke (TR)^{2}FRET data to a double exponential function. (**C**) (TR)^{2}FRET of the power stroke. 160 nM MV and 10 μM ATP was mixed with 5.0 mM ADP, and varying actin concentrations. (**D**) The summary of rate constants from fitting the power stroke (TR)^{2}FRET data to a single exponential function.

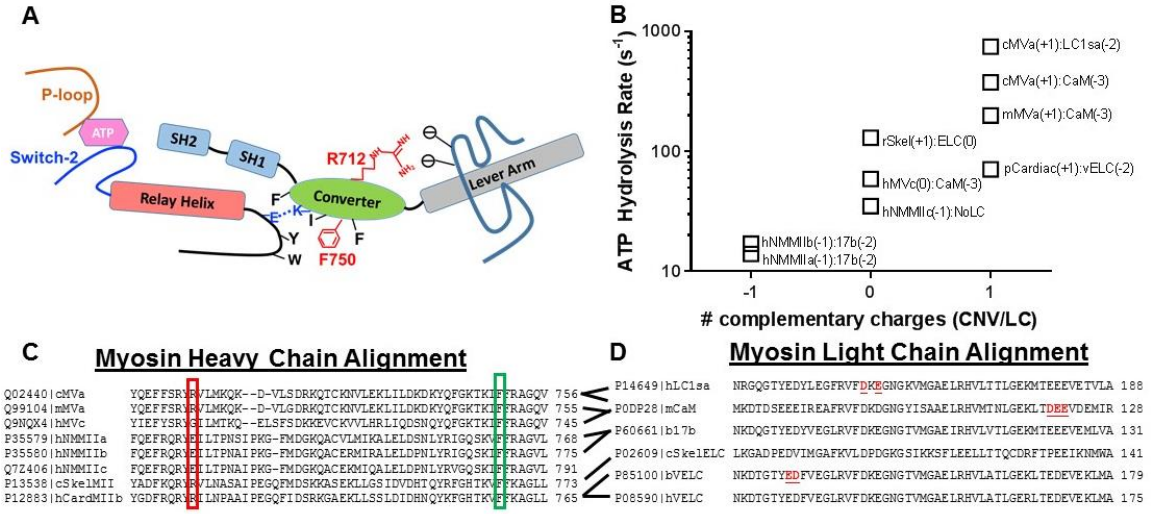

Fig. 54. Summary of allosteric interactions associated with the converter/relay helix/lever arm region

(**A**) Diagram of the key structural elements that allow communication between the nucleotide binding region and the lever arm (switch II, relay helix/loop, SH1-SH2 helix, converter domain). (**B**) Graph representing the correlation between the ATP hydrolysis rate constant and potential interactions between the converter domain (R712 site) and the light chain bound to the first IQ motif. (**C**) An alignment of several myosin heavy chains demonstrating conservation of the R712 (red box) and F750 (green box) residues. (**D**) An alignment of several myosin light chains demonstrating negatively charged residues in close proximity to the R712 site. The red underlined residues were found to be in close proximity to the R712 site in several crystal structures (PDB ID: 1OE9, 1W7J, 4ZLK and 5N69). The following abbreviations were used for the myosin heavy chains (Chicken MYO5A, cMVa; Mouse MYO5A, mMVa; Human MYO5A, hMVc; Human MYH9, hNMMIIa; Human MYH10, hNMMIIb; Human MYH14, hNMMIIc; Chicken MYSS; cSkelMII; Rabbit MYSS, rSkel; Human MYH7, hCardMIIb; Porcine MYH7, pCardiac) and myosin light chains (Human MYL6B, hLC1sa; Mouse CALM3, mCaM; Bovine Ventricular MYL3, bVELC; Human Ventricular MYL3, hVELC; Bovine Non-Muscle MYL6, bLC17b; Chicken Skeletal MLRS, cSkelELC). The data in panel B were taken from the following references: cMVa:LC1sa [147], cMVa:CaM [166], mMVa:CaM [174], rSkel:ELC [175], pCardiac:vELC [17], hMVc:CaM [167], hNMMIIc:NoLC [176], hNMMIIb:17b [177], hNMMIIa:17b [178].

Table 11. Rate constants used for kinetic simulations

Constants for the power stroke, phosphate release, steady-state ATPase, and duty ratio:
Kinetic pathway is depicted in Fig. 46 (box) with forward rate constants going from left to right and actin binding/dissociation steps in the M.ATP and M.ADP.Pi stated indicated by $k_{\pm A(ATP)}$ and $k_{\pm A(ADP.Pi)}$, respectively. The rate constants in bold/italics are different between the WT, R712G, and F750L.

Rate/ Eq.Constant	WT	R712G	F750L
[a] $1/K'_{1T}$ (μM)	413	412	383
[a] k'_{+2T} (sec^{-1})	699	661	631
[a] k'_{-2T} (sec^{-1})	≤0.1	≤0.1	≤0.1
[a] $k_{+A(ATP)}$ (sec^{-1})	1000	1000	1000
[a] $k_{-A(ATP)}$ (μM·sec^{-1})	10	10	10
[b] k_{+H} (sec^{-1})	***195***	***149***	***376***
[b] k_{-H} (sec^{-1})	***96***	***70***	***220***
[c] $k_{+A(ADP.Pi)}$ (μM·sec^{-1})	25-45	25-60	25-45
[c] $k_{-A(ADP.Pi)}$ (sec^{-1})	500	500	500
[d] k'_{+PWF} (sec^{-1})	355	368-450	406
[d] k'_{-PWF} (sec^{-1})	≤0.1	≤0.1	≤0.1
[d] k_{+Pi} (sec^{-1})	1000	1000	1000
[d] k_{-Pi} (μM·sec^{-1})	≤0.1	≤0.1	≤0.1
[d] k'_{+PWS} (sec^{-1})	63	121	69
[d] k'_{-PWS} (sec^{-1})	9	11	7
[e] k'_{+ADP} (sec^{-1})	25	25	25
[e] k'_{-ADP} (sec^{-1})	2	2	2
[f] k'_{+ADP} (sec^{-1})	***25***	***25***	***33***
[f] k'_{-ADP} (μM·sec^{-1})	≤0.1	≤0.1	≤0.1
Steady-state Parameter	**WT**	**R712G**	**F750L**
k_{cat} $(sec)^{-1}$	7.9	9.1	9.8
K_{ATPase} (μM)	1.3	1.4	2.2
Duty Ratio @ 40μM Actin	0.93	0.91	0.93

[a]Estimated from ATP induced dissociation from pyrene actin (Fig. 49)
[b]Calculated from recovery stroke experiment (Fig. 51) and mole fractions in the ADP.Pi state (Table 10)
[c]Estimated from reference #27 (Yengo et al, Biochemistry 41, 8508-8517)
[d]Calculated from power stroke experiments (Fig. 52) and kinetic simulations
[e]Estimated from simulations of ATPase activity
[f]Calculated from *mant*ADP release experiments (Fig. 50B)

Table 12. Transient Time-resolved donor-only fluorescence parameters
Error estimates are ±67% confidence interval determined by error plane analysis.

	Amplitudes		**Lifetimes**	
Construct	**A_1 (fraction)**	**A_2 (fraction**	**τ_1 (ns)**	**τ_2 (ns)**
WT	0.746 ± 0.015	0.254 ± 0.015	4.716 ± 0.055	1.205 ± 0.039
R712G	0.746 ± 0.015	0.254 ± 0.015	4.716 ± 0.055	1.205 ± 0.039
F750L	*0.647 ± 0.023* ***	*0.353 ± 0.023* ***	4.716 ± 0.055 N.S.; global fit	*1.140 ± 0.011* ***
All parameters were globally fit, except for F750L. This construct affects donor-only fluorescence in a statistically significant manner. For each construct $n \geq 36$. N.S.: $p \geq 0.05$. *: $p < 0.05$. **: $p < 0.01$. ***: $p < 0.001$.				

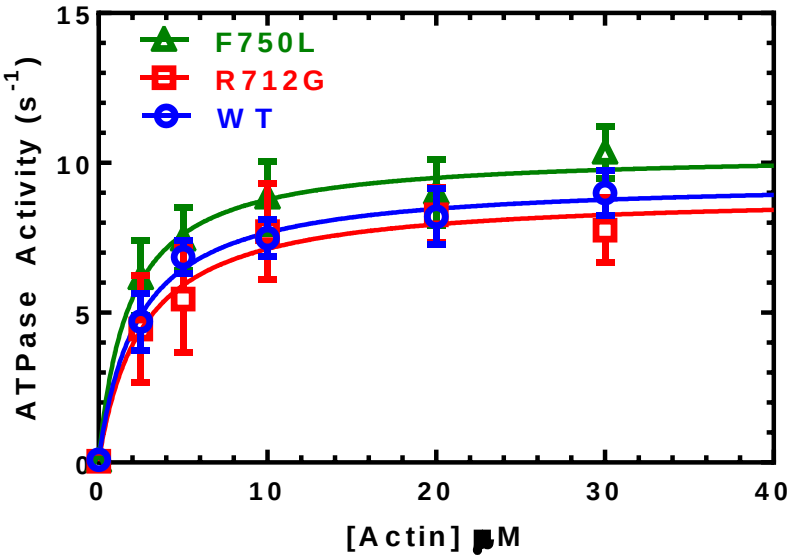

Fig. 55. Actin-activated ATPase activity
The MV converter mutants were compared in the NADH coupled ATPase assay. The average ATPase activity (±SE) is plotted as a function of actin concentration for 4 protein preparations and fit to the Michaelis-Menten relationship. The k_{cat} and K_{ATPase} values for WT, R712G, F750L are summarized in Table 8.

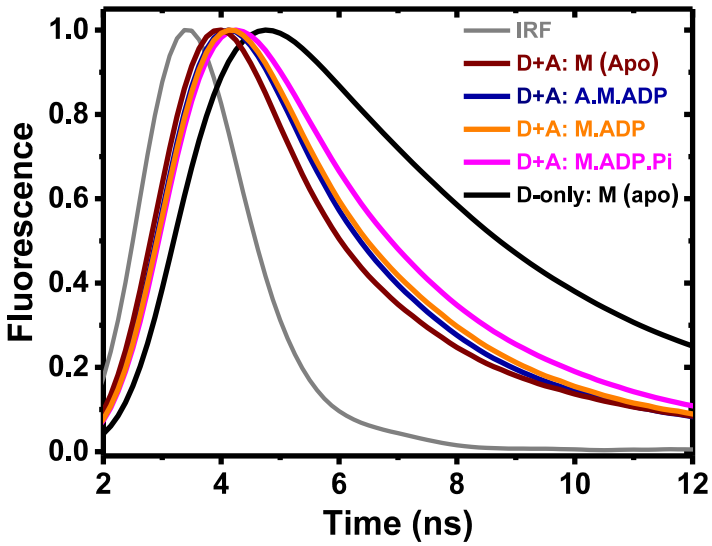

Fig. 56. Fluorescence lifetime waveforms under steady-state conditions, detecting time-resolved FRET (TR-FRET)

Time-resolved FRET measurements acquired under equilibrium or steady-state ATPase cycling biochemical conditions. The instrument response function (IRF), or detected laser pulse, is shown in gray. Time-resolved fluorescence decays of FRET labeled MV samples (160 nM MV FlAsH.QSY-CaM (Donor + Acceptor, D+A)) in four biochemical states: Apo (maroon), with 20 μM Actin and 4.0 mM ADP (navy), with 4.0 mM ADP (orange), or with 4.0 mM ATP (magenta). The donor-only fluorescence of 160 nM MV FlAsH is shown for comparison (black).

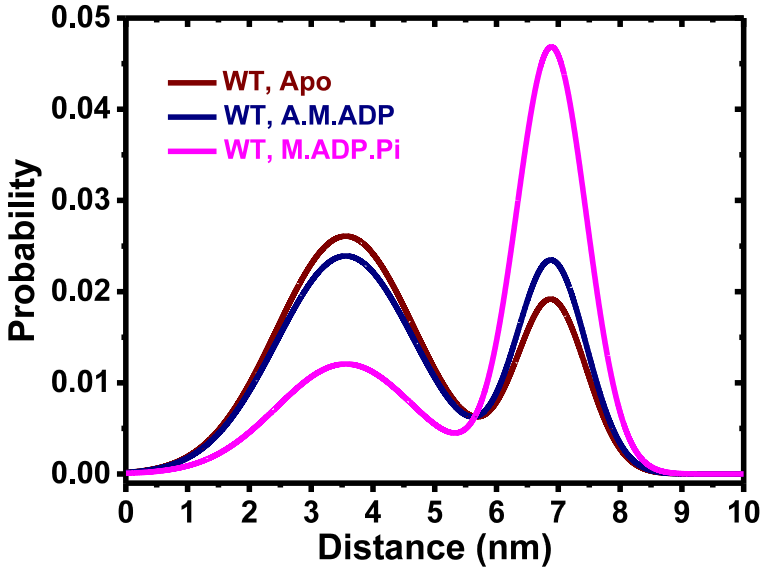

Fig. 57. Best-fit two-Gaussian distance distribution model describing TR-FRET between donor and acceptor probes

Interprobe distance distributions under Apo (maroon), in the presence of saturating actin and ADP, and under steady-state ATPase cycling conditions (magenta).

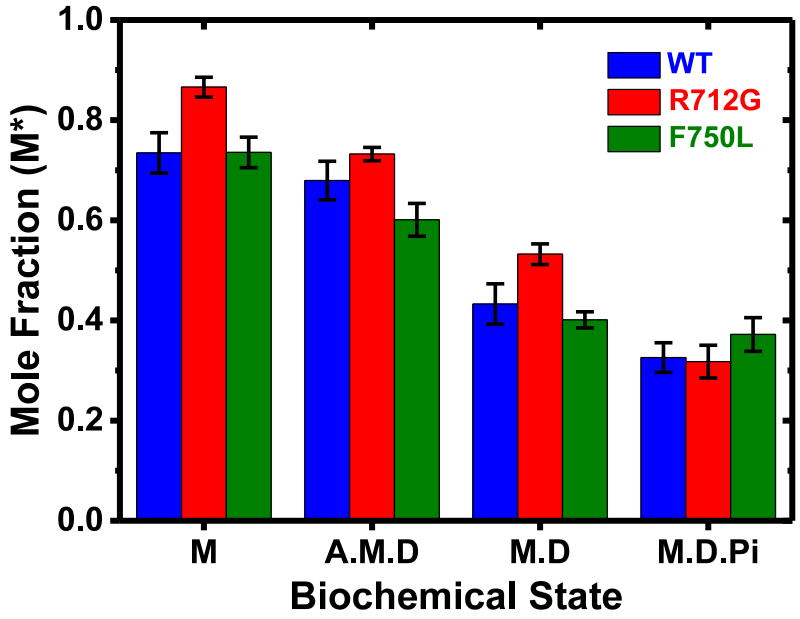

Fig. 58. Mole fractions of lever arm orientation in the post-power stroke state

Mole fraction of the post-power stroke state (M*) determined by fitting a two-Gaussian distance distribution model fit to time-resolved waveforms acquired under varied biochemical conditions for wild type MV (WT) or R712G and F750L constructs. Data summarized in Table 10. Error estimates are ±67% confidence interval determined by error plane analysis.

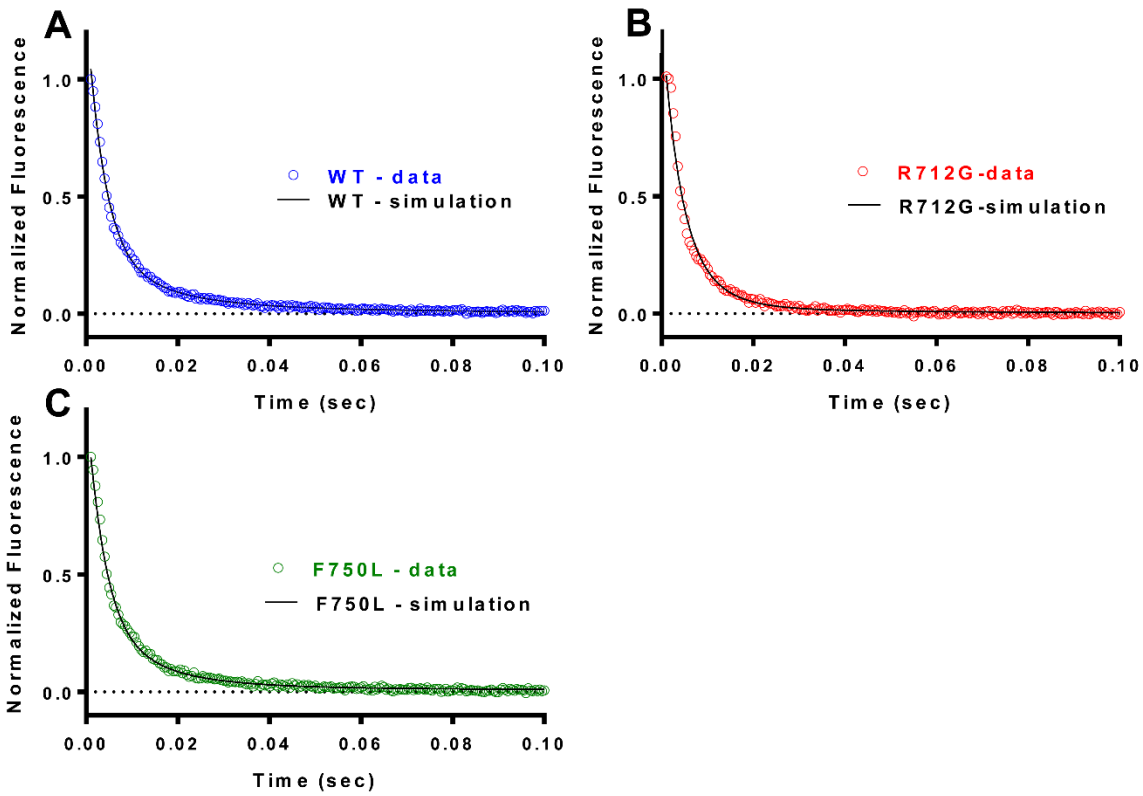

Fig. 59. Kinetic simulations of the power stroke

The traces acquired at 40 µM actin were fit to a kinetic model using the rate constants in Table 11. The specific rate constants (k_{+A} (µM·sec^{-1}), k_{-A} (sec^{-1}), k'_{+PWF} (sec^{-1}), k'_{-PWF} (sec^{-1}), k'_{+Pi} (sec^{-1}), k'_{-Pi} (µM·sec^{-1}), k'_{+PWS} (sec^{-1}), k'_{-PWS} (sec^{-1}) that best fit the WT data were (45, 500, 355, 0.001, 1000, 0.001, 63, 9, respectively), and for the R712G data were (45, 500, 368, 0.001, 1000, 0.001, 121,11, respectively), and for the F750L data were (30, 500, 406, 0.001, 1000, 0.001, 69, 7, respectively).

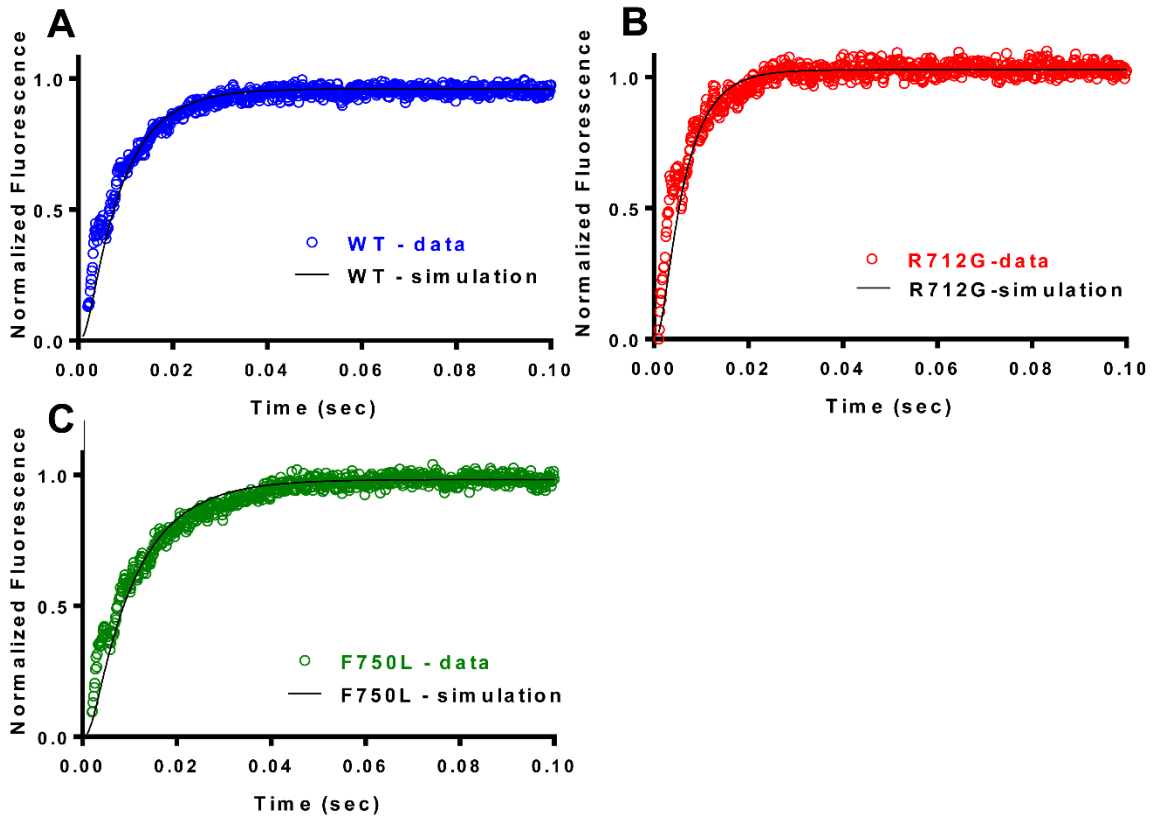

Fig. 60. Kinetic simulations of the phosphate release

The traces acquired at 10 µM actin were fit to a kinetic model using the rate constants in Table 11. The specific rate constants (k_{+A} (µM·sec^{-1}), k_{-A} (sec^{-1}), k'_{+PWF} (sec^{-1}), k'_{-PWF} (sec^{-1}), k'_{+Pi} (sec^{-1}), k'_{-Pi} (µM·sec^{-1}) that best fit the WT data were (45, 500, 355, 0.001, 1000, 0.001, respectively), and for the R712G data were (60, 500, 450, 0.001, 1000, 0.001, respectively), and for the F750L data were (30, 500, 406, 0.001, 1000, 0.001, respectively).

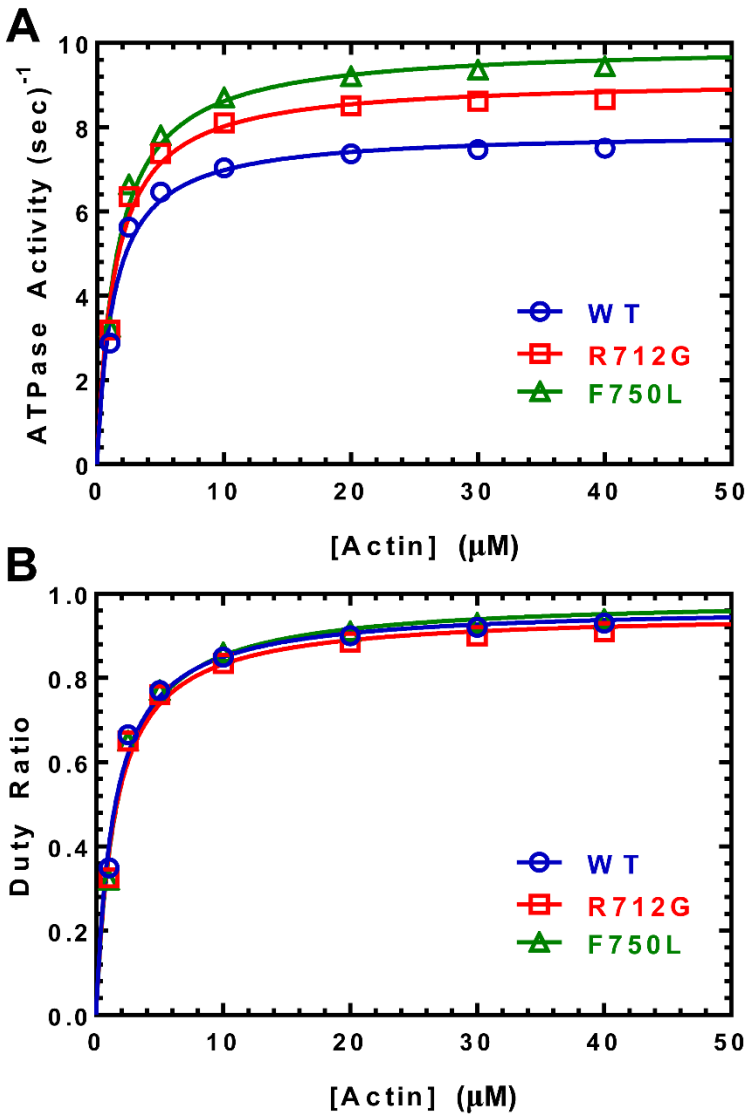

Fig. 61. Kinetic simulations of steady-state ATPase Activity and duty ratio
(**A**) The rate of product formation over time was determined at a series of actin concentrations and fit to the Michaelis-Menten equation to determine k_{cat} and K_{ATPase}. (**B**) The duty ratio was determined by finding the steady state population of each of the intermediates in the ATPase cycle and plotting the fraction of the actin-attached states as a function of actin concentration. The rate constants used for the simulations were as given in Table 11, except that k_{+A} ($\mu M \cdot sec^{-1}$) = 25 for WT, R712G, and WT; and k'_{+PWF} (sec^{-1}) = 368 for R712G.

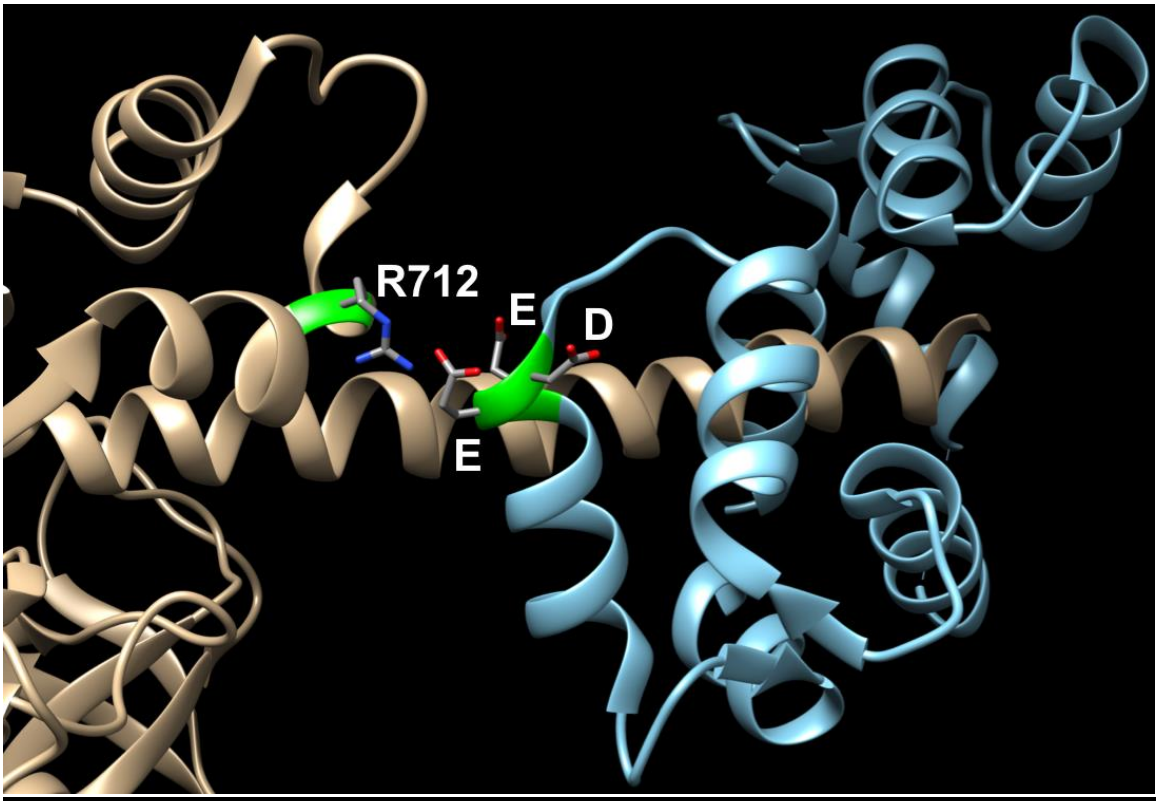

Fig. 62. Close-up of the potential interactions between R712 and negatively charged amino acids of the essential light chain

The crystal structure of myosin V complexed with calmodulin (PDB: 4ZLK) which demonstrates the negatively charged amino acids that could potentially interact with R712 of the converter domain. The calmodulin is highlighted in blue and the myosin heavy chain is shown in brown. The negatively charged amino acids in calmodulin depicted are D118, E119 and E12

CHAPTER 6: FUTURE DIRECTIONS AND CONCLUSIONS

This chapter contains material derived from my published papers[1-4], including reproduced and adapted figure subpanels, paraphrased sections, and sentences that succinctly summarize these published topics.

6.1 FUTURE DIRECTIONS 1

Topic 1: (TR)2FRET in intact skeletal muscle fibers

HYPOTHESIS:

The mechanical work performed by striated muscle, and the effect of mechanical load on that muscle, has been studied in numerous ways for over 90 years [179]. Structural characterizations of myosin, the force generating molecule in muscle, has been performed in the absence of load using techniques such as X-ray crystallography [85] and cryo-electron microscopy [180]. While the presence of load has a known effect on the mechanochemical coupling and function of myosin, load has only been studied with techniques that lack direct structural information of the myosin molecule itself. These techniques include motility assays [181], single-molecule laser traps [182], the inferred but unquantified internal strain of two-headed heavy meromyosin (HMM) in solution [183], and muscle fibers [184]. A strategy to bridge these areas of myosin research, unloaded high-resolution structure on the one hand and loaded studies lacking structural information on the other, is an identified direction for future study in the field [30] ,[185]. *My central hypothesis is that structural information on the myosin lever arm swing, associated with the weak-to-strong transition and force generation in myosin's ATPase cycle, can be directly measured in the presence of load in permeabilized muscle fibers using a myosin biosensor and the FRET between two fluorophores. Further, I hypothesize that the*

structural transitions observed in the presence of load will differ from unloaded FRET-based measurements of lever-arm swing [43] by slowing the kinetics of this transition.

SPECIFIC AIMS:

1. *Investigate the structural kinetics of myosin's lever arm helix (LAH) in detergent-permeabilized skeletal muscle fibers through site-directed labeling and the detection of transient time-resolved FRET (TR^{2}FRET).* The coupling of structural and biochemical kinetics of myosin in muscle fibers will be elucidated with single-turnover ATPase experiments using photo-activated and fluorescently-labeled "caged ATP" [186]. This investigation will be performed in the absence and presence of steady-state load, achieved through the use of muscle fibers suspended between a force transducer (FT) and servomotor (SM), also called an electromagnetic puller. Known and effective labeling sites from previous characterizations of protease-digested myosin fragments—on the regulatory light chain (RLC) and nucleotide—will be used [43]. I predict that structural transitions of full length myosin in muscle fibers, even in the absence of load, will differ from *in vitro* experiments using digested fragments of myosin due to compliance in the S2 region of myosin and from thick and thin filament-associated proteins such as myosin binding protein-C (MyBP-C) that will be present in fibers. In addition, I predict that the presence of load on the muscle fiber will slow the powerstroke transient given that load has been shown to slow the rate-limiting step of strong binding between actin and myosin in recent single molecule studies [185].
2. *Directly observe structural kinetics of myosin's LAH during transient millisecond-scale stretch and relaxation in skeletal muscle fibers between a FT and SM.* In Aim #1 the structural kinetics of myosin's LAH will be measured in the absence of load, and

under steady-state load. But in order to observe structural kinetics during transient forces, both external and internal to the fiber, the use of an ATP regenerating system will be necessary, to ensure that the fiber stretch and the associated structural perturbations in myosin is the only transient being detected via FRET, and not the binding and turn-over of caged ATP. The same labeling scheme and structural detection method, TR^2FRET, will be used to characterize the structural transitions of myosin in real-time. The structural characterization of myosin's LAH swing under load and during active force generation has never been directly measured in intact muscle fibers before, but as mentioned earlier has been identified as an intriguing area of future research in myosin that remains unexplored [30], [185].

3. *Further characterize the structural kinetics of myosin's LAH swing in muscle fibers using known disease-causing mutations, as well as phosphorylation in the expressed and exchanged-on fluorescently-labeled RLC. In addition, known myosin effectors will be characterized, including cardiac myosin effectors in cardiac muscle fibers.* Hypertrophic and dilated cardiomyopathy mutations in myosin [158], phosphorylation of myosin's RLC [187], and mutations in the RLC [188] have been shown to cause kinetic changes in loaded cardiac myosin. But such studies lack the insight of potential perturbation to the structural kinetics of myosin that mutation and phosphorylation likely cause. In addition, high-throughput drug discovery primary screens are performed in *in vitro* conditions to achieve consistent conditions and higher speeds, in the case of myosin this means working with the S1 or HMM subfragments to ensure solubility. Thus, the potential hits identified from the primary screen are not well characterized and further characterization with secondary assays is required for

validation. The experiments described in Aims #1 and #2 allow for a more physiologically relevant characterization of HCM and DCM causing myosin heavy chain and RLC mutations, as well as any potential structural consequences of RLC phosphorylation.

SIGNIFICANCE:

The principal function of muscle is to exert force, but actomyosin's structural transitions under load have never been directly measured. The goal of this study is to determine the structural dynamics of myosin's lever arm during steady-state load (Aim #1) as well as loaded muscle fibers during active contraction and relaxation (Aim #2), which will allow for further characterization of disease causing mutations, RLC phosphorylation, and small-molecule effectors (Aim #3). The importance of understanding the actomyosin interaction is clear from the wide range of disease conditions that result from mutations to the thick and thin filament proteins [158], and the promising prospect of small-molecule myosin effectors for treating these disease states [16].

While the structure of myosin has been characterized by X-ray crystallography [85] and cryo-EM [180], and structural transitions have been probed with tryptophan fluorescence and site-directed spectroscopy [189], these studies have all been performed in the absence of load on the myosin motor and also lack compliance in the S2 region of myosin, which is thought to peel back from the thick filament during active force generation *in vivo*. Numerous studies have been performed under load, including loaded gliding actin filament motility assays [50], three-bead optical trap experiments [185], and muscle fiber experiments [53] in which the fiber is stretched between a force transducer (FT) and servomotor (SM), but these studies all lack structural information about myosin

during force generation. What is needed is structural information on loaded single molecule myosins or an ensemble measurement of the physiologically relevant muscle fiber. An ensemble intermolecular measurement of full length myosin structural transitions of myosin's lever arm helix (LAH) is proposed here. Note that the "intermolecular" measurement is essentially intermolecular because the labeling sites on the bound RLC and bound nucleotide results in labeling during the entire ATPase kinetic cycle of myosin.

This study aims to measure the structural dynamics of myosin in chemically skinned skeletal muscle fibers from rabbit during load, stretch, and relaxation. This increase in technical capability from previous published work from our lab and other myosin labs is achieved by combining two techniques: 1) single muscle fiber preparations in which the fiber is suspended between a force transducer to measure steady state and transient forces, and a servomotor or electromagnetic puller to achieve variable loads [190], and 2) transient time-resolved FRET measuring intermolecular distance changes between myosin's catalytic domain and lever arm helix [43].

The first technique, single muscle fiber preps, has been used to characterize the numerous isoforms of the myosin heavy chain gene (MYH) ranging from fast and slow twitch skeletal muscles, as well as cardiac, embryonic, extraocular and jaw muscle isoforms [190]. In addition, the technique also has been used to characterize differences between striated muscle across species: insect, frog, mice, rabbits, and humans [190]. Through the use of detergents, the muscle fibers are permeablized or "skinned" to allow varying degrees of Ca^{2+} activation (full activation at pCa = 4.5, partial activation at pCa 5.8) [191]. In addition, this technique allows for the characterization of a broad range of contractile properties of the sarcomere: from length-tension relationships (Fig. 63), force-

velocity relationships, power output, maximum speed of shortening, force enhancement during stretch, and force reduction after load [190]. Kinetic properties including rates of force development following fiber shortening, to cross-bridge (XB) stiffness, and rates of XB attachment and XB detachment in stretch activation experiments (Fig. 64) [53] can also be determined for systematic comparisons.

The second technique, TR^2FRET, has been used in unloaded *in vitro* experiments to provide direct measurement of intermolecular structural transients in myosin during force generation or the weak-to-strong transition [189], [43]. This technique utilizes direct-waveform recording of the fluorescence emission spectra from the donor fluorophore after a five-nanosecond laser pulse to excite the donor fluorophore, followed by sub-nanosecond detection of the fluorescent decay time constant. Model dependent fitting of the amplitudes and time constants describing these decay parameters are directly related donor fluorophore. Further model dependent fitting of the distances and FWHM of a Gaussian distribution of that distance between donor and acceptor fluorophores allows for direct, real-time detection of myosin's lever arm swing.

A recently developed labeling scheme [43] allows for the measurement of TR^2FRET without mutating the heavy chain. The novel application of TR^2FRET to single muscle fibers stretched between a FT and SM is possible because the labeling scheme leaves the myosin heavy chain unperturbed, allowing for the use of tissue-derived muscle fibers and leaving associated thick and thin filament proteins intact.

In addition to initial characterization of intermolecular structural kinetics of myosin in intact loaded detergent-permeablized muscle fibers, further insight into the structure-function relationship of myosin will be possible including known affectors of sacromeric

contractility such as phosphorylation [187], mutation [188], [158], known myosin and thin filament effectors [53], and cardiac muscle fibers [192]. This approach is distinguished by 1) its dual emphasis on structure and kinetics achieved through nanosecond-resolved FRET during the millisecond-resolved transient phase of fiber stretch and relaxation, and 2) the addition of load to this structural technique with single muscle fibers between a FT and SM.

Feasibility of nucleotide-to-light-chain FRET in skinned muscle fibers has been established [193], showing 15% FRET efficiency changes. This work, however, lacked transient information during force generation because only steady-state FRET measurements have been performed. In addition, low exchange rates for the fluorescently labeled light chain were observed from labeling of the essential light chain (ELC) instead of the RLC, which I propose.

RESEARCH DESIGN AND METHODOLOGY:

Single muscle fibers will be obtained from mice or rabbits with the tibialis anterior used for fast twitch glycolytic skeletal muscle characterization [194] and the soleus used for slow twitch [195]. In addition, the trabeculae from the ventricles of the myocardium from mice will also be characterized for cardiac muscle [53]. To provide a quantitative profile of the myosin isoforms present in the muscles used, immunohistochemical characterization will be performed using known MYH anti-bodies sufficient to distinguish between various muscle types [196].

In Aim 1, the use of caged-ATP has been shown to be effective for the study of ATPase kinetics [186], and in single muscle fiber preparations [184] for the study of force development. In addition, this will allow a lower concentration of labeled ATP,

such as Cy3ATP, to be used and allow single turnover experiments to be performed in the absence and presence of steady-state load.

In Aim 2, the use of an ATP-regenerating system for a fixed concentration of saturating labeled ATP will be required to simultaneous detect force-transients and TR^2FRET to observe the structural kinetics of loaded myosin. Several potential ATP regenerating systems are available, including common choices such as pyruvate kinase and PEP, creatine kinase and phosphocreatine, and in addition more exotic ATP regenerating systems [197] are available. It is likely that several ATP regenerating systems must be attempted because the ATP used will be fluorescently labeled in order to detect TR^2FRET.

The preparation of detergent-permeabilized or "skinned" skeletal muscle fibers is well reported [192], and briefly, it involves incubation in detergent such as 1% Triton-X 100 for one hour. The experimental single muscle fiber apparatus [53] required consists of a flow-cell between a FT and SM where the prepared muscle fiber is suspended between the two attachments. A laser excites the donor fluorophore through an optical path such as described in the literature, [43] and the emitted light is detected after passing through a band pass filter. A specialized detector developed by our lab is capable of detecting waveforms with sub-nanosecond resolution, as well as the detection of thousands of separate waveforms every 200 microseconds.

The detection of FRET using a donor fluorophore on expressed light chain that is labeled, purified, and then exchanged onto myosin, including intact thick filaments in skinned fibers has been reported [193]. While Caorsi et al. labeled the ELC, I propose exchanging onto the RLC which has also been demonstrated, and with higher efficiency

[198]. The acceptor fluorophore will be placed on the nucleotide [43], [193]. A large selection of labeled nucleotides are available commercially (Jena Biosciences), or may be synthesized and purified using HPLC. This labeling scheme is successful because nucleotide is bound to myosin for nearly its entire kinetic cycle, and importantly, the nucleotide is bound during myosin's detachment from actin, the recovery stroke, the rebinding to actin, and the power stroke [30].

Data collection and analysis:

Force transducer recordings of force and length, including unloaded fibers undergoing shortening upon activation with caged-ATP, steady state load, transient-stretch, and transient-relaxation will be fit to *n* exponentials through the use of common fitting software packages available in our lab such as Origin, and Kintek Explorer.

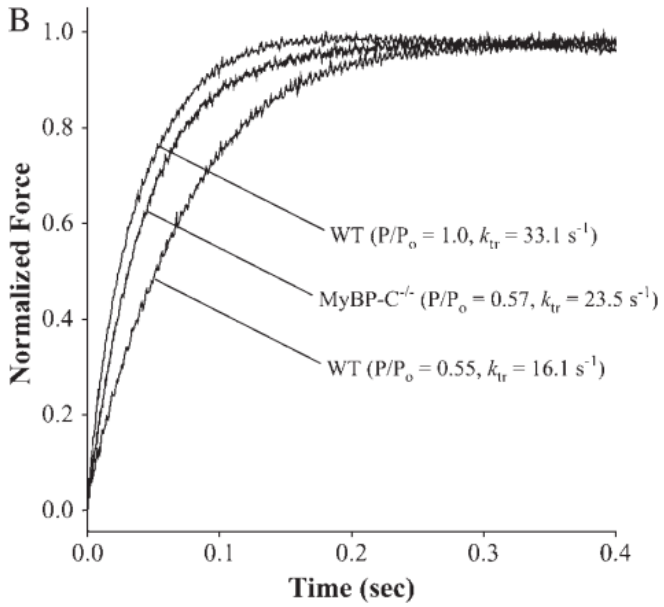

Fig. 63. Exemplar data of skinned myocardium strip illustrating loaded length shortening followed by force redevelopment
Labels apply to two fiber types and two pCa conditions (data from ref. [192]), from top label to bottom: WT fiber at full activation (pCa = 4.5), fiber from myosin binding protein-C deficient mouse model, and WT fiber at partial activation (pCa = 5.8).

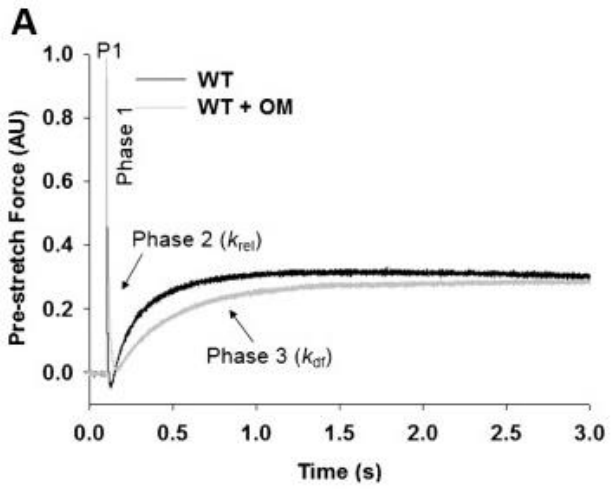

Fig. 64. Exemplar data of single human cardiac myocardium strip in a stretch activation response experiment
Comparison between skinned myocardium without the small-molecule effector omecamtiv mecarbil (OM) (data from ref. [53]). The fibers in high Ca^{2+} buffer were stretched by 2% at the 0.1 second time point and held at this length for several seconds. Four pieces of information are obtained from this experiment: P1 is the instantaneous rise in force. Phase 1 is the rise of the curve, indicative of the immediate force response. Phase 2, fit to the rate constant k_{rel}, indicates rapid actomyosin cross bridge (XB) detachment during relaxation under strain. Phase 3, fit to the rate constant k_{df}, indicates XB recruitment during the delayed force development after the stretch (phase 1 to P1) and relaxation (P2).

The detection of TR^2FRET, and recording of thousands of transient fluorescent waveforms after pulsed laser excitation, requires complex instrumentation and ultra-fast digitization of the waveforms, which was first demonstrated in our lab [43]. The TR^2FRET data is analyzed globally using a software package FargoFit developed in our lab. The data analysis involves fitting the donor-only exponential to one or more amplitudes and lifetimes based on the shape of excitatory laser pulse or IRF. This donor-only waveform serves as a no FRET limit to fit donor plus acceptor samples where model-dependent global analysis of the detected waveforms' altered lifetimes in the presence of FRET is analyzed and fit to one or more Gaussian distance distributions where peak center and full-width half max are calculated [189]. The model-dependent fit

used assumes the observed FRET changes correspond to structural transitions within myosin heavy chain, namely the bending of the LAH. The FRET changes observed for protease-digested myosin fragments in solution studied in our lab are best fit to a model in which the mole fraction of myosin molecules in the bent (lever up in crystal structure 2MYS) and straight (lever down in crystal structure 1BR1), and thus, in ensemble measurements, is the main change observed during the recovery and power stroke.

Alternative approaches:

While the RLC labeling site proposed has been shown to be effective [43], alternative labeling sites, including on the ELC are possible [193]. Single skeletal muscle fibers have been used to measure FRET changes between the exchanged-on and labeled recombinant ELC and fluorescently-labeled nucleotide bound in myosin's nucleotide pocket [193]. In this ELC-exchanged study in muscle fibers, both confocal microscopy and fluorescent lifetime imaging (FLIM) were used. While this study lacked dynamic force or dynamic fluorescent measurements, which this proposal sets-out to do (Aims #1 and #2), it does establish the possibility of using recombinant light chains allowing for several possible labeling sites on the light chain.

Fluorescently labeled nucleotides are readily available (Jena Biosciences), and have been shown to be effective in providing what is essentially intermolecular FRET between the bound nucleotide in myosin's nucleotide-binding pocket and the fluorescently labeled light chain [193], [43]. The Cy3-ATP used previously in our lab [43] involves labeling on the 2' or 3' hydroxyl of the ribose (ribose modified). Several additional fluorescently labeling sites on the ATP base (base modified) are commercially available (Jena Biosciences).

Single muscle fiber experiments have been performed on a range of skeletal muscles including the diaphragm, psoas, flexor digitorum brevis, and in a range of species such as mouse, rabbit, pig or cow for cardiac [190]. Recently, the ability to use cultured mouse embryonic stem cells to generate striated and contractile muscle fibers has been demonstrated [199]. These studies allow for the potential to study heavy chain mutations in myosin with or without reliance on animal models.

While loaded muscle fibers containing a biosensor capable of detecting intermolecular conformation changes in myosin associated with force generation is the best technique to test the hypotheses laid out in the proposal, an alternative technique, which lacks the clear quantification of the load experienced by the ensemble of myosin molecules of Aims #1 and #2, is possible through the use of *in vitro* gliding filament motility assays which include utrophin or α-actinin for simulating load [50]. In this cited study truncated utrophin molecules are laid down on the cover slip to bind to and provide resistance to the gliding actin filaments which move due to association with recombinant myosin S1 fragments containing a C-terminal GFP bound to an anti-GFP tag bound on the coverslip. Using the same myosin biosensor proposed (labeled RLC to labeled nucleotide), and using TIRF microscopy to detect both the fluorescently labeled gliding actin and the FRET changes of the biosensors associated with the myosin bound to the gliding actin, the role of force and load on myosin's structural kinetics could also be elucidated. This approach, however, lacks several advantages of the single skinned muscle fibers proposed, namely the 3D geometry of the intact sarcomere, the compliance of myosin's S2 domain, and the actin-associated regulatory proteins such as the troponins and tropomyosin.

Finally, the quintessential technique to study load in myosin is the single molecule three-bead optical trap experiment [200] in which an anti-GFP coated silica bead is bound to a cover slip. These bound beads are sparsely coated with GFP-tagged recombinant myosin, and finally an actin "dumbbell," suspended between two streptavidin coated polystyrene beads in solution are held in a dual laser trap and suspended over a fixed bead containing bound myosin [185]. This technique has yet to be used in combination with single molecule FRET because the overwhelming amount of light from the laser traps. By extending the distance from the actin dumbbell beads to the actin filament between the beads, using DNA extensions for example, the emitted fluorescence due to FRET may be detectable.

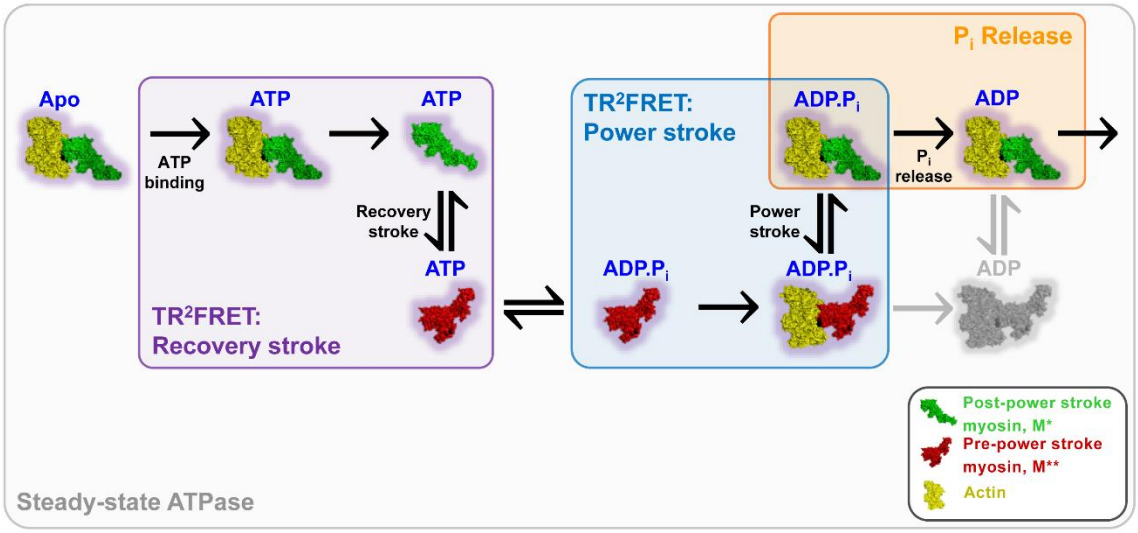

Fig. 65. Myosin's chemomechanical kinetic cycle
The four colored rectangles above (purple, blue, orange, and grey) highlight key biochemical and structural transitions investigated in Aim #1. Myosin undergoes three major changes in this cycle: biochemical state (blue text), actin-association state (yellow actin), and structural state (vertical transitions).

Topic 2: $(TR)^2$FRET in intact cardiac muscle fibers

Significance

My fundamental focus is to elucidate the kinetics of cardiac myosin's force-generating lever arm swing using direct, real-time detection, and to connect this molecular information to the macroscopic phenomenon of muscle contraction. Uncovering the link between protein function and physiology, in health and disease, is among the most important problem in biology and biophysics. Existing schemes for myosin's kinetic cycle attempt to explain actin-myosin-ATP energy transduction (Fig. 65), including the allosteric coupling between proteins and substrates, but they remain speculative because high-resolution protein structures obtained with X-ray crystallography only reveal discrete, stationary structural states of myosin[30, 161]. This proposal aims to elucidate how lever arm rotation in the myosin motor protein is coupled to force generation in the myocardium, and how this coupling is perturbed by myosin-targeted heart failure therapeutics, using a transient structural measurement to simultaneously acquire and relate molecular changes with muscle contraction. Our lab has developed technology to detect fluorescence resonance energy transfer (FRET)-based distances on fluorescently labeled myosin (Fig. 66A) as a function of time, following stopped-flow, biochemically-initiated mixes. Furthermore, using direct waveform recording (Fig. 66B), we are able to acquire fluorescence decays 100,000 times faster than traditional single photon counting[201]. This technology, currently applied *in vitro*[43], provides insight on the allosteric communication among the key elements of the molecular motor myosin. Model-dependent fitting of the fluorescence decay of FRET between the fluorescent probes—with FRET serving as a molecular ruler—results in sub-nanometer, structurally resolved populations (Fig. 66C,D) that closely match

the distances predicted from crystal structures[31, 202] (Fig. 66A). Using a 5 kHz pulsed laser, we rapidly detect fluorescence waveforms to generate time-resolved kinetics data (Fig. 66E-G). Combining structural kinetics with experiments on myosin's key entropic drive, inorganic phosphate (Pi) release, has allowed us to directly detect and elucidate the chemomechanical coupling of skeletal myosin[43] and cardiac myosin[44] in solution.

This novel fluorescence technology, $(TR)^2$FRET, that I have applied in two publications in PNAS—a second-author and a first author manuscript currently undergoing minor revisions—offers the first true capability for quantifying "structural kinetics:" resolving protein structural states in real time during a sub-millisecond-resolved biochemically-initiated transient. My proposal will apply this technology to resolve the effects of recently discovered and clinically relevant heart failure drugs to perturb the allosteric coupling of cardiac myosin, providing otherwise unobtainable insight into these small molecules' mode of action. Recent discoveries indicate that effective treatments for heart failure can be obtained by perturbing the kinetics of myosin's actin-activated ATP enzymatic activity with a small molecule, omecamtiv mecarbil (OM)[16]. OM directly binds to and increases myosin's force generation[53], but dramatically slows its motility[50], and sits at a novel binding site near myosin's converter domain and lever arm helix (LAH)[49]. My recent work currently in revision, utilizing $(TR)^2$FRET, has provided a molecular explanation for all of these results[44]. Briefly, my data reveal that OM alters cardiac myosin's force-generating structural transition, the powerstroke, by causing the accumulation of actin-bound pre-powerstroke cross-bridges that causes a large lag in

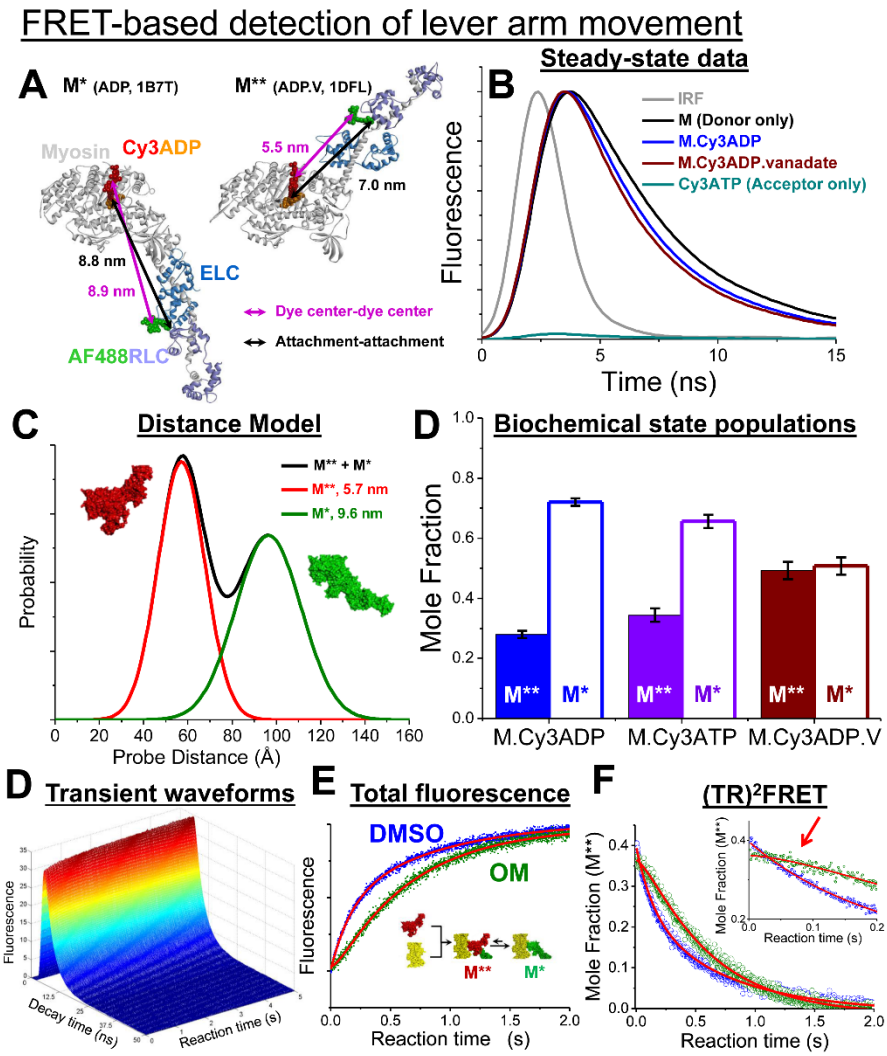

Fig. 66. Labeled myosin for use in time-resolved FRET experiments.
A) Myosin biochemical state transitions shown in crystal structures 1B7T and 1DFL with modeled fluorescent dyes. RLC is labeled with donor probe, AF488, via single Cys, then exchanged with endogenous RLC. The acceptor fluorophore, Cy3, is attached to the nucleotide, ATP or ADP. While HMM will be used, only S1 fragment of myosin is shown. **B)** Normalized steady-state fluorescence intensities reveal a change in lifetime, dependent on the biochemical state of myosin. Instrument response function (IRF) is detected laser pulse of non-fluorescent sample. **C)** Best fit of fluorescence decay waveforms of B, the two-Gaussian distance distribution closely match the expected distances of panel A. **D)** The population of each structural state from distance distribution fit to data in B. **E)** The time-resolved FRET (TR-FRET) waveforms in B are collected in rapid succession every 0.2 ms following mixing in a stopped-flow apparatus called “transient TR-FRET,” or (TR)^{2}FRET. **F)** Total fluorescence of waveforms in E. Inset: two-syringe stopped flow mix and predicted structural changes. **G)** Waveform decays for every time point in E, fit to a two-distance model as in C, plotting the mole fractions of the lever up M** state shown in A and depicted in D. Inset: first 200 ms highlighting the OM-induced lag in the power stroke.

the powerstroke (Fig. 66F,G, G inset: red arrow). This was not detected with biochemical assays[16, 17], and was only revealed with our assay with structural sensitivity[44]. This work is timely as OM just entered Phase III clinical trials in December of 2016. Further insights of OM's effect *in situ*, in skinned myocardium, will be investigated in Aim 2, using the methodology and novel application of $(TR)^2$FRET in loaded myocardium, developed in Aim 1. The acquisition of high-resolution structural information on myosin's lever arm orientation in skinned myocardium will provide clearer insight into how this orientation and its kinetics is coupled to force generation. I will also be able to compare solution experiments to myocardium mechanics experiments, to discover how the sarcomere's 3D structure and additional sarcomeric proteins such as myosin binding protein-C (MyBP-C)[203] may affect myosin's force-generating structural transitions. Small molecules have proven to be powerful probes for dissecting protein structure-function relationships when coupled with $(TR)^2$FRET[43].

Heart failure is the leading cause of mortality in the United States[204]. A primary defect in heart failure is a loss in cardiac contractility[205] resulting from disruption to a range of molecular factors, including: Ca^{2+} homeostasis, metabolism, gene expression levels, and mutations in sarcomeric proteins[206]. Muscle myosin couples the free-energy associated with myosin binding to actin and ATP, and the sequential release of products, to drive force-generating structural transitions, notably LAH rotation[161]. This rotation, termed the power stroke, converts the free energy liberated from ATP hydrolysis into mechanical work (Fig. 65)[53, 207]. Structural changes in the myosin nucleotide-binding pocket, following actin binding, are hypothesized to initiate these transitions, and thus, initiate force generation[53, 207]. This allosterically regulated, mechanochemically

coupled motor protein is also regulated by small-molecule effectors[9, 16, 134], altered by the presence of load[53, 181-183] (Aim 1), and perturbed by mutations in the RLC[188] (Aim 2).

APPROACH:

Aim 1: Expand $(TR)^2$FRET to skinned myocardium: investigate the effects of the 3D myofilament lattice and load on cardiac myosin's structural dynamics.

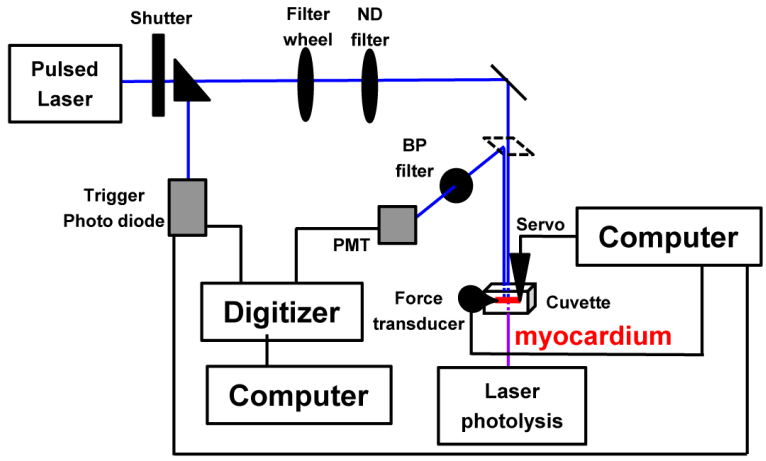

Fig. 67. Skinned myocardium mechanics
Proposed experimental apparatus for simultaneous detection of myocardium mechanics as in A with a force transducer, and pulsed laser $(TR)^2$FRET.

a) **Structural kinetics of myosin's lever arm helix (LAH) in the presence and absence of steady-state load.** The coupling of structural and biochemical kinetics of myosin in detergent-permeabilized myocardium will be elucidated with single-turnover experiments using commercially-available, photo-labile, and fluorescently-labeled

"caged ATP"[186]. This investigation will be performed in the absence and presence of steady-state load, with skinned myocardium suspended between a force transducer (FT) and servomotor (SM) (Fig. 67). I hypothesize that myosin's structural dynamics in myocardium in the absence of load will differ from *in vitro* experiments due to compliance in the S2 region of myosin, and because of thick and thin filament-associated proteins such as myosin binding protein-C (MyBP-C) will affect myosin's function. I hypothesize that the presence of steady-state load on the myocardium will slow the powerstroke transient. Load is known to slow the rate-limiting step of ADP release, gating strong binding between actin and myosin, in recent single molecule studies[185].

- *Myocardium*: The left ventricular myocardium of rabbits will be characterized[208]. To provide a quantitative profile of the myosin isoforms present in the tissue used, established immunohistochemical characterization will be performed using known myosin heavy chain anti-bodies sufficient to distinguish between various myosin isoforms[196].
- *Skinning and RLC exchange*: To exchange the endogenous RLC for expressed, AlexaFluor 488 labeled RLC (Fig. 66A, AF488RLC), the myocardium must be permeabilized. The preparation of detergent-permeabilized or "skinned" myocardium is well reported[192], and involves incubation in detergent such as 1% Triton-X 100 for one hour. Light chain exchange in skinned trabeculae is demonstrated in the literature[209].
- *Steady-state load*: To fully utilize the capabilities of $(TR)^2$FRET, a transient is required. To cause a rapid perturbation in the skinned myocardium and then detect the response

of myosin's LAH orientation, I will initiate a biochemical transient with commercially available photo-labile "caged"-Ca^{2+}, or caged-ATP in saturating Ca^{2+}, to activate the thin filament regulatory proteins[210].

- *Caged-ATP*: Slow diffusion in skinned myocardium preparations prevents the use of stopped-flow mixing and I will instead use caged-ATP, which has been shown to be effective for characterizing ATPase kinetics[186], and skinned myocardium mechanics assays to study force development[184], as has caged-Ca^{2+} [211]. Nucleotides that are both fluorescently labeled and caged are commercially available (Jena Biosciences), as is caged-Ca^{2+} (ThermoFisher).
- *Myocardium mechanics*: The muscle fiber apparatus[53] required (Fig. 67B) consists of a flow-cell between a FT and SM where the prepared skinned myocardium is suspended between the two attachments. This experimental apparatus is commercially available (Aurora Scientific, 1500A) and also available for my use in my building in the lab for Dr. Osha Roopnarine; and the expertise to run the instrument will be part of my fellowship training. The University of Minnesota has a large range of muscle researchers with expertise in fiber and myocardium mechanics measurements, including Drs. Joseph Metzger, Dawn Lowe, Osha Roopnarine, and Vincent Barnett.
- *Intermolecular FRET to detect myosin's structure*: The detection of FRET using a donor fluorophore on expressed and exchanged light chain and an acceptor fluorophore in the nucleotide pocket, within skinned fibers has been reported with sizeable 15% FRET changes[193]. Caorsi et al. labeled the essential light chain, ELC; I propose exchanging onto the RLC which has also been demonstrated, and with higher exchange efficiency[198]. The acceptor fluorophore will be placed on the nucleotide[43, 193].

This labeling scheme is successful because a single nucleotide is bound to myosin for nearly its entire kinetic cycle: myosin's detachment from actin, the recovery stroke, the rebinding to actin, and the power stroke[30] (Fig. 65). An alternative labeling scheme with preliminary data is discussed in Aim 2 and Fig. 68.

b) Structural kinetics of myosin's LAH during transient millisecond-scale stretch and relaxation in skinned myocardium. In Aim #1a the structural kinetics of myosin's LAH will be measured both in the absence and presence of steady-state load. Further insight into how myosin's lever arm orientation is coupled to force generation will be investigated using structural kinetics during transient forces. A high-resolution structural characterization of myosin's LAH swing during myocardium relaxation and active force generation has not been reported in skinned myocardium, as of yet. I hypothesize that the structural transitions observed in the presence of load will differ from unloaded FRET-based measurements of lever-arm swing[43] by slowing the kinetics of this transition in a force-dependent manner, and may reveal a two-part power stroke suggested by recent studies[153, 212].

- *Transient forces*: In addition to a biochemically-initiated transient (Aim 1a), a mechanically-initiated transient from rapid stretch or relaxation of the skinned myocardium by the servomotor of the fiber mechanics apparatus (Fig. 67B) will be examined. I will use an ATP regenerating system to maintain a constant concentration of ATP to ensure the stretch or relaxation of the myocardium, and not ATP binding, is the transient detected. The central goal is the simultaneous detection of force-transients (Fig. 67A) and $(TR)^2$FRET (Fig. 66E-G) to directly observe the structural kinetics of loaded myosin in relation to force generation.

- *ATP regenerating system*: Pyruvate kinase and PEP, creatine kinase and phosphocreatine, or less common ATP regenerating systems[197] may be required because $(TR)^2$FRET utilizes a fluorescently labeled nucleotide. However, ribose-modified fluorescent nucleotides have a small effect on myosin[213], and like myosin, pyruvate kinase binds ATP with the ribose partially solvent exposed (PDB: 4FXF).

***Outcomes and alternatives for Aims 1a and 1b*:**

Applying $(TR)^2$FRET technology developed in solution (my previous work[43]) to skinned myocardium (Aim 1a-b) will allow detailed structural insight to the connection between LAH structural kinetics and load on the myocardium.

- While the RLC labeling site proposed has been shown to be effective[43, 44], alternative labeling sites, including on the ELC are possible[193]. Feasibility for light chain exchange within permeabilized muscle fibers has been demonstrated. Single skeletal muscle fibers have been used to measure FRET changes between the exchanged-on and labeled recombinant ELC and fluorescently-labeled nucleotide bound in myosin's nucleotide pocket[193]. In this cited ELC-exchanged study, confocal microscopy and fluorescent lifetime imaging (FLIM) were used, but it lacked dynamic force or dynamic fluorescent measurements, which this proposal sets-out to do (Aims 1a-b). This study does establish the possibility of using recombinant and fluorescently labeled light chains and fluorescent nucleotides in skinned muscle tissue.

Aim 2: Skinned myocardium perturbed by small-molecule effectors and RLC mutations.

Building on the methodology of Aim 1, I will also apply $(TR)^2$FRET in skinned myocardium, with disease-relevant mutations in myosin's regulatory light chain (RLC), R58Q and N47K, that cause kinetics changes in loaded cardiac myosin[188]. A small-

molecule cardiac myosin effector in clinical trials dramatically affects myosin's kinetics[9, 16, 134], structural dynamics *in vitro*[44], and skinned myocardium mechanics (Fig. 67A)[53]. I will characterize how these mutations and small-molecule effectors affect myosin's structural dynamics in skinned myocardium, including the ability of these heart failure therapeutics to alleviate the mutations' perturbations.

***Outcomes and alternatives for Aim 2*:**

- Skinned myocardium is a logical approach to determine the connection between myosin's LAH orientation and force generation in cardiac tissue. However, an alternative technique, the loaded *in vitro* gliding filament motility assay, with utrophin or α-actinin for simulating load [50] could also be developed. Using the same labeling scheme proposed (Fig. 66A), and using TIRF microscopy to detect both the fluorescently labeled gliding actin and the FRET changes of the biosensors associated with the myosin bound to the gliding actin, the role of force and load on myosin's structural kinetics could also be elucidated as an alternative strategy.
- If the fluorescent nucleotide-labeling scheme is ineffective in skinned myocardium mechanics experiments an alternative approach is to use fluorescently labeled and expressed myosin V (provided by Dr. Yengo's Lab at Penn State), for which I have acquired preliminary data in solution (Fig. 68). The Yengo Lab is developing this same labeling scheme in expressed human beta-cardiac myosin, which could be used in loaded *in vitro* motility assays[50] described above.

Summary and Outlook – This is an ambitious project and my preliminary data indicates the feasibility of the project. My experiences over the past two years, and the collaborative community at UMN, prepare me to succeed. I have demonstrated my capability with two

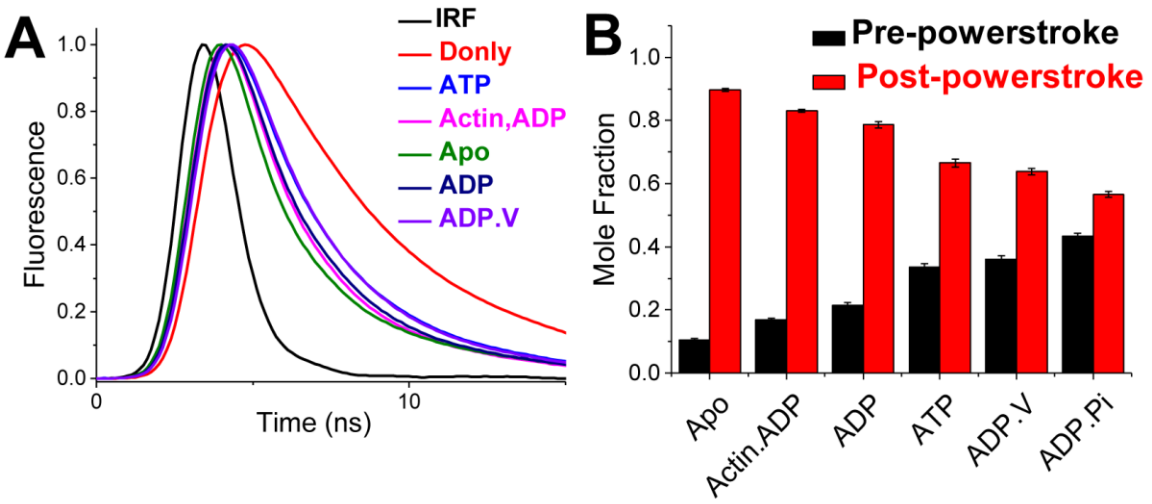

Fig. 68. Alternative labeling scheme
A) FlAsH tagged N-terminus on recombinant myosin V heavy chain and exchanged, labeled calmodulin. **B)** Best-fit model of two distances, termed pre- and post-powerstroke, and the relative mole fractions of each over varied biochemical conditions.

publications in closely related work. I have familiarized myself with, and contributed to, the literature in the field. I have established feasibility of all three aims, and many of the optimizations that could be time consuming have been completed in solution-based $(TR)^2$FRET,[43] or demonstrated in other labs. I am positioned to make efficient progress, and publish, on all of the proposed aims.

6.2 FUTURE DIRECTIONS 2

Topic 2: $(TR)^2$FRET in the in vitro motility assay

Significance

Hypertrophic cardiomyopathy (HCM) is the most common inherited disease of the human heart. HCM results in left ventricular wall thickening in patients (Fig. 4C-D) [9, 16, 120, 214], affecting 1-in-500 individuals[23]. 80% of patients with HCM have a mutation

in the force-generating motor protein myosin, or proteins that bind myosin[8]. In just the last decade it has been hypothesized that dimeric myosin is biochemically regulated via an auto-inhibited structural state involving protein-protein interactions (Fig. 5A) [208, 215, 216]. Disruption of this state is hypothesized to be a molecular cause of HCM[120, 214]. Regulation of this state is thought to be important for both muscle contraction and relaxation[119]. My most recent work[2] has provided the first biochemical characterization of this auto-inhibited state in vitro, and showed that a putative drug (mavacamten) stabilizes this state (Fig. 5A).

In my thesis research I have characterized the molecular mode of action of OM, now in phase III clinical trials. I found that omecamtiv mecarbil inhibits the force-generating powerstroke and changes the rate-limiting kinetic step in the ATPase cycle [217]. Thus, my thesis research has resulted in the molecular characterization of two new myosin-targeting drugs currently in clinical trials[217], [3].

I have also characterized disease-causing mutations[7], and collaborated with the lab of Professor Chris Yengo at Penn State's Hershey Medical School on studies of human β-cardiac myosin and a non-muscle myosin isoform (two manuscripts in preparation, one co-first author). Our lab's newest and most exciting direction is the use of structural biophysics, including fluorescently-labeled myosin, to discover and design new small-molecule drugs for the treatment of heart failure and heart disease [218, 219]. My thesis work has contributed to the proof-of-concept results that have advanced these drug-discovery efforts. Our lab has recently collaborated with one of the largest pharmaceutical companies in America to expand our drug-discovery capabilities.

My thesis work has also focused on basic science research, including directly characterizing the structural kinetics of skeletal and cardiac myosin, elucidating two distinct kinetic pathways by which myosin converts the free energy of ATP into mechanical work [43, 217].

Proposed Research Projects for research at a Primarily Undergraduate Institution (PUI):

To tailor my expertise in biochemistry and biophysics to a research program appropriate for undergraduate students at a primarily undergraduate institution, I have identified three feasible research topics that will provide students at UWEC with challenging projects that they will be able to make significant progress on during a summer, or over a one- to two-year time period. Project #1 closely aligns with my current expertise and my thesis advisor's current interests, but applies the technology and methodology in new directions. Project #2 builds on my experience purifying muscle proteins, and utilizes these proteins in different applications, to directly visualize myosin motors moving actin, via fluorescence microscopy. Project #3 diverges from my thesis research on motor proteins and focuses on the polymer biophysics of protein folding, protein dynamics, and folding stability; while still making use of my experience with fluorescence spectroscopy. Together, these three research projects will provide students with several exciting opportunities to gain proficiency in a wide-array of techniques to study the biochemistry of proteins. The knowledge and skills that students acquire will be valuable to those pursuing multidisciplinary careers in scientific research, or continuing on to graduate school.

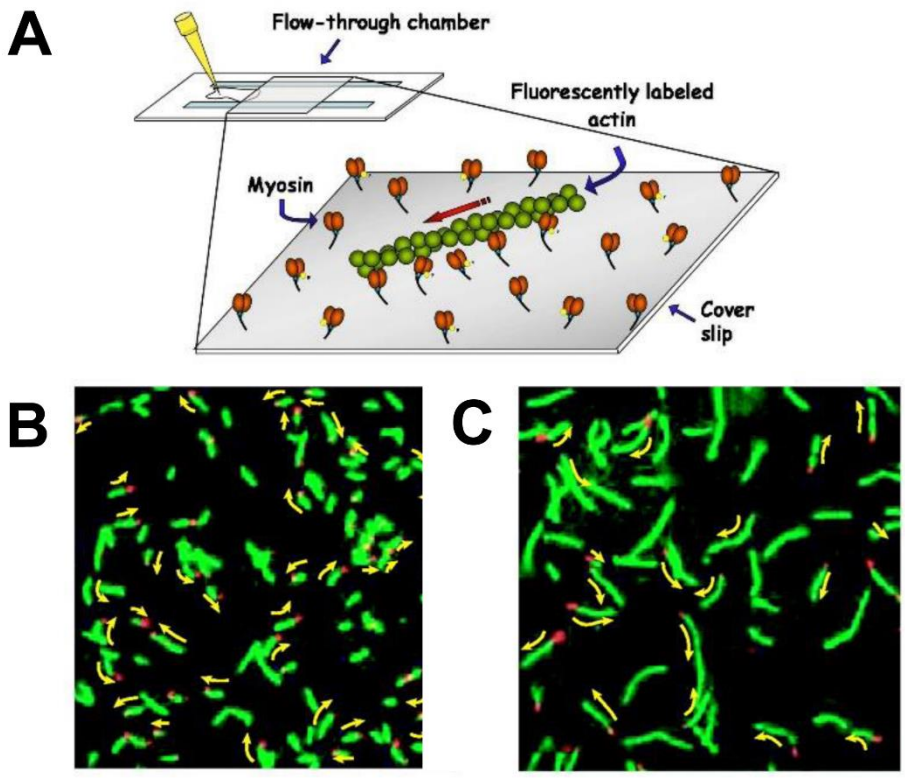

Fig. 69. The gliding-actin motility assay allows the direct visualization of myosin motors moving fluorescently labeled actin
(**A**) This simple and inexpensive assay involves a glass microscope slide coated in nitrocellulose that myosin motors (orange) are immobilized on. Double-sided tape and a glass cover slip form a flow chamber via capillary action. Fluorescently-labeled actin is then flowed in, and the movement of actin, due to an ensemble of myosin motors, causes movement of the actin filaments. (**B-C**) Exemplary data where researchers varied the length of myosin's lever arm [220]. They showed that with short lever arms, the actin traveled in one direction (B), but with longer lever arms the actin filaments reversed direction (C).

Project #1: Characterization of the motor protein myosin using biophysical and biochemical transient kinetics experiments.

- Muscle proteins can be purified from rabbit skeletal and porcine or bovine cardiac muscle that is commercially available, shipped fresh, and relatively inexpensive (Pel-Freez Inc.). The extracted and purified protein can be stored at -80 °C for 1-2 years, ideal for undergraduate research projects.

- Myosin's ATPase cycle can be analyzed at every step[88] using fluorescent actin or fluorescent ATP, and with methodology I developed as a graduate student [217].
- There are numerous important questions to be addressed in the myosin field, as simple as temperature and ionic strength dependencies of key steps in the cycle, to more advanced studies with disease-causing mutations and drug screening that could be accomplished with collaborations at the University of Minnesota.

Project #2: Mechanical characterization of myosin with the *in vitro* motility assay.

- Purified protein from muscle preps can be studied with spectroscopic techniques (Project #1), or with fluorescence microscopy using the *in vitro* gliding-actin motility assay (Fig. 69A). This technique involves direct visualization of fluorescently-labeled actin gliding on immobilized myosin attached to a glass cover slip (Fig. 69A).
- Movies of the mobile actin filaments are analyzed with software to determine velocity distributions. These velocities are related to an important parameter: the time each myosin spends strongly bound to actin (t_s). This is essential for determining how the ensemble force (F_e) of myosin motors in the assay, and also in intact muscle, arises from each single motor's force (f), the total time of ATP cycling (t_c), and the number of myosin heads available to generate force (N_a), see Eqn. 2 [8].

$$F_e = f\left(\frac{t_s}{t_c}\right) N_a \qquad \text{[Eq. 39]}$$

- Additional proteins, such as the actin-binding protein utrophin, can also be immobilized to the cover slip to approximate a resistive load against the force-generating myosin [50].

- As in Project #1, numerous parameters can be varied, including physiological stresses normally encountered in the cellular environment, such as oxidative stress that results in covalent modifications of the myosin protein [221].

Project #3: Protein folding, stability, and dynamics investigated with spectroscopy, molecular dynamics simulations, and commercially-available peptide synthesis.

- Numerous proteins have disordered structures, making them difficult to study with traditional structural techniques, such as X-ray crystallography and electron microscopy. These intrinsically disordered proteins (IDPs) or proteins with intrinsically disordered regions (IDRs, Fig. 70A) exist as an ensemble of structural states and may adopt conventional, well-folded secondary or tertiary structures when bound by a ligand or substrate, or when the chemical or dielectric environment of the protein changes.
- Recent work[222] studied a protein anchored in the lipid bilayer of the cell that contains an IDR that lies in a transitional dielectric region of the cell, between the aqueous extracellular region ($\varepsilon = 80$) and the lipid bilayer ($\varepsilon = 2$) (**Fig. 70**A). This portion of the protein, containing 60 amino acids, was commercially and inexpensively custom-synthesized and purified (Selleck Chemicals), (**Fig. 70**B, C).
- The protein was fluorescently labeled (**Fig. 70**C, green and blue circles) in the same way I label proteins, allowing FRET-based measurements to probe whether the protein was in an open and disordered, or compact and folded structural state under a range of solvent conditions. Computational software packages, termed molecular dynamics

simulations, allow for model-dependent and force-field dependent protein dynamics predictions to be compared to experimental results [222].

- IDPs are an exciting and relatively new area of research, and well suited to spectroscopic analyses because of their dynamic nature. Inexpensive commercial peptide synthesis permits a large number of polymer biochemistry questions to be asked and analyzed, including still fairly opaque topics such as protein folding[223] and the origins of life—hypothesizing that early life utilized a smaller toolkit of 5 to 12 building blocks (amino acids), instead of the 20 that all life uses today, to build the proteins that fold and function as enzymes and motors [224].

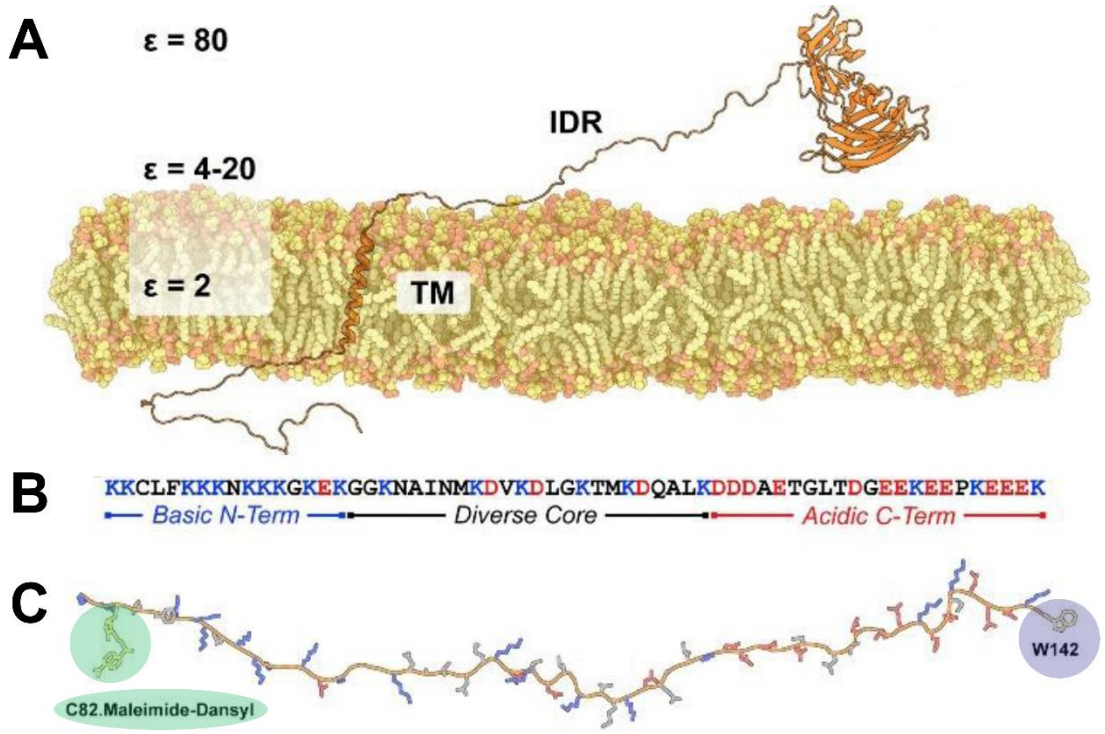

Fig. 70. Peptide synthesis allows small proteins, or portions of proteins, to be inexpensively studied with spectroscopic techniques
(**A**) In a recent publication [222], researchers chose an "unstructured" portion of a protein, or an IDR (intrinsically-disordered region), that lies in an area outside the cell with a range of dielectric constants, ε = 4-20. They hypothesized that this region of the protein would become structured or folded in certain conditions. (**B**) The peptide sequence studied, with positively charged (blue) and negatively charged (red) amino acids indicated with one letter codes. (**C**) The protein was fluorescently labeled at both ends to determine whether the polymer adopted a compact and folded or extended and disorder structural state under a range of solvent conditions.

Summary

Together, these three projects provide a multi-faceted undergraduate research plan to study protein biophysics and biochemistry using a variety of spectroscopy-based, microscopy-based and theoretical approaches. All three build on the expertise I gained as a graduate student.

6.3 CONCLUSIONS

Myosin family proteins use ATP hydrolysis to generate force and movement required for normal physiology. They drive muscle contraction, help control cell division and cellular motility, move organelles through the cytoplasm, and are important elements of the cellular mechanical-sensing machinery. The key to understanding how myosin and related enzymes function in cells, and how to modulate their activity in the presence of small-molecule effectors to treat disease or disease-causing mutations, is to determine how the protein's structural dynamics and biochemical kinetics are coupled. In the five published manuscripts I have been lucky to contribute to, in the David D. Thomas Lab at the University of Minnesota, I have made significant progress towards these goals.

First, the Thomas Lab and I used $(TR)^2$FRET and transient phosphate release assays to determine the coordination of LCD rotation and actin-induced dissociation of hydrolyzed P_i in fast skeletal muscle myosin. The detection of nanosecond-resolved TR-FRET in real time during the millisecond-resolved biochemical transient allowed direct and quantitative measurement of the mole fraction of pre- and post-power stroke LCD structural states and thus the transient state distribution of these states during the critical actin-activated power stroke. The major change in Gibbs free energy is associated with phosphate release and the weak-to-strong actin binding transition and not the large structural reorientation of the LCD. These results provide direct and vivid insight into one of the most enigmatic aspects of myosin enzymology. Our work also serves as an important primer for future studies of other enzymes such as kinesins, dyneins, small GTPases, nucleotide polymerases, and kinases, where questions regarding the coupling of allosteric structural and biochemical transitions remain unanswered.

Second, the Thomas Lab and I investigated the actin-induced structural kinetics of cardiac myosin's light-chain domain during the powerstroke, in order to determine how OM modulates the coordination between the phosphate release biochemical step and the force-generating rotation of the myosin LCD. Our results reveal a previously unknown aspect of OM's mode of action: the small molecular therapeutic changes the coordination between phosphate release and the powerstroke and inhibits the powerstroke by increasing the transition state free energy for actin-induced LCD rotation. These results provide novel molecular insight into OM's diverse range of effects in patients and *in vitro* biochemical studies.

Next, the Thomas Lab and I detected a biochemically auto-inhibited state in tissue-purified cardiac HMM. The kinetics and energetics of this state are consistent with the SRX observed in permeablized myocardium and thus we argue that the SRX state can be detected in solution. Mavacamten stabilizes this state, revealing a new mechanism for a drug's inhibition of two-headed cardiac myosin that was not previously seen in studies of single headed myosin. Actin interaction is able to disrupt the auto-inhibited state and accelerate the rate-limiting structural transition of head-head splaying that limits ATP turnover in HMM. Thus, weak interaction with actin and cardiac myosin can disrupt auto-inhibition, indicating that how the auto-inhibited myosin heads are tethered to the thick-filament backbone in muscle is critical. Mechanisms likely regulating this tethering include cardiac myosin RLC phosphorylation[130], binding of myosin-binding protein-C to the HMM portion of intact myosin in the thick filament [124], thick-filament mechano-sensing[131], and small molecules[132].

Finally, the Yengo and Thomas Labs and I demonstrated direct evidence for an allosteric pathway in myosin associated with positioning the lever arm in the pre- and post-power stroke states. We found that the two myosin-V mutations disrupt ensemble force, likely by altering intrinsic force or strain dependent detachment. We highlighted the importance of key residues and interactions in the allosteric pathway and identified potentially new mechanisms for positioning the force generating lever arm. Our work highlighted that mutations in this key allosteric pathway can change the kinetics of the recovery and power stroke as well as the equilibrium between the pre- and post-power stroke states. In addition, our studies demonstrated that point mutations can alter the rate and equilibrium constants that control the population of structural states without altering the overall conformation of the lever arm. Thus, therapies designed to shift the equilibrium between major structural states may be effective at rescuing the structural impact of the disease mutations. Our work provides a basis for future studies designed to examine the impact of disease mutations on key structural changes as a method of determining the mechanism of motor impairment and potential for therapeutic strategies to correct specific impairments.

BIBLIOGRAPHY

1. Muretta, J.M., et al., *Direct real-time detection of the structural and biochemical events in the myosin power stroke.* Proceedings of the National Academy of Sciences of the United States of America, 2015. **112**(46): p. 14272-7.
2. Rohde, J.A., D.D. Thomas, and J.M. Muretta, *Heart failure drug changes the mechanoenzymology of the cardiac myosin powerstroke.* Proceedings of the National Academy of Sciences of the United States of America, 2017. **114**(10): p. E1796-E1804.
3. Rohde, J.A., et al., *Mavacamten stabilizes an autoinhibited state of two-headed cardiac myosin.* Proc Natl Acad Sci U S A, 2018. **115**(32): p. E7486-E7494.
4. Gunther, L.K., et al., *Converter domain mutations in myosin alter structural kinetics and motor function.* J Biol Chem, 2019. **294**(5): p. 1554-1567.
5. Houdusse, A. and H.L. Sweeney, *Myosin motors: missing structures and hidden springs.* Current opinion in structural biology, 2001. **11**(2): p. 182-94.
6. Sweeney, H.L. and A. Houdusse, *Structural and functional insights into the Myosin motor mechanism.* Annual review of biophysics, 2010. **39**: p. 539-57.
7. Guhathakurta, P., et al., *A Cardiomyopathy Mutation in the Myosin Essential Light Chain Alters Actomyosin Structure.* Biophys J, 2017. **113**(1): p. 91-100.
8. Spudich, J.A., *Hypertrophic and dilated cardiomyopathy: four decades of basic research on muscle lead to potential therapeutic approaches to these devastating genetic diseases.* Biophysical journal, 2014. **106**(6): p. 1236-49.
9. Green, E.M., et al., *A small-molecule inhibitor of sarcomere contractility suppresses hypertrophic cardiomyopathy in mice.* Science, 2016. **351**(6273): p. 617-21.
10. Muretta, J.M., K.J. Petersen, and D.D. Thomas, *Direct real-time detection of the actin-activated power stroke within the myosin catalytic domain.* Proceedings of the National Academy of Sciences of the United States of America, 2013. **110**(18): p. 7211-6.
11. Malnasi-Csizmadia, A. and M. Kovacs, *Emerging complex pathways of the actomyosin powerstroke.* Trends in biochemical sciences, 2010. **35**(12): p. 684-90.
12. Llinas, P., et al., *How actin initiates the motor activity of Myosin.* Developmental cell, 2015. **33**(4): p. 401-12.
13. Caremani, M., et al., *The working stroke of the myosin II motor in muscle is not tightly coupled to release of orthophosphate from its active site.* The Journal of physiology, 2013. **591**(Pt 20): p. 5187-205.
14. Bloemink, M., et al., *The hypertrophic cardiomyopathy myosin mutation R453C alters ATP binding and hydrolysis of human cardiac beta-myosin.* The Journal of biological chemistry, 2014. **289**(8): p. 5158-67.
15. Sommese, R.F., et al., *Molecular consequences of the R453C hypertrophic cardiomyopathy mutation on human beta-cardiac myosin motor function.* Proceedings of the National Academy of Sciences of the United States of America, 2013. **110**(31): p. 12607-12.
16. Malik, F.I., et al., *Cardiac myosin activation: a potential therapeutic approach for systolic heart failure.* Science, 2011. **331**(6023): p. 1439-43.

17. Liu, Y., et al., *Omecamtiv Mecarbil modulates the kinetic and motile properties of porcine beta-cardiac myosin.* Biochemistry, 2015. **54**(10): p. 1963-75.
18. Humphreys, E. *Exploring the Human Cardiac Stem Cell Receptome*. Proteomics, Cardiovascular 2015 [cited 2019 03/05]; Blog]. Available from: https://www.thermofisher.com/blog/proteomics/exploring-the-human-cardiac-stem-cell-receptome/.
19. ABDPVTLTD.COM. *Cell Diagrams*. 2017 [cited 2019 20/01]; Available from: http://abdpvtltd.com/.
20. Warshaw, D. *Research Interests*. 2018 [cited 2018; Lab website]. Available from: http://physioweb.uvm.edu/warshaw-lab/research-interests/myosin-binding-protein-c-mybp-c/.
21. Jeremy Berg, J.T., Lubert Stryer, *Biochemistry*. 5th ed. 2002: W.H. Freeman and Company.
22. Homburger, J.R., et al., *Multidimensional structure-function relationships in human beta-cardiac myosin from population-scale genetic variation.* Proc Natl Acad Sci U S A, 2016. **113**(24): p. 6701-6.
23. Semsarian, C., et al., *New perspectives on the prevalence of hypertrophic cardiomyopathy.* J Am Coll Cardiol, 2015. **65**(12): p. 1249-1254.
24. Maron, B.J., et al., *Demographics and Epidemiology of Sudden Deaths in Young Competitive Athletes: From the United States National Registry.* Am J Med, 2016. **129**(11): p. 1170-1177.
25. Spudich, J.A., *Hypertrophic and dilated cardiomyopathy: four decades of basic research on muscle lead to potential therapeutic approaches to these devastating genetic diseases.* Biophys J, 2014. **106**(6): p. 1236-49.
26. Watkins, H., H. Ashrafian, and C. Redwood, *Inherited cardiomyopathies.* N Engl J Med, 2011. **364**(17): p. 1643-56.
27. Maron, B.J. and M.S. Maron, *Hypertrophic cardiomyopathy.* Lancet, 2013. **381**(9862): p. 242-55.
28. Park, H.Y., *Hereditary Dilated Cardiomyopathy: Recent Advances in Genetic Diagnostics.* Korean Circ J, 2017. **47**(3): p. 291-298.
29. Tayal, U., S. Prasad, and S.A. Cook, *Genetics and genomics of dilated cardiomyopathy and systolic heart failure.* Genome Med, 2017. **9**(1): p. 20.
30. Sweeney, H.L. and A. Houdusse, *Structural and functional insights into the Myosin motor mechanism.* Annu Rev Biophys, 2010. **39**: p. 539-57.
31. Houdusse, A., A.G. Szent-Gyorgyi, and C. Cohen, *Three conformational states of scallop myosin S1.* Proc Natl Acad Sci U S A, 2000. **97**(21): p. 11238-43.
32. Preller, M. and D.J. Manstein, *Myosin structure, allostery, and mechano-chemistry.* Structure, 2013. **21**(11): p. 1911-22.
33. Houdusse, A. and H.L. Sweeney, *How Myosin Generates Force on Actin Filaments.* Trends Biochem Sci, 2016. **41**(12): p. 989-997.
34. Manstein, D.J., *Molecular engineering of myosin.* Philos Trans R Soc Lond B Biol Sci, 2004. **359**(1452): p. 1907-12.
35. Sweeney, H.L. and A. Houdusse, *The motor mechanism of myosin V: insights for muscle contraction.* Philos Trans R Soc Lond B Biol Sci, 2004. **359**(1452): p. 1829-41.

36. Mehta, A.D., et al., *Myosin-V is a processive actin-based motor.* Nature, 1999. **400**(6744): p. 590-3.
37. Rief, M., et al., *Myosin-V stepping kinetics: a molecular model for processivity.* Proc Natl Acad Sci U S A, 2000. **97**(17): p. 9482-6.
38. Trybus, K.M., *Myosin V from head to tail.* Cell Mol Life Sci, 2008. **65**(9): p. 1378-89.
39. Enjuto, M., et al., *Malignant hypertrophic cardiomyopathy caused by the Arg723Gly mutation in beta-myosin heavy chain gene.* J Mol Cell Cardiol, 2000. **32**(12): p. 2307-13.
40. Kamisago, M., et al., *Mutations in sarcomere protein genes as a cause of dilated cardiomyopathy.* N Engl J Med, 2000. **343**(23): p. 1688-96.
41. Thomas, D.D., D. Kast, and V.L. Korman, *Site-directed spectroscopic probes of actomyosin structural dynamics.* Annu Rev Biophys, 2009. **38**: p. 347-69.
42. Muretta, J.M., et al., *High-performance time-resolved fluorescence by direct waveform recording.* The Review of scientific instruments, 2010. **81**(10): p. 103101.
43. Muretta, J.M., et al., *Direct real-time detection of the structural and biochemical events in the myosin power stroke.* Proc Natl Acad Sci U S A, 2015. **112**(46): p. 14272-7.
44. Rohde, J.A., Thomas, D.D., and Muretta, J.M., *A heart failure drug changes the mechano-enzymology of the cardiac myosin powerstroke.* Proc Natl Acad Sci U S A, Manuscript in Review, 2016.
45. Mozaffarian, D., et al., *Heart Disease and Stroke Statistics-2016 Update: A Report From the American Heart Association.* Circulation, 2016. **133**(4): p. e38-e360.
46. Fonarow, G.C., et al., *Characteristics, treatments, and outcomes of patients with preserved systolic function hospitalized for heart failure: a report from the OPTIMIZE-HF Registry.* J Am Coll Cardiol, 2007. **50**(8): p. 768-77.
47. Solaro, R.J. and J.C. Tardiff, *Biophysics of the failing heart : physics and biology of heart muscle*. Biological and medical physics, biomedical engineering,. vi, 253 pages.
48. Teerlink, J.R., et al., *Acute Treatment With Omecamtiv Mecarbil to Increase Contractility in Acute Heart Failure: The ATOMIC-AHF Study.* J Am Coll Cardiol, 2016. **67**(12): p. 1444-1455.
49. Winkelmann, D.A., et al., *Structural basis for drug-induced allosteric changes to human beta-cardiac myosin motor activity.* Nat Commun, 2015. **6**: p. 7974.
50. Aksel, T., et al., *Ensemble force changes that result from human cardiac myosin mutations and a small-molecule effector.* Cell Rep, 2015. **11**(6): p. 910-20.
51. Cleland, J.G., et al., *The effects of the cardiac myosin activator, omecamtiv mecarbil, on cardiac function in systolic heart failure: a double-blind, placebo-controlled, crossover, dose-ranging phase 2 trial.* Lancet, 2011. **378**(9792): p. 676-83.
52. Greenberg, B.H., et al., *Safety and tolerability of omecamtiv mecarbil during exercise in patients with ischemic cardiomyopathy and angina.* JACC Heart Fail, 2015. **3**(1): p. 22-9.

53. Mamidi, R., et al., *Molecular effects of the myosin activator omecamtiv mecarbil on contractile properties of skinned myocardium lacking cardiac myosin binding protein-C.* J Mol Cell Cardiol, 2015. **85**: p. 262-72.
54. Woody, M.S., et al., *Positive cardiac inotrope omecamtiv mecarbil activates muscle despite suppressing the myosin working stroke.* Nat Commun, 2018. **9**(1): p. 3838.
55. Nanasi, P., Jr., et al., *Omecamtiv mecarbil activates ryanodine receptors from canine cardiac but not skeletal muscle.* Eur J Pharmacol, 2017. **809**: p. 73-79.
56. Medicine, U.S.N.L.o., *GALACTIC-HF*. 2019, NIH: ClinicalTrials.gov.
57. Permissions, S.R., *Reprints and Permissions.* Science, 2019.
58. Permissions, N.R., *Reprints & Permissions.* Nature, 2019.
59. Maron, B.J., et al., *Prevalence of hypertrophic cardiomyopathy in a general population of young adults. Echocardiographic analysis of 4111 subjects in the CARDIA Study. Coronary Artery Risk Development in (Young) Adults.* Circulation, 1995. **92**(4): p. 785-9.
60. Kawas, R.F., et al., *A small molecule modulator of cardiac myosin acts on multiple stages of the myosin chemomechanical cycle.* The Journal of biological chemistry, 2017.
61. Stern, J.A., et al., *A Small Molecule Inhibitor of Sarcomere Contractility Acutely Relieves Left Ventricular Outflow Tract Obstruction in Feline Hypertrophic Cardiomyopathy.* PLoS One, 2016. **11**(12): p. e0168407.
62. Stewart, M.A., et al., *Myosin ATP turnover rate is a mechanism involved in thermogenesis in resting skeletal muscle fibers.* Proceedings of the National Academy of Sciences of the United States of America, 2010. **107**(1): p. 430-5.
63. Hooijman, P., M.A. Stewart, and R. Cooke, *A new state of cardiac myosin with very slow ATP turnover: a potential cardioprotective mechanism in the heart.* Biophysical journal, 2011. **100**(8): p. 1969-76.
64. Wilson, C., et al., *The myosin inhibitor blebbistatin stabilizes the super-relaxed state in skeletal muscle.* Biophysical journal, 2014. **107**(7): p. 1637-46.
65. Xu, S., et al., *Stabilization of helical order in the thick filaments by blebbistatin: further evidence of coexisting multiple conformations of myosin.* Biophysical journal, 2009. **96**(9): p. 3673-81.
66. Zoghbi, M.E., et al., *Three-dimensional structure of vertebrate cardiac muscle myosin filaments.* Proceedings of the National Academy of Sciences of the United States of America, 2008. **105**(7): p. 2386-90.
67. Jung, H.S., et al., *Head-head and head-tail interaction: a general mechanism for switching off myosin II activity in cells.* Mol Biol Cell, 2008. **19**(8): p. 3234-42.
68. Gyimesi, M., et al., *The mechanism of the reverse recovery step, phosphate release, and actin activation of Dictyostelium myosin II.* The Journal of biological chemistry, 2008. **283**(13): p. 8153-63.
69. Lee, K.H., et al., *Interacting-heads motif has been conserved as a mechanism of myosin II inhibition since before the origin of animals.* Proceedings of the National Academy of Sciences of the United States of America, 2018. **115**(9): p. E1991-E2000.
70. Wendt, T., et al., *Three-dimensional image reconstruction of dephosphorylated smooth muscle heavy meromyosin reveals asymmetry in the interaction between*

myosin heads and placement of subfragment 2. Proceedings of the National Academy of Sciences of the United States of America, 2001. **98**(8): p. 4361-6.
71. Craig, R. and J.L. Woodhead, *Structure and function of myosin filaments.* Current opinion in structural biology, 2006. **16**(2): p. 204-12.
72. Burgess, S.A., et al., *Structures of smooth muscle myosin and heavy meromyosin in the folded, shutdown state.* Journal of molecular biology, 2007. **372**(5): p. 1165-78.
73. Al-Khayat, H.A., et al., *Atomic model of the human cardiac muscle myosin filament.* Proceedings of the National Academy of Sciences of the United States of America, 2013. **110**(1): p. 318-23.
74. Nag, S., et al., *The myosin mesa and the basis of hypercontractility caused by hypertrophic cardiomyopathy mutations.* Nature structural & molecular biology, 2017. **24**(6): p. 525-533.
75. Anderson, R., DV Trivedi, SS Sarkar, M Henze, W Ma, H Gong, CS Rogers, FL Wong, M Morck, JG Seidman, KM Ruppel, TC Irving, R Cooke, EM Green, JA Spudich *Mavacamten stabilizes a folded-back sequestered super-relaxed state of β-cardiac myosin*. BioRxiv, 2018. DOI: https://doi.org/10.1101/266783.
76. PNAS. *Rights and Permissions*. 2019 [cited 2019; Available from: http://www.pnas.org/page/about/rights-permissions.
77. Nesmelov, Y.E., et al., *Structural kinetics of myosin by transient time-resolved FRET.* Proceedings of the National Academy of Sciences of the United States of America, 2011. **108**(5): p. 1891-6.
78. Thomas, D.D., D. Kast, and V.L. Korman, *Site-directed spectroscopic probes of actomyosin structural dynamics.* Annual review of biophysics, 2009. **38**: p. 347-69.
79. Agafonov, R.V., et al., *Structural dynamics of the myosin relay helix by time-resolved EPR and FRET.* Proceedings of the National Academy of Sciences of the United States of America, 2009. **106**(51): p. 21625-30.
80. Kintses, B., Z. Yang, and A. Malnasi-Csizmadia, *Experimental investigation of the seesaw mechanism of the relay region that moves the myosin lever arm.* The Journal of biological chemistry, 2008. **283**(49): p. 34121-8.
81. Dominguez, R., et al., *Crystal structure of a vertebrate smooth muscle myosin motor domain and its complex with the essential light chain: visualization of the pre-power stroke state.* Cell, 1998. **94**(5): p. 559-71.
82. Kuhlman, P.A. and C.R. Bagshaw, *ATPase kinetics of the Dictyostelium discoideum myosin II motor domain.* Journal of muscle research and cell motility, 1998. **19**(5): p. 491-504.
83. Conibear, P.B., P.A. Kuhlman, and C.R. Bagshaw, *Measurement of ATPase activities of myosin at the level of tracks and single molecules.* Advances in experimental medicine and biology, 1998. **453**: p. 15-26; discussion 26-7.
84. Chaen, S., et al., *Measurement of ATP turnover during shortening and lengthening of rabbit psoas myofibrils using a fluorescent ATP analog.* Advances in experimental medicine and biology, 1998. **453**: p. 569-76.
85. Rayment, I., et al., *Three-dimensional structure of myosin subfragment-1: a molecular motor.* Science, 1993. **261**(5117): p. 50-8.
86. White, H.D., B. Belknap, and M.R. Webb, *Kinetics of nucleoside triphosphate cleavage and phosphate release steps by associated rabbit skeletal actomyosin,*

measured using a novel fluorescent probe for phosphate. Biochemistry, 1997. **36**(39): p. 11828-36.
87. Lakowicz, J.R., *Principles of Fluorescent Spectroscopy*. 3rd ed. 2006: Springer.
88. De La Cruz, E.M. and E.M. Ostap, *Kinetic and equilibrium analysis of the myosin ATPase.* Methods in enzymology, 2009. **455**: p. 157-92.
89. Brune, M., et al., *Direct, real-time measurement of rapid inorganic phosphate release using a novel fluorescent probe and its application to actomyosin subfragment 1 ATPase.* Biochemistry, 1994. **33**(27): p. 8262-71.
90. Capitanio, M., et al., *Ultrafast force-clamp spectroscopy of single molecules reveals load dependence of myosin working stroke.* Nature methods, 2012. **9**(10): p. 1013-9.
91. Allingham, J.S., R. Smith, and I. Rayment, *The structural basis of blebbistatin inhibition and specificity for myosin II.* Nature structural & molecular biology, 2005. **12**(4): p. 378-9.
92. Smith, C.A. and I. Rayment, *X-ray structure of the magnesium(II).ADP.vanadate complex of the Dictyostelium discoideum myosin motor domain to 1.9 A resolution.* Biochemistry, 1996. **35**(17): p. 5404-17.
93. Takacs, B., et al., *Myosin complexed with ADP and blebbistatin reversibly adopts a conformation resembling the start point of the working stroke.* Proceedings of the National Academy of Sciences of the United States of America, 2010. **107**(15): p. 6799-804.
94. Huxley, A.F. and R.M. Simmons, *Proposed mechanism of force generation in striated muscle.* Nature, 1971. **233**(5321): p. 533-8.
95. Margossian, S.S. and S. Lowey, *Preparation of myosin and its subfragments from rabbit skeletal muscle.* Methods in enzymology, 1982. **85 Pt B**: p. 55-71.
96. Kast, D., et al., *Phosphorylation-induced structural changes in smooth muscle myosin regulatory light chain.* Proceedings of the National Academy of Sciences of the United States of America, 2010. **107**(18): p. 8207-12.
97. Prochniewicz, E., T.F. Walseth, and D.D. Thomas, *Structural dynamics of actin during active interaction with myosin: different effects of weakly and strongly bound myosin heads.* Biochemistry, 2004. **43**(33): p. 10642-52.
98. Hopkins, S.C., et al., *Orientation changes of the myosin light chain domain during filament sliding in active and rigor muscle.* Journal of molecular biology, 2002. **318**(5): p. 1275-91.
99. Brissette, P., D.P. Ballou, and V. Massey, *Determination of the dead time of a stopped-flow fluorometer.* Analytical biochemistry, 1989. **181**(2): p. 234-8.
100. Beechem, J.M., *Global analysis of biochemical and biophysical data.* Methods in enzymology, 1992. **210**: p. 37-54.
101. Johnson, K.A., *Fitting enzyme kinetic data with KinTek Global Kinetic Explorer.* Methods in enzymology, 2009. **467**: p. 601-26.
102. Johnson, K.A., Z.B. Simpson, and T. Blom, *Global kinetic explorer: a new computer program for dynamic simulation and fitting of kinetic data.* Analytical biochemistry, 2009. **387**(1): p. 20-9.
103. Johnson, K.A., Z.B. Simpson, and T. Blom, *FitSpace explorer: an algorithm to evaluate multidimensional parameter space in fitting kinetic data.* Analytical biochemistry, 2009. **387**(1): p. 30-41.

104. Trivedi, D.V., et al., *Direct measurements of the coordination of lever arm swing and the catalytic cycle in myosin V.* Proceedings of the National Academy of Sciences of the United States of America, 2015. **112**(47): p. 14593-8.
105. Muretta, J.M., et al., *Loop L5 assumes three distinct orientations during the ATPase cycle of the mitotic kinesin Eg5: a transient and time-resolved fluorescence study.* The Journal of biological chemistry, 2013. **288**(48): p. 34839-49.
106. Muretta, J.M., et al., *The structural kinetics of switch-1 and the neck linker explain the functions of kinesin-1 and Eg5.* Proceedings of the National Academy of Sciences of the United States of America, 2015. **112**(48): p. E6606-13.
107. Deacon, J.C., et al., *Identification of functional differences between recombinant human alpha and beta cardiac myosin motors.* Cellular and molecular life sciences : CMLS, 2012. **69**(13): p. 2261-77.
108. Wang, Y., K. Ajtai, and T.P. Burghardt, *Analytical comparison of natural and pharmaceutical ventricular myosin activators.* Biochemistry, 2014. **53**(32): p. 5298-306.
109. Baker, J.E. and D.D. Thomas, *A thermodynamic muscle model and a chemical basis for A.V. Hill's muscle equation.* Journal of muscle research and cell motility, 2000. **21**(4): p. 335-44.
110. Baker, J.E. and D.D. Thomas, *Thermodynamics and kinetics of a molecular motor ensemble.* Biophysical journal, 2000. **79**(4): p. 1731-1736.
111. Karatzaferi, C., M.K. Chinn, and R. Cooke, *The force exerted by a muscle cross-bridge depends directly on the strength of the actomyosin bond.* Biophysical journal, 2004. **87**(4): p. 2532-2544.
112. Kovacs, M., et al., *Mechanism of blebbistatin inhibition of myosin II.* The Journal of biological chemistry, 2004. **279**(34): p. 35557-63.
113. Malnasi-Csizmadia, A., R.J. Woolley, and C.R. Bagshaw, *Resolution of conformational states of Dictyostelium myosin II motor domain using tryptophan (W501) mutants: implications for the open-closed transition identified by crystallography.* Biochemistry, 2000. **39**(51): p. 16135-46.
114. Eyring, H., *The activated complex in chemical reactions.* The Journal of Chemical Physics, 1935. **3**(2): p. 107-115.
115. Fusi, L., Z. Huang, and M. Irving, *The Conformation of Myosin Heads in Relaxed Skeletal Muscle: Implications for Myosin-Based Regulation.* Biophysical journal, 2015. **109**(4): p. 783-92.
116. Huxley, H.E. and W. Brown, *The low-angle x-ray diagram of vertebrate striated muscle and its behaviour during contraction and rigor.* J Mol Biol, 1967. **30**(2): p. 383-434.
117. Xu, S., et al., *Temperature and ligand dependence of conformation and helical order in myosin filaments.* Biochemistry, 2003. **42**(2): p. 390-401.
118. Reconditi, M., et al., *Sarcomere-length dependence of myosin filament structure in skeletal muscle fibres of the frog.* The Journal of physiology, 2014. **592**(5): p. 1119-37.
119. Kampourakis, T., S. Ponnam, and M. Irving, *Hypertrophic cardiomyopathy mutation R58Q in the myosin regulatory light chain perturbs thick filament-based regulation in cardiac muscle.* J Mol Cell Cardiol, 2018. **117**: p. 72-81.

120. Trivedi, D.V., et al., *Hypertrophic cardiomyopathy and the myosin mesa: viewing an old disease in a new light.* Biophys Rev, 2018. **10**(1): p. 27-48.
121. Reconditi, M., et al., *Motion of myosin head domains during activation and force development in skeletal muscle.* Proceedings of the National Academy of Sciences of the United States of America, 2011. **108**(17): p. 7236-40.
122. Woodhead, J.L., et al., *Atomic model of a myosin filament in the relaxed state.* Nature, 2005. **436**(7054): p. 1195-9.
123. Woodhead, J.L., F.Q. Zhao, and R. Craig, *Structural basis of the relaxed state of a Ca2+-regulated myosin filament and its evolutionary implications.* Proc Natl Acad Sci U S A, 2013. **110**(21): p. 8561-6.
124. McNamara, J.W., et al., *MYBPC3 mutations are associated with a reduced super-relaxed state in patients with hypertrophic cardiomyopathy.* PLoS One, 2017. **12**(6): p. e0180064.
125. Cooke, R., *The role of the myosin ATPase activity in adaptive thermogenesis by skeletal muscle.* Biophys Rev, 2011. **3**(1): p. 33-45.
126. Trybus, K.M., et al., *Spare the rod, spoil the regulation: necessity for a myosin rod.* Proc Natl Acad Sci U S A, 1997. **94**(1): p. 48-52.
127. Ellison, P.A., J.R. Sellers, and C.R. Cremo, *Kinetics of smooth muscle heavy meromyosin with one thiophosphorylated head.* The Journal of biological chemistry, 2000. **275**(20): p. 15142-51.
128. Zhang, X., et al., *Distinct contributions of the thin and thick filaments to length-dependent activation in heart muscle.* eLife, 2017. **6**.
129. Kampourakis, T., et al., *Omecamtiv mercabil and blebbistatin modulate cardiac contractility by perturbing the regulatory state of the myosin filament.* The Journal of physiology, 2018. **596**(1): p. 31-46.
130. Naber, N., R. Cooke, and E. Pate, *Slow myosin ATP turnover in the super-relaxed state in tarantula muscle.* J Mol Biol, 2011. **411**(5): p. 943-50.
131. Fusi, L., et al., *Thick filament mechano-sensing is a calcium-independent regulatory mechanism in skeletal muscle.* Nat Commun, 2016. **7**: p. 13281.
132. Kampourakis, T., et al., *Omecamtiv Mercabil and Blebbistatin modulate cardiac contractility by perturbing the regulatory state of the myosin filament.* The Journal of physiology, 2017.
133. Kouyama, T. and K. Mihashi, *Fluorimetry study of N-(1-pyrenyl)iodoacetamide-labelled F-actin. Local structural change of actin protomer both on polymerization and on binding of heavy meromyosin.* Eur J Biochem, 1981. **114**(1): p. 33-8.
134. Sirigu, S., et al., *Highly selective inhibition of myosin motors provides the basis of potential therapeutic application.* Proc Natl Acad Sci U S A, 2016. **113**(47): p. E7448-E7455.
135. Lanzetta, P.A., et al., *An improved assay for nanomole amounts of inorganic phosphate.* Anal Biochem, 1979. **100**(1): p. 95-7.
136. JBC, *Editorial Policies: Copyright and license to publish.* Journal of Biological Chemistry, 2019.
137. De La Cruz, E.M. and E.M. Ostap, *Relating biochemistry and function in the myosin superfamily.* Curr Opin Cell Biol, 2004. **16**(1): p. 61-7.
138. Syamaladevi, D.P., J.A. Spudich, and R. Sowdhamini, *Structural and functional insights on the Myosin superfamily.* Bioinform Biol Insights, 2012. **6**: p. 11-21.

139. Heissler, S.M. and J.R. Sellers, *Myosin light chains: Teaching old dogs new tricks.* Bioarchitecture, 2014. **4**(6): p. 169-88.
140. Jacobs, D.J., et al., *Kinetics and thermodynamics of the rate-limiting conformational change in the actomyosin V mechanochemical cycle.* J Mol Biol, 2011. **407**(5): p. 716-30.
141. Swenson, A.M., et al., *Magnesium modulates actin binding and ADP release in myosin motors.* J Biol Chem, 2014. **289**(34): p. 23977-91.
142. Trivedi, D.V., et al., *Direct measurements of the coordination of lever arm swing and the catalytic cycle in myosin V.* Proc Natl Acad Sci U S A, 2015. **112**(47): p. 14593-8.
143. Trivedi, D.V., et al., *Magnesium impacts myosin V motor activity by altering key conformational changes in the mechanochemical cycle.* Biochemistry, 2013. **52**(27): p. 4710-22.
144. Yengo, C.M., et al., *Kinetic characterization of the weak binding states of myosin V.* Biochemistry, 2002. **41**(26): p. 8508-17.
145. Yengo, C.M. and H.L. Sweeney, *Functional role of loop 2 in myosin V.* Biochemistry, 2004. **43**(9): p. 2605-12.
146. De La Cruz, E.M. and E.M. Ostap, *Kinetic and equilibrium analysis of the myosin ATPase.* Methods Enzymol, 2009. **455**: p. 157-92.
147. De La Cruz, E.M., et al., *The kinetic mechanism of myosin V.* Proc Natl Acad Sci U S A, 1999. **96**(24): p. 13726-31.
148. Greenberg, M.J., et al., *A Perspective on the Role of Myosins as Mechanosensors.* Biophys J, 2016. **110**(12): p. 2568-2576.
149. Fenn, W.O., *The relation between the work performed and the energy liberated in muscular contraction.* J Physiol, 1924. **58**(6): p. 373-95.
150. Mentes, A., et al., *High-resolution cryo-EM structures of actin-bound myosin states reveal the mechanism of myosin force sensing.* Proc Natl Acad Sci U S A, 2018. **115**(6): p. 1292-1297.
151. Shuman, H., et al., *A vertebrate myosin-I structure reveals unique insights into myosin mechanochemical tuning.* Proc Natl Acad Sci U S A, 2014. **111**(6): p. 2116-21.
152. Greenberg, M.J., et al., *Mechanochemical tuning of myosin-I by the N-terminal region.* Proc Natl Acad Sci U S A, 2015. **112**(26): p. E3337-44.
153. Wulf, S.F., et al., *Force-producing ADP state of myosin bound to actin.* Proc Natl Acad Sci U S A, 2016. **113**(13): p. E1844-52.
154. Kawana, M., et al., *Biophysical properties of human beta-cardiac myosin with converter mutations that cause hypertrophic cardiomyopathy.* Sci Adv, 2017. **3**(2): p. e1601959.
155. Nyitrai, M. and M.A. Geeves, *Adenosine diphosphate and strain sensitivity in myosin motors.* Philos Trans R Soc Lond B Biol Sci, 2004. **359**(1452): p. 1867-77.
156. Brenner, B., et al., *Familial hypertrophic cardiomyopathy: functional variance among individual cardiomyocytes as a trigger of FHC-phenotype development.* Front Physiol, 2014. **5**: p. 392.
157. Kohler, J., et al., *Mutation of the myosin converter domain alters cross-bridge elasticity.* Proc Natl Acad Sci U S A, 2002. **99**(6): p. 3557-62.

158. Seebohm, B., et al., *Cardiomyopathy mutations reveal variable region of myosin converter as major element of cross-bridge compliance.* Biophys J, 2009. **97**(3): p. 806-24.
159. Debold, E.P., et al., *Hypertrophic and dilated cardiomyopathy mutations differentially affect the molecular force generation of mouse alpha-cardiac myosin in the laser trap assay.* Am J Physiol Heart Circ Physiol, 2007. **293**(1): p. H284-91.
160. Schmitt, J.P., et al., *Cardiac myosin missense mutations cause dilated cardiomyopathy in mouse models and depress molecular motor function.* Proc Natl Acad Sci U S A, 2006. **103**(39): p. 14525-30.
161. Llinas, P., et al., *How actin initiates the motor activity of Myosin.* Dev Cell, 2015. **33**(4): p. 401-12.
162. Fischer, S., et al., *Structural mechanism of the recovery stroke in the myosin molecular motor.* Proc Natl Acad Sci U S A, 2005. **102**(19): p. 6873-8.
163. Chinthalapudi, K., et al., *Mechanistic insights into the active site and allosteric communication pathways in human nonmuscle myosin-2C.* Elife, 2017. **6**.
164. Bloemink, M.J., et al., *The Relay/Converter Interface Influences Hydrolysis of ATP by Skeletal Muscle Myosin II.* J Biol Chem, 2016. **291**(4): p. 1763-73.
165. Kronert, W.A., et al., *Mapping interactions between myosin relay and converter domains that power muscle function.* J Biol Chem, 2014. **289**(18): p. 12779-90.
166. De La Cruz, E.M., et al., *Actin and light chain isoform dependence of myosin V kinetics.* Biochemistry, 2000. **39**(46): p. 14196-202.
167. Takagi, Y., et al., *Human myosin Vc is a low duty ratio, nonprocessive molecular motor.* J Biol Chem, 2008. **283**(13): p. 8527-37.
168. Whittaker, M., et al., *A 35-A movement of smooth muscle myosin on ADP release.* Nature, 1995. **378**(6558): p. 748-51.
169. Trivedi, D.V., et al., *Switch II mutants reveal coupling between the nucleotide- and actin-binding regions in myosin V.* Biophys J, 2012. **102**(11): p. 2545-55.
170. Pardee, J.D. and J.A. Spudich, *Purification of muscle actin.* Methods Enzymol, 1982. **85 Pt B**: p. 164-81.
171. Criddle, A.H., M.A. Geeves, and T. Jeffries, *The use of actin labelled with N-(1-pyrenyl)iodoacetamide to study the interaction of actin with myosin subfragments and troponin/tropomyosin.* Biochem J, 1985. **232**(2): p. 343-9.
172. Sasaki, N. and K. Sutoh, *Structure-mutation analysis of the ATPase site of Dictyostelium discoideum myosin II.* Adv Biophys, 1998. **35**: p. 1-24.
173. De La Cruz, E.M., H.L. Sweeney, and E.M. Ostap, *ADP inhibition of myosin V ATPase activity.* Biophys J, 2000. **79**(3): p. 1524-9.
174. Trybus, K.M., E. Krementsova, and Y. Freyzon, *Kinetic characterization of a monomeric unconventional myosin V construct.* J Biol Chem, 1999. **274**(39): p. 27448-56.
175. Marston, S.B. and E.W. Taylor, *Comparison of the myosin and actomyosin ATPase mechanisms of the four types of vertebrate muscles.* J Mol Biol, 1980. **139**(4): p. 573-600.
176. Heissler, S.M. and D.J. Manstein, *Comparative kinetic and functional characterization of the motor domains of human nonmuscle myosin-2C isoforms.* J Biol Chem, 2011. **286**(24): p. 21191-202.

177. Wang, F., et al., *Kinetic mechanism of non-muscle myosin IIB: functional adaptations for tension generation and maintenance.* J Biol Chem, 2003. **278**(30): p. 27439-48.
178. Kovacs, M., et al., *Functional divergence of human cytoplasmic myosin II: kinetic characterization of the non-muscle IIA isoform.* J Biol Chem, 2003. **278**(40): p. 38132-40.
179. Fenn, W.O., *A quantitative comparison between the energy liberated and the work performed by the isolated sartorius muscle of the frog.* J Physiol, 1923. **58**(2-3): p. 175-203.
180. Jontes, J.D. and R.A. Milligan, *Brush border myosin-I structure and ADP-dependent conformational changes revealed by cryoelectron microscopy and image analysis.* J Cell Biol, 1997. **139**(3): p. 683-93.
181. Greenberg, M.J. and J.R. Moore, *The molecular basis of frictional loads in the in vitro motility assay with applications to the study of the loaded mechanochemistry of molecular motors.* Cytoskeleton (Hoboken), 2010. **67**(5): p. 273-85.
182. Debold, E.P., J.B. Patlak, and D.M. Warshaw, *Slip sliding away: load-dependence of velocity generated by skeletal muscle myosin molecules in the laser trap.* Biophys J, 2005. **89**(5): p. L34-6.
183. Kovacs, M., et al., *Load-dependent mechanism of nonmuscle myosin 2.* Proc Natl Acad Sci U S A, 2007. **104**(24): p. 9994-9.
184. He, Z.H., et al., *ATP consumption and efficiency of human single muscle fibers with different myosin isoform composition.* Biophys J, 2000. **79**(2): p. 945-61.
185. Sung, J., et al., *Harmonic force spectroscopy measures load-dependent kinetics of individual human beta-cardiac myosin molecules.* Nat Commun, 2015. **6**: p. 7931.
186. McCray, J.A., et al., *A new approach to time-resolved studies of ATP-requiring biological systems; laser flash photolysis of caged ATP.* Proc Natl Acad Sci U S A, 1980. **77**(12): p. 7237-41.
187. Karabina, A., et al., *Myosin regulatory light chain phosphorylation enhances cardiac beta-myosin in vitro motility under load.* Arch Biochem Biophys, 2015. **580**: p. 14-21.
188. Greenberg, M.J., et al., *Cardiomyopathy-linked myosin regulatory light chain mutations disrupt myosin strain-dependent biochemistry.* Proc Natl Acad Sci U S A, 2010. **107**(40): p. 17403-8.
189. Muretta, J.M., K.J. Petersen, and D.D. Thomas, *Direct real-time detection of the actin-activated power stroke within the myosin catalytic domain.* Proc Natl Acad Sci U S A, 2013. **110**(18): p. 7211-6.
190. Edman, K.A., *Contractile performance of striated muscle.* Adv Exp Med Biol, 2010. **682**: p. 7-40.
191. Schiaffino, S. and C. Reggiani, *Fiber types in mammalian skeletal muscles.* Physiol Rev, 2011. **91**(4): p. 1447-531.
192. Stelzer, J.E., D.P. Fitzsimons, and R.L. Moss, *Ablation of myosin-binding protein-C accelerates force development in mouse myocardium.* Biophys J, 2006. **90**(11): p. 4119-27.
193. Caorsi, V., et al., *FRET characterisation for cross-bridge dynamics in single-skinned rigor muscle fibres.* Eur Biophys J, 2011. **40**(1): p. 13-27.

194. Hamalainen, N. and D. Pette, *The histochemical profiles of fast fiber types IIB, IID, and IIA in skeletal muscles of mouse, rat, and rabbit.* J Histochem Cytochem, 1993. **41**(5): p. 733-43.
195. Agbulut, O., et al., *Myosin heavy chain isoforms in postnatal muscle development of mice.* Biol Cell, 2003. **95**(6): p. 399-406.
196. Kammoun, M., et al., *A simplified immunohistochemical classification of skeletal muscle fibres in mouse.* Eur J Histochem, 2014. **58**(2): p. 2254.
197. Kim, D.M. and J.R. Swartz, *Prolonging cell-free protein synthesis with a novel ATP regeneration system.* Biotechnol Bioeng, 1999. **66**(3): p. 180-8.
198. Kast, D., et al., *Phosphorylation-induced structural changes in smooth muscle myosin regulatory light chain.* Proc Natl Acad Sci U S A, 2010. **107**(18): p. 8207-12.
199. Chal, J., et al., *Differentiation of pluripotent stem cells to muscle fiber to model Duchenne muscular dystrophy.* Nat Biotechnol, 2015. **33**(9): p. 962-9.
200. Clemen, A.E., et al., *Force-dependent stepping kinetics of myosin-V.* Biophys J, 2005. **88**(6): p. 4402-10.
201. Muretta, J.M., et al., *High-performance time-resolved fluorescence by direct waveform recording.* Rev Sci Instrum, 2010. **81**(10): p. 103101.
202. Houdusse, A., et al., *Atomic structure of scallop myosin subfragment S1 complexed with MgADP: a novel conformation of the myosin head.* Cell, 1999. **97**(4): p. 459-70.
203. Harris, S.P., et al., *Hypertrophic cardiomyopathy in cardiac myosin binding protein-C knockout mice.* Circ Res, 2002. **90**(5): p. 594-601.
204. Writing Group, M., et al., *Heart Disease and Stroke Statistics-2016 Update: A Report From the American Heart Association.* Circulation, 2016. **133**(4): p. e38-360.
205. Fonarow, G.C., et al., *Characteristics, treatments, and outcomes of patients with preserved systolic function hospitalized for heart failure: a report from the OPTIMIZE-HF Registry.* J Am Coll Cardiol, 2007. **50**(8): p. 768-77.
206. Maron, B.J., et al., *Contemporary definitions and classification of the cardiomyopathies: an American Heart Association Scientific Statement from the Council on Clinical Cardiology, Heart Failure and Transplantation Committee; Quality of Care and Outcomes Research and Functional Genomics and Translational Biology Interdisciplinary Working Groups; and Council on Epidemiology and Prevention.* Circulation, 2006. **113**(14): p. 1807-16.
207. Nesmelov, Y.E., et al., *Structural kinetics of myosin by transient time-resolved FRET.* Proc Natl Acad Sci U S A, 2011. **108**(5): p. 1891-6.
208. Hooijman, P., M.A. Stewart, and R. Cooke, *A new state of cardiac myosin with very slow ATP turnover: a potential cardioprotective mechanism in the heart.* Biophys J, 2011. **100**(8): p. 1969-76.
209. Kampourakis, T. and M. Irving, *Phosphorylation of myosin regulatory light chain controls myosin head conformation in cardiac muscle.* J Mol Cell Cardiol, 2015. **85**: p. 199-206.
210. Manning, E.P., J.C. Tardiff, and S.D. Schwartz, *A model of calcium activation of the cardiac thin filament.* Biochemistry, 2011. **50**(34): p. 7405-13.

211. Sugi, H., et al., *Evidence for the load-dependent mechanical efficiency of individual myosin heads in skeletal muscle fibers activated by laser flash photolysis of caged calcium in the presence of a limited amount of ATP.* Proc Natl Acad Sci U S A, 1998. **95**(5): p. 2273-8.
212. Greenberg, M.J., H. Shuman, and E.M. Ostap, *Inherent force-dependent properties of beta-cardiac myosin contribute to the force-velocity relationship of cardiac muscle.* Biophys J, 2014. **107**(12): p. L41-4.
213. Woodward, S.K., J.F. Eccleston, and M.A. Geeves, *Kinetics of the interaction of 2'(3')-O-(N-methylanthraniloyl)-ATP with myosin subfragment 1 and actomyosin subfragment 1: characterization of two acto-S1-ADP complexes.* Biochemistry, 1991. **30**(2): p. 422-30.
214. Nag, S., et al., *The myosin mesa and the basis of hypercontractility caused by hypertrophic cardiomyopathy mutations.* Nat Struct Mol Biol, 2017. **24**(6): p. 525-533.
215. Zoghbi, M.E., et al., *Three-dimensional structure of vertebrate cardiac muscle myosin filaments.* Proc Natl Acad Sci U S A, 2008. **105**(7): p. 2386-90.
216. Stewart, M.A., et al., *Myosin ATP turnover rate is a mechanism involved in thermogenesis in resting skeletal muscle fibers.* Proc Natl Acad Sci U S A, 2010. **107**(1): p. 430-5.
217. Rohde, J.A., D.D. Thomas, and J.M. Muretta, *Heart failure drug changes the mechanoenzymology of the cardiac myosin powerstroke.* Proc Natl Acad Sci U S A, 2017. **114**(10): p. E1796-E1804.
218. Schaaf, T.M., et al., *High-Throughput Spectral and Lifetime-Based FRET Screening in Living Cells to Identify Small-Molecule Effectors of SERCA.* SLAS Discov, 2017. **22**(3): p. 262-273.
219. Rebbeck, R.T., et al., *High-Throughput Screens to Discover Small-Molecule Modulators of Ryanodine Receptor Calcium Release Channels.* SLAS Discov, 2017. **22**(2): p. 176-186.
220. Bryant, Z., D. Altman, and J.A. Spudich, *The power stroke of myosin VI and the basis of reverse directionality.* Proc Natl Acad Sci U S A, 2007. **104**(3): p. 772-7.
221. Coirault, C., et al., *Oxidative stress of myosin contributes to skeletal muscle dysfunction in rats with chronic heart failure.* Am J Physiol Heart Circ Physiol, 2007. **292**(2): p. H1009-17.
222. Fealey, M.E., et al., *Structural Impact of Phosphorylation and Dielectric Constant Variation on Synaptotagmin's IDR.* Biophys J, 2018. **114**(3): p. 550-561.
223. Piana, S., K. Lindorff-Larsen, and D.E. Shaw, *Protein folding kinetics and thermodynamics from atomistic simulation.* Proc Natl Acad Sci U S A, 2012. **109**(44): p. 17845-50.
224. Tanaka, J., et al., *Comparative characterization of random-sequence proteins consisting of 5, 12, and 20 kinds of amino acids.* Protein Sci, 2010. **19**(4): p. 786-95.